I.R.Iran

ISSN:2423-5547
e-ISSN:2423-7469

JREE

Journal of Renewable Energy and Environment

Journal of Renewable Energy and Environment

Volume 10, Number 3, Summer 2023

Materials and Energy Research Center

Iranian Association of Chemical Engineers

In the Name of God

Journal of Renewable Energy and Environment

DIRECTOR-IN-CHARGE

H. Omidvar

Amirkabir University of Technology (Tehran Polytechnic), Tehran, Iran

EDITOR-IN-CHIEF

M. Pazouki

Materials and Energy Research Center, Karaj, Iran

EDITORIAL BOARD

M. Ameri, Shahid Beheshti University, Tehran, Iran

S. S. Chandel, Shoolini University, Solan, Himachal Pradesh, India

J. Chaouki, Polytechnique Montréal, Montreal, Canada

H. Ghadamian, Materials and Energy Research Center, Karaj, Iran

B. Ghobadian, Tarbiat Modares University, Tehran, Iran

W. K. H. Hogland, Linnaeus University, Kalmar, Sweden

S. M. Hosseinalipoor, Iran University of Science and Technology, Tehran, Iran

H. A. Kazem, Sohar University, Sohar, Sultanate of Oman

K. Kaygusuz, Karadeniz Technical University, Trabzon, Turkey

A. Mostafaeipour, Yazd University, Yazd, Iran

G. H. Najafi, Tarbiat Modares University, Tehran, Iran

M. R. Omidkhah, Tarbiat Modares University, Tehran, Iran

M. H. Panjeshahi, Tehran University, Tehran, Iran

M. Pazouki, Materials and Energy Research Center, Karaj, Iran

R. Roshandel, Sharif University of Technology, Tehran, Iran

M. B. Shafii, Sharif University of Technology, Tehran, Iran

J. Shayegan, Sharif University of Technology, Tehran, Iran

T. Yusaf, Federation University Australia, Ballarat, Australia

S. A. H. Zamzamian, Materials and Energy Research Center, Karaj, Iran

EDITORIAL ADVISORY BOARD

N. Azbar, Ege University, Izmir, Turkey

M. El Haj Assad, University of Sharjeh, Sharjah, United Arab Emirates

A. Maheri, University of Aberdeen, Aberdeen, United Kingdom

M. Mohanraj, Hindusthan College of Engineering and Technology, Coimbatore, Tamil Nadu, India

A. Sedaghat, Australian College of Kuwait, Kuwait

MANAGING EDITOR

M. Fouladian

LANGUAGE EDITOR

S. Saberi

PAGE DESIGNER

F. Hajizadeh

JOURNAL STAFF

M. Fouladian,V. Hajabdolali Bazzaz, E. Pouladi, R. Chaluei

DISCLAIMER

The publication of articles in *Journal of Renewable Energy and Environment* does not imply that the editorial board, reviewers, or the publisher accept, approve, or endorse the data and conclusions of authors.

Journal of Renewable Energy and Environment: (ISSN: 2423-5547) (e-ISSN: 2423-7469)

Website: www.jree.ir, E-mail: jree@merc.ac.ir

Tel: (+9826)36280040-49 (Ext. 381), Fax: (+9826)36201888

Journal of Renewable Energy and Environment, P. O. Box: 13145-1659, Tehran, Islamic Republic of Iran

Materials and Energy Research Center (MERC); Iranian Association of Chemical Engineers (IAChE)

ISSN: 2423-5547; e-ISSN: 2423-7469

Journal of Renewable Energy and Environment (JREE): Vol. 10, No. 3, (Summer 2023), 1-113

CONTENTS

AIMS AND SCOPE

Journal of Renewable Energy and Environment (JREE) publishes original papers, review articles, short communications and technical notes in the field of science and technology of renewable energies and environmental-related issues including:

- Generation
- Storage
- Conversion
- Distribution
- Management (economics, policies and planning)
- Environmental Sustainability

INSTRUCTIONS FOR AUTHORS

Submission of manuscript represents that it had neither been published nor submitted for publication elsewhere and is result of research carried out by author(s). Only the extended and upgraded articles presented in a conference and/or appeared in a symposium proceedings could be evaluated for publication.

Authors are required to include a list describing all the symbols and abbreviations in the paper. Use of the international system of measurement units is mandatory.

- On-line submission of manuscripts results in faster publication process and is recommended. Instructions are given in the JREE web sites: www.jree.ir
- References should be numbered in brackets and appear in sequence through the text. List of references should be given at the end of the paper. All journal articles listed in the References section must follow with article doi.
- Figure captions are to be indicated under the illustrations. They should sufficiently explain the figures.
- Illustrations should appear in their appropriate places in the text.
- Tables and diagrams should be submitted in a form suitable for reproduction.
- Photographs should be of high quality saved as jpg files.
- Tables' illustrations, figures and diagrams will be normally printed in single column width (8 cm). Exceptionally large ones may be printed across two columns (17 cm).

JREE: Vol. 10, No. 3, (Summer 2023) 1-12

Journal of Renewable Energy and Environment

Journal Homepage: www.jree.ir

Materials and Energy Research Center

MERC

Research Article

Investigation of the Height Distribution Effect of Residential Complex Blocks on Optimization of Cooling and Heating Loads (Tehran, District 9)

Zeinab Ghasemi Sangi, Abbas Tarkashvand, Haniyeh Sanaieian *

Department of Building and Environment, School of Architecture and Environmental Design, Iran University of Science and Technology, P. O. Box: 1684613114, Tehran, Iran.

P A P E R I N F O

Paper History:
Received: 29 May 2022
Revised: 08 October 2022
Accepted: 13 October 2022

Keywords:
Energy Optimization,
Height Distribution,
Urban Blocks,
Residential Complex,
Layout,
Simulation

A B S T R A C T

The height of buildings is one of the main features of urban configuration that affects energy consumption. However, to our knowledge, the complexity of relationships between the height parameters and energy use in urban blocks is poorly understood. In this context, the present study investigates the effect of the height distribution of buildings located in a residential complex on the energy consumption required for cooling and heating. This research simulates different possible layouts through computational software. For this purpose, first, the density of a residential complex was determined based on the rules and regulations of Tehran city and according to the site dimensions and certain site coverage. Then, the required building density was distributed in different layouts based on their diversity at different heights. The product of this stage involved 7 different layouts in which the height varied from 1 floor to the maximum number calculated in each part of the simulation. In the next step, the annual energy consumption for cooling and heating the complex was calculated for each of these layouts and compared with each other. The parametric generative model was created in the Grasshopper plugin from Rhino software, and the energy consumption was evaluated with the Honeybee plugin over one year. Also, the research findings were validated through DesignBuilder software using the EnergyPlus engine. The results of the energy simulation indicate that the height distribution of the blocks can have a significant effect on energy consumption. In the optimal case, proper layout reduces the annual cooling and heating energy consumption by 28 % and 13 %, respectively. Therefore, achieving an optimal value for each of the cooling and heating loads depends on the specific priorities and conditions of the design project. If the design project's priority is to reduce heating energy consumption, increasing the height and distributing the floors evenly between the blocks is a better answer. However, if the priority is to mitigate cooling energy consumption, the optimal layout can include low-rise blocks and a single very high-rise block.

https://doi.org/10.30501/jree.2022.344678.1380

1. INTRODUCTION

Today, more than half of the world's population live in cities, accounting for nearly two-thirds of global energy demand and 70 % of energy-related CO_2 emissions (Poponi et al., 2016). Therefore, cities are at the forefront of the need to reduce energy consumption and carbon dioxide emissions. Thus, the development of various aspects of urban layout and configuration will lock the energy use pattern for decades to come. In other words, the combination of increasing urbanization and infrastructure that is still subject to variability provides a rare time window to realize energy efficiency (Resch et al., 2016). Therefore, with the increasing development of cities worldwide, understanding the interrelationship between the characteristics of urban environments and the physical features of buildings is essential to achieving local and global sustainability goals. Since residential buildings form a major part of the urban artificial environment, investigating the interactions of residential buildings in an urban layout is very important. It can be a good way for future decisions in urban planning, urban design, and architecture, especially in the early stages of design. In this context, according to numerous studies, the early design stage is very effective in achieving the optimal performance of sustainable buildings (Konis et al., 2016; Li et al., 2018).

Therefore, although it is difficult to achieve an accurate analysis of the energy performance of the building without considering the environment and the interaction of the buildings with each other, most studies in the field of energy consumption of residential buildings have examined each building separately. Research findings on single-building design contain valuable information on energy-efficient design. However, generalization of these findings to layout is impossible and, sometimes, creates conflicting situations. In a single building, the cooling and heating load is directly related to the receivable solar radiation, the surface-to-volume ratio,

*Corresponding Author's Email: sanayeayan@iust.ac.ir (H. Sanaieian)
URL: https://www.jree.ir/article_160049.html

Please cite this article as: Ghasemi Sangi, Z., Abbas Tarkashvand, A., & Sanaieian, H. (2023). Investigation of the height distribution effect of residential complex blocks on optimization of cooling and heating loads (Tehran, district 9). *Journal of Renewable Energy and Environment (JREE)*, *10*(3), 1-12. https://doi.org/10.30501/jree.2022.344678.1380.

2423-7469/© 2023 The Author(s). Published by MERC. This is an open access article under the CC BY license (https://creativecommons.org/licenses/by/4.0/).

the size of the windows, and many other things. In cold regions, due to the need for more heating energy, it is better to increase the radiation received on the bodies, especially the south sides and, at the same time, prevent the heat exchange between inside and outside the building. This indicates a decrease in the surface-to-volume ratio on the one hand and an increase in the south surfaces and roof area, on the other hand. This relatively clear logic in the vicinity of several buildings becomes doubly complex. Increasing the south surfaces requires more buildings; this, in turn, increases the surface-to-volume ratio and the likelihood of double shading. This complexity of this situation is intensified in complex climatic situations. Therefore, despite the relatively useful information about the design of single-buildings, it is not easy to generalize energy-efficient design strategies to multi-building complexes, indicating the need for conducting independent research in this area.

Among the important and effective parameters in the layout of buildings and their interactions with each other, we can mention the issues related to the vertical layout and height of buildings in a composition consisting of several buildings, which is one of the important issues in improving building energy performance. In the present study, one of the main indicators of this issue, namely "the height distribution of the buildings in a residential complex", is examined. This study aims to fill the research gaps by exploring the relationship between the changes in the height of the blocks in a residential complex and the energy consumption required for cooling and heating. The research uses computational methods and energy simulations to explore the research questions: How to generate different strategies for different configurations and height distribution of buildings according to the specific density and cover ratio based on city zoning parameters? how does the height distribution of buildings in a residential complex affect the energy consumption required for cooling and heating? To answer these questions, first, previous studies, the final analysis of indicators, and the development of a possible correlation between independent and dependent variables were reviewed. Then, the generative model was developed to create different modes of height distribution. The obtained samples have undergone energy simulation in several stages to evaluate the cooling and heating loads, and their values are compared. Finally, after validating the findings and analyzing them, the research results have been presented. To our knowledge, no attempt has been made to optimize the height distribution of blocks in a residential complex with a comprehensive computational approach and parametric modeling in Tehran city's geographical and climatic conditions thus far. This is, thus, the first attempt to develop a mathematical model to investigate the relationship between the height parameters of blocks in a residential complex and the energy used for cooling and heating, which helps to create an optimal layout. The results obtained can pave the way for many design decisions at the early phases of the project.

2. BACKGROUND AND THEORETICAL FRAMEWORK

Research on building energy consumption is generally divided into single-building and urban scales (Rode et al., 2014; Toutou et al., 2018; Wong et al., 2011; Zhang et al., 2020), neither of which pays sufficient attention to the importance of the smaller components of the urban context. Since the 1960s, planners and architects have realized that focusing solely on individual buildings is not enough; rather, they need to extend the analysis to a group of urban buildings or blocks (Steemers, 2003). Among these, only a limited number of researches have been done on the scale of the neighborhood and urban blocks (Asfour & Alshawaf, 2015; Chen et al., 2020; Yang & Li, 2015). Regarding the larger scale of a single building, researchers have identified several physical features of the urban environment as factors affecting energy consumption in the buildings. These include horizontal building compaction (Asfour & Alshawaf, 2015; Salvati et al., 2017; Salvati et al., 2019; Trepci et al., 2020), vertical density (Li et al., 2018; Salvati et al., 2019), and differences in building height (Chen et al., 2017; Deng et al., 2016). The effect of the mentioned variables on environmental factors and building energy consumption has been studied in several types of research. Table 1 contains some of these studies.

Table 1. Several previous studies on the neighborhood and urban block scale

Study	Independent variables	Dependent variables	Year	Method	Results	Drawback
Urban block configuration and the impact on energy consumption: A case study of sinuous morphology (Shareef & Altan, 2022)	Building morphology and urban block configuration	Outdoor and indoor thermal performance	2022	Simulation	The results show the significant impact of the urban block sinuous configuration on outdoor thermal performance.	This study considers a uniform height for all buildings of sinuous configurations.
Energy efficient neighborhood design under residential zoning regulations in Shanghai (Quan, 2017)	Density, different building heights, and different layouts	Energy consumption	2017	Computational simulation experiments	The results show the great impact of the building height and the limited influence of neighborhood layout on building energy use.	This study considers the same height for all buildings in each scenario.
A parametric sensitivity analysis of the influence of urban form on domestic energy consumption for heating and cooling in a Mediterranean city (Vartholomaios, 2017)	Urban form parameters: number of floors, open space width, orientation, …	Residential energy consumption for heating and cooling	2017	Building energy simulation	There is a synergy between the strategies of high urban compactness and passive solar design, and this synergy can be achieved at different urban densities.	This research has been done in a relatively limited context.
The effect of surrounding	Arrangement of	Energy	2022	Building	The proper arrangement	This study

buildings' height and the width of the street on the building's energy consumption (Mirashk-Daghiyan et al., 2022)	adjacent buildings: number of floors and width of streets	consumption		energy simulation	of adjacent buildings can reduce energy consumption by 14.13 % compared to the initial state.	considers the same height for adjacent buildings and does not focus on the height distribution.
The study of the effects of building arrangement on microclimate and energy demand of CBD in Nanjing, China (Deng et al., 2016)	Building arrangement variations	Outdoor thermal conditions and building energy performance	2016	Numerical calculations and building energy simulation	The results indicate a quantitative correlation between building arrangement and the microclimate and building energy performance on the urban design scale.	This study only focuses on the urban scenarios with buildings in aligned arrangement, without considering the staggered arrangement.
The impacts of building height variations and building packing densities on flow adjustment and city breathability in idealized urban models (Chen et al., 2017)	Building height variation	Flow adjustment and city breathability	2017	Simulation	Taller buildings experience larger drag force and city breathability than lower buildings and those in uniform-height cases.	This study only considers six standard deviations of building height, whereas realistic cities are more complicated.
The impact of urban morphology and building's height diversity on energy consumption at the urban scale. The case study of Dubai (Shareef, 2021)	Urban morphology and building's height diversity	Cooling load	2021	Building energy simulation	The changes in the urban block morphology, particularly height diversity, have a notable impact on the cooling load.	In this research, the effect of intervening factors on the results has not been considered.
Evaluating the impact of the building density and height on the block surface temperature (Chen et al., 2020)	Building density and height	Block surface temperature	2020	Simulation model	Urban surface structures affect block surface temperatures, thermal loading of pedestrians, wind patterns, and more.	This study is only applicable to configurations with uniform height.

According to the results of studies, it can be expressed that the outdoor components, including buildings, streets, and vegetation, as well as micro-climate parameters including temperature, wind speed, relative humidity, and solar access are significantly subject to the influence of different parameters of the urban context. These factors have complex interactions with each other (Xu et al., 2020). On the other hand, microclimatic parameters also significantly affect outdoor thermal comfort and building energy demand. However, due to the lack of knowledge and tools, these issues, despite their importance, have not been well discussed in current regulations and procedures (Quan et al., 2015). In general, the urban geometry and layout of buildings, in addition to creating shadows, can greatly affect the temperature and thermal comfort; at the same time, they can trap solar radiation between surfaces, increase its wavelength, and create heat traps (Terjung & Louie, 1973). In addition, the layout of the buildings directs air flows, affecting temperature and humidity (Quan et al., 2015).

Therefore, in the layout of a complex, various factors such as granularity and proportions of blocks, orientation, compactness, and height parameters of the building are important (Leng et al., 2020), acknowledged the strong relationship of building site cover, floor area ratio, building height, road height-width ratio, green space ratio, and total wall surface area with heating energy consumption.

The parameter used in this study, namely height distribution, changes the surface-to-volume ratio and can affect the heat loss and, in general, the procedure of energy exchange with the outside environment (Figure 1).

On the other hand, by affecting the number and height of blocks in the complex, the height distribution process changes the solar radiation received by the buildings (Figure 2).

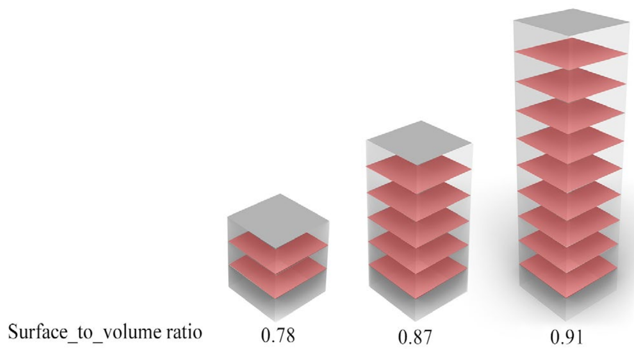

Figure 1. Variation of the surface-to-volume ratio by changing height

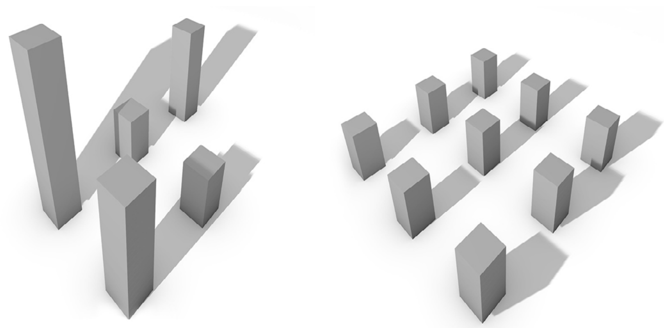

Figure 2. The effect of height distribution on the number of blocks and the quality of shading despite the constant number of floors in both cases

Due to the multiple effects of height distribution on the performance of the building and the surrounding micro-climate, predicting the energy consumption of a building under the influence of these factors is ambiguous and complex and requires research and study. For this reason, the results of previous studies are different due to the complex interaction between different patterns of space use, climatic contexts, and energy balance between different urban form factors.

3. METHOD

In general, the thermal performance of the built area can be evaluated at two levels: 1) outdoor thermal performance Chen et al., 2020; Mohajeri et al., 2016; Yang & Li, 2015) and 2) indoor thermal performance (Quan, 2017; Trepci et al., 2020; Vartholomaios, 2017). Outdoor thermal performance directly affects indoor thermal performance (Deng et al., 2016; Shareef, 2021). Thermal performance inside the building determines energy consumption. The energy inside the building is spent on various elements, such as lighting, ventilation, cooling, and heating (Shareef, 2021). The heating load is defined as the total heat energy required to maintain the temperature in an acceptable range. In contrast, the cooling load is the total heat energy that must be removed from the space to maintain the temperature in the appropriate range (Sekhar et al., 2018). A kilowatts (kW) unit or BTU[2] is used to measure the cooling or heating load.

Four tools are used to predict buildings' heating and cooling load: modeling and simulation, engineering calculations, statistical models, and machine learning-based models (Seyedzadeh et al., 2018). In general, due to the expansion of studies in this field and due to the complexity of the thermal environment of building blocks in recent years, numerical or computer simulations have become important tools for energy studies. They have successfully simulated various models from building scale to urban scale (Chen et al., 2020). Therefore, three-dimensional models representing different blocks' layout modes have been used in this study to achieve a possible relationship between the height distribution and the required energy for the heating and cooling of the building. The development of evaluated models has been carried out with a parametric modeling approach.

The research process consists of seven general steps: 1) determination of variables, 2) preparation of the modeling platform, 3) development of a generative model and different scenarios, 4) Building energy simulation, 5) review of findings and their analysis, 6) validation, and 7) conclusion (Figure 3). These cases will be discussed in more detail below.

The Grasshopper plugin in Rhino software was used to develop a parametric generator model, making algorithmic modeling and parametric simulation possible. Climate information (in this case for Tehran) has been added to the algorithm using the Ladybug plugin. The obtained information has been transferred to the EnergyPlus engine to simulate energy. This is done by the Honeybee plugin. Ladybug and Honeybee connect the Grasshopper plugin to reputable simulation engines such as EnergyPlus, Radiance, Daysim, and OpenStudio to calculate and simulate building energy, natural and artificial lighting, and more (Roudsari et al., 2013).

Finally, after completing the energy simulation process in the Grasshopper plugin, the data is re-introduced into the DesignBuilder software to test the accuracy of the findings (Figure 4).

3.1. Study area

The city of Tehran has been selected as the study area. For climate analysis, hourly data of the Tehran Climate Information File, taken from Mehrabad Airport Synoptic Meteorological Station, have been used. Table 2 summarizes the essential climate points of the study area.

[2] British Thermal Unit

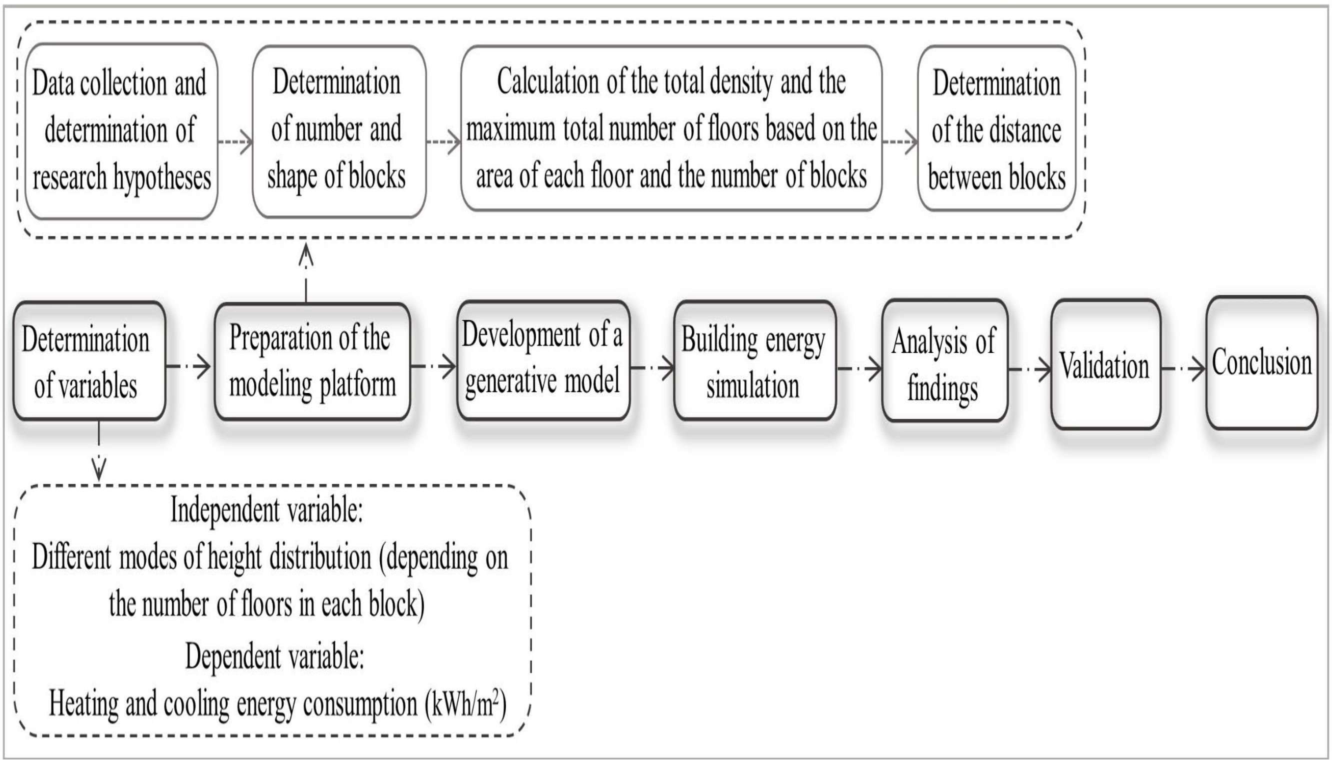

Figure 3. The research process steps

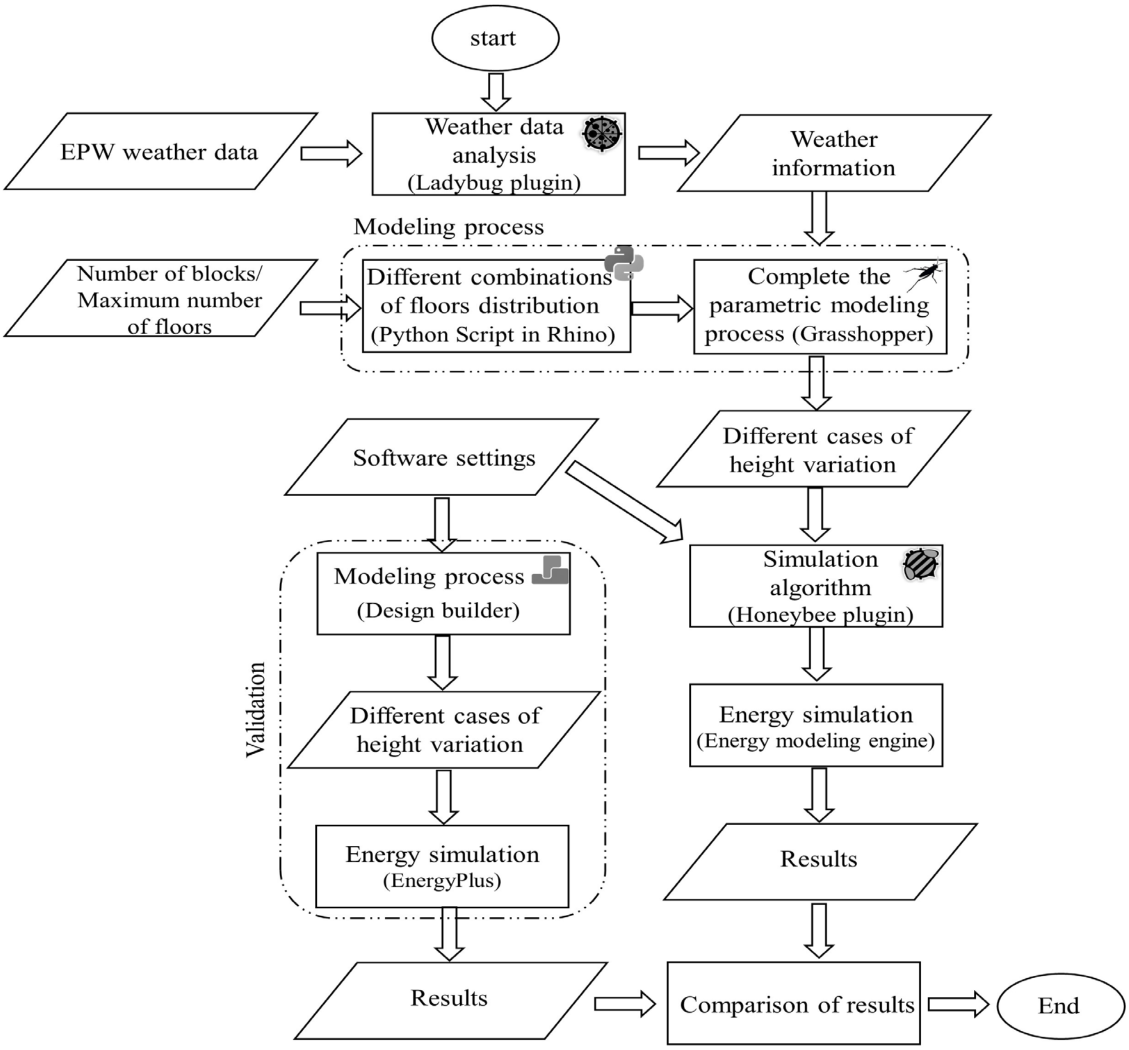

Figure 4. Method and software tools used in the building energy modeling process

Table 2. A summary of some climatic features of Tehran

Title	Description
Climate zone	Cold semi-arid climate (Köppen climate classification: BSk)
Thermal comfort condition	Summer condition: 21.5 °C to 27 °C, Winter condition: 20 °C to 23.5 °C, and relative humidity: 20 % to 65 %
Dominant requirement	Heating
Relative humidity	In summer, the relative humidity is less than in winter and dryness occurs in this season
Wind direction and wind speed	The prevailing wind blows from the west with an average speed of about 3 meters per hour

3.2. Simulation considerations

A set of assumptions is needed to start the process, including the maximum allowable density, the maximum allowable site coverage, and other basic information. In this regard, some construction rules and regulations in the city of Tehran were used. However, considering that one of the goals of this research is to employ a method to extract a proper layout from any other place, the research generative model algorithm was defined such that the rules and regulations of the same region could be utilized in the generative model for each area where the designer's intended site was located. The following initial number of blocks and their form was determined. In this regard, a residential complex consisting of 16 building blocks with a square plan, or the so-called "pavilions" form presented by Martin and March (1972), was developed. The "pavilions" form is a prevalent urban layout, and its main feature is the square shape of buildings surrounded by streets, passages, walkways, or even green paths.

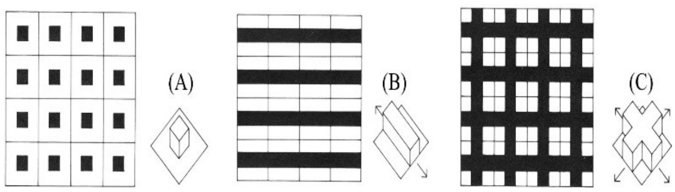

Figure 5. Buildings typology forms: (A) Pavilion, (B) Street, and (C) Court (Martin & March, 1972)

Therefore, the 4 × 4 square matrix (layout (A) in Figure 5) was selected from three different arrays presented by Martin and Mars due to the absence of the elongation interfering factor in building form and block layout. The number of blocks was selected in such a way that they would have the potential to create different modes of height distribution and prevent the creation of duplicate and innumerable modes of the layout, at the same time. According to the initial number set for the blocks, the area intended for the site, the maximum permitted building density (315 %), the maximum site coverage (35 %), and the maximum total number of floors in the complex (144 floors) were considered. Given that the obtained number indicates the "maximum" total number of floors on the site, in some stages of research, according to the requirements of that section, a smaller number of floors were used as default.

The distance between the blocks was also considered so that by removing the shading factor, the effect of height distribution on energy consumption could be investigated without the intervention of the interfering factor. In this approach, the distance between buildings is determined to as large as possible such that it is practically impossible for a building to cast shadow on another. Since the height of each floor was set at 3.5 meters, the distance between the building blocks was determined by calculating the maximum possible height of each block and then using the building shadow display tools in the Grasshopper plugin (Figure 6).

3.3. Steps and process of research

This research was conducted in three main stages:

A. Generative model

At this stage, a code or algorithm is needed that can automatically access all possible methods of distributing floors between blocks. This can be achieved through mathematical concepts such as permutations and combinations and their derivatives. With the help of the mentioned mathematical functions and by determining the number of blocks and the total number of floors required, all possibilities of height distribution between blocks can be achieved. It is important to note that the total built-up area must be considered the same in all scenarios. Figure 7 shows a part of the process that creates different scenarios of height distribution.

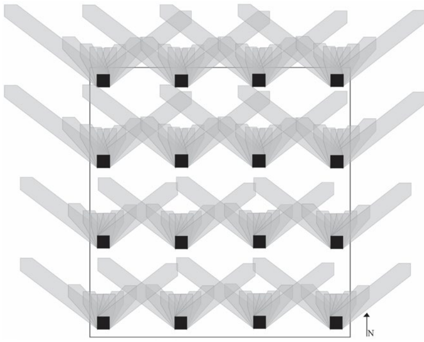

Figure 6. Achieving the right distance without shading at different times

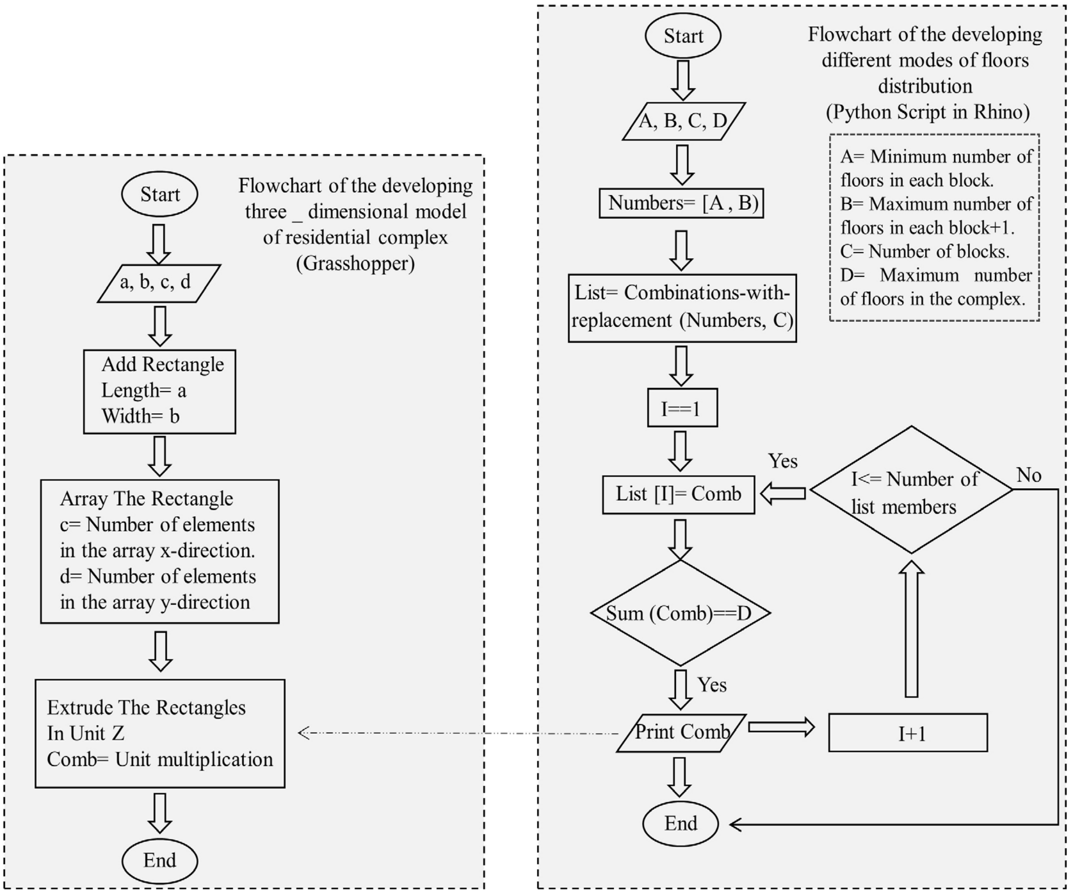

Figure 7. Flowchart of the modeling process

B. Applying settings to the software

Since energy simulations are performed in this research to compare different scenarios, the initial settings were considered in a simplified form to facilitate comparison and improve the speed of the simulation process (Table 3).

Table 3. Settings for the building energy simulation

Setpoint	Heating setpoint	20 °C
	Cooling setpoint	26 °C
Setback	Heating setback	13 °C
	Cooling setback	32 °C
Thermal resistance [m².K/W]	External walls	1.77
	Internal floor	1.42
	Ground floor	0.6
	Roof	1.55
Others	Number of people per area	0.028
	Building program	Midrise apartment

- The HVAC schedule was determined in proportion to the average monthly temperature values throughout the year and based on the occupancy schedules.
- The lighting system was switched off to remove the resulting heat in a controlled way from the simulation equations.
- The internal floors were set to "Surface" to ensure heat flows through the interfaces between the two zones.

C. Energy simulation

In this section, the energy exchange in the selected cases is simulated using the Honeybee plugin. The effect of height distribution on energy consumption was initially investigated when the shading factor was removed and the restricted number of floors was applied for each block. According to the number of blocks determined for energy simulation (16 blocks) and the maximum number of total floors (144 floors), each block can occupy a maximum of 9 floors. If all 16 blocks have 9 floors, the total number of floors in the complex will reach 144, which is maximum. Since this study aims to investigate different modes of height distribution, in this stage, a total of 88 floors were considered as a basis. In this situation, all blocks could occupy values between 1 and 9 floors in different layouts. Considering these items, several cases of unequal distribution of floors were generated by the created algorithm. In the initial study, 4 different layouts with significant differences in height distribution were selected from the produced cases to simulate energy and compare their values with each other (Figure 8). Then, if there are significant differences in the energy consumption of the samples, the vast majority of them should be examined.

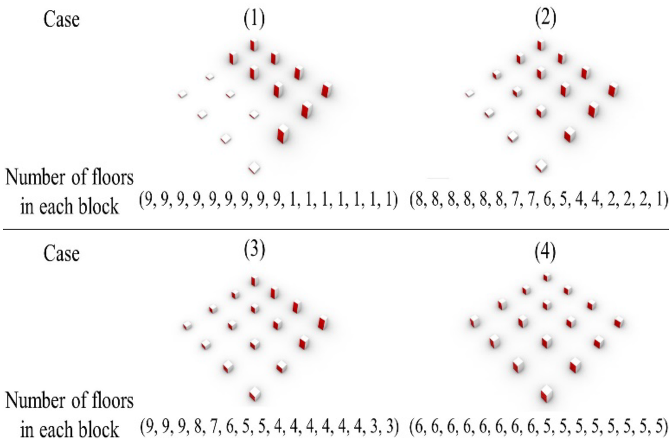

Figure 8. Selected cases of the first part of energy simulation

According to Figure 9, there is no significant difference among the 4 cases in the study of the annual heating load. However, the highest amount of cooling load (Case 3) differs 0.638 kWh/m^2 (about 0.5 %) from the lowest one (Case 1).

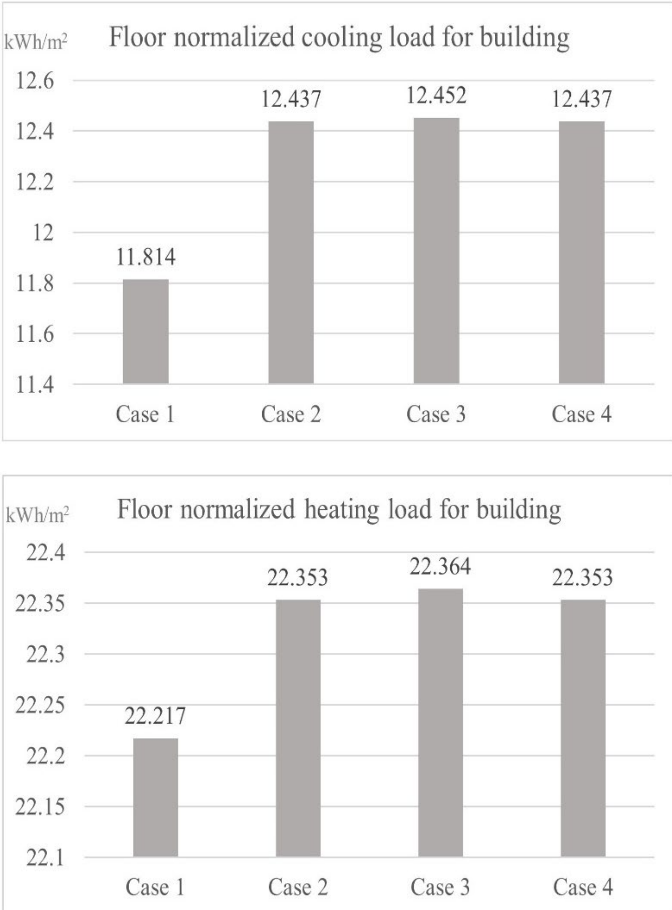

Figure 9. Comparison diagrams of annual cooling and heating energy consumption in selected cases of the first part simulation

In the following, the limit on the number of floors in each block is removed to ensure the accuracy of the results. Despite the large number of blocks (16 blocks) and in conditions where each block can have a maximum of 9 floors, the distribution of floors may be relatively homogeneous and this homogeneity affects the results of this simulation. Therefore, in this step, new cases are generated and the effect of height distribution considering the total number of 144 floors in the complex is studied.

Among the produced cases, three different scenarios were selected with significant differences in height distribution to simulate energy (Table 4).

Table 4. Selected scenarios of the second part of energy simulation

Height distribution scenario	**Case**
One of the blocks is a tall tower (129 floors) while the rest of the blocks are low-rise buildings.	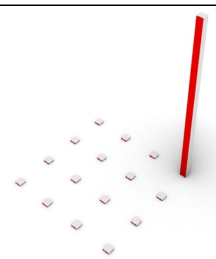 (1)

The height of all blocks is equal (9 floors).	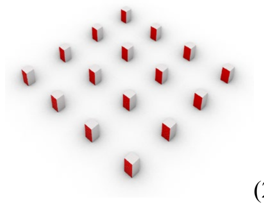 (2)
Half of the blocks are high-rise (17 floors) and the rest are low-rise (1 floor).	 (3)

4. RESULTS AND DISCUSSION

Finally, the selected scenarios were simulated (Figure 10). In the cooling energy consumption diagram, the highest value (Case 2) differs by 3.11 kWh/m^2 (about 28 %) from the lowest value (Case 1). Case 1 consists of several single-story blocks and a very high-rise block. Single-story blocks are adjacent to the ground and transfer much of their heat to the ground. Moreover, they do not receive heat from other floors. In most high-rise block floors, the cooling energy consumption rate decreases due to the higher wind speed and air temperature at altitudes is reduced. Therefore, Case 1 performs better in the summer.

On the other hand, Case 2 consists of several mid-rise blocks, all of which are located in the lower altitude range (relative to the Case 1), with higher air temperatures. Therefore, in this layout, the energy consumption for cooling increases. However, of all the reasons mentioned, the cold season is subject to different results. Thus, according to the heating energy consumption diagram, the highest energy consumption is associated with Case 1, and the lowest value is related to Case 2. Between these two cases, there is a difference of 2.34 kWh/m^2 (about 13 %) in the heating energy consumption.

In general, among the 3 cases studied, the lowest annual energy consumption (total cooling and heating load) belongs to Case 1 while the highest one belongs to Case 2 with a difference of 2.8 %.

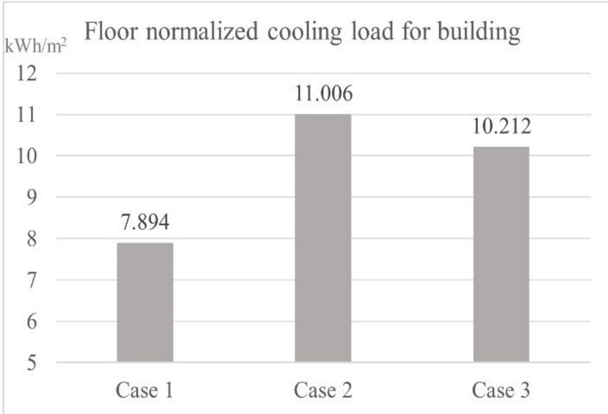

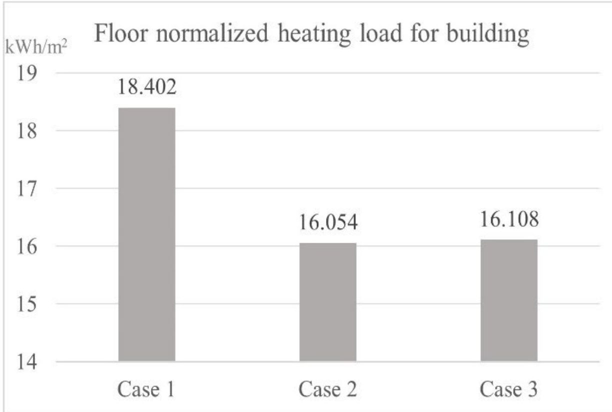

Figure 10. Annual cooling and heating energy consumption in the second part of the simulation

Comparison of the heating load on the floors shows that the heating load decreases as the number of floors in a block increases (Table 5), because significant heat loss occurs from the floor to the ground and through the ceiling to the environment. Therefore, stacking more floors on top of each other increases the ratio of floor area to envelope area, and heat loss on each floor is effectively reduced. This finding is consistent with the results of Resch et al. (2016). At higher heights, due to the increase in wind speed and decrease in air temperature, the energy required to heat the space increases to some extent (Figure 11), although it is negligible compared to the reduction of heating energy consumption made possible through increase in the number of floors.

Table 5. Distribution of cooling and heating loads among the floors

Case	Cooling load	Heating load
1	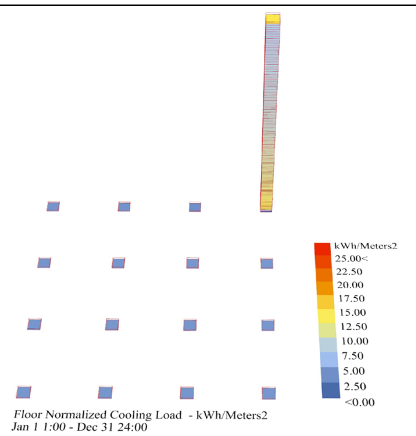	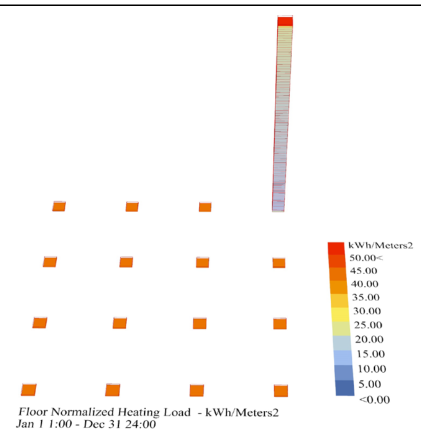

2	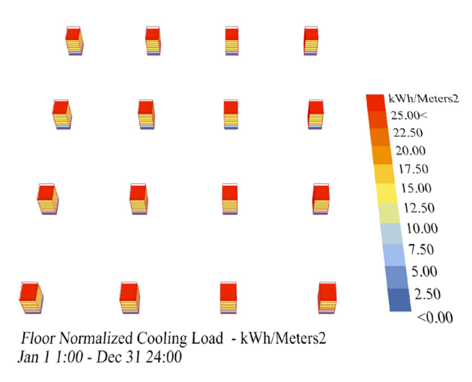	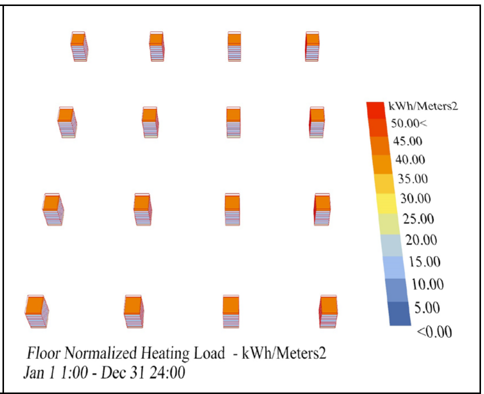
3	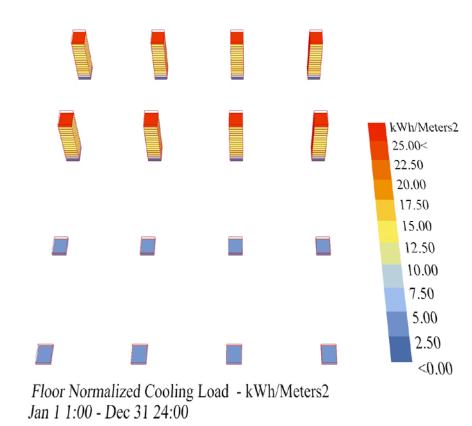	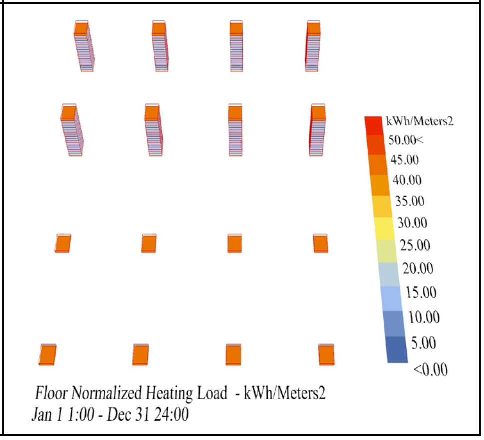

A comparison of the cooling load on the floors shows that the average cooling energy consumption increases with increasing the number of floors in a block (Table 5). For example, the average cooling energy consumption in each of the high-rise blocks of Case 3 is about 3.5 times higher than the consumption of single-story blocks. Increased cooling load probably results from less surface contact with the airflow and reduction of heat loss. However, when the number of floors in a block exceeds the range of 5 floors, some cooling load is reduced due to increased wind speed and lower air temperature at altitudes (Figure 11).

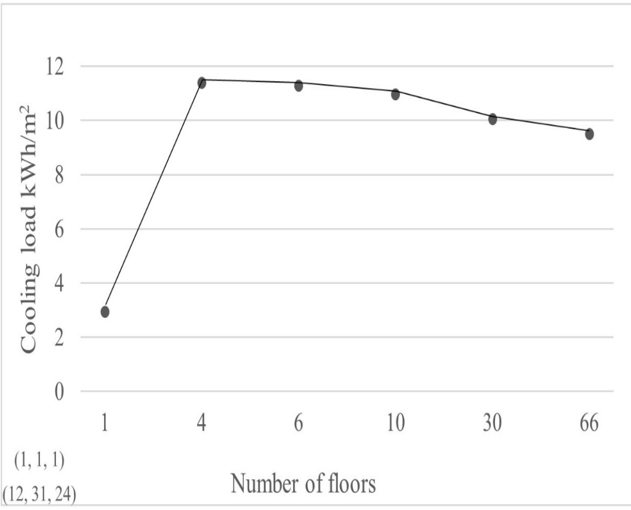

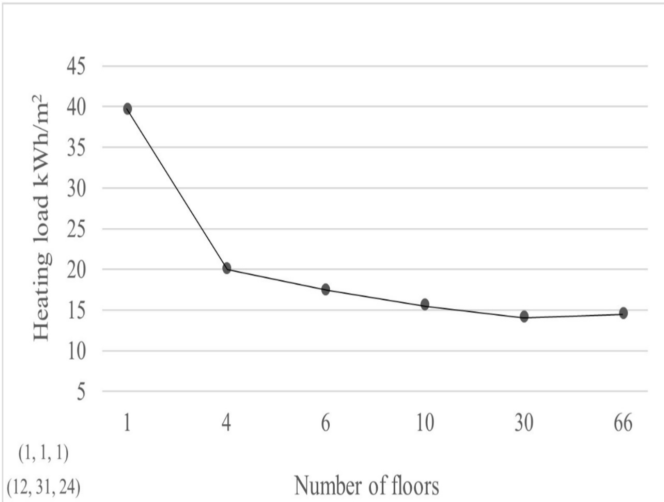

Figure 11. Comparison of average cooling and heating load in blocks with different numbers of floors

Another result is the high energy consumption on the last floor of each block (Table 5). In this regard, creating a protective surface on the roof helps reduce energy consumption.

5. VALIDATION

In the next step, to ensure the accuracy of the simulation in Grasshopper, we will validate the results with DesignBuilder software (Figure 12). DesignBuilder, the specialized software for energy simulation, is one of the most widely used and accurate software products in the energy field (Saebi Safa et al., 2020).

The specified set of the DesignBuilder software is similar to the Honeybee plugin in creating the same conditions for both emulators. The results obtained and compared with previous results are shown in Figures 13 and 14.

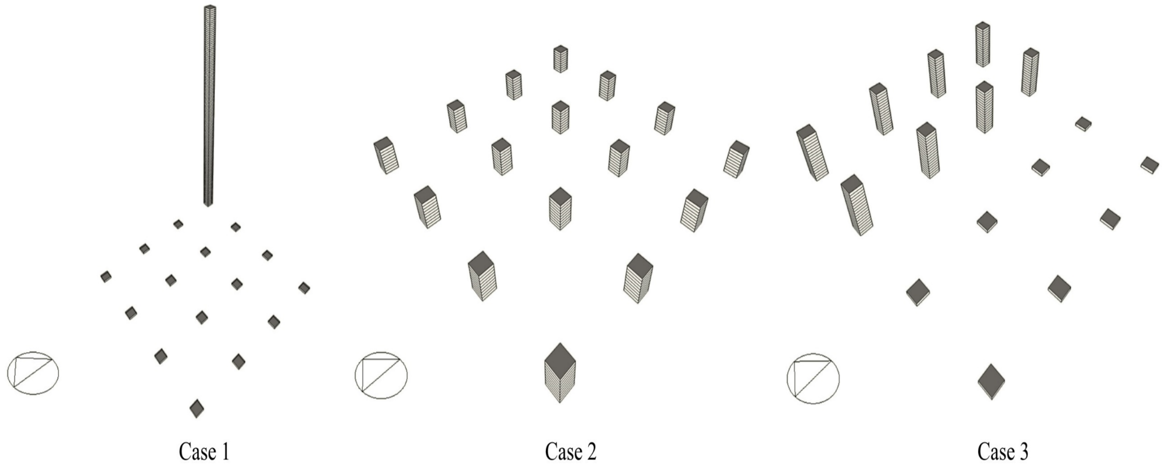

Figure 12. Modeling of the studied cases in DesignBuilder

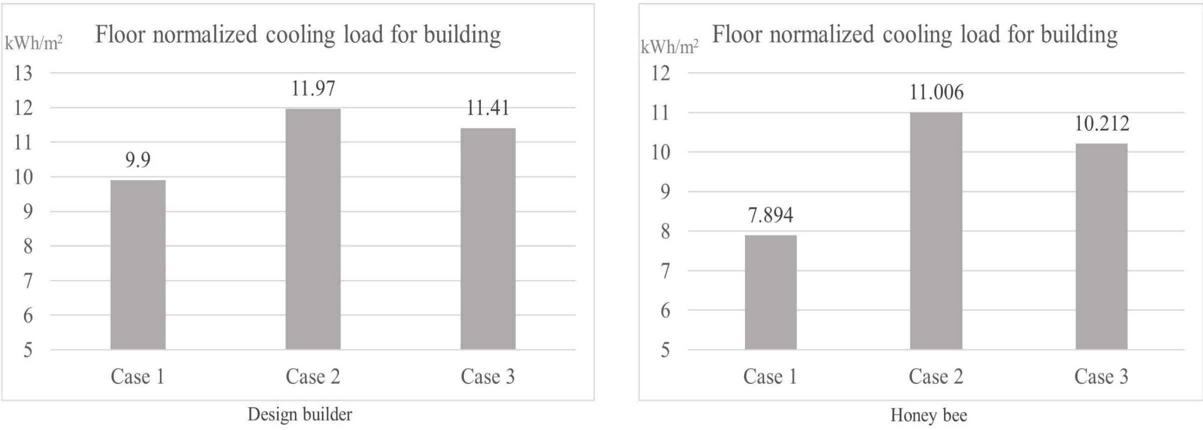

Figure 13. Comparison of cooling load consumption results obtained by Design Builder and Honeybee

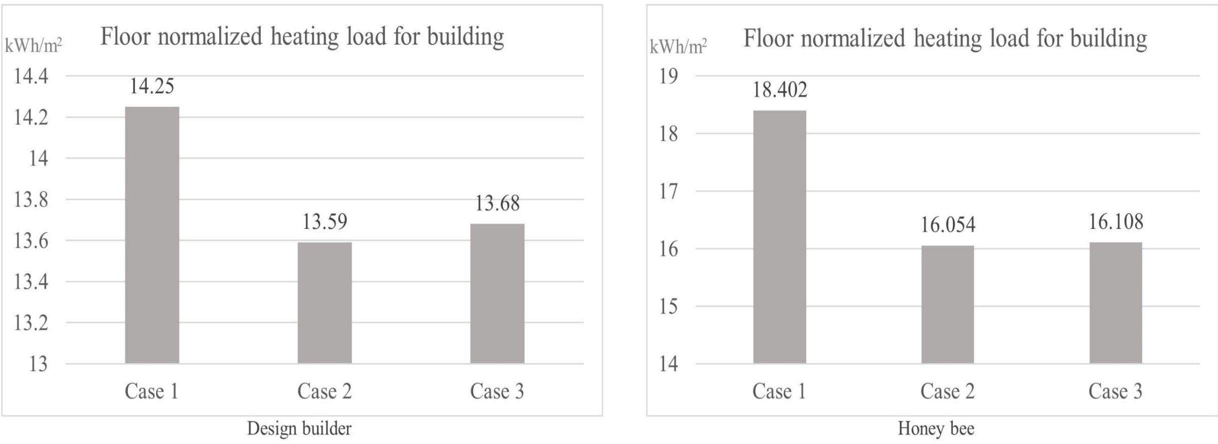

Figure 14. Comparison of heating load consumption results obtained by Design Builder and Honeybee

The general form of the diagrams in both software is similar. Also, in both software, Case 1 has the lowest annual energy consumption rate (total heating and cooling load), while Case 2 has the highest. The difference between the largest and smallest values is about 2.8 % in the Honeybee plugin and about 5.5 % in the DesignBuilder software, which can be ignored due to the minor difference.

6. CONCLUSIONS

In this research, several different layout scenarios with significant differences in the height distribution of blocks in a complex were investigated via a numerical simulation process to find a possible relationship between the height distribution and the cooling and heating load. According to the energy simulation results, the change in the height distribution of the blocks reduced the annual cooling energy consumption by 28 % and the heating energy consumption by about 13 %. Also, findings indicated that upon increasing the number of floors, the cooling energy consumption of the block increased. The average cooling energy consumption in each of the high-rise blocks of Case 3 was about 3.5 times higher than the consumption of single-story blocks. However, the decreasing trend of air temperature and increasing wind speed at high altitudes reduced the cooling load. On the other hand, the thermal energy consumption rate decreased sharply with the number of floors in a block increasing. Therefore, after determining the priorities regarding energy consumption issues in each project, a decision was made for the height distribution of the blocks to optimize the cooling or heating load, depending on the specific project conditions, costs, location, and available fuel. Then, necessary planning was made for the height layout of the complex blocks based on the leading research or other similar research. Another finding of this research was to create a protective surface on the roof of the blocks, which could reduce the heating and cooling energy consumption of the last floor by at least 50 %. The results of this research confirmed the previous research findings and complemented them. Finally, it should be noted that the present study does not consider the effect of shading in investigating different cases of height distribution. This point will be examined in future studies.

7. ACKNOWLEDGEMENT

This research has received no external funding.

REFERENCES

1. Asfour, O.S., & Alshawaf, E.S. (2015). Effect of housing density on energy efficiency of buildings located in hot climates. *Energy and Buildings*, *91*, 131-138. https://doi.org/10.1016/j.enbuild.2015.01.030
2. Chen, L., Hang, J., Sandberg, M., Claesson, L., Di Sabatino, S., & Wigo, H. (2017). The impacts of building height variations and building packing densities on flow adjustment and city breathability in idealized urban models. *Building and Environment*, *118*, 344-361. https://doi.org/10.1016/j.buildenv.2017.03.042
3. Chen, Y., Wu, J., Yu, K., & Wang, D. (2020). Evaluating the impact of the building density and height on the block surface temperature. *Building and Environment*, *168*, 106493. https://doi.org/10.1016/j.buildenv.2019.106493
4. Deng, J.-Y., Wong, N. H., & Zheng, X. (2016). The study of the effects of building arrangement on microclimate and energy demand of CBD in Nanjing, China. *Procedia Engineering*, *169*, 44-54. https://doi.org/10.1016/j.proeng.2016.10.006
5. Konis, K., Gamas, A., & Kensek, K. (2016). Passive performance and building form: An optimization framework for early-stage design support. *Solar Energy*, *125*, 161-179. https://doi.org/10.1016/j.solener.2015.12.020
6. Leng, H., Chen, X., Ma, Y., Wong, N.H., & Ming, T. (2020). Urban morphology and building heating energy consumption: Evidence from Harbin, a severe cold region city. *Energy and Buildings*, *224*, 110143. https://doi.org/10.1016/j.enbuild.2020.110143
7. Li, C., Song, Y., & Kaza, N. (2018). Urban form and household electricity consumption: A multilevel study. *Energy and Buildings*, *158*, 181-193. https://doi.org/10.1016/j.enbuild.2017.10.007
8. Li, Z., Chen, H., Lin, B., & Zhu, Y. (2018). Fast bidirectional building performance optimization at the early design stage. *Building Simulation*, *11*(4), 647-661. https://www.researchgate.net/publication/322873680_Fast_bidirectional_building_performance_optimization_at_the_early_design_stage
9. Martin, L., & March, L. (1972). *Urban Space and Structures*. Cambridge University Press. London.
10. Mirashk-Daghiyan, M., Dehghan-Touran-Poshti, A., Shahcheragi, A., & Kaboli, M.H. (2022). The effect of surrounding buildings' height and the width of the street on a building's energy consumption. *International Journal of Energy and Environmental Engineering*, *13*(1), 207-217. https://doi.org/10.1007/s40095-021-00420-1
11. Mohajeri, N., Upadhyay, G., Gudmundsson, A., Assouline, D., Kämpf, J., & Scartezzini, J.-L. (2016). Effects of urban compactness on solar energy potential. *Renewable Energy*, *93*, 469-482. https://doi.org/10.1016/j.renene.2016.02.053
12. Poponi, D., Bryant, T., Burnard, K., Cazzola, P., Dulac, J., Fernandez Pales, A., Husar, J., Janoska, P., Masanet, E. R., Munuera, L., Remme, U., Teter, J., & West, K. (2016). *Energy Technology Perspectives 2016: Towards Sustainable Urban Energy Systems*. International Energy Agency. https://iea.blob.core.windows.net/assets/37fe1db9-5943-4288-82bf-13a0a0d74568/Energy_Technology_Perspectives_2016.pdf
13. Quan, S.J. (2017). Energy efficient neighborhood design under residential zoning regulations in Shanghai. *Energy Procedia*, *143*, 865-872. https://doi.org/10.1016/j.egypro.2017.12.775
14. Quan, S.J., Li, Q., Augenbroe, G., Brown, J., & Yang, P.P.J. (2015). Urban data and building energy modeling: A GIS-based urban building energy modeling system using the urban-EPC engine. In S. Geertman, J. Jr. Ferreira, R. Goodspeed, & J. Stillwell (Eds.), *Planning Support Systems and Smart Cities* (pp. 447-469). Springer International Publishing. https://doi.org/10.1007/978-3-319-18368-8_24
15. Resch, E., Bohne, R. A., Kvamsdal, T., & Lohne, J. (2016). Impact of urban density and building height on energy use in cities. *Energy Procedia*, *96*, 800-814. https://doi.org/10.1016/j.egypro.2016.09.142
16. Rode, P., Keim, C., Robazza, G., Viejo, P., & Schofield, J. (2014). Cities and energy: Urban morphology and residential heat-energy demand. *Environment and Planning B: Planning and Design*, *41*(1), 138-162. https://doi.org/10.1068/b39065
17. Roudsari, M., Pak, M., & Smith, A. (2013). *Ladybug: A parametric environmental plugin for grasshopper to help designers create an environmentally-conscious design*. Proceedings of the 13th Conference of the International Building Performance Simulation Association (pp. 3128-3135). France. https://www.researchgate.net/publication/287778694_Ladybug_A_parametric_environmental_plugin_for_grasshopper_to_help_designers_create_an_environmentally-conscious_design#fullTextFileContent
18. Saebi Safa, B., Heidari, F., & Soleimanpour, N. (2020). Audit of energy loss through exterior walls of buildings and impact of thermal insulation with simulation in design builder software (Case study: Office building in Tehran). *Journal of Science and Engineering Elites*, *5*(3), 169-179. https://www.magiran.com/paper/2166038?lang=en (In Persian).
19. Salvati, A., Coch, H., & Morganti, M. (2017). Effects of urban compactness on the building energy performance in Mediterranean climate. *Energy Procedia*, *122*, 499-504. https://doi.org/10.1016/j.egypro.2017.07.303
20. Salvati, A., Monti, P., Coch Roura, H., & Cecere, C. (2019). Climatic performance of urban textures: Analysis tools for a Mediterranean urban context. *Energy and Buildings*, *185*, 162-179. https://doi.org/10.1016/j.enbuild.2018.12.024
21. Sekhar Roy, S., Roy, R., & Balas, V. E. (2018). Estimating heating load in buildings using multivariate adaptive regression splines, extreme learning machine, a hybrid model of MARS and ELM. *Renewable and Sustainable Energy Reviews*, *82*, 4256-4268. https://doi.org/10.1016/j.rser.2017.05.249
22. Seyedzadeh, S., Rahimian, F., Glesk, I., & Roper, M. (2018). Machine learning for estimation of building energy consumption and performance: A review. *Visualization in Engineering*, *6*(5), 1-20. https://doi.org/10.1186/s40327-018-0064-7
23. Shareef, S., & Altan, H. (2022). Urban block configuration and the impact on energy consumption: A case study of sinuous morphology. *Renewable and Sustainable Energy Reviews*, *163*, 112507. https://doi.org/10.1016/j.rser.2022.112507
24. Shareef, S. (2021). The impact of urban morphology and building's height diversity on energy consumption at urban scale. The case study of Dubai. *Building and Environment*, *194*, 107675. https://doi.org/10.1016/j.buildenv.2021.107675
25. Steemers, K. (2003). Cities, energy and comfort: A PLEA 2000 review. *Energy and Buildings*, *35*(1), 1-2. https://doi.org/10.1016/S0378-7788(02)00074-9
26. Terjung, W.H., & Louie, S.S.F. (1973). Solar radiation and urban heat islands. *Annals of the Association of American Geographers*, *63*(2), 181-207. https://doi.org/10.1111/j.1467-8306.1973.tb00918.x
27. Toutou, A., Fikry, M., & Mohamed, W. (2018). The parametric based optimization framework daylighting and energy performance in residential buildings in hot arid zone. *Alexandria Engineering Journal*, *57*(4), 3595-3608. https://doi.org/10.1016/j.aej.2018.04.006
28. Trepci, E., Maghelal, P., & Azar, E. (2020). Effect of densification and compactness on urban building energy consumption: Case of a transit-oriented development in Dallas, TX. *Sustainable Cities and Society*, *56*, 101987. https://doi.org/10.1016/j.scs.2019.101987
29. Vartholomaios, A. (2017). A parametric sensitivity analysis of the influence of urban form on domestic energy consumption for heating

and cooling in a Mediterranean city. *Sustainable Cities and Society*, *28*, 135-145. https://doi.org/10.1016/j.scs.2016.09.006

30. Wong, N.H., Jusuf, S.K., Syafii, N.I., Chen, Y., Hajadi, N., Sathyanarayanan, H., & Manickavasagam, Y.V. (2011). Evaluation of the impact of the surrounding urban morphology on building energy consumption. *Solar Energy*, *85*(1), 57-71. https://doi.org/10.1016/j.solener.2010.11.002

31. Xu, X., AzariJafari, H., Gregory, J., Norford, L., & Kirchain, R. (2020). An integrated model for quantifying the impacts of pavement albedo and urban morphology on building energy demand. *Energy and Buildings*, *211*, 109759. https://doi.org/10.1016/j.enbuild.2020.109759

32. Yang, X., & Li, Y. (2015). The impact of building density and building height heterogeneity on average urban albedo and street surface temperature. *Building and Environment*, *90*, 146-156. https://doi.org/10.1016/j.buildenv.2015.03.037

33. Zhang, J., Liu, N., & Wang, S. (2020). A parametric approach for performance optimization of residential building design in Beijing. *Building Simulation*, *13*(2), 223-235. https://link.springer.com/article/10.1007/s12273-019-0571-z

Journal of Renewable Energy and Environment

Journal Homepage: www.jree.ir

Materials and Energy Research Center

MERC

Research Article

Mitigating Energy Consumption of Educational Buildings Using a Novel Simulation Method (Case Study: Faculty of Oil and Petrochemical Engineering, Razi University, Iran)

Soheil Fathi [a], Abbas Mahravan [b*]

[a] Department of Architecture, Faculty of Architecture and Urbanism, Art University of Isfahan, Isfahan, Iran.
[b] Department of Architectural Engineering, Faculty of Engineering, Razi University, Kermanshah, Iran.

P A P E R I N F O

Paper History:
Received: 28 June 2022
Revised: 16 August 2022
Accepted: 28 August 2022

Keywords:
Educational Buildings,
Energy Retrofit,
Shading Devices,
Window,
Insulation

A B S T R A C T

In many middle- and high-income countries, existing buildings will occupy the majority of building areas by 2050 and measures are needed to upgrade the mentioned buildings for a sustainable transition. This research proposes a method to mitigate the energy consumption of existing educational buildings using four energy efficiency measures (EEMs). The proposed method divides simulations into two main parts: simulations with and without using heating, ventilating, and air conditioning (HVAC) systems. Four passive EEMs are used, including window replacement, proposed shading devices, new insulations, and installing a new partition wall for the entrance part of the building. This research uses a simulation-based method to examine the effect of each EEM on the energy consumption of the building using DesignBuilder software. The steps of data collection and modeling in this research include collecting raw data related to the physical characteristics of the building experimentally and creating a basic model. Afterwards, simulation scenarios were defined based on the proposed method, and several simulations were carried out to examine the impact of each EEM on the energy performance of the building. Two environmental parameters of the simulation process, including indoor air temperature (IAT) and relative humidity (RH), were used. The measures reduced the heating and cooling demands in the building by 80.14 % and 15.70 %, respectively. Moreover, the results indicated that the total energy consumption of the building were reduced by 10.44 % after retrofitting measures.

https://doi.org/10.30501/jree.2022.349282.1394

1. INTRODUCTION

Over the past decades, global energy demand has increased significantly and caused numerous problems, such as global warming escalation, air pollution, and other environmental disasters. Moreover, non-renewable energy sources are not permanent, and it is necessary to find ways to reduce the increasing global energy demand and greenhouse gases emisions (Abu-hamdeh et al., 2022; Alah Rezazadeh et al., 2014; Chien et al., 2021). Buildings consume nearly 40 % of the total energy consumption in Iran (Bagheri et al., 2013). Iran is a developing country whose energy demand will increase on average by 2.80 % annually (Moshiri et al., 2012). It is essential to reduce the energy consumption of buildings as much as possible to mitigate this annual growth. Accordingly, it is necessary to find various solutions to impede the growth of energy demand in developing countries like Iran. This research offers a new energy retrofitting method to reduce the energy consumption of educational buildings.

*Corresponding Author's Email: a.mahravan@razi.ac.ir (A. Mahravan)
URL: https://www.jree.ir/article_157492.html

Energy retrofitting, defined as upgrading a building's components (Ahmed & Asif, 2020; Jafari & Valentin, 2017; Ahmed & Asif, 2021), can reduce the energy consumption of a building. It is able to positively affect the energy consumption of building stocks on an urban scale (Ascione et al., 2021; Dall'O' et al., 2012; Hirvonen et al., 2021; Magnani et al., 2020; Mata et al., 2018; Ozarisoy & Altan, 2021; Torabi Moghadam & Lombardi, 2019; Wang & Holmberg, 2015). Previous research works have offered various Energy Efficiency Measures (EEMs) on a building scale and indicated energy, cost, and carbon reduction of EEMs in their research works (Dabaieh & Elbably, 2015; Kadrić et al., 2022; Mejjaouli & Alzahrani, 2020; Rabani et al., 2020; Thomsen et al., 2016). Ahmed and Asif (Ahmed & Asif, 2020) investigated the techno-economic feasibility of retrofitting existing buildings in Saudi Arabia using two case studies (a villa and an apartment). They used eight various EEMs at three levels, including low-cost (minor retrofit), medium-cost (major retrofit), and high-cost measures (deep retrofit). Their research indicated that deep retrofit measures reduced the annual energy consumption in the villa and apartment buildings by 56.90 % and 58.50 %, respectively. Besides, the amount of CO_2 emission was reduced up to 56.90 % in the

Please cite this article as: Fathi, S., & Mahravan, A. (2023). Mitigating energy consumption of educational buildings using a novel simulation method (Case study: Faculty of oil and petrochemical engineering, Razi University, Iran). *Journal of Renewable Energy and Environment (JREE)*, *10*(3), 13-28. https://doi.org/10.30501/jree.2022.349282.1394.

2423-7469/© 2023 The Author(s). Published by MERC. This is an open access article under the CC BY license (https://creativecommons.org/licenses/by/4.0/).

villa and 58.54 % in the apartment building. Moreover, they indicated that the deep retrofit measures would pay back the initial investment in 25.15 years for villa buildings and 24.60 years for the apartment building.

Furthermore, several previous studies have focused on the effect of EEMs on the energy consumption of various building types (Ascione et al., 2017; Huang et al., 2013; Piccardo et al., 2020; Urbikain, 2020; Zhou et al., 2016). Song, Ye, Li, Wang and Ma (Song et al., 2017) used various EEMs, including EEMs in exterior walls, infiltration rate, and shading coefficient in a 10-story office building. Results of this research demonstrated that EEMs could reduce the cooling demand of the building by 16.47 %. El-Darwish and Gomaa (El-Darwish & Gomaa, 2017) proposed a retrofit strategy to improve the energy performance of higher educational buildings in Egypt. This study used various EEMs including insulation and thermal bridge, airtightness and infiltration, window glazing, and solar shading. Moreover, they used a simulation-based method and indicated that these EEMs could reduce the energy consumption of a building by 33 %. Li, Zhang, Zhang, and Wu (Li et al., 2021) used a simulation-based approach to evaluate the effect of various EEMs on energy performance and environmental comfort level of occupants in a school building in China. They focused on external wall insulation, roof insulation, windows solar heat gain coefficient (SHGC), and window-to-wall ratio (WWR). As demonstrated by the research results, EEMs reduced energy consumption by 4 % and improved the environmental comfort level of occupants, too.

Previous research works have assessed the effect of various EEMs on the energy consumption of educational buildings in Iran. Tahsildoost and Zomorodian (Tahsildoost & Zomorodian, 2015) used an energy retrofit procedure to reduce the energy consumption of two schools in Iran. They employed various retrofitting techniques, including infiltration reduction, building envelope thermal improvement, building energy management system (BEMS), mechanical, electrical, and plumbing services (MEP) renovation/overhaul, and solar energy utilization. Their research indicated that the energy consumption was reduced up by 38.29 % and 29.87 % in old and new cases. Moreover, they compared the cost of energy retrofit actions and showed payback analysis for both cases in three categories (low, medium, and high-cost). Their results demonstrated that the low-cost measures had the longest down payback time (PBT) in the old school, while the medium-cost retrofit actions had the shortest PBT in the new school.

Zomorodian and Nasrollahi (Zomorodian & Nasrollahi, 2013) used various EEMs to improve the energy performance and thermal comfort in a typical school building in Iran. They used multiple EEMs, including orientation, WWR, space organization, sun shading, and building shape. Results of their research demonstrated that using the mentioned EEMs could reduce the energy consumption of the building by 31 % while maintaining the visual and thermal comfort levels of occupants. Pazouki, Rezaie and Bozorgi-Amiri (Pazouki et al., 2021) employed a multi-objective optimization method to evaluate the effect of various EEMs on the energy consumption of a university building in Iran. They applied multiple EEMs including retrofitting lighting systems, windows, roof insulation, wall insulation, and PV system. As indicated by the results, using the latter EEMs reduced the energy consumption of the building by 40 %.

Besides, the effect of user behavior and different behavioral patterns during the retrofit design procedures was assessed in previous research works (Gui et al., 2021; Lu et al., 2021). Jami, Forouzandeh, Zomorodian, Tahsildoost and Khoshbakht (Jami et al., 2021) utilized an integrated method (field measurements, questionnaire survey, and simulation) to assess the behavioral patterns of occupants during the retrofitting procedure of two dormitory buildings in Iran. Their research showed that energy conservation measures (ECM) could reduce buildings' energy consumption in energy spender, conventional, and austerity occupant energy behavior (OEB) models by about 32 %, 56 %, and 60 %, respectively.

Furthermore, previous research works illustrated the impact of EEMs on indoor environmental quality (IEQ) of various building types (Heidari et al., 2021; Liu et al., 2015; Maleki & Dehghan, 2021). Pungercar, Zhan, Xiao, Musso, Dinkel and Pflug (Pungercar et al., 2021) utilized various EEMs using prefabricated elements to improve the IEQ of a residential building in Germany. They replaced windows, installed insulation for exterior walls, installed covers for interior openings, and installed covers for ventilation units and exterior finishing. Their retrofitting plan reduced the heating demand of the building by 77 %, increased CO_2 concentration, reduced relative humidity (RH), and increased indoor air temperature (IAT). Alazazmeh and Asif (Alazazmeh & Asif, 2021) used ten different EEMs to improve the energy performance and IEQ in a commercial building. Their research indicated that application of various EEMs could decrease energy consumption by 39 %, improve IEQ, including thermal comfort, illumination, and noise control, and reduce air pollution.

Previous studies used various EEMs, including passive, active, and mixed measures (Amani & Reza Soroush, 2021; Dabaieh et al., 2016; Huang et al., 2020; Lolli et al., 2019; Qu et al., 2021; Sun et al., 2021; Wang et al., 2021; Yang et al., 2021). Serrano-Jiménez, Lizana, Molina-Huelva and Barrios-Padura (Serrano-Jiménez et al., 2019) introduced a new procedure for the decision-making process, which evaluated the profitability of various EEMs using parametric analysis. They employed four scenarios according to operating conditions and fixed parameters (Scenario 1), the highest energy consumption pattern (Scenario 2), the medium energy consumption pattern (Scenario 3), and the lowest energy consumption pattern (Scenario 4). Moreover, they used three groups of EEMs, including passive, active, and mixed measures. Their research showed that energy-saving potential ranged from 20 to 80 % using various measures. In addition, the results indicated that each EEM must be thoroughly analyzed so that each energy consumption pattern could reach high cost-effectiveness.

According to these previous research works, energy retrofitting has positive effects on the energy performance of educational buildings. Moreover, it is possible to reduce energy consumption and improve the IEQ of the mentioned buildings simultaneously. In addition, use of both active and passive EEMs contributes to upgrading the energy performance of the existing buildings. Table 1 shows EEMs, research methods, and simulation software used in previous studies.

These previous studies indicate that it is important to use passive EEMs to reduce the energy consumption of educational buildings. One of the main questions is: How is it possible to use computer simulations to select passive EEMs to optimize the energy consumption of educational buildings? Accordingly, this research attempts to improve the energy consumption of educational buildings using passive EEMs via computer simulations. This study introduces a new method, focusing on upgrading the energy performance of an existing faculty building on campus using a novel simulation process. Various research methods can be utilized based on the function of the proposed method via computer simulations. This simulation process can be used in future studies that use passive EEMs in educational buildings.

Table 1. Previous studies with various EEMs, research methods, and simulation software

Author	Climate region	EEM	Method	Simulation software
(Tahsildoost & Zomorodian, 2015)	Tehran	Thermal insulation	Simulation-based	DesignBuilder
		BEMS		
		Window replacement		
		External shading		
		MEP		
		PV panel		
(El-Darwish & Gomaa, 2017)	Tanta	Insulation	Simulation-based	DesignBuilder
		Infiltration		
		Window glazing		
		Shading		
(Pazouki et al., 2021)	Tehran	Lighting system	Simulation-based	DesignBuilder
		Windows		
		Roof insulation		
		Wall insulation		
		PV		
(Lu et al., 2021)	Singapore	Heating, ventilating, and air conditioning (HVAC)	Simulation-based	IES-EV
		Lighting system		
		Equipment		
		Wall insulation		
		Green roof		
		Occupant's behavior		
(Ascione et al., 2017)	Benevento	Special plasters	Simulation-based	DesignBuilder
		Innovative coatings		
		Thermal insulation		
		Thermal mass		
		New windows		
		Solar screen		
		HVAC		
		PV		
(Li et al., 2021)	Wuhan	External wall	Simulation-based	DesignBuilder
		Roof insulation		
		SHGC of windows		
		WWR		
(Zomorodian & Nasrollahi, 2013)	Shiraz	Orientation	Simulation-based	DesignBuilder
		WWR		
		Space organization		
		Shading		
		Building shape		

2. Methodology

This research investigates the effect of various passive EEMs on the energy consumption of an educational building in Iran. The main difference between this research and other similar research works is that this research introduces a new simulation method to select passive EEMs. The overall research process includes five main steps, shown in Figure 1.

2.1. Data collection

This research uses existing data on an educational building during the research process. This building is a large-scale building with a 5056 m^2 floor area and is located on the University Campus of Razi University, Iran (Figure 2). Figure 3, Figure 4, and Figure 5 show the architectural plans of the building, including the ground floor, first floor, and second-floor plans. This building is oriented at 10 degrees to the West and has a north-south slope. In the first part of this research, experimental data and physical characteristics of the building are collected. The experimental data are collected from various sources, including the number of people, working hours, domestic hot water (DHW), HVAC type, etc. Moreover, the physical characteristics data of the building are collected from the as-built maps and catalogs (windows, building materials, etc.).

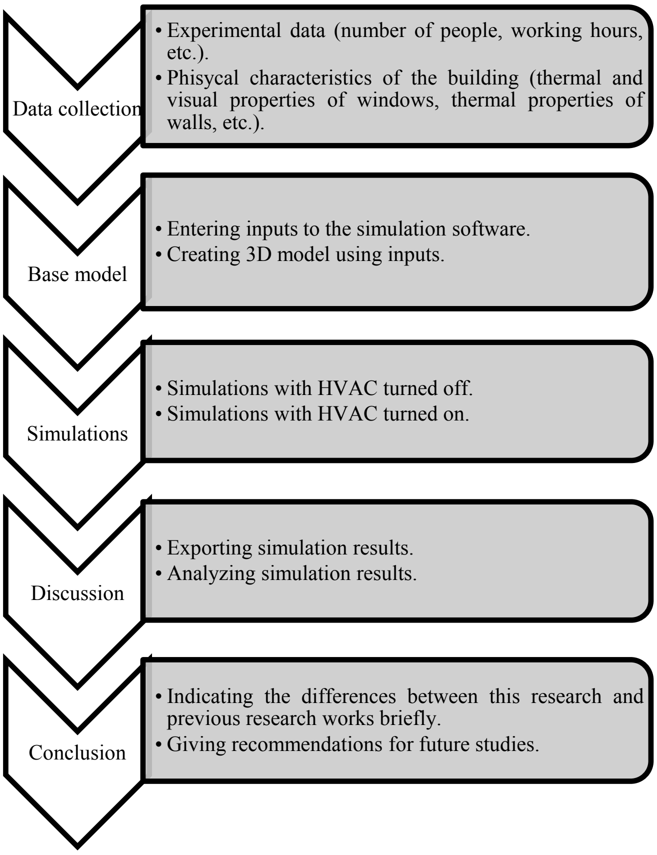

Figure 1. Overall research process

Figure 2. Faculty of oil and petrochemical building at Razi University: (a) Site plan view from Google Earth; (b) Perspective view of the building (from the southwest part of the site)

2.2. Base model

In the second step, inputs are added to the simulation software. Table 2 shows the added inputs in the simulation software. This research uses DesignBuilder as the simulation software. In addition, DesignBuilder uses the EnergyPlus simulation engine to run energy simulations. Besides, at the end of this step, a 3D model is created in the simulation software. Figure 6 represents a perspective view of the base model in the DesignBuilder software.

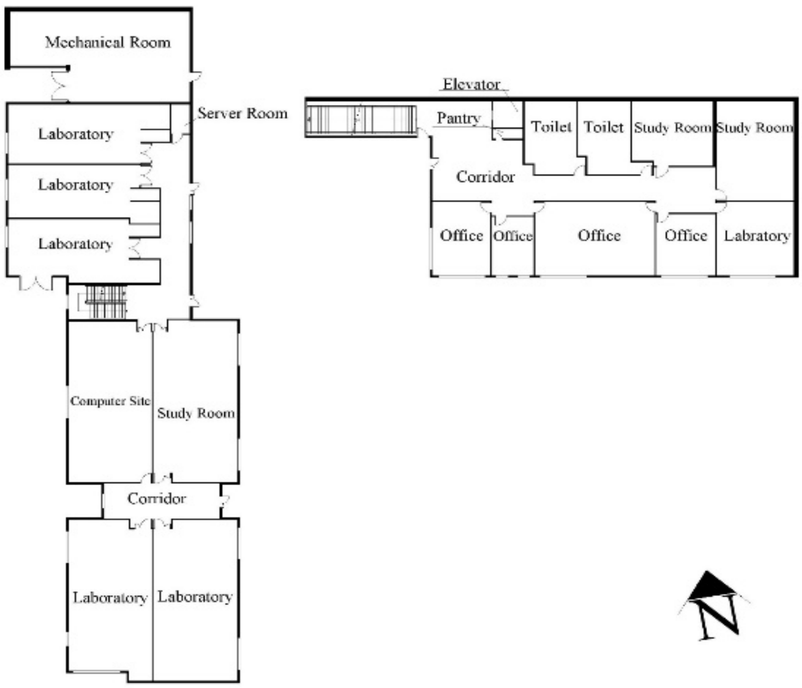

Figure 3. Ground floor plan of the building

Figure 4. First-floor plan of the building

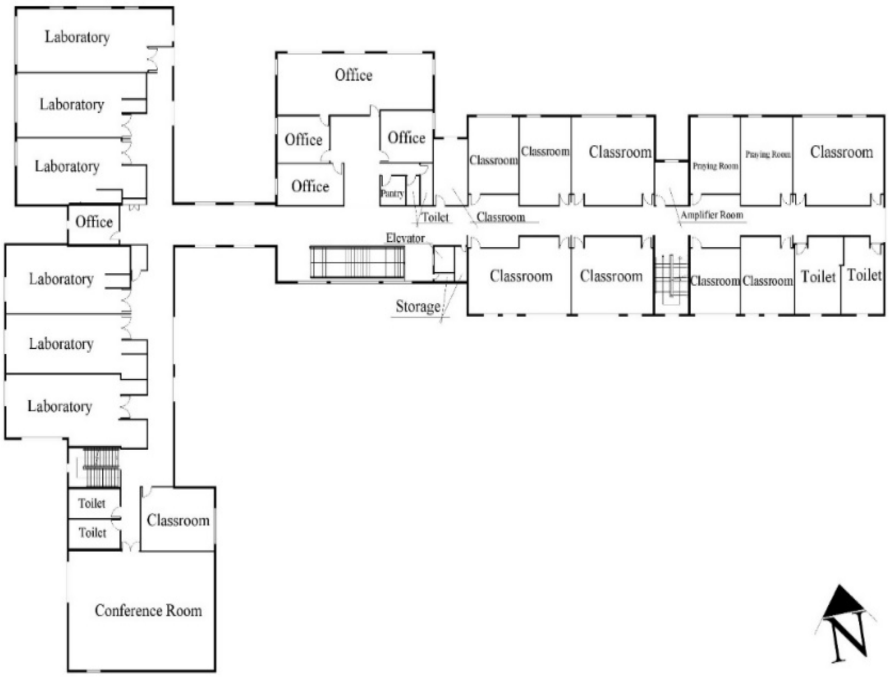

Figure 5. Second-floor plan of the building

Table 2. Inputs of the base model

No.	Design parameter	Value
1	Heating setpoint (°C)	25
2	Cooling setpoint (°C)	25
3	Natural ventilation set point (°C)(HVAC turned off)	21

4	Minimum fresh air (L/s per person)	7.50
		10 (laboratories)
		25 (Toilets, corridors)
5	Computers (W)	26332
6	Office equipment (monitor, printer, and projector) (W)	5844
7	Miscellaneous (W)	110700
8	Lighting (W)	39012
9	Glazing type	Double-glazed/3mm/10mm Air
10	T_{vis}	0.812
11	SHGC	0.763
12	U-value (W/m^2.K)	2.816
13	Above ground WWR (%)	15.57
14	HVAC type	VAV, Water-cooled Chiller (Airwasher)
15	Fuel	Electricity, Natural Gas
16	Maximum supply air temperature (°C)	66.50
17	Minimum supply air temperature (°C)	8.50

Figure 6. View of the base model of the building in the simulation software

2.3. Simulation

In this step, several simulations are performed to assess the effect of passive EEMs on the energy performance of the building. The main difference between this research and previous studies is that it uses a novel simulation method to evaluate the effect of passive EEMs on the energy performance of the building. The novelty of the simulation process is that it uses two different simulation types including simulations without using the HVAC systems and simulations using the HVAC systems. This research uses four EEMs: including window shading, insulation, replacing windows, and adding a partition to the entrance part of the building. This building has double-pane clear windows filled with air insulation. The existing type of window is replaced with a double-pane green window type. Besides, the glass thickness is changed from 3 mm to 4 mm. The insulation type is changed from air to argon gas.

Table 3 shows the thermal and visual characteristics of the traditional window and other available types of windows. The data are collected from the window manufacturer's company catalog (www.kosarwin.ir). As shown in Table 3, the selected window type has an ideal U-value (2.594 (W/m^2.K)) and has the highest visual transmittance (Tvis) value (68 %). Therefore, it can provide an appropriate view to the outdoor environment better than other window types, and it can impede heat transfer as low as windows with blue, bronze, and grey colors. In addition, the color of the northern windows of the building will not change (double-pane, clear, 4mm, argon, 10 mm) since there is no direct solar radiation on these windows.

Table 3. Thermal and visual properties of different window types (Reference: www.kosarwin.ir)

Window type (panes, color, glass thickness, insulation type, and insulation thickness)	U-value (W/m^2.K)	SHGC	T_{vis}
Double-pane, clear, 3 mm, air, 10 mm	2.816	0.763	0.812
Double-pane, blue, 4 mm, argon, 10 mm	2.594	0.450	0.326
Double-pane, bronze, 4 mm, argon, 10 mm	2.594	0.584	0.471
Double-pane, green, 4 mm, argon, 10 mm	2.594	0.574	0.680
Double-pane, grey, 4 mm, argon, 10 mm	2.594	0.567	0.375
Double-pane, tinted, 4 mm, argon, 10 mm	2.600	0.516	0.395

The base model uses the physical characteristics data of the existing building for the initial simulation. The mentioned data indicate the existing layers of walls, floors, and roof of the building. Since the main objective of this research is to reduce the energy consumption of the building, it is necessary to reduce heat transfer as much as possible in this section. Table 4 shows the physical characteristics of the walls, floors, and roof of the building before and after the retrofitting process. As shown in the proposed scenarios, the interior walls and the ground floor remain unchanged, and the exterior walls, roof, and floors are upgraded. The prefabricated 3D panels are added to each exterior wall to stabilize IAT as much as possible. In addition, an expanded polystyrene (EPS) insulation layer is used in the outer part of the roof to avoid absorbing solar radiation as much as possible. Moreover, the EPS insulation layers are used on the internal floors to prevent heat transfer as much as possible.

Table 4. Physical characteristics of the building before and after the energy retrofitting process

Building component	Layers		U-value (W/m^2.K)	
	Before	After	Before	After
External wall	Brick (outermost) 30 mm, Mortar 30 mm, Brick 210 mm, Plaster (dense) 30 mm, Plaster (lightweight) 20 mm (innermost layer)	Brick (outermost) 30 mm, Mortar 30 mm, Brick 210 mm, Plaster (lightweight) 10 mm, EPS Expanded Polystyrene 50 mm, Plywood Coating 5 mm	1.251	0.556
Roof	Asphalt-reflective coating (outermost) 40 mm, Mortar 30 mm, Concrete (cells empty) 80 mm, Cast concrete 310 mm, Plaster (dense) 30 mm, Plaster (lightweight) 10 mm	Asphalt-reflective coating (outermost) 40 mm, Mortar 30 mm, EPS Expanded Polystyrene 100 mm, Mortar 30 mm, Concrete (cells empty) 100 mm, Cast concrete 310 mm, Plaster (dense) 30 mm, Plaster (lightweight) 10 mm	1.592	0.350
Internal floors	Plaster (lightweight) 10 mm, Plaster (dense) 30 mm, Cast concrete 310 mm, Concrete (cells empty) 50 mm, Mortar 50 mm, Ceramic 10 mm	Plaster (lightweight) 10 mm, Plaster (dense) 30 mm, Cast concrete 310 mm, Concrete (cells empty) 100 mm, Mortar 50 mm, EPS Expanded Polystyrene 100 mm, Mortar 30 mm, Ceramic 10 mm	1.377	0.335
Internal walls	Plaster (lightweight) 10 mm, Plaster (dense) 30 mm, Brick 210 mm, Plaster (dense) 30 mm, Plaster (lightweight) 10 mm	Not changed	1.444	1.444
Ground floor	Mortar (outermost) 10 mm, Marble stone 250 mm, Mortar 30 mm, Asphalt 30 mm, Mortar 150 mm, Concrete (cells empty) 100 mm, Mortar 150 mm, Ceramic 20 mm	Not changed	1.244	1.244

This research proposes an innovative method for using external window shadings. A fixed overhang is employed for the southern windows of the building (Figure 7). The fixed overhang is utilized in an innovative method in this building. The computer simulations are performed annually, and it is possible to export daily simulation results from the simulation software. Therefore, daily simulations are carried out in this research to find the maximum IAT on the building scale. The maximum IAT was 36.38 °C on August 2. Accordingly, the solar radiation angle can be identified on this day using the Grasshopper plugin, which gives the monthly, daily, and hourly solar radiation angles of the climate region (Kermanshah). Accordingly, the highest solar radiation angle is 72.22° at 12 PM. (on August 2). This research uses the mentioned angle to find the depth of the fixed overhangs. The depth of the fixed overhangs can be calculated using Eq. (1) and Eq. (2), where (b) is the angle between the solar radiation and the exterior part of the window, (a) is the solar radiation angle (altitude of the climate region), (h) is the height of the window, and (x) is the depth of the overhang.

$$b = 90 - a \tag{1}$$

$$x = \tan b \times h \tag{2}$$

Figure 8 shows the innovative fixed louver system proposed for the eastern and western windows of the building. The mentioned louvers can impede overheating in the mornings and afternoons. Figure 9 shows pictures of the proposed louver system. The louvered canopy has already been used for the east-facing windows of the faculty of electrical and computer engineering at Razi University. This research uses a fixed louver system for the east and west-facing windows. The east-facing windows receive solar radiation in the beginning hours, and the west-facing windows receive solar radiation until the last hours of the day.

This research proposes a method to find the distance between the louver blades for the east-facing and the west-facing windows. The installed blades can reduce the direct solar absorption as much as possible. The solar radiation angle is 28.72° at 8:00 AM, and the solar radiation angle is 27.69° at 5:00 PM. Accordingly, the distance between the louver blades can be calculated using Eq. (3), where (b) is the solar radiation angle, (a) is the depth of the louver blades, and (h) is the distance between the louver blades.

$$h = \tan b \times a \tag{3}$$

The entrance part of this building is located in the northern part of the building. This entrance is open in cold seasons, and cold air enters the building in winters. Accordingly, the entrance space is separated from other zones using an internal partition. Figure 10 shows the first-floor plan of the building with the proposed partition wall in the entrance part. The partition wall is made of the double-glazed glass and consists of an automatic door that prevents heat transfer between the inside and outside of the building.

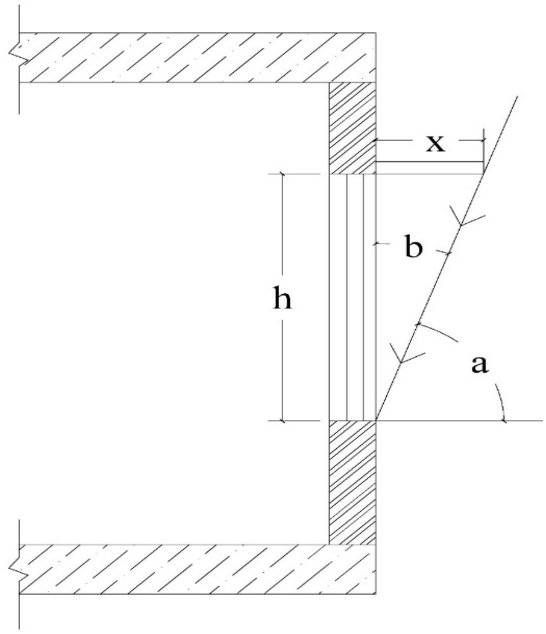

Figure 7. Section of a southern window with a fixed overhang

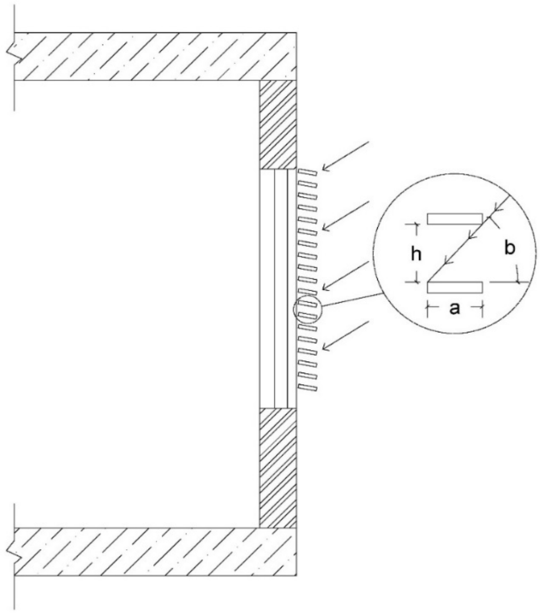

Figure 8. Section of east-facing and west-facing windows using the proposed fixed louver system

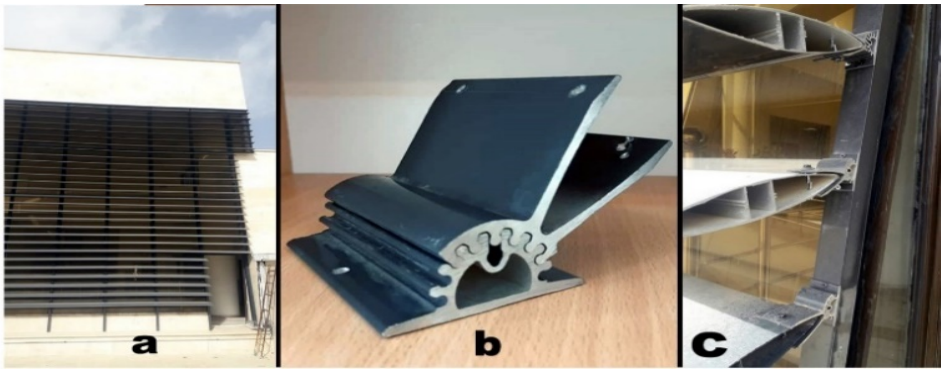

Figure 9. The proposed louver system: (a) front view; (b) the fixed support of the louver blades; (c) details of the connection between the fixed supports and louvers

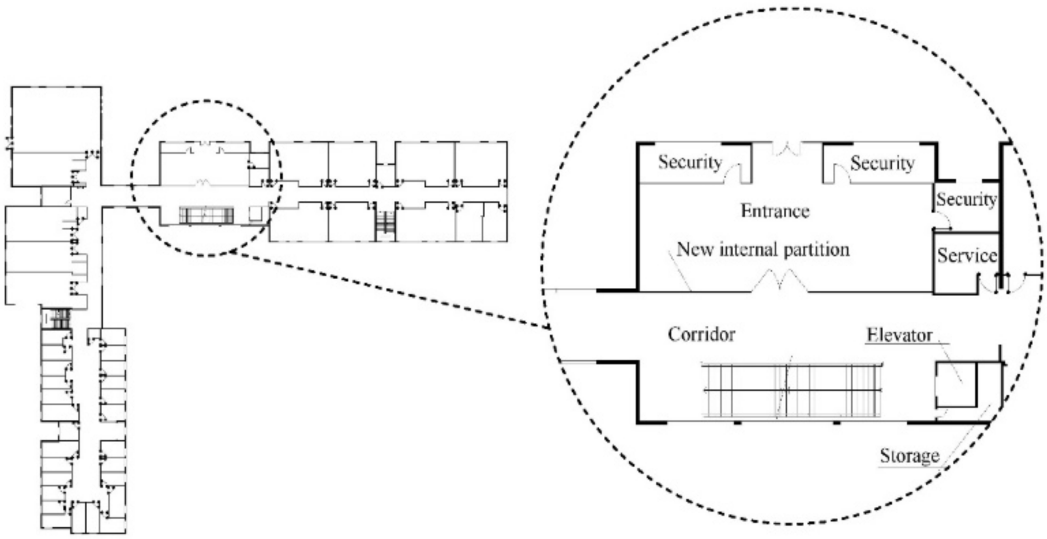

Figure 10. First-floor plan of the building and its entrance space

2.3.1. Simulations without using the HVAC systems

In the first part of the simulation process, several simulations assess the effect of EEMs on the energy consumption of the building. The simulations without using the HVAC systems indicate two environmental parameters, including IAT and RH of the building. These parameters are used to compare the comfort conditions of occupants in the building. In addition, the simulations are performed with natural ventilation in each zone. The setpoint for the natural ventilation is 21 °C and is added according to the comfort range of the site (Kermanshah).

2.3.2. Simulations using the HVAC systems

The second part of the simulation process includes several simulations using the HVAC systems in the building. These simulations compare new IAT and RH values with the previous ones. Moreover, the natural ventilation is turned off in these simulations since the windows are closed according to the behavioral patterns of the current occupants. Therefore, these simulations prove the energy-saving potential of each EEM and compare the IAT and RH values with previous values.

3. RESULTS AND DISCUSSION

Simulation results are divided into two main parts: the results without using the HVAC systems and the results using the HVAC systems. These simulations are performed with passive EEMs, including window replacement, shading devices, insulation, and addition of a new partition to the entrance part of the building. Accordingly, six different scenarios are defined for the simulation process (Table 5).

Table 5. Different scenarios used in the simulation process

Scenario	EEM(s)
1	-
2	Window replacement
3	Shading devices
4	Insulation
5	New partition for the entrance
6	Window replacement, Shading devices, Insulation, and New partition for the entrance

3.1. Simulations without using the HVAC systems

The first part of the simulation process consists of six separate simulations. These simulations without using the HVAC systems indicate IAT and RH values on a building scale. Accordingly, it is possible to identify the hottest and coldest days without using the HVAC systems. Therefore, daily simulations were performed to find the minimum and maximum IAT and RH values. The daily simulation results were added to an EXCEL file, and the IAT and RH values were identified in each scenario. According to these results, the hottest day is August 2 when the IAT of the building is 36.38 °C. Also, the coldest day is February 3 when the IAT is 12.17 °C. Accordingly, these passive EEMs were defined to reduce the heating and cooling demands of the building using these simulation results. For instance, the shading devices were designed according to the solar altitude on the hottest day (August 2).

3.2. Simulations using the HVAC systems

After performing the simulations without using the HVAC systems, various simulations using the HVAC systems were conducted that indicate the effect of each scenario on the energy performance of the building. These simulations showed the impact of each EEM on the heating and cooling demands of the building. Moreover, these simulations specify the IAT and RH values in different scenarios. Firstly, daily simulation results compare the minimum, maximum, and mean IAT and RH values.

Tables 6 and 7 show the minimum, maximum, and mean IAT and RH values in each scenario. As shown in Table 6, the mean monthly IAT values in Scenario 6 have changed considerably. In the cold season, from October to April, the IAT values increased. Moreover, the IAT values in the warm season, from May to September, increased slightly. The main reason is that these EEMs trap internal heat. Figure 11 shows the monthly IAT changes when the HVAC systems are turned off (simulations without using the HVAC systems). Since this building is in a heating dominant climate, these EEMs should increase the building IAT in the cold season. According to Figure 11, the minimum monthly IAT increased by 5.29 °C in December. Also, the maximum monthly IAT increased up to 3.11 °C in January. In addition, the average monthly IAT increased up to 3.87 °C in January. These results indicate that these passive EEMs could increase the IAT of the building remarkably. On the other hand, the maximum monthly IAT was reduced by 0.09 °C in July, which indicated the positive effect of using the EEMs in warm seasons.

Table 6. The minimum, maximum, and mean IAT values in each scenario

			Jan.	Feb.	Mar.	Apr.	May	Jun.	Jul.	Aug.	Sep.	Oct.	Nov.	Dec.
Scenario 1	HVAC Off	Mean IAT	15.39	15.96	18.31	22.71	26.83	31.92	34.84	34.79	31.13	24.87	20.11	16.02
	HVAC On		19.18	19.39	20.02	22.59	24.43	26.12	26.54	26.54	25.73	23.18	20.82	19.48
Scenario 2	HVAC Off		15.13	15.66	17.98	22.40	26.53	31.62	34.52	34.53	30.90	24.79	20.04	15.80
	HVAC On		19.10	19.28	19.86	22.37	24.25	26.03	26.49	26.48	25.63	22.97	20.63	19.09
Scenario 3	HVAC Off		15.05	15.51	17.74	22.06	26.08	31.18	34.04	34.05	30.50	24.54	19.98	15.75
	HVAC On		19.11	19.27	19.79	22.18	24.04	25.90	26.40	26.39	25.51	22.91	20.64	19.11
Scenario 4	HVAC Off		20.02	20.28	22.07	25.38	29.06	35.14	36.39	36.72	33.84	28.44	23.94	20.52
	HVAC On		21.25	21.52	22.37	24.14	25.07	26.03	26.27	26.33	25.88	24.57	23.17	21.46
Scenario 5	HVAC Off		15.38	15.95	18.30	22.70	26.83	31.92	34.87	34.79	31.14	24.87	20.10	16.01
	HVAC On		19.18	19.40	20.02	22.59	24.43	26.11	26.54	26.54	25.73	23.18	20.83	19.18
Scenario 6	HVAC Off		19.26	19.34	20.94	24.12	27.69	32.26	34.84	35.11	32.31	27.17	23.00	19.80
	HVAC On		20.83	21.00	21.63	23.45	24.55	25.65	25.99	26.01	25.51	24.12	22.69	21.07

Table 7. The minimum, maximum, and mean RH values in each scenario

			Jan.	Feb.	Mar.	Apr.	May	Jun.	Jul.	Aug.	Sep.	Oct.	Nov.	Dec.
Scenario 1	HVAC Off	Mean RH	32.01	35.20	34.93	33.62	34.04	16.27	22.17	24.25	23.92	29.50	33.04	39.64
	HVAC On		25.47	29.08	32.28	34.03	36.90	19.22	28.50	29.88	28.59	31.59	32.50	32.99
Scenario 2	HVAC Off		32.71	36.03	35.77	34.32	34.67	16.88	22.82	24.94	24.53	30.17	33.69	40.40
	HVAC On		25.70	29.40	32.66	34.68	37.17	19.38	28.68	30.08	28.97	32.20	33.01	33.30
Scenario 3	HVAC Off		32.90	36.41	36.54	35.08	35.68	17.74	23.82	24.16	25.25	30.46	33.86	40.62
	HVAC On		25.59	29.37	32.83	35.27	37.85	19.57	28.83	30.32	29.19	32.23	32.91	33.18
Scenario 4	HVAC Off		28.51	30.75	31.64	32.70	34.75	20.15	27.11	28.47	26.34	27.75	31.18	34.21
	HVAC On		31.46	33.13	33.74	32.93	37.00	23.84	32.60	33.30	31.34	30.85	33.11	36.62
Scenario 5	HVAC Off		32.14	35.17	34.97	33.67	34.05	16.23	22.16	24.09	23.90	29.52	33.06	39.68
	HVAC On		25.45	29.08	32.22	33.99	36.61	19.18	28.53	29.92	28.62	31.61	32.51	32.98
Scenario 5	HVAC Off		30.69	33.41	34.45	35.42	37.95	23.62	31.01	32.26	29.44	29.96	33.18	36.14
	HVAC On		32.63	34.86	36.72	36.14	40.04	25.21	34.11	35.08	33.41	32.89	35.09	37.88

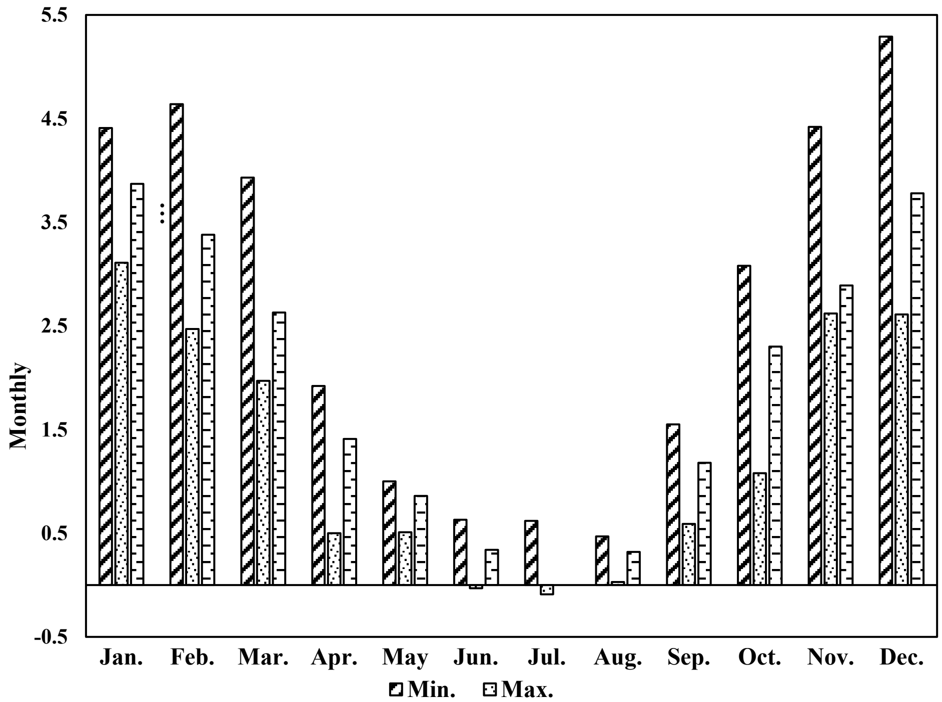

Figure 11. Monthly IAT changes of the building without using the HVAC systems

Figure 12 shows the monthly IAT changes for the building when the HVAC systems are turned on (simulations using the HVAC systems). According to Figure 12, the minimum monthly IAT increased by 5.12 °C in December. Also, the maximum monthly IAT increased up to 1.43 °C in December. Moreover, the average monthly IAT increased up to 1.89 °C in December. On the other hand, the maximum monthly IAT was reduced by about 2.17 °C in July, which indicated the positive effect of these EEMs in warm seasons. The mean monthly IAT was reduced considerably in warm seasons, from May to September, and increased remarkably in cold seasons.

Table 7 indicates the RH values before and after using the HVAC systems in the building. The mean monthly RH values increased considerably. In Scenario 6, the maximum mean RH value reached 53.22 % on November 15, which was in the acceptable thermal comfort range, according to the American Society of Heating, refrigerating, and Air-Conditioning Engineers (ASHRAE) Standard 55-2010 metrics (ASHARE, 2013). Also, the average minimum monthly RH value was 25.21 % in June. Figure 13 shows the monthly RH changes for the building without using the HVAC systems. According to Figure 13, the minimum monthly RH value increased by 7.27 % in April. Also, the maximum monthly RH value increased 14.77 % in June, and the average monthly RH value increased 8.84 % in July. Furthermore, the maximum monthly RH value decreased by 6.38 % in December.

Figure 14 shows the monthly RH changes using the HVAC systems in the building. According to Figure 14, the minimum monthly RH value increased 10.27 % in June. Also, the maximum monthly RH value increased up to 6.84 % in February, and the average monthly RH value increased up to 7.16 % in January. Accordingly, the RH value for the building increased after the retrofitting process.

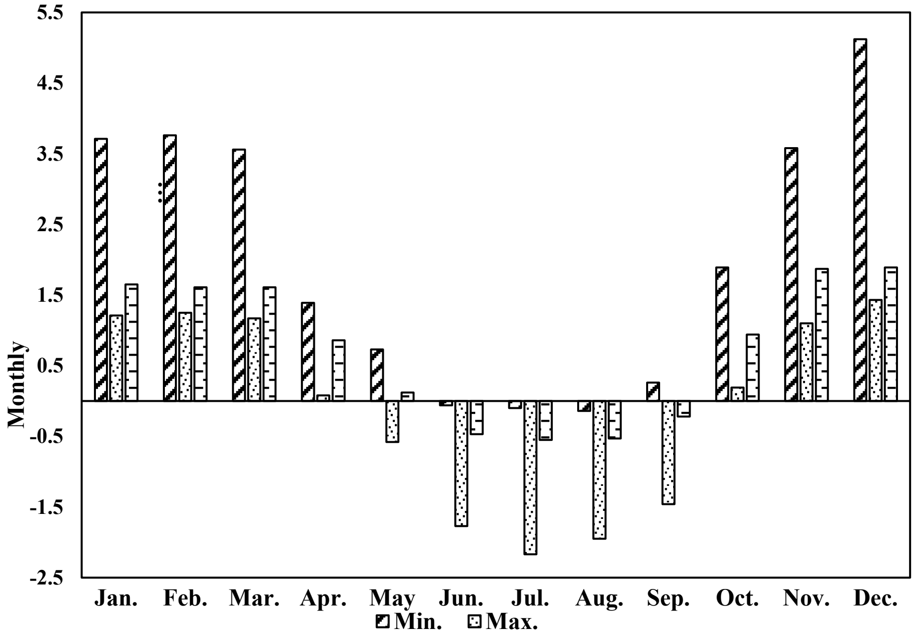

Figure 12. Monthly IAT changes for the building using the HVAC systems

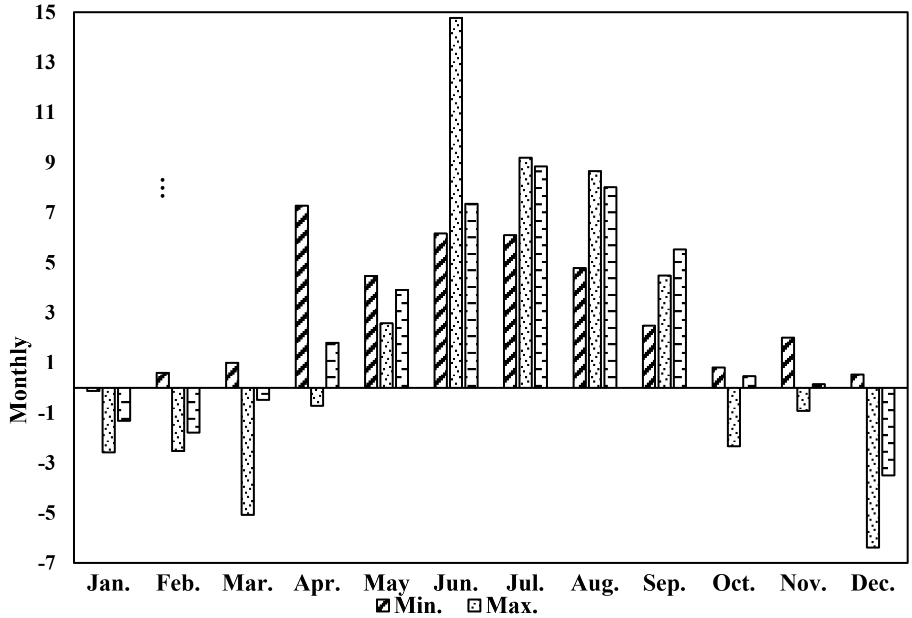

Figure 13. Monthly RH changes without using the HVAC systems

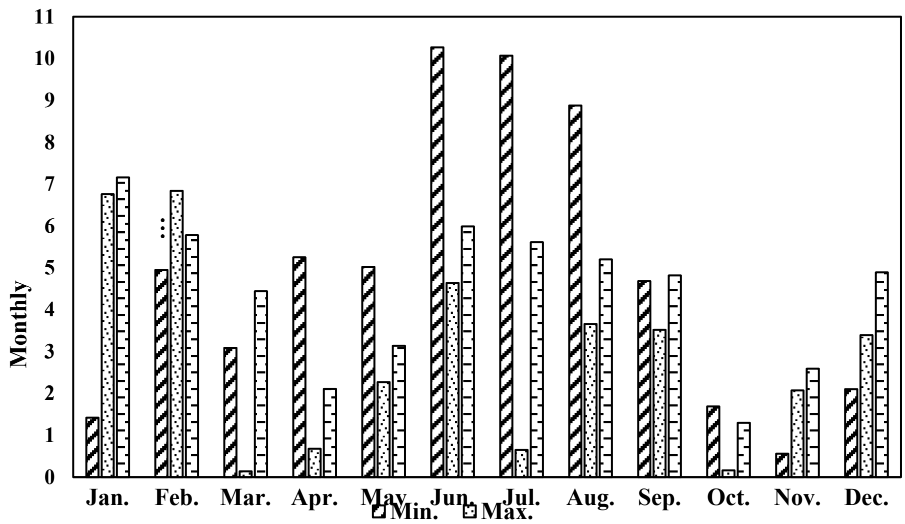

Figure 14. Monthly RH changes using the HVAC systems

Figure 15 indicates the monthly IAT of the building when the HVAC systems are turned off during the simulation process. Figure 15 represents the monthly IAT values before and after the retrofitting process. According to Figure 15, the monthly IAT of the building increased considerably in the cold seasons, and it is within the comfort range in the cold seasons. This comfort range is defined according to ASHRAE Standard 55-2010 metrics (ASHARE, 2013). The results show that the EEMs can affect the heating demand of the building positively. Furthermore, Figure 16 shows the monthly IAT of the building using the HVAC systems. According to Figure 16, the IAT increases in cold seasons, which confirms the simulation results of the previous section without using the HVAC systems.

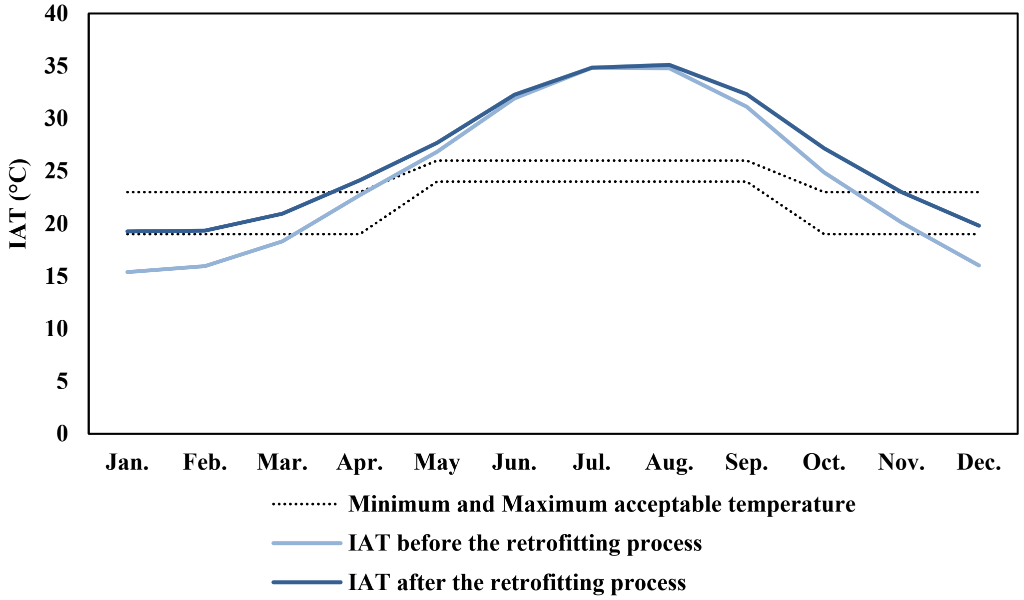

Figure 15. The monthly IAT of the building without using the HVAC systems before and after the retrofitting process

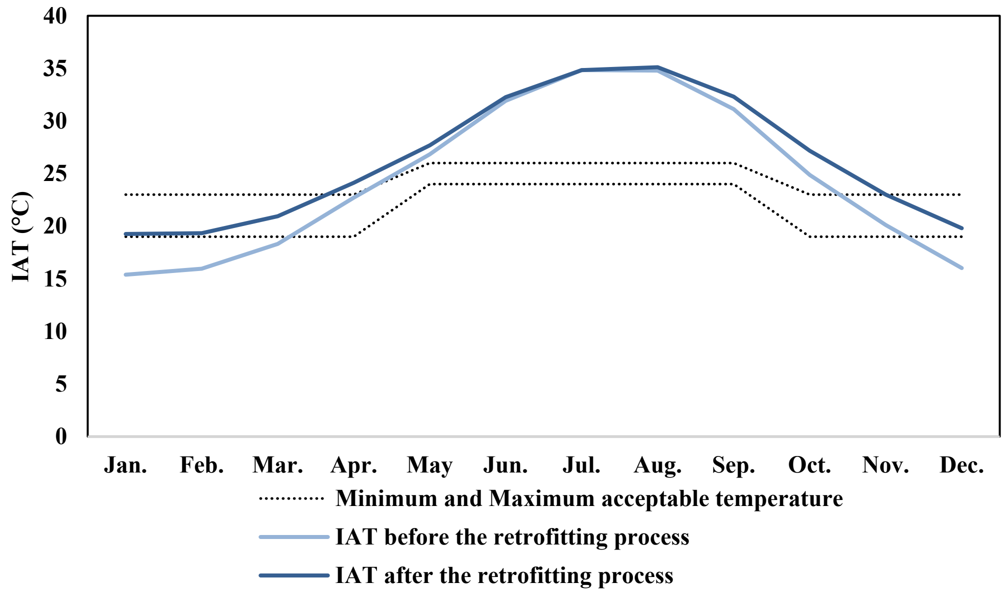

Figure 16. The monthly IAT of the building using the HVAC systems before and after the retrofitting process

Since the primary purpose of this research is to demonstrate the positive effects of passive EEMs on the energy consumption of educational buildings, this section introduces the energy-saving potential of the EEMs. This section uses simulation data of the building using the HVAC systems since the simulations without using the HVAC systems cannot show the heating and cooling demand of the building. Figure 17 shows the mentioned heating and cooling demand in each scenario. In Scenario 2, the new window type increased the heating demand by 6.51 %, while the cooling demand was reduced up to 3.42 %. In Scenario 3, the heating demand increased by 8.79 %, and the cooling demand was reduced by 7.73 % using the new shading devices.

The proposed insulations reduced the heating and cooling demand of the building by 84.52 % and 4.56 %, respectively. The main reason for this considerable reduction is that the infiltration rate of the building changed from 1 to 0.50 (ac/h) after using the new insulations. The new partition in the entrance part of the building did not affect the overall energy performance of the building, but it could increase the IAT values on a building scale. The last scenario indicates the effect of all EEMs on the energy performance of the building. These EEMs reduced the heating demand up to 80.14 % and reduced the cooling-demand up to 15.70 %.

Figure 18 shows the energy consumption of the building in each scenario. The Energy Use Intensity (EUI) of the building was 394.30 (kWh/m^2. year) before the retrofitting process. After replacing the existing windows with the proposed new windows, the building energy consumption decreased by 0.15 %. The proposed shading devices mitigated the energy consumption of the building by 0.88 %. The most effective EEM was using the new insulations, which reduced the energy consumption by 8.46 %. Also, the new partition had no considerable effect on the energy consumption of the building. The latest scenario indicated a 10.44 % reduction in energy consumption of the building. According to the simulation results of the mentioned scenario, each EEM had a positive effect during the retrofitting process of the building.

3.3. Validation

This research uses a simulation-based method during the research process. It is necessary to compare simulation results with experimental data, including electricity and natural gas bills. This research compares the simulation results with the monthly electricity bill of the building. Figure 19 shows the difference between the simulation results and the electricity bill of the building. The minimum difference between the simulation results and the monthly electricity bill of the building was 1.60 %. Moreover, the maximum difference between the simulation results and the monthly electricity bill of the building was 4.98 %.

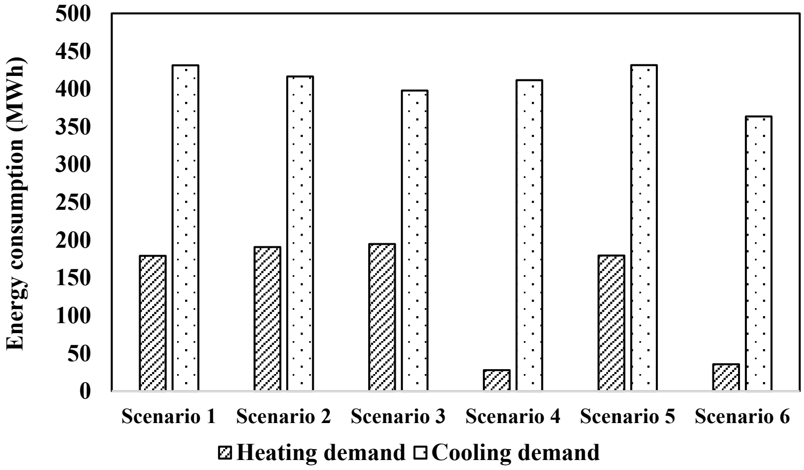

Figure 17. The heating and cooling demand of the building in each scenario

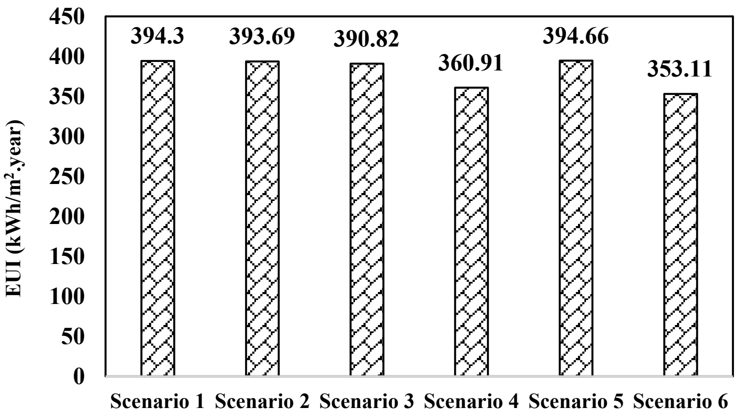

Figure 18. Energy consumption of the building in each scenario

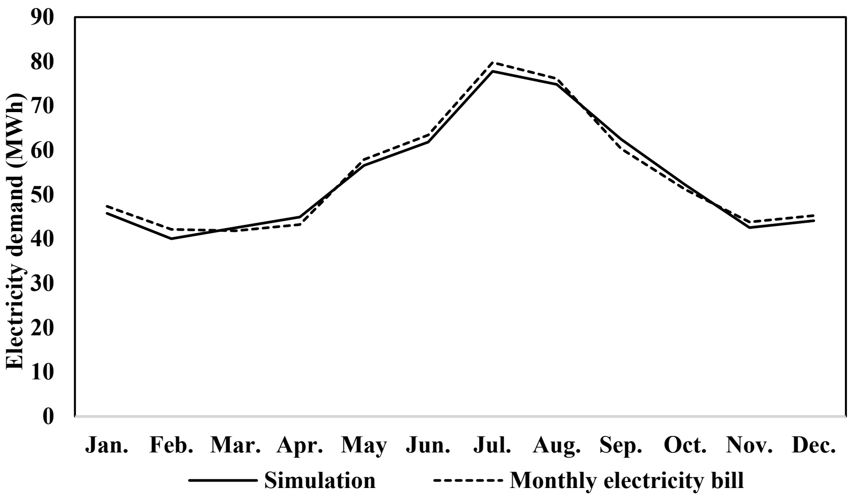

Figure 19. A comparison between the simulation results and the monthly electricity bill of the building

4. CONCLUSIONS

This research investigated the effect of various passive EEMs on the energy performance of an existing educational building. A new simulation method was introduced that divided the simulations into two main parts. This new method consisted of simulations without using the HVAC systems and simulations using the HVAC systems. Simulations without using the HVAC systems gave an overview of the current IAT and RH values for the building. This initial step was taken to offer some passive EEMs to enhance the IAT of the studied building, located in a heating-dominated region. Since the main focus of this research was to reduce the energy consumption of the building, the positive effects of these EEMs on the cooling demand of the building were identified, too.

This research used a simulation-based method to examine the effect of each EEM and the total effect of using the integrated retrofitting EEMs on the building energy efficiency. The data collection and modeling in this research include collecting raw data related to the physical characteristics of the building experimentally and creating a basic model in DesignBuilder software by entering the mentioned data and the official climate information. The next step included examining the impacts of the proposed EEMs on the energy consumption of the building by performing several simulations using the proposed simulation method. The latest stage of the research included comparing the energy performance of the building in each scenario by analyzing the simulation results. The results confirmed that the use of the proposed integrated retrofitting EEMs could contribute to mitigating the heating and cooling energy demands of the building. The results showed that the building heating demand was reduced up to 80.14 %, like the results of the previous research obtained in (Pungercar et al., 2021). In addition, using the EEMs reduced 15.70 % of the building cooling demand, which is in line with the results of the previous research in (Song et al., 2017). The final simulation illustrated that using the EEMs reduced 10.44 % of the total energy demand of the building.

However, combining the proposed passive EEMs with other passive and active retrofitting measures such as using the building integrated photovoltaic system, phase change materials, solar chimney, and prefabricated hybrid passive cooling and heating systems still needs further research. This study focused on the importance of simulations without using the HVAC systems in the case study building. Then, these simulation results were compared with normal simulations using the HAVC systems in the building. Therefore, this research did not find optimal solutions for this case study building. Future studies can focus on finding optimal solutions for educational buildings and other building types using the method used in this research.

5. ACKNOWLEDGEMENT

The authors appreciate the help of Razi University for giving the required data during the initial stages of this research.

NOMENCLATURE

ASHRAE	American Society of Heating, Refrigerating, and Air-conditioning Engineers
BEMS	Building Energy Management System
CHP	Combined Heat and Power System
DHW	Domestic Hot Water
ECM	Energy Conservation Measures
EEM	Energy Efficiency Measure
EPS	Expanded Polystyrene
EUI	Energy Use Intensity (kWh/m^2.year)
HVAC	Heating, Ventilating, and Air Conditioning
IAT	Indoor Air Temperature (°C)
IEQ	Indoor Environmental Quality
MEP	Mechanical, Electrical, and Pumping Services
OEB	Occupant Energy Behavior
PBT	Payback Time
PV	Photovoltaic
RH	Relative Humidity (%)
SHGC	Solar Heat Gain Coefficient
Tvis	Visual Transmittance
VAV	Various Air Volume
WWR	Window to Wall Ratio (%)

REFERENCES

1. Abu-Hamdeh, N.H., Khoshaim, A., Alzahrani, M.A., & Hatamleh, R.I. (2022). Study of the flat plate solar collector's efficiency for sustainable and renewable energy management in a building by a phase change material: Containing paraffin-wax/graphene and paraffin-wax/graphene oxide carbon-based fluids. *Journal of Building Engineering*, *57*, 104804. https://doi.org/https://doi.org/10.1016/j.jobe.2022.104804
2. Ahmed, W., & Asif, M. (2020). BIM-based techno-economic assessment of energy retrofitting residential buildings in hot humid climate. *Energy and Buildings*, *227*, 110406. https://doi.org/https://doi.org/10.1016/j.enbuild.2020.110406
3. Ahmed, W., & Asif, M. (2021). A critical review of energy retrofitting trends in residential buildings with particular focus on the GCC countries. *Renewable and Sustainable Energy Reviews*, *144*, 111000. https://doi.org/https://doi.org/10.1016/j.rser.2021.111000
4. Alah Rezazadeh, S., Mirzaie, I., Pourmahmoud, N., & Ahmadi, N. (2014). Three dimensional computational fluid dynamics analysis of a proton exchange membrane fuel cell. *Journal of Renewable Energy and Environment (JREE)*, *1*(1), 30-42. https://doi.org/10.30501/jree.2014.70054
5. Alazazmeh, A., & Asif, M. (2021). Commercial building retrofitting: Assessment of improvements in energy performance and indoor air quality. *Case Studies in Thermal Engineering*, *26*, 100946. https://doi.org/https://doi.org/10.1016/j.csite.2021.100946
6. Amani, N., & Reza Soroush, A.A. (2021). Energy consumption management of commercial buildings by optimizing the angle of solar panels. *Journal of Renewable Energy and Environment (JREE)*, *8*(3), 1-7. https://doi.org/10.30501/jree.2020.241836.1134
7. Ascione, F., Bianco, N., De Masi, R.F., Mauro, G.M., & Vanoli, G.P. (2017). Energy retrofit of educational buildings: Transient energy simulations, model calibration and multi-objective optimization towards nearly zero-energy performance. *Energy and Buildings*, *144*, 303-319. https://doi.org/https://doi.org/10.1016/j.enbuild.2017.03.056
8. Ascione, F., Bianco, N., Mauro, G.M., & Napolitano, D.F. (2021). Knowledge and energy retrofitting of neighborhoods and districts. A comprehensive approach coupling geographical information systems, building simulations and optimization engines. *Energy Conversion and Management*, *230*, 113786. https://doi.org/https://doi.org/10.1016/j.enconman.2020.113786
9. ASHARE. (2013). ASHRAE Standard 55-2010: Thermal environmental conditions for human occupancy. *American Society of Heating, Refrigeration and Air Conditioning Engineers, ASHRAE Sta*. https://www.ashrae.org/technical-resources/bookstore/standard-55-thermal-environmental-conditions-for-human-occupancy
10. Bagheri, F., Mokarizadeh, V., & Jabbar, M. (2013). Developing energy performance label for office buildings in Iran. *Energy and Buildings*, *61*, 116-124. https://doi.org/https://doi.org/10.1016/j.enbuild.2013.02.022
11. Chien, F., Ajaz, T., Andlib, Z., Chau, K.Y., Ahmad, P., & Sharif, A. (2021). The role of technology innovation, renewable energy and globalization in reducing environmental degradation in Pakistan: A step towards sustainable environment. *Renewable Energy*, *177*, 308-317. https://doi.org/https://doi.org/10.1016/j.renene.2021.05.101
12. Dabaieh, M., & Elbably, A. (2015). Ventilated trombe wall as a passive solar heating and cooling retrofitting approach; A low-tech design for

off-grid settlements in semi-arid climates. *Solar Energy*, *122*, 820-833. https://doi.org/https://doi.org/10.1016/j.solener.2015.10.005

13. Dabaieh, M., Makhlouf, N.N., & Hosny, O.M. (2016). Roof top PV retrofitting: A rehabilitation assessment towards nearly zero energy buildings in remote off-grid vernacular settlements in Egypt. *Solar Energy*, *123*, 160-173. https://doi.org/https://doi.org/10.1016/j.solener.2015.11.005
14. Dall'O', G., Galante, A., & Pasetti, G. (2012). A methodology for evaluating the potential energy savings of retrofitting residential building stocks. *Sustainable Cities and Society*, *4*, 12-21. https://doi.org/https://doi.org/10.1016/j.scs.2012.01.004
15. El-Darwish, I., & Gomaa, M. (2017). Retrofitting strategy for building envelopes to achieve energy efficiency. *Alexandria Engineering Journal*, *56*(4), 579-589. https://doi.org/https://doi.org/10.1016/j.aej.2017.05.011
16. Gui, X., Gou, Z., & Lu, Y. (2021). Reducing university energy use beyond energy retrofitting: The academic calendar impacts. *Energy and Buildings*, *231*, 110647. https://doi.org/https://doi.org/10.1016/j.enbuild.2020.110647
17. Heidari, A., Taghipour, M., & Yarmahmoodi, Z. (2021). The effect of fixed external shading devices on daylighting and thermal comfort in residential building. *Journal of Daylighting*, *8*(2). https://doi.org/10.15627/JD.2021.15
18. Hirvonen, J., Heljo, J., Jokisalo, J., Kurvinen, A., Saari, A., Niemelä, T., Sankelo, P., & Kosonen, R. (2021). Emissions and power demand in optimal energy retrofit scenarios of the Finnish building stock by 2050. *Sustainable Cities and Society*, *70*, 102896. https://doi.org/https://doi.org/10.1016/j.scs.2021.102896
19. Huang, H., Binti Wan Mohd Nazi, W.I., Yu, Y., & Wang, Y. (2020). Energy performance of a high-rise residential building retrofitted to passive building standard – A case study. *Applied Thermal Engineering*, *181*, 115902. https://doi.org/https://doi.org/10.1016/j.applthermaleng.2020.115902
20. Huang, Y., Niu, J., & Chung, T. (2013). Study on performance of energy-efficient retrofitting measures on commercial building external walls in cooling-dominant cities. *Applied Energy*, *103*, 97-108. https://doi.org/https://doi.org/10.1016/j.apenergy.2012.09.003
21. Jafari, A., & Valentin, V. (2017). An optimization framework for building energy retrofits decision-making. *Building and Environment*, *115*, 118-129. https://doi.org/https://doi.org/10.1016/j.buildenv.2017.01.020
22. Jami, S., Forouzandeh, N., Zomorodian, Z.S., Tahsildoost, M., & Khoshbakht, M. (2021). The effect of occupant behaviors on energy retrofit: A case study of student dormitories in Tehran. *Journal of Cleaner Production*, *278*, 123556. https://doi.org/https://doi.org/10.1016/j.jclepro.2020.123556
23. Kadrić, D., Aganovic, A., Martinović, S., Delalić, N., & Delalić-Gurda, B. (2022). Cost-related analysis of implementing energy-efficient retrofit measures in the residential building sector of a middle-income country – A case study of Bosnia and Herzegovina. *Energy and Buildings*, *257*, 111765. https://doi.org/https://doi.org/10.1016/j.enbuild.2021.111765
24. Li, Q., Zhang, L., Zhang, L., & Wu, X. (2021). Optimizing energy efficiency and thermal comfort in building green retrofit. *Energy*, *237*, 121509. https://doi.org/https://doi.org/10.1016/j.energy.2021.121509
25. Liu, L., Rohdin, P., & Moshfegh, B. (2015). Evaluating indoor environment of a retrofitted multi-family building with improved energy performance in Sweden. *Energy and Buildings*, *102*, 32-44. https://doi.org/https://doi.org/10.1016/j.enbuild.2015.05.021
26. Lolli, N., Nocente, A., Brozovsky, J., Woods, R., & Grynning, S. (2019). Automatic vs manual control strategy for window blinds and ceiling lights: consequences to perceived visual and thermal discomfort. *Journal of Daylighting*, *6*, 112-123. https://doi.org/10.15627/jd.2019.11
27. Lu, Y., Li, P., Lee, Y.P., & Song, X. (2021). An integrated decision-making framework for existing building retrofits based on energy simulation and cost-benefit analysis. *Journal of Building Engineering*, *43*, 103200. https://doi.org/https://doi.org/10.1016/j.jobe.2021.103200
28. Magnani, N., Carrosio, G., & Osti, G. (2020). Energy retrofitting of urban buildings: A socio-spatial analysis of three mid-sized Italian cities. *Energy Policy*, *139*, 111341. https://doi.org/https://doi.org/10.1016/j.enpol.2020.111341
29. Maleki, A., & Dehghan, N. (2021). Optimum characteristics of windows in an office building in Isfahan for save energy and preserve visual comfort. *Journal of Daylighting*, *8*(2). https://doi.org/10.15627/JD.2021.18
30. Mata, É., Kalagasidis, A.S., & Johnsson, F. (2018). Contributions of building retrofitting in five member states to EU targets for energy savings. *Renewable and Sustainable Energy Reviews*, *93*, 759-774. https://doi.org/https://doi.org/10.1016/j.rser.2018.05.014
31. Mejjaouli, S., & Alzahrani, M. (2020). Decision-making model for optimum energy retrofitting strategies in residential buildings. *Sustainable Production and Consumption*, *24*, 211-218. https://doi.org/https://doi.org/10.1016/j.spc.2020.07.008
32. Moshiri, S., Atabi, F., Panjehshahi, M.H., & Lechtenböehmer, S. (2012). Long run energy demand in Iran: A scenario analysis. *International Journal of Energy Sector Management*, *6*(1), 120-144. https://doi.org/10.1108/17506221211216571
33. Ozarisoy, B., & Altan, H. (2021). A novel methodological framework for the optimisation of post-war social housing developments in the South-Eastern Mediterranean climate: Policy design and life-cycle cost impact analysis of retrofitting strategies. *Solar Energy*, *225*, 517-560. https://doi.org/https://doi.org/10.1016/j.solener.2021.07.008
34. Pazouki, M., Rezaie, K., & Bozorgi-Amiri, A. (2021). A fuzzy robust multi-objective optimization model for building energy retrofit considering utility function: A university building case study. *Energy and Buildings*, *241*, 110933. https://doi.org/https://doi.org/10.1016/j.enbuild.2021.110933
35. Piccardo, C., Dodoo, A., Gustavsson, L., & Tettey, U. (2020). Retrofitting with different building materials: Life-cycle primary energy implications. *Energy*, *192*, 116648. https://doi.org/https://doi.org/10.1016/j.energy.2019.116648
36. Pungercar, V., Zhan, Q., Xiao, Y., Musso, F., Dinkel, A., & Pflug, T. (2021). A new retrofitting strategy for the improvement of indoor environment quality and energy efficiency in residential buildings in temperate climate using prefabricated elements. *Energy and Buildings*, *241*, 110951. https://doi.org/https://doi.org/10.1016/j.enbuild.2021.110951
37. Qu, K., Chen, X., Wang, Y., Calautit, J., Riffat, S., & Cui, X. (2021). Comprehensive energy, economic and thermal comfort assessments for the passive energy retrofit of historical buildings - A case study of a late nineteenth-century Victorian house renovation in the UK. *Energy*, *220*, 119646. https://doi.org/https://doi.org/10.1016/j.energy.2020.119646
38. Rabani, M., Bayera Madessa, H., Mohseni, O., & Nord, N. (2020). Minimizing delivered energy and life cycle cost using graphical script: An office building retrofitting case. *Applied Energy*, *268*, 114929. https://doi.org/https://doi.org/10.1016/j.apenergy.2020.114929
39. Serrano-Jiménez, A., Lizana, J., Molina-Huelva, M., & Barrios-Padura, Á. (2019). Decision-support method for profitable residential energy retrofitting based on energy-related occupant behaviour. *Journal of Cleaner Production*, *222*, 622-632. https://doi.org/https://doi.org/10.1016/j.jclepro.2019.03.089
40. Song, X., Ye, C., Li, H., Wang, X., & Ma, W. (2017). Field study on energy economic assessment of office buildings envelope retrofitting in southern China. *Sustainable Cities and Society*, *28*, 154-161. https://doi.org/https://doi.org/10.1016/j.scs.2016.08.029
41. Sun, H., Heng, C.K., Reindl, T., & Lau, S.S.Y. (2021). Visual impact assessment of coloured building-integrated photovoltaics on retrofitted building facades using saliency mapping. *Solar Energy*, *228*, 643-658. https://doi.org/https://doi.org/10.1016/j.solener.2021.09.087
42. Tahsildoost, M., & Zomorodian, Z.S. (2015). Energy retrofit techniques: An experimental study of two typical school buildings in Tehran. *Energy and Buildings*, *104*, 65-72. https://doi.org/https://doi.org/10.1016/j.enbuild.2015.06.079
43. Thomsen, K.E., Rose, J., Mørck, O., Jensen, S.Ø., Østergaard, I., Knudsen, H.N., & Bergsøe, N.C. (2016). Energy consumption and indoor climate in a residential building before and after comprehensive energy retrofitting. *Energy and Buildings*, *123*, 8-16. https://doi.org/https://doi.org/10.1016/j.enbuild.2016.04.049
44. Torabi Moghadam, S., & Lombardi, P. (2019). An interactive multi-criteria spatial decision support system for energy retrofitting of building stocks using CommuntiyVIZ to support urban energy planning. *Building and Environment*, *163*, 106233. https://doi.org/https://doi.org/10.1016/j.buildenv.2019.106233
45. Urbikain, M.K. (2020). Energy efficient solutions for retrofitting a residential multi-storey building with vacuum insulation panels and low-E windows in two European climates. *Journal of Cleaner Production*,

269, 121459. https://doi.org/https://doi.org/10.1016/j.jclepro.2020.121459

46. Wang, Q., & Holmberg, S. (2015). A methodology to assess energy-demand savings and cost effectiveness of retrofitting in existing Swedish residential buildings. *Sustainable Cities and Society*, *14*, 254-266. https://doi.org/https://doi.org/10.1016/j.scs.2014.10.002
47. Wang, Z., Liu, X., Deng, G., Shen, H., & Xu, Z. (2021). A framework for retrofitting existing houses to nearly zero energy buildings: Development and a real-life case study. *Energy and Buildings*, *252*, 111438. https://doi.org/https://doi.org/10.1016/j.enbuild.2021.111438
48. Yang, S., Cho, H.M., Yun, B.Y., Hong, T., & Kim, S. (2021). Energy usage and cost analysis of passive thermal retrofits for low-rise residential buildings in Seoul. *Renewable and Sustainable Energy Reviews*, *151*, 111617. https://doi.org/https://doi.org/10.1016/j.rser.2021.111617
49. Zhou, Z., Zhang, S., Wang, C., Zuo, J., He, Q., & Rameezdeen, R. (2016). Achieving energy efficient buildings via retrofitting of existing buildings: A case study. *Journal of Cleaner Production*, *112*, 3605-3615. https://doi.org/https://doi.org/10.1016/j.jclepro.2015.09.046
50. Zomorodian, M., & Nasrollahi, F. (2013). Architectural design optimization of school buildings for reduction of energy demand in hot and dry climates of Iran. *International Journal of Architectural Engineering & Urban Planning*, *23*, 41-50. http://ijaup.iust.ac.ir/article-1-152-en.html

JREE: Vol. 10, No. 3, (Summer 2023) 29-37

Journal of Renewable Energy and Environment

Journal Homepage: www.jree.ir

Materials and Energy Research Center

MERC

Research Article

Enhancement of 5-Hydroxymethylfurfural and 2,5-Furandicarboxylic Acid Extractions into Bio-Plastic Production from Renewable Sources

Payam Ghorbannezhad [a,b*], Behnam Dehbandi [c], Imtiaz Ali [d]

[a] *Department of Biorefinery, Faculty of New Technologies Engineering, Shahid Beheshti University, Tehran, Iran.*
[b] *Alliance for Biomass and Sustainability Research–ABISURE, National University of Colombia, Campus Robledo, M3-214, Medellín, Colombia.*
[c] *Department of Chemistry, Science and Research Branch, Islamic Azad University, Tehran, Iran.*
[d] *Department of Chemical and Materials Engineering, King Abudlaziz University, Rabigh, Suadia Arabia.*

PAPER INFO

Paper History:
Received: 28 July 2022
Revised: 08 October 2022
Accepted: 21 October 2022

Keywords:
5-Hydroxymethylfurfural (HMF),
2,5-Furandicarboxylic Acid (FDCA),
Renewable Sources,
Density Function Theory (DFT)

ABSTRACT

Furandicarboxylic acid (FDCA) is recognized as a valuable product of hydroxymethylfurfural (HMF) derived from cellulosic materials as an abundant renewable source. It could find future bioplastic application if a feasible separation process is developed. To find a commercially available solvent, FDCA should be selectively separated from HMF and the downstream process be supported by pyrolysis-gas chromatography-mass spectrometry experiments in line with density functional theory (DFT). Evaluation of the sigma potential and sigma surface analysis demonstrated that benzene and ethyl acetate enjoyed better extraction and HMF selectivity, whereas FDCA exhibited ideal behavior in the presence of DMF and DMSO solvents. It was proved that the hydrophobicity could be changed by improving the hydrogen-bonding interaction between them. Moreover, the up-down selection of classes of solvents based on the experimental data found by GC-MS revealed that polar molecular solvents (ethanol-water) were more compatible with carboxylic acids and alcohol compounds, while n-hexane was a desirable solvent for phenolic compounds. It was found that levoglucosan retained a significant fraction of water compared to other solvents, which need to be considered for further economic and environmental analysis under the multifaceted framework of biomass-derived products.

https://doi.org/10.30501/jree.2022.353576.1415

1. INTRODUCTION

Recently, bioplastics have become promising feedstocks for value-added products that have the potential to replace fossil fuel-based petrochemicals. Petrochemicals pose environmental and climate-related challenges to our society. Environmental concerns increase when chemical manufacturers expand their product portfolio and increase production due to the continuously increasing demand for polymeric materials. More than 8000 Mt of plastics continue to be consumed annually, roughly 80 % of which have ended up in landfills and oceans (Geyer et al., 2017). This is because as consumers, we are becoming more addicted to single-use disposable plastics. Based on the prediction made by the U.S. Department of Energy (DOE), plastic manufacturers will consume 20 % of all petroleum materials with a share of 15 % annual global carbon emissions by the year 2050 (Perlack et al., 2011). The global warning that arises from plastic production, consumption, and waste management requires renewable chemical strategies (Erickson & Winters, 2012; Zheng & Suh, 2019).

Biorefinery is recognized as a valuable route to biomass as a feedstock that can reduce our dependence on fossil fuels (Stuart & El-Halwagi, 2012). Biomass is an abundant feedstock with great potential to produce biofuels, biochemical, and bioproducts (Bilal et al., 2021; Ghorbannezhad et al., 2020). Today, more than 100 billion tons of biomass is available around the world, most of which end up as waste due to ineffective technologies (Dutta et al., 2014; Searle & Malins, 2015). Biomass can completely boost bioeconomy by rebuilding fuel and chemical manufacturing processes.

Lignocellulosic biomass is made up of carbohydrate polymers, such as cellulose (40-50 %) and hemicellulose (20-40 %), and aromatic polymers, such as lignin (20-30 %). These chemical components are the main building blocks of many biochemical platforms (Figure 1).

5-hydroxymethylfurfural (HMF) is recognized as a high-value building block compound of cellulose that can be transformed into a variety of value-added chemicals (Davidson et al., 2021; Kuster, 1990; Rosatella et al., 2011). HMF is recognized as the "top 10" chemical platform in the

*Corresponding Author's Email: p_ghorbannezhad@sbu.ac.ir (P. Ghorbannezhad)
URL: https://www.jree.ir/article_160756.html

Please cite this article as: Ghorbannezhad, P., Dehbandi, B. & Ali, I. (2023). Enhancement of 5-hydroxymethylfurfural and 2,5-furandicarboxylic acid extractions into bio-plastic production from renewable sources. *Journal of Renewable Energy and Environment (JREE)*, *10*(3), 29-37. https://doi.org/10.30501/jree.2022.353576.1415.

2423-7469/© 2023 The Author(s). Published by MERC. This is an open access article under the CC BY license (https://creativecommons.org/licenses/by/4.0/).

circular bioeconomy by DOE. It is synthesized by the dehydration of mono and polysaccharides present in lignocellulosic biomass. Furandicarboxylic acid (FDCA) is one of the most valuable biochemicals that can be derived from HMF via biological or chemical oxidation (Arikan et al., 2021). During conversion, the oxidation of the aldehyde of HMF produces 5-hydroxymethyl-2-furan carboxylic acid, which is an intermediate compound. Further oxidation of 5-hydroxymethyl-2-furan carboxylic acid produces furan carboxylic acid (FFCA), which finally turns into FDCA. The schematic of cellulose conversion is shown in Figure 2.

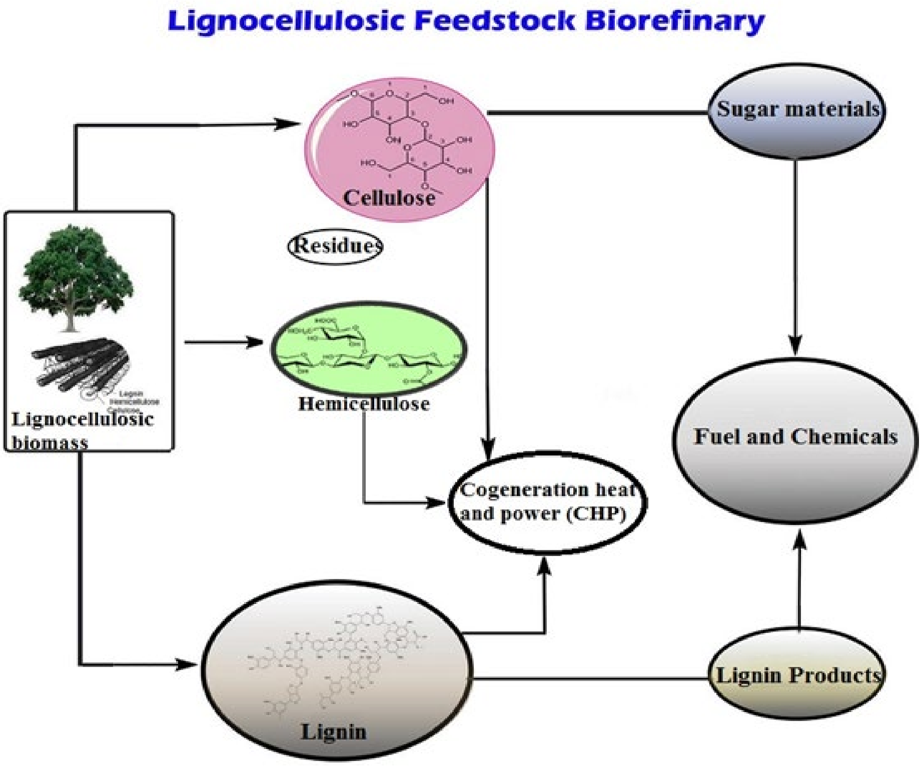

Figure 1. Pathways of value-added products from lignocellulosic components

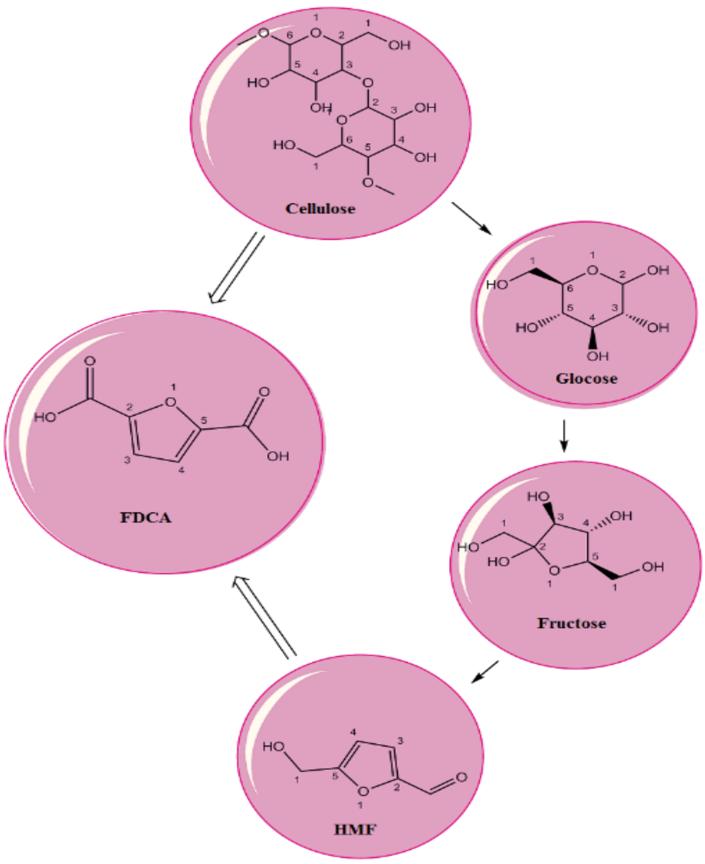

Figure 2. Overview of FDCA production pathways from cellulose

Therefore, one of the most cost-effective FDCA production routes is the direct conversion of biomass into desired products on a commercial scale (Arikan et al., 2021; Hwang et al., 2020). In this regard, condensation reactions under acidic aqueous conditions must be suppressed by substituting an organic solvent during the rehydration process (Bonner et al., 1960). Solvents are vital to obtain a higher yield of HMF and its derivatives. Currently, direct dehydration of glucose to produce HMF and its derivatives is limited by an inefficient separation process (Bello Ould-Amer et al., 2020; Cai et al., 2013; Hou et al., 2017; Motagamwala et al., 2019; Zunita et al., 2021). FDCA exhibits low solubility in water and the problem of deactivation during the direct conversion of glucose into HMF in water as a solvent (Esteban et al., 2020; Zhang et al., 2018). The weak separation efficiency for short-chain solvents led to high volumetric consumption of organic solvents and salts to make a biphasic system. However, selecting an efficient solvent for purification and separation of products is a new research area to develop biorefinery processes. Methyl isobutyl ketone (MIBK), tetrahydrofuran (THF), and dimethyl sulfoxide (DMSO) have been used as moderately polar and highly dielectric solvents to promote the dehydration reaction for HMF production (Weingarten et al., 2014). The authors have indicated that the solvents increased the dehydration reaction, but reduced the polymerization of HMF. Some studies revealed that biphasic system aims to improve the HMF yield via in situ extraction of HMF at the organic phase. A higher partition coefficient of HMF can lead to increased productivity and make the process cost-effective (Blumenthal et al., 2016). The computational method applies a heuristic approach that estimates the activity coefficient to identify appropriate solvents. The combination of quantum mechanics and statistical mechanics presents multifunctional models to better describe molecular thermodynamics. Unlike empirical models such as UNIFAC, ASOG, etc., the conductor-like screening model for real solvents (COSMO-RS) can explain intermolecular interactions (Balchandani & Singh, 2021; Klamt, 2018). An ensemble of pairwise intermolecular interactions in COSMO-RS provides a significant deviation in phase behavior, leading to crucial insights on different solvent classes (Eckert & Klamt, 2018). Density Function Theory (DFT) can be combined with COSMO-RS to optimize the performance of models (Momany & Schnupf, 2014; Wang et al., 2020). This work aims to investigate and predict the thermodynamic properties of cellulose derivatives obtained from biomass. Five samples including HMF, DFF, HMFCA, FDCA, and FFCA were studied. Flash points, boiling points, Henry's constant, activity coefficients, Vapor-Liquid Equilibrium (VLE), and Liquid-Liquid Equilibrium (LLE) were obtained for various solvents and different dielectric constants. The products were identified and predicted via thermodynamic properties that have not been reported before.

2. MATERIALS AND METHODS

2.1. Pyrolysis tandem microreactor

The experimental pyrolysis of biomass was performed in Rx-300 TR, a tandem micropyrolyzer system from Frontier Laboratories, Japan. The system is classified into two parts: a) pyrolysis reactor with a steady amount of biomass of 1-2 mg and b) catalyst bed reactor. Hence, you do not use the catalysts; you can set the reactor temperature to the same value as the pyrolysis reactor temperature. About 2 g of the milled biomass samples were placed in a stainless steel cup to drop into the first reactor. Helium as a neutral carrier gas (1 ml/min) transfers the vaporized biomass compound from the thermal degradation reactor to the catalyst bed reactor. A temperature of 500 °C with a heating rate of 10 °C.min^{-1} is fitted by a programmable temperature control to maintain a constant process condition. The hot vapor (syngas) is retained in the first reactor for less than 2 seconds and, then, goes into the catalyst bed reactor, which is finally detected by GC-MS interfaced with the pyrolysis system. The percentage area peak of each compound could be determined to estimate the yield of products individually.

2.2. Computational methods and theory

COSMO-RS is the conductor-like screening model for real solvation that uses Quantum Chemistry (QC) to predict the thermodynamic properties of molecules (Klamt., 1995; Klamt., 2005). The molecules are embedded in a virtual conductor based on the polarization charge densities of the solute and solvent molecules. DFT can be combined with the COSMO as it is available in most quantum chemical programs. The structure of the biomass used in this study was drawn manually using the Gauss view software, which was further optimized with the Gaussian 09 program (Forlemu et al., 2017). From the optimized structure, COSMO, sigma profile potential, and frequency files were generated. With the level of theory, Becke's three-parameter functional for exchange was combined with the nonlocal correlation potential of the Lee-Yang-Parr functional and the DGTZVP basis set (Godbout et al., 1992; Klamt et al., 2016). One of the important COSMO-RS calculations is to estimate the sigma profile of each sample studied. The specific interactions of each of the molecules at the aqueous phase were defined in COSMO-RS. The quantum mechanical characterization of solvents, such as electrostatic interactions and hydrogen bonding as well as local interactions of surface segments, was calculated and screened by the charge density profile σ and stored in the COSMO-RS database. The segment interaction of individual solvents determined the efficiency and solubility of the compositions via statistical thermodynamic calculations for the interacting surfaces. The free energies and chemical potentials of the molecules in pure and mixed solvents result from the efficiency of solubility and separation for each composition.In this work, the COSMO-RS calculations were performed using the COSMOtherm (Cosmologic GmbH, Leverkusen, Germany) program with BP_TZVPD_18 (Zhao et al., 2020). The geometries and conformations used for the solutes and solvents were generated and handled in the COSMO-RS calculations, as described before (Eckert & Klamt, 2018). By using the COSMOtherm program, the thermodynamic properties of the extracted chemical compounds can be predicted, such as flashpoints, boiling point, density, activity coefficient, σ surface, σ potential, Liquid Vapor Equilibrium (VLE), Liquid-Liquid Equilibrium (LLE),vapor pressure, Henry's law coefficient, and hexane-water partition coefficients at different solvents, temperatures, and and pressures. In COSMO, the σ profile of molecule X (Equation 1) and the chemical potential of a surface segment with screening charge density (Equation 2) were obtained. Each molecule X is described by its surface composition histogram with respect to σ, the so-called σ-profile pX(σ), and a pure or mixed liquid system is characterized by its solvent σ-profile.

$$p^{x_i}(\sigma) = \frac{n_i(\sigma)}{n_i} = \frac{A_i(\sigma)}{A_i} \quad (1)$$

where $A_i(\sigma)$ is the segment surface area that has charge density σ, x_i the mole fraction of the ith molecule x, A_i the area of the whole surface cavity rooted in the medium.

$$\mu_s(\sigma) = -\frac{RT}{a_{eff}} \ln\left[\int p_s(\sigma') \exp\left\{\frac{a_{eff}}{RT}[\mu_s(\sigma') - e(\sigma,\sigma')]\right\} d\sigma'\right] \quad (2)$$

where $\mu_s(\sigma')$ is the chemical potential of a surface segment. $\mu_s(\sigma)$ expresses the attraction of a solvent S to surface segments of polarity σ. σ is the polarity of the surface under study.

Table 1. Properties, energy efficacy, and toxicity of the studied solvents (Zhao et al., 2020)

Solvents	Properties				Energy efficiency			
	Molecular weight (g/mol)	Viscosity (mPa/s)	Log P	Flash point (°C)	Boiling point (°C)	ΔH vap. (kJ/mol)	Cp liq. ($J.kg^{-1}K^{-1}$)	Energy evaporation (kJ/mol)
Water	18.01	1.0016	-0.65	N/A	100	40.65	4185.5	40.6
Ethanol	46.07	0.983	-0.24	12	78	38.56	2.57	38.5
Methanol	32.04	0.543	-0.76	11	65	35.21	2.53	35.2
DMSO	78.13	2	-1.37	88.88	189	52.9	149.40	52,5
DMF	73.09	0.92	-1	60	153	56.7	146.05	46.7
Benzene	78.11	0.603	2	-11	80	30.72	133	33.8
Ethyl-Acetate	88.11	0.426	0.71	-4.44	77	31.94	161.47	31,9
CCl_4	153.82	0.965	2.8	982	77	29.82	133.0	30
Hexane	86.18	0.3	3.764	-7	69	28.85	265.2	28.8

3. RESULTS AND DISCUSSION

3.1. Sigma potential analysis

The δ-potential describes the possible interaction of compounds with solvents according to polarity and hydrogen bonding. Molecular interactions between the solvents and HMF play a vital role in HMF solubility. The shape, size, and initial components of the molecule are essential for molecular interaction. Caloric profiles provide important information to predict molecular interactions at the fluid phase. The hydrogen bond acceptor, hydrogen bond donor, and non-polar area associated with red, blue, and green, respectively, are shown in Figure 3. For δ-surface, the negative screening charge density represented the positive polarity. In general, acceptor hydrogen bonds have a negative charge density, whereas the donor hydrogen shows a positive charge density. For example, there are negative and positive sides to n-hexane. The negative side corresponds to hydrogens, whereas the positive side corresponds to carbons. In general, n-hexane shows a polar alkane characterization when the δ-potential in near zero.

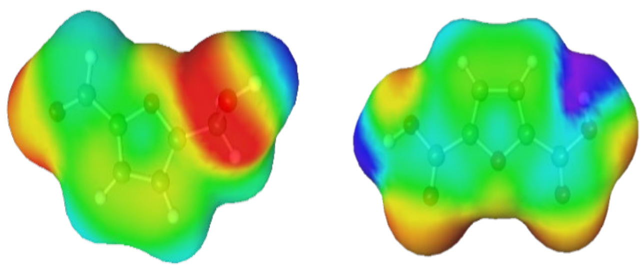

HMF FDCA

Figure 3. Sigma surface of HMF, HFDCA, FFCA, and FDCA

3.2. Chemical compositions of solvents

Several chemical compositions were obtained by GC-MS of biomass. The concentrated aqueous solution of cellulose enhances the generation of HMF. Water as a solvent resulted in higher HMF and levulinic acid converted into 2-MTHMF, butanols, and acid. Table 2 shows the chemical composition of cellulose in different solvents identified by GC-MS. The results showed that the DMF exhibited lower performance than ethyl acetate and hexane in water. More acid and esters (aliphatic compounds) were separated by ethanol-water solvents, whereas more aromatic compounds could be extracted by hexane and benzene as solvents. It is assumed that the low solubility of hydrocarbons in water results from the reduction of the polarity differences. Typically, polar solvents enhance HMF and carboxylic acid extraction by 20 %. Cellulose is anticipated to reduce the solubility of phenolic compounds in water and affect the overall separation process.

3.3. Excess energies of FDCA and HMF solvents

The free energy derivative validated the simulation of the interaction of FDCA separation in water and n-hexane, which corresponded to the process. The interaction of FDCA separation in n-hexane showed a Gibbs free energy value of + 0.8 $kcal.mol^{-1}$, whereas the same purification process in water is - 0.9 $kcal.mol^{-1}$ (Figure 4). However, n-hexane can be placed in the middle of the solvents, which could theoretically dissolve all compounds equally. Gibbs free energy is positive for n-hexane, illustrating low solubility limits for all concentration levels. The solubility of water at the organic phase of FDCA is lower than that of n-hexane. Thus, the Gibbs free energy presents a highly negative area in water.

Table 2. Chemical compositions of solvent extraction by GC-MS

Compounds	Water	Ethanol	Methanol	DMSO	DMF	Benzene	Ethyl acetate	CCl_4	Hexane
	Acids								
Acetic acid	2.6	2.7	2.1	1.9	1.2	1.6	1.5	1.6	1.5
Formic acid	0.8	0.9	0.4	0.4	0.5	0.5	0.5	0.6	0.5
Propionic acid	0.8	1.1	0.5	0.7	0.6	0.7	0.7	0.8	0.6
Hexadeconoic acid	0.5	0.7	0.4	0.3	0.1	0.3	0.2	0.2	0.3
Benzeoic acid	0.4	0.7	0	0.4	0.2	0.4	0.3	0.4	0.4
Levulinic acid	1.2	1.7	1.4	0.9	0.9	0.9	1.1	1.1	0.8
	Ketones								
1-Hedroxy-2-propanone	1.6	1.6	1.2	1.3	1.4	1.4	1.4	1.4	1.4
Butanone	0.5	0.7	0.3	0.2	0.2	0.2	0.2	0.2	0.2
1,2-Cyclopentanedione	1.1	1.5	1.2	1.1	0.9	0.9	1.2	0.8	0.6
3-Methyl-1,2-cyclopentadione	0.7	1.1	1.6	0.7	0.6	0.7	0.5	0.5	0.6
Furanones	0.9	1.2	0.7	0.2	0	0.2	0.2	0.3	0.2
	Furans								
Furfural	0.6	0.5	0.6	1.7	1.8	1.7	1.7	0.9	1
Hydroxymethylfurfural	0.4	0.6	0.6	1.5	1.5	1.9	1.8	1.3	1.1
Methylfurfural	0.2	0.3	0	1.1	1.2	0.8	0.9	0.2	0
	Phenols								
Ethyl-Phenol	0.5	0.4	0.4	0.4	0.4	0.3	0.3	0.3	2. 3
Phenol	1.4	1.8	2.1	2.1	2.25	2.1	1.1	1.5	4.5
Guaicols	1.9	1.1	1.02	1.4	1.5	1.4	1.2	1.15	3.35
Cresol	0	0.3	0.1	0.3	0.2	0. 5	0.1	0.3	2.1
Methoxyphenols	0.4	0.5	0.3	0.5	0.3	0. 4	0.3	0.3	2.3
Vaniline	0	0.4	0	0.4	0.3	0.4	0.3	0.3	0.7
	Anhydro sugars								
Levoglocosan	10.1	9.3	6.7	6.35	6.85	4.75	7.1	4.1	4.1
1,6-Anhydro-a-d-galactofuranose	4.6	5.1	3.1	3.5	3.6	3.5	4.2	3.8	2.1
Cellobiosan	1.1	1.9	1.3	0.8	0.9	1.2	1.2	1.2	0.8

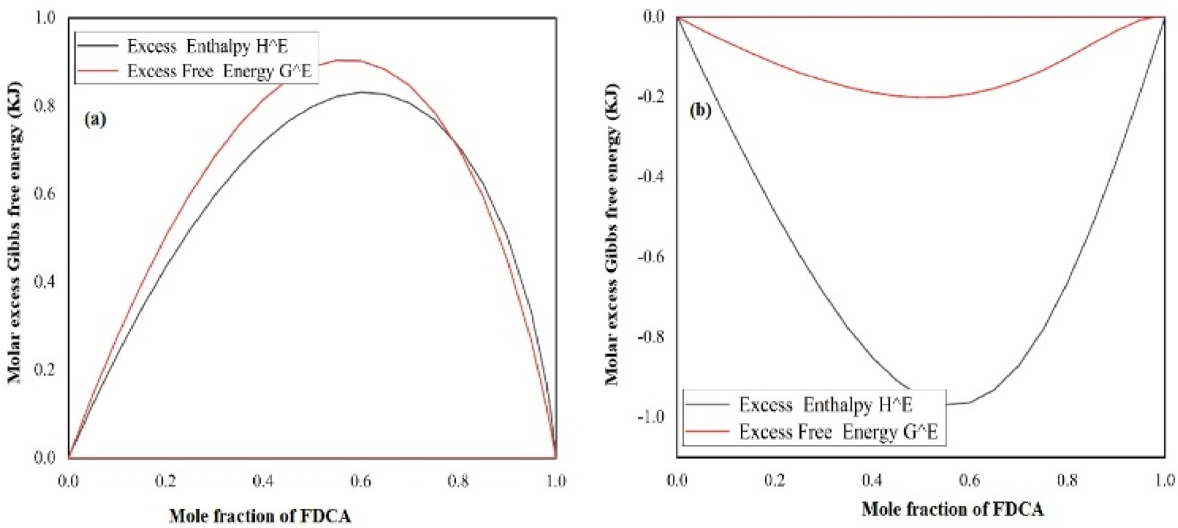

Figure 4. Gibbs tangent plane diagram for FDCA solvents (a: n-hexane; b: water)

On the other hand, Gibbs energy of mixing is positive for an HMF-water system for the entire concentration range due to its very low mutual solubility limits. Given that HMF-water is partially miscible, the solubility of water at the organic phase is higher than the aqueous solubility. Thus, the Excess Enthalpy of the mixing plot shows the negative region in the HMF region, as shown in Figure 5. The HMF-water shows a maximum miscibility gap of a mole fraction of 0.9. Moreover, the Gibbs energy and excess enthalpy of mixing are negative for an FDCA-water system in the entire concentration range due to its mutual solubility limits. FDCA-water is partially miscible and the solubility of water at the organic phase is higher than the aqueous solubility. Therefore, the Gibbs energy and excess enthalpy of the mixing plot show the negative region in the middle of the FDCA-water region, as shown in Figure 4 (b).

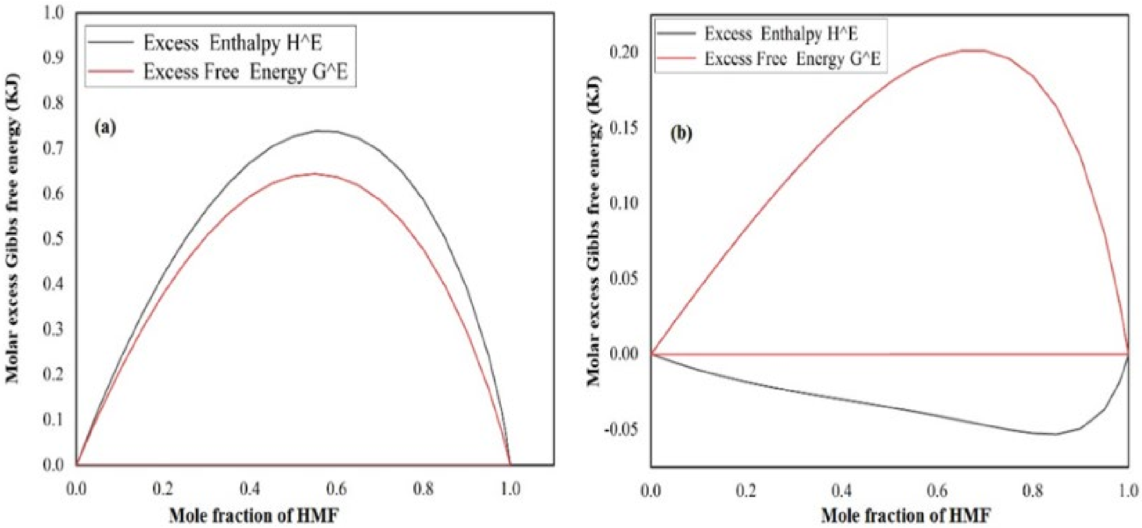

Figure 5. Gibb's tangent plane diagram for the HMF solvents (a: n-hexane; b: water)

The excess energies (Gex and Hex) for HMF at solvents of water, hexane at 298.15 K is shown Figure 5. The Gex energy of HMF mixture with water indicated the positive value of ~ 0.2 kJ/mol at x1 = 0.7 while Hex energy of HMF mixture with water is with a minimum of - 0.05 kJ/mol at x1 = 0.8. The HMF mixture with hexane showed a value Gex energy of ~ 0.6 kJ/mol at x1 = 0.6 and the Hex with a minimum of 0.7 kJ/mol at x1 = 0.65. In the present work, we investigate the solvents system and mole fraction solvents for the solubility of a solid solute in the liquid mixture using COSMO-RS and COSMO SAC methods. Optimized maximum solubility using COSMO-RS and COSMO SAC methods revealed that DMSO solvent was the best solvent for Hydroxymethylfurfural solubility. The value of HMF mole fraction was obtained X = 0.707986 and for DMSO X = 0.29201 through COSMO-RS method and also via COSMO SAC methods. The mole fraction values of 0.656330, 0.34367 were calculated for HMF and DMSO, repectively. Therefore, DMSO is selected as the best solvent for solubility 2, 5-Furandicarboxylic. In this regards, mole fraction value of FDCA were X = 0.372261, DMSO x = 0.29201 via the COSMO SAC methods while the mole fraction value of FDCA was 0.156783, and a DMSO is 0.84322 via COSMO-RS method.

3.4. Activity coefficients and validation

To calculate activity coefficients on the mole fraction scale for each solute (HMF/FDCA) in an infinite dilution state using COSMO-RS and COSMO SAC methods, the mole fraction of the solute is set to zero in the composition of the solution and the reference state is the pure solute. Cosmotherm calculates the natural logarithmic value of the activity coefficient using the pseudo-chemical potentials of the compound both in its pure and fully dissolved forms in a solvent. It can be observed that the activity coefficient for the components HMF and FDCA is quite high in case of infinite dilution at hexane higher than water. This means that the activity coefficients and intermolecular interactions of different solutes in solvents are quite dependent on the chemical structure of solute HMF and FDCA.

This non-ideality is attributed to the degree of dissociation/reaction of the solute in the solute-solvent interactions such as complex ion formation and in the solute-solute interactions such as ion pairing. An activity coefficient incorporates particle interactions into a single term so that the formal concentration can be modified to give an estimate of the effective concentration, or activity, of each ion. The partition coefficients (log P) of infinitely diluted solutes in a mixture of two immiscible solvents can be calculated with Partition Coefficients (LogP). They were used for calculating ethanol/water, benzene/water, ether/water, and hexane/water partition coefficients (Table 3). In the case of partly miscible liquids, like the ethanol-rich phase of ethanol and water, both components have nonzero mole fractions. The following table presents the value of the molar volume quotient of the two solvents.

Table 3. The partition coefficient (LOG P) of mixture solvents

Compound	Ethanol/Water	Benzene/Water	Hexane/Water	Ether/Water
HMF	-0.8337	-1.9507	-3.5269	0.1151
FDCA	0.4527	-3.4778	-5.1710	2.9823

3.5. COSMO-RS prediction optimized by DFT

The sigma potential determines the pseudochemical potential of the molecular surface. The chemical potential of the surface segment was obtained by thermodynamics of molecular interactions. Using COSMO-RS theory, one can calculate the thermodynamic properties of fluids from the 3D polarized charge distribution of individual molecules (σ-surface) in terms of σ-profile (2D histogram). Thus, valuable information regarding the polarity of a compound and its interaction with other surrounding molecules in the fluid media can be deduced from these σ-profile histograms. Figure 6 shows PX (σ), the charge density of these compounds in the polarized field (σ). The following criteria can be applied to divide the field into three regions: σ > + 0.0082 e/Å^{-2} as the hydrogen bond (HB) acceptor region; the hydrogen bond (HB) donor region having $\sigma < -0.0082$ e/Å^{-2}; and the nonpolar region between $-0.0082 < \sigma < +0.0082$ e/Å^{-2}. The sigma profile of ethanol and methanol exhibited a positive potential for the polar surface segment ($\delta > 0.05$ e.Å^{-2}), implying unfavorable solvation for HMF extraction. It is manifested that ethanol and methanol are miscible with water. It is revealed that the HMF is a strong hydrogen bond donor because of the higher profile area which facilitates water interaction. In order to evaluate the validation of Cosmo-RS models, the experimental data of mixture solvents is performed. The experimental attempts on mixture solvents validated these predictions at room temperature. σ-potential of thanol/water is similar to benzen/water for extraction of HMF while DMF solvent nearly is immiscible in water. It is revealed that the hydroxylmethyl group of HMF is a hydrogen-bonding donor from aqueous media. On the contrary, benzene and ethyl acetate solvents show a descending sigma potential sinking below - 0.15 kcal.mol^{-1}.Å^{-2} for the surface charge density at 0.05 e Å^{-2}, where efficient HMF separation takes place (Figure 6).

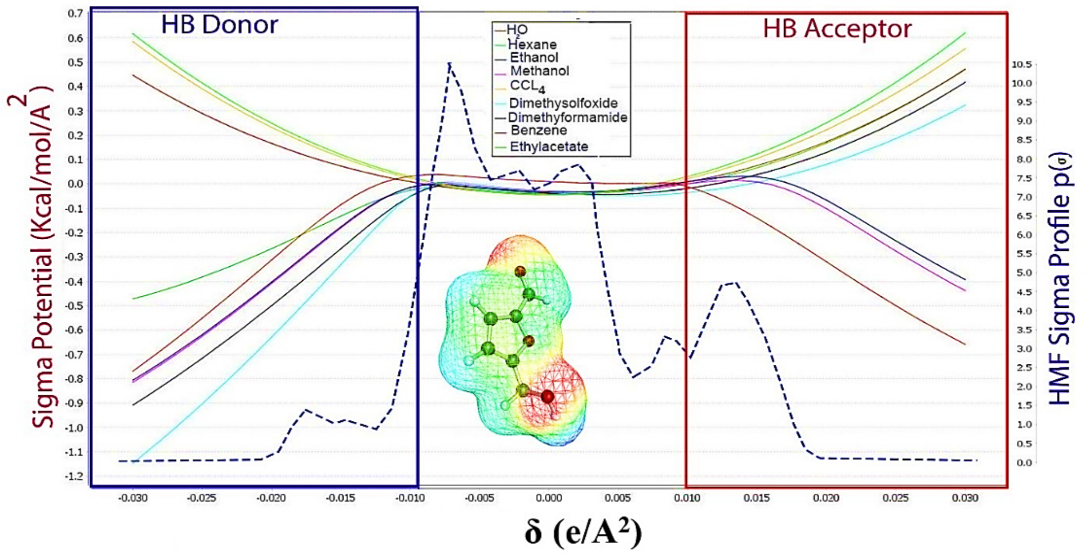

Figure 6. δ-potential & profile of HMF (dotted line) with solvents (solid lines)

The sigma potential profiles suggest DMF and DMSO as the alternative and most promising solvents for FDCA extraction. The hydrophobicity region at $\delta = 0$ reflected the potential difference in the solubility of the solvents with water. Benzene and ethyl acetate enable direct bonding to the OH group, resulting in increase in the nonpolar alkyl group and the rise of the hydrophobicity. On the other hand, DMF and DMSO replace the hydrophilic environment to improve the selectivity and overall yield of FCDA (Figure 7). In fact, the low mutual solubility of DMF and DMSO makes them not eligible to interact on hydrogen bonding. Thus, DMF and DMSO exhibited a lower charge density in hydrogen bonding, which results in less interaction with water and better fractionation of the organic phase. Thus, nonpolar organic and hydrocarbon compounds with π-π bond are more favorable with DMF and DMSO solvents because of fewer interactions with the hydrogen bond. Nevertheless, it is interesting to note that there are clear differences in the interactions of solvents with HMF and FDCA. In FDCA, these peaks were found at higher positive polarity, showing a stronger HB acceptor character of the carboxylate group rather than the hydroxyl methyl group in the homologous HMF.

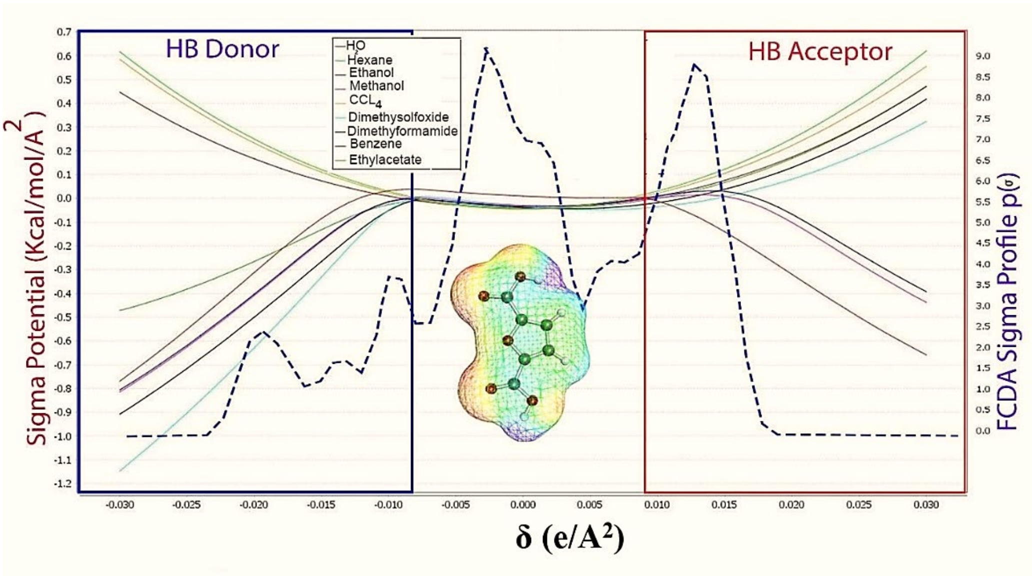

Figure 7. δ-potential & profile of FDCA with solvents

Thus, different profiles of σ-surface are contributed independently of each atom related to its charge density as well as the descriptor of each constituent in the solvents. Finally, with stronger HB donor and HB acceptor groups, COSMO-RS describes FDCA as a more polar structure than those of the homolog HMF. Consequently, the results of this study aimed to develop a framework of models that could predict the quantum-chemical properties of solvents to screen the interactions between them. It is purely a prediction approach to COSMO-RS optimized by the DFT methodology. On the other hand, it provides an efficient final product that is rich in HMF and FDCA and approves the emerging biobased molecules for commercializing green processes. Therefore, the efficient solvent design approach would be highly reliable based on experimental data in the applicability domain for green and sustainable bioplastic manufacturing processes.

4. CONCLUSIONS

This study aims to evaluate the efficiency of different solvents for the desirable extraction of HMF and FDCA for future bioplastic industries. A multiscale COSMO-RS model on a desirable solvent system was optimized by DFT methodology. Evaluation of the sigma potential and sigma surface analysis showed that benzene and ethyl acetate had better extraction and selectivity toward HMF. Moreover, FDCA exhibited ideal behavior in DMF and DMSO solvents. GC-MS data revealed that the polar molecular solvent (ethanol-water) extracted more carboxylic acids and alcohols, while n-hexane lied in the middle of the solvents for phenolic compounds. Experimental data confirmed that HMF was more convenient by polar molecular solvents that were miscible in water while the FDCA extraction solvents were immiscible in water. It is worth noting that the higher aromatics in HMF promote the Diels-Alder reaction as well as the dehydration reaction. Thus, a promising route for the generation of FDCA from HMF could be through the use of strong concentrations of cellulose. In addition, DMF and DMSO improved the hydrogen bonding interaction between FDCA and solvent molecules and, thus, led to efficient separation. However, the strategy employed in this study could be considered as a computational prediction to select a favorable solvent with efficient bioplastic manufacturing processes.

5. ACKNOWLEDGEMENT

This study was supported partially by department of biorefinery engineering at Shahid Beheshti University, Iran (award number: 397081). The authors also want to thank the Alliance for Biomass and Sustainability Research-ABISURE “Universidad Nacional de Colombia” Hermes code 5302, for the partial support to this work.

REFERENCES

1. Arikan, E.B., Bouchareb, E.M., Bouchareb, R., Yağcı, N., & Dizge, N. (2021). Innovative technologies adopted for the production of bioplastics at industrial level. In: Kuddus, M., Roohi (eds), *Bioplastics for Sustainable Development* (pp. 83-102), Springer, Singapore. https://doi.org/10.1007/978-981-16-1823-9_3
2. Balchandani, S., & Singh, R. (2021). Thermodynamic analysis using COSMO-RS studies of reversible ionic liquid 3-aminopropyl triethoxysilane blended with amine activators for CO_2 absorption. *Journal of Molecular Liquids*, *324*, 114713. https://doi.org/10.1016/j.molliq.2020.114713
3. Bello Ould-Amer, S., Méndez Trelles, P., Rodil Rodríguez, E., Feijoo Costa, G., & Moreira Vilar, M.T. (2020). Towards improving the sustainability of bioplastics: Process modelling and life cycle assessment of two separation routes for 2, 5-furandicarboxylic acid. *Seperation and Purification Technology*, *233*, 116056. https://doi.org/10.1016/j.seppur.2019.116056
4. Bilal, M., Vilar, D.S., Eguiluz, K.I.B., Ferreira, L.F.R., Bhatt, P., & Iqbal, H.M.N. (2021). Biochemical conversion of lignocellulosic waste into renewable energy. In *Advanced Technology for the Conversion of Waste into Fuels and Chemicals* (pp. 147-171), Elsevier. https://doi.org/10.1016/B978-0-12-823139-5.00007-1
5. Blumenthal, L.C., Jens, C.M., Ulbrich, J., Schwering, F., Langrehr, V., Turek, T., Kunz, U., Leonhard, K., & Palkovits, R. (2016). Systematic identification of solvents optimal for the extraction of 5-hydroxymethylfurfural from aqueous reactive solutions. *ACS Sustainable Chemistry & Engineering*, *4*(1), 228-235. https://doi.org/10.1021/acssuschemeng.5b01036
6. Bonner, T.G., Bourne, E.J., & Ruszkiewicz, M. (1960). The iodine-catalysed conversion of sucrose into 5-hydroxy-methylfurfuraldehyde. *Journal of the Chemical Society* (Resumed), 787-791. https://doi.org/10.1039/JR9600000787
7. Cai, C.M., Zhang, T., Kumar, R., & Wyman, C.E. (2013). THF co-solvent enhances hydrocarbon fuel precursor yields from lignocellulosic biomass. *Green Chemistry*, *15*(11), 3140-3145. https://doi.org/10.1039/C3GC41214H
8. Davidson, M.G., Elgie, S., Parsons, S., & Young, T.J. (2021). Production of HMF, FDCA and their derived products: A review of life cycle assessment (LCA) and techno-economic analysis (TEA) studies. *Green Chemistry*, *23*, 3154-3171. https://doi.org/10.1039/D1GC00721A
9. Dutta, S., Bhaumik, A., & Wu, K.C.-W. (2014). Hierarchically porous carbon derived from polymers and biomass: effect of interconnected pores on energy applications. *Energy & Environmental Science*, *7*(11), 3574-3592. https://doi.org/10.1039/C4EE01075B
10. Eckert, F., & Klamt, A. (2018). *COSMOtherm*, version 18.0.0. COSMOlogic GmbH & CoKG: Leverkusen, Germany.
11. Erickson, B., & Winters, P. (2012). Perspective on opportunities in industrial biotechnology in renewable chemicals. *Biotechnology Journal*, *7*(2), 176-185. https://doi.org/10.1002/biot.201100069
12. Esteban, J., Vorholt, A.J., & Leitner, W. (2020). An overview of the biphasic dehydration of sugars to 5-hydroxymethylfurfural and furfural: A rational selection of solvents using COSMO-RS and selection guides. *Green Chemistry*, *22*(7), 2097-2128. https://doi.org/10.1039/C9GC04208C
13. Forlemu, N., Watkins, P., & Sloop, J. (2017). Molecular docking of selective binding affinity of sulfonamide derivatives as potential antimalarial agents targeting the glycolytic enzymes: GAPDH, Aldolase and TPI, *Open Journal of Biophysics*, *7*, 41-57. http://dx.doi.org/10.4236/ojbiphy.2017.71004
14. Geyer, R., Jambeck, J.R., & Law, K. L. (2017). Production, use, and fate of all plastics ever made. *Science Advances*, *3*(7), e1700782-e1700782. https://doi.org/10.1126/sciadv.1700782
15. Ghorbannezhad, P., Park, S., & Onwudili, J.A. (2020). Co-pyrolysis of biomass and plastic waste over zeolite- and sodium-based catalysts for enhanced yields of hydrocarbon products. *Waste Management*, *102*(December), 909-918. https://doi.org/10.1016/j.wasman.2019.12.006
16. Godbout, N., Salahub, D.R., Andzelm, J., Wimmer, E. (1992). Optimization of Gaussian-type basis sets for local spin density functional calculations. Part I. Boron through neon, optimization technique and validation. *Canadian Journal of Chemistry*, *70*, 560-571. https://doi.org/10.1139/v92-079
17. Hou, Q., Li, W., Zhen, M., Liu, L., Chen, Y., Yang, Q., Huang, F., Zhang, S., & Ju, M. (2017). An ionic liquid–organic solvent biphasic system for efficient production of 5-hydroxymethylfurfural from carbohydrates at high concentrations. *RSC Advances*, *7*(75), 47288-47296. https://doi.org/10.1039/C7RA10237B
18. Hwang, K.-R., Jeon, W., Lee, S. Y., Kim, M.-S., & Park, Y.-K. (2020). Sustainable bioplastics: Recent progress in the production of bio-building blocks for the bio-based next-generation polymer PEF. *Chemical Engineering Journal*, *390*, 124636. https://doi.org/10.1016/j.cej.2020.124636
19. Klamt, A. (1995). Conductor-like screening model for real solvents: A new approach to the quantitative calculation of solvation phenomena. *The Journal of Physical Chemistry*, *99*, 2224-2235. https://doi.org/10.1021/j100007a062
20. Klamt, A. (2005). *COSMO-RS from Quantum Chemistry to Fluid Phase Thermodynamics and Drug Design* (pp.246), Elsevier: Amsterdam, The

Netherlands. https://www.sciencedirect.com/book/9780444519948/cosmo-rs#book-info

21. Klamt, A., Eckert, F., Reinisch, J., & Wichmann K. (2016). Prediction of cyclohexane-water distribution coefficients with COSMO-RS on the SAMPL5 data set. *Journal of Computer Aided. Molcular Design*, *30*, 959-967. https://doi.org/10.1007/s10822-016-9927-y
22. Klamt, A. (2018). The COSMO and COSMO-RS solvation models. *Wiley Interdisciplinary Reviews: Computational Molecular Science*, *1*(5), 699-709. https://doi.org/ 10.1002/wcms.56
23. Kuster, B.F.M. (1990). 5-Hydroxymethylfurfural (HMF). A review focussing on its manufacture. *Starch‐Stärke*, *42*(8), 314-321. https://doi.org/10.1002/star.19900420808
24. Momany, F., & Schnupf, U. (2014). DFT optimization and DFT-MD studies of glucose, ten explicit water molecules enclosed by an implicit solvent, COSMO. *Computational and Theoretical Chemistry*, *1029*, 57-67. https://doi.org/10.1016/j.comptc.2013.12.007
25. Motagamwala, A.H., Huang, K., Maravelias, C.T., & Dumesic, J.A. (2019). Solvent system for effective near-term production of hydroxymethylfurfural (HMF) with potential for long-term process improvement. E*nergy & Environmental Science*, *12*(7), 2212-2222. https://doi.org/10.1039/C9EE00447E
26. Perlack, R.D., Eaton, L.M., Turhollow Jr, A.F., Langholtz, M.H., Brandt, C.C., Downing, M.E., Graham, R.L., Wright, L.L., Kavkewitz, J.M., & Shamey, A.M. (2011). *US billion-ton update: Biomass supply for a bioenergy and bioproducts industry*. https://www1.eere.energy.gov/bioenergy/pdfs/billion_ton_update.pdf
27. Rosatella, A.A., Simeonov, S.P., Frade, R.F.M., & Afonso, C.A.M. (2011). 5-Hydroxymethylfurfural (HMF) as a building block platform: Biological properties, synthesis and synthetic applications. *Green Chemistry*, *13*(4), 754-793. https://doi.org/10.1039/C0GC00401D
28. Searle, S., & Malins, C. (2015). A reassessment of global bioenergy potential in 2050. *GCB-Bioenergy*, *7*(2), 328-336. https://doi.org/10.1111/gcbb.12141
29. Stuart, P.R., & El-Halwagi, M.M. (2012). *Integrated biorefineries: design, analysis, and optimization*. CRC press. https://www.amazon.com/Integrated-Biorefineries-Optimization-Chemistry-Engineering/dp/1439803463S
30. Wang, Z., Bhattacharyya, S., & Vlachos, D.G. (2020). Solvent selection for biphasic extraction of 5-hydroxymethylfurfural via multiscale modeling and experiments. *Green Chemistry*, *22*(24), 8699-8712. https://doi.org/10.1039/D0GC03251D
31. Weingarten, R., Rodriguez-Beuerman, A., Cao, F., Luterbacher, J.S., Alonso, D.M., Dumesic, J.A., & Huber, G.W. (2014). Selective conversion of cellulose to hydroxymethylfurfural in polar aprotic solvents. *ChemCatChem*, *6*(8), 2229-2234. https://doi.org/10.1002/cctc.201402299
32. Zhang, Y., Guo, X., Tang, P., & Xu, J. (2018). Solubility of 2, 5-furandicarboxylic acid in eight pure solvents and two binary solvent systems at 313.15-363.15 K. *Journal of Chemical & Engineering Data*, *63*(5), 1316-1324. https://doi.org/10.1021/acs.jced.7b00927
33. Zhao, X., Farajtabar, A., Han, G., Zhao, H. (2020). Phenformin in aqueous co-solvent mixtures of N, N-dimethylformamide, ethanol, N-methylpyrrolidone and dimethyl sulfoxide: Solubility, solvent effect and preferential solvation. *Journal of Chemmical Thermodynamics*, *144*, 106085. https://doi.org/10.1016/j.jct.2020.106085
34. Zheng, J., & Suh, S. (2019). Strategies to reduce the global carbon footprint of plastics. *Nature Climate Change,* *9*(5), 374-378. https://www.nature.com/articles/s41558-019-0459-z
35. Zunita, M., Wahyuningrum, D., Bundjali, B., Wenten, I.G., & Boopathy, R. (2021). Conversion of glucose to 5-hydroxymethylfurfural, levulinic acid, and formic acid in 1, 3-dibutyl-2-(2-butoxyphenyl)-4, 5-diphenylimidazolium iodide-based ionic liquid. *Applied Sciences*, *11*(3), 989. https://doi.org/10.3390/app11030989

JREE: Vol. 10, No. 3, (Summer 2023) 38-50

Journal of Renewable Energy and Environment

Journal Homepage: www.jree.ir

Materials and Energy Research Center

MERC

Research Article

Energy Efficiency Assessment and Optimization of Solar Organic Rankine Cycle for Combined Heat and Power Generation for a Residential Building: Case Study of Baghdad City, Iraq

Mohammed Ali Sami Mahmood [a,b*], Sergei Kuzmin [a]

[a] *Department of Energy Supply for Enterprise and Thermal Engineering, Tambov State Technical University, Tambov, Russia.*
[b] *Department of Machines and Equipment Engineering Techniques, Al-Mussaib Technical College, Al-Furat Al-Awsat Technical University, Babil, Iraq.*

PAPER INFO

Paper History:
Received: 07 September 2022
Revised: 22 October 2022
Accepted: 28 October 2022

Keywords:
Energy Efficiency Assessment,
Solar Organic Rankine Cycle,
CHP,
Baghdad,
Republic of Iraq

ABSTRACT

Solar Organic Rankine Cycle (SORC) is a successful approach to sustainable development and exploiting clean energy sources. The research aims to improve and evaluate the energy efficiency of the SORC for combined heat and power generation for a residential home under the climatic conditions of Baghdad, Iraq. Thermoeconomic analysis was carried out for the proposed energy supply system. Refrigerant HFC-245fa was used as a working fluid in a solar organic Rankine cycle, and oil poly alkyl benzene (TLV-330) was suggested as a heat transfer fluid in the solar collector field. Parametric studies for some key parameters were conducted to examine the impact of various operating conditions on energy efficiency. The results showed a significant improvement in energy efficiency. The maximum efficiency of SORC CHPG reached 79.14 % when solar heat source temperatures were in the range of 100 to 150 °C and the solar radiation was at a maximum value of 870 W/m^2 at noon on the 15th day of July in Baghdad. The maximum energy produced by SORC CHPG was 472.5 kW when the optimal average value of global solar radiation was 7.5 kWh/m^2/day in June. The economic investigations revealed that the payback period of the new energy supply system was 10 years with the positive net present cost when the solar power plant was working 18 h/day.

https://doi.org/10.30501/jree.2022.360155.1440

1. INTRODUCTION

Currently, fossil fuels are used to meet 70 % of the world's energy demands, 40 % of which are spent in building sectors for various purposes, including air conditioning, ventilation, cooling, and heating (Razmi et al., 2019). Today, oil and gas are the main and dominant sources of energy supply in Iraq. The combustion products of conventional fuels lead to serious environmental problems (Saeed et al., 2016; Martins et al., 2019; Solarin, 2020a). The emergence of recent technology and an increase in population have led to an increase in energy consumption worldwide and in the Republic of Iraq particularly. The use of non-conventional solar energy sources for energy supply addresses these issues (Solarin, 2020b; Bigerna et al., 2021). Renewable solar energy is characterized by stability and purity. Iraq is a country located near the Sun Belt and characterized by high solar radiation intensity and brightness throughout the year. Therefore, solar energy can be used as an alternative source of energy to meet energy needs and address the acute shortage of energy supply in Iraq (Al-Hamdani, 2017; Chaichan and Kazem, 2018; Al-Kayiem and Mohammad, 2019; Kazem and Chaichan, 2012). An organic Rankine cycle (ORC) has become a reliable technology to convert heat into electricity using various heat sources such as biomass, geothermal, heat recovery, solar, and heat from industrial processes (Malwe et al., 2022; Oyekale and Emagbetere, 2022). The heat sources divide into high, medium, and low depending on the temperature range between 50 °C and 350 °C. Moreover, the advantages of ORC technology include extremely high turbine efficiency (up to 90 %), high system efficiency, low peripheral speed, low turbine mechanical stress, low turbine rotation speed, dry expansion process, low environmental impact, and simplicity of expander design, thus making it desirable (Oyekale and Emagbetere, 2022; Malwe et al., 2021). Organic fluids with a lower boiling point and higher vapor pressure are utilized as heat carriers in the ORC cycle. Over the past years, the small-scale Solar Organic Rankine Cycle (SORC) has become a mature technology and a topic of extensive research by researchers (Gupta et al., 2022). Organic working fluids are selected according to the specified criteria involving environmentally-friendly, non-flammable, and appropriate physical properties that meet the system requirements for optimum efficiency. The working fluids can be

*Corresponding Author's Email: mohammed.sami@atu.edu.iq (M.A.S. Mahmood)
URL: https://www.jree.ir/article_160878.html

Please cite this article as: Mahmood, M.A.S., & Kuzmin, S. (2023). Energy efficiency assessment and optimization of solar organic Rankine cycle for combined heat and power generation for a residential building: Case study of Baghdad city, Iraq. *Journal of Renewable Energy and Environment (JREE)*, *10*(3), 38-50. https://doi.org/10.30501/jree.2022.360155.1440.

2423-7469/© 2023 The Author(s). Published by MERC. This is an open access article under the CC BY license (https://creativecommons.org/licenses/by/4.0/).

hydrofluorocarbons, hydrocarbons, siloxanes, and mixtures of these components (Herath et al., 2020). In this regard, many studies have been conducted to examine the performance of ORC using various organic fluids, taking into account solar energy as a heat source under different conditions (Tchanche et al., 2009; Rayegan and Tao, 2011). In recent years, many studies have investigated the SORC for poly-generating applications. Yang et al., (2019) constructed a new SORC for generating 1 MW. Different working fluids were used in the performance evaluation for the new mode. Outcomes revealed that the efficiency was elevated by 4.2 % higher than an unstable operating. Freeman et al., (2017) tested an SORC for Combined Heat and Power Generation (CHPG) integrated with a thermal energy storage unit with phase change materials. They investigated the efficiency of the system under UK and Cyprus conditions. The results pointed out that hydrated-salt PCMs provided high performance and power output. Bouvier, (2016) performed experimental investigation for micro SORC CHPG. The obtained energies were 1.3 kW of electricity and 19 kW of heat energy. The efficiency of converting solar energy into electricity and heat energy reached 3 % and 38 %, respectively. Garcia-Saez et al., (2019) conducted thermal and economic research on the implementation of SORC CHPG in residential sectors for various scenarios. They used on-grid and off-grid operating modes. The results showed the feasibility of applying the system in locations characterized by specific climatic conditions. The main indicators of an economic analysis estimated 13 % IRR, 3.1 years PP, and positive NPV. Habka and Ajib, (2016) considered the utilization of zeotropic mixtures in SORC for CHPG. Numerical simulations were carried out for predicting energy efficiency and feasibility. The outcomes confirmed that the use of R409A in ORC was ideal and the cost of energy production was reduced by 16.20 %. Yüksel, (2018) applied SORC for power, cooling, and hydrogen generation. Hydrogen is produced using produced electricity. The findings showed that the energy efficiency of the system increased from 58 % to 64 % when solar radiation increased from 400 W/m^2 to 1000 W/m^2, and the rate of hydrogen generation rose from 0.1016 kg/h to 0.1028 kg/h. Singh and Mishra, (2018) carried out exergy and energy analysis of both supercritical CO_2 (SCO_2) cycle and organic Rankine cycle (ORC) driven by solar energy to produce power. It was found that the exergetic and thermal efficiency of all the combined cycles increased when the direct normal irradiance rose from 0.5 kW/m^2 to 0.95 kW/m^2. The maximum thermal and exergetic efficiency was around 78.07 % and 43.49 %, respectively. Despite the reported attractive results of the SORC technology, it has not been simulated in the climatic conditions of Baghdad, Iraq. In this study, by contributing to the enhancement of the energy efficiency of the current system, this paper analyzes a new model of SORC CHPG to meet the needs of electric power, Domestic Hot Water (DHW), and heating for a typical residential building in the conditions of Baghdad city. The suggested technique is not dependent on the grid or fossil fuels. It appears that the suggested solution is extremely realistic due to the presence of both low- and high-temperature water for usage at home. A calculation method for the main performance indicators associated with the proposed solar energy system is developed, taking into account the peculiarities of the new design and the potential of solar radiation in Baghdad.

2. MATERIAL AND METHODS

The research methodology relies on theoretical and experimental studies of previous research on the topic of SORC CHPG. To calculate the main parameters and energy efficiency of the proposed system, the basic concepts of thermodynamics were applied (Çengel, 2004; Rajput, 2007). Commercial software "Engineering Equation Solution (EES)" was used for simulating and obtaining the results of the study (F-Chart Software, 2022). The indispensable operating parameters were added to the EES to obtain the full outcomes of the proposed solar system. An optimized model of SORC CHPG was employed to obtain initial results from the available parameters. Modeling of the obtained results was conducted by considering various operating parameters to help determine the optimal operating conditions of the system to provide maximum performance. The findings were compared with reported investigations for the model verification and validation of results, taking into account the small deviations and loads of case studies. Iraq is characterized by the abundance of incoming solar radiation during the year thanks to its location. Solar radiation of 1000 W/m^2 for one hour is equal to one kWh/m^2 (Akram Al-Khazzar, 2018). The maximum measured value of solar radiation at noon is about 950 W/m^2 (Al-Obaidi et al., 2020). The received average daily solar radiation ranges between 4.4-5.45 kWh/m^2/day, as shown in Figure 1. The incident average value of solar radiation in Baghdad is about 5 kWh/m^2/day (Chaichan and Kazem, 2018).

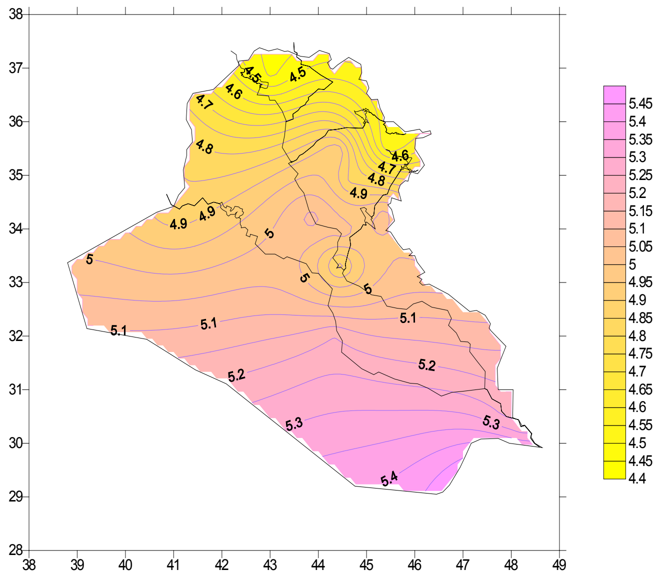

Figure 1. Average daily solar radiation for different locations in Iraq (Chaichan and Kazem, 2018)

The recorded average values of global solar radiation (AGSR) and high/low ambient temperature for Baghdad city are tabulated in Table 1.

Baghdad city is the capital of Iraq and located in the central region (latitude 33°.33´, longitude 44°.39´), which was selected as the location of a residential home. The thermal loads for heating, DHW, and electrical loads of the residential home were calculated, as shown in Table 2.

In this work, in response to the climatic conditions of Baghdad and the requirements of the energy system, it is proposed that oil poly alkyl benzene (TLV-330) be used as a new Heat Transfer Fluid (HTF). The characteristics and thermophysical properties of HTF are presented in Table 3.

Table 1. AGSR data and ambient temperatures by month for Baghdad (Hassan et al., 2021)

Month	GSR ($MJ/m^2/day$)	GSR ($kWh/m^2/day$)	Average high temperature (°C)	Average low temperature (°C)
January	10.6	2.9	16	4
February	13.33	3.7	19	6
March	17.7	4.9	24	10
April	21.6	6	30	15
May	23.4	6.5	37	20
June	27.0	7.5	42	24
July	26.0	7.2	44	26
August	24.6	6.8	44	25
September	20.8	5.7	40	22
October	15.8	4.3	33	16
November	11.9	3.3	24	9
December	9.8	2.7	17	5
Total average yearly	18.6	5.2	30.8	15

Table 2. Calculated loads of the case study (Mohammed Ali, 2020)

Type of load	Value (kW)
Electrical loads (P_{ele})	15
Thermal load for heating (Q_h)	29
Domestic hot water demand (Q_{DHW})	19

Table 3. Characteristics of TLV-330 (https://termolan.ru/tlv-330m/)

Name of an indicator	Norm
Appearance	Light yellow oily, homogeneous liquid
Minimum operating temperature	40 °C
Maximum operating temperature of the liquid phase	330 °C
Maximum operating temperature of the vapor phase	330 °C
Density 20 °C	850-870 kg/m^3
Average specific heat	2.2 kJ/kg.°C
Freezing temperature	− 30 °C
Boiling temperature	330 °C
Manufacturer country	Russia

2.1. System description

The basic SORC standalone (SORC SA) for the generation of electricity is illustrated in Figure 2a. The proposed new SORC system for providing electricity, DHW, and hot water for a heating purpose depending on solar energy as a heat source is shown in Figure 2b. The novel design of SORC CHPG works as follows. The liquid working fluid (R-245fa) flows by the pump (1) to the ORC evaporator (2). It absorbs the heat in the evaporator and then, converts it into steam. The vapor working fluid enters the expander (3) under given thermodynamic conditions to drive it and generate electricity via an electric generator (4). Then, vapor enters the condenser (5) to be condensed. The hot water at the outlet of the condenser at an accepted temperature is used as DHW. The liquid working fluid enters the pump and the cycle repeats. The thermal energy storage unit (9) is integrated to ensure that the system operates stably throughout the day, avoids the influence of climate changes, and fills the collector with non-freezing liquid. The HTF enters the SORC evaporator (2) and the outlet HTF flows via the heat exchanger (9) where hot water is released for heating purposes in the winter season. In the end, the working fluid returns to the heat storage unit (9) and is reheated thanks to the solar energy, and the next cycle begins. A three-way valve is utilized to control the flow direction of the liquid and shut off the heating system in the summer season. These two proposed variants of heating consider a successful solution under Baghdad conditions. In this system, there is no demand for fuel to heat the water.

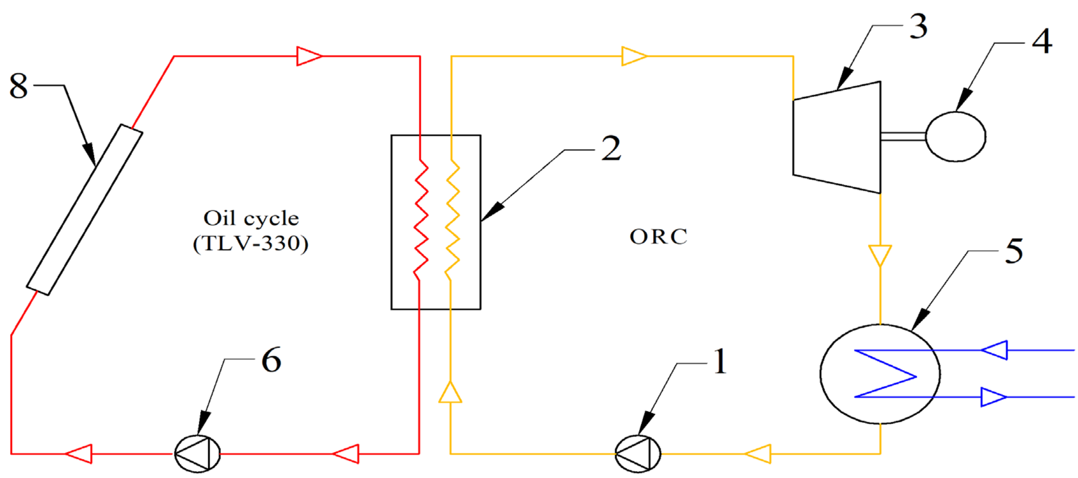

(a)

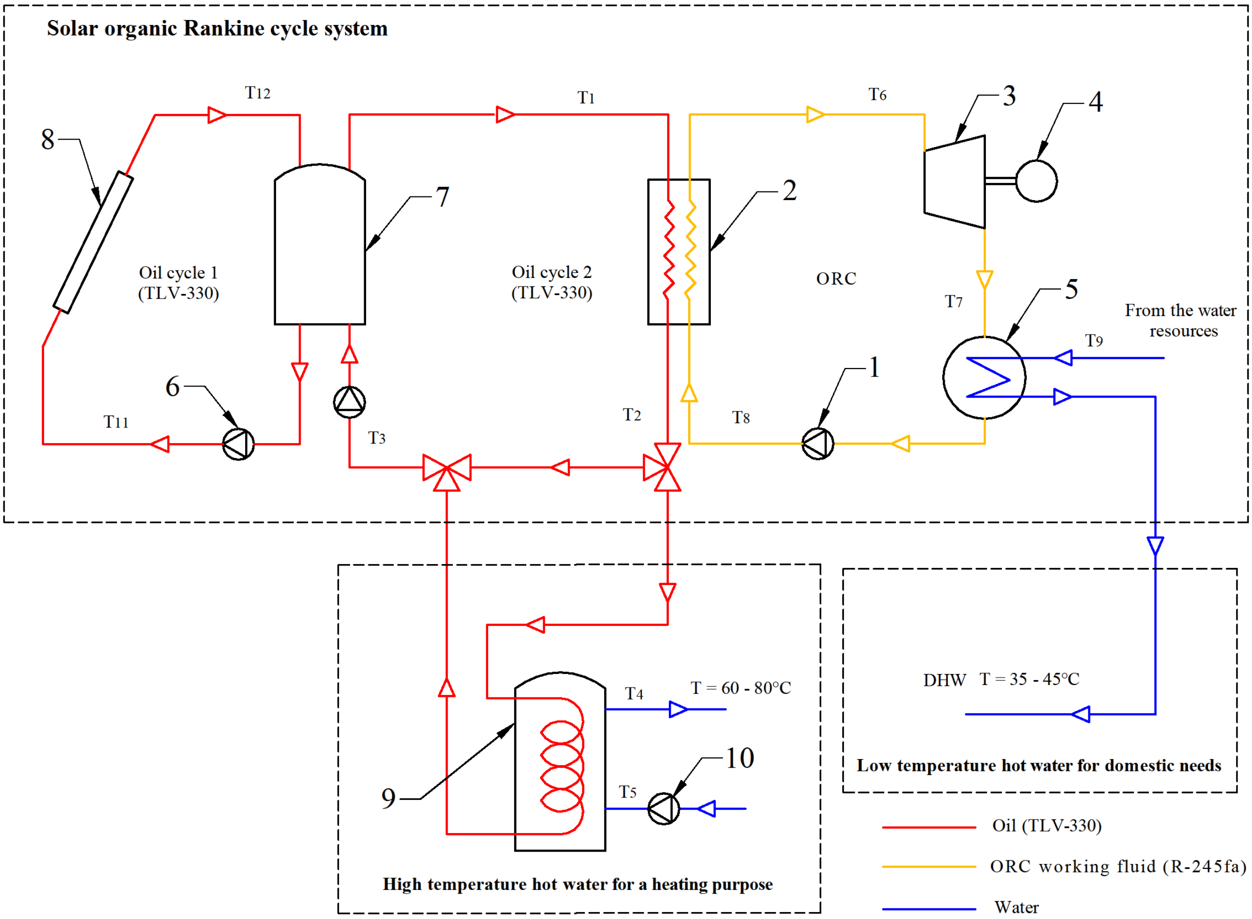

(b)

Figure 2. Schematic diagram of (a) basic SORC SA for generation of electricity and (b) proposed developed design of SORC CHPG: 1. organic fluid circulation pump, 2. evaporator, 3. expander/ turbine, 4. electric generator, 5. condenser, 6. oil circulation pumps, 7. heat storage tank, 8. solar thermal collector, 9. heat exchanger for heating purposes, 10. hot water circulating pump

2.2. Thermodynamic analysis and mathematical modeling

The analysis and calculations were built on the following assumptions:

1. The efficiency rates of the ORC generator, expander, and pump are constant and non-dependent in the operating mode.
2. Hydraulic resistance of heat exchangers and pipelines is not considered.
3. No heat is exchanged with the environment.
4. Changes in kinetic and potential energy are not considered.
5. Refrigerant HFC-245fa is used as working fluid in the SORC cycle due to its thermophysical characteristics and for economic grounds.

Table 4 presents the required operating parameters for modeling the proposed SORC CHPG under Baghdad conditions.

Table 4. Design parameters of the proposed SORC CHPG (Aghaziarati and Aghdam, 2021)

Parameter	Value
Power output (P_{ele})	15 kW
Cooling water temperature at the inlet of the condenser (T_9)	15 °C
Hot water temperature at the outlet of the condenser (T_{10})	40 °C
SORC condensation temperature (T_8)	50 °C
Maximum operating temperature of ORC (T_6)	140 °C
Maximum working pressure of ORC (P_{evap})	2828.7 kPa
Ambient temperature (T_{am})	25 °C
The temperature at the evaporator inlet (T_1)	150 °C
The temperature at the evaporator outlet (T_2)	110 °C
The temperature at the heat exchanger (9) inlet (T_2)	110 °C
The temperature at the heat exchanger (9) outlet (T_3)	80 °C
Water temperature at the inlet of the heat exchanger (T_5)	60 °C

water temperature at the outlet of the heat exchanger (T_4)	75 °C
The temperature of HTF at the inlet of the heat storage tank (T_{12})	150 °C
The temperature of HTF at the outlet of the heat storage tank (T_{11})	130 °C
Isentropic efficiency of the ORC expander (η_e)	80 %
Efficiency of the ORC pump (η_p)	80 %
Efficiency of the ORC generator (η_g)	96 %
Solar collector efficiency (η_{sc})	70 %
Solar radiation (G)	1000 kWh/m^2

The equations of mass and energy balance for control volume in SORC CHPG are as follows (Rajput, 2007):

$$\left.\begin{array}{c}\sum m_{in} - \sum m_{out} = 0 \\ \sum Q_{in} - \sum Q_{out} = 0 \\ Q_{in} - W_{in} + \sum_{in} m.h - \sum_{out} m.h = 0\end{array}\right] \quad (1)$$

2.2.1. Modeling of solar field

The energy collected by the solar collector and transmitted to the HTF is determined via the application of the thermo-balance as follows (Bellos and Tzivanidis, 2017):

$$Q_{sc} = G(\tau).\,A_{sc}.\eta_{sc}(\tau) = m_{HTF}.C_{HTF}.(T_{out} - T_{in})_{HTF} \quad (2)$$

The following empirical equation can be utilized to estimate the mass flow rate of oil (Bellos and Tzivanidis, 2017; Baral and Kim, 2014):

$$m_{HTF} = 0.02.A_{sc} \quad (3)$$

The solar collector area is used to calculate the volume of the thermal storage tank (Bellos and Tzivanidis, 2017):

$$V_{HST} = \frac{A_{sc}}{80} \quad (4)$$

The system is examined in the stable mode; therefore, the results are not significantly affected by the volume and shape assumptions made for the storage tank (Aghaziarati and Aghdam, 2021). The required area of the collector for a solar plant is calculated as follows:

$$A_{sc} = \frac{Q_h + Q_{DHW} + P_{ele}}{G(\tau).\eta_{sc}(\tau)} \quad (5)$$

The collector efficiency is expressed in the following formula (Gupta et al., 2022):

$$\eta_{sc} = \eta_o + a_1.\frac{(T_{av} + T_{am}(\tau))}{G(\tau)} - a_2.\frac{(T_{av} + T_{am}(\tau))^2}{G(\tau)} \quad (6)$$

where η_o represents optical efficiency. a_1 W/(m^2.°C) and a_2 W/(m^2.°C) are coefficients of heat loss. The values of these parameters were taken 0.825, 0.91, 0.0006, respectively (Hossin and Mahkamov, 2015). The average collector temperature is calculated as:

$$T_{av} = \frac{T_{sc,in} + T_{sc,out}}{2} \quad (7)$$

2.2.2. Devices modeling of ORC unit

The power required to operate the ORC pump is calculated as (Wang et al., 2012):

$$W_p = \frac{m_{wf}.\,v_1.\,(P_{evap} - P_{cond})}{\eta_p} = m_{wf}.\,(h_2 - h_1) \quad (8)$$

The mass flow rate m_{wf} kg/s flowing in the ORC cycle is calculated using the following formula:

$$m_{wf} = \frac{P_{ele}}{(h_3 - h_4).\eta_g} \quad (9)$$

The rate of heat transmitted in the ORC evaporator is determined as (Hossin and Mahkamov, 2015):

$$Q_{evap} = m_{wf}.(h_3 - h_2) = m_{HTF}.C_{HTF}.(T_{in} - T_{out})_{HTF} \quad (10)$$

An ORC turbine power output is determined as (Hossin and Mahkamov, 2015):

$$P_{ele} = m_{wf}.\,(h_3 - h_4).\,\eta_e.\,\eta_g = m_{wf}.\,(h_3 - h_4).\,\eta_g \quad (11)$$

The heat removal in the condenser can be expressed as (Hossin and Mahkamov, 2015):

$$Q_{cond} = m_{wf}.(h_4 - h_1) = m_w.C_w.(T_{out} - T_{in})_w \quad (12)$$

The volumetric flow rate is calculated using the following formula:

$$V = m_{wf}.\,v_{wf} \quad (13)$$

The application of a heat balance determines the mass flow rate of cooling water in a condenser as follows:

$$m_w = \frac{m_{wf}.(h_4 - h_1)}{C_w.(T_{out} - T_{in})} \quad (14)$$

The work performed by the SORC cycle is calculated as follows (Bellos and Tzivanidis, 2017):

$$P_{net} = P_{ele} - W_p \quad (15)$$

The thermal efficiency of the ORC is expressed as follows:

$$\eta_{ORC} = \frac{P_{net}}{Q_{evap}}.100 \quad (16)$$

2.2.3. Energy efficiency

The energy efficiency of the proposed SORC in various energy generation scenarios is defined as follows (Bellos and Tzivanidis, 2017):

- For electrical generation standalone:

$$\eta_{SORC\,SA} = \frac{P_{net}}{G(\tau)\,.A_{sc}(\tau)}.100 \quad (17)$$

- For multi-generation of energy:

$$\eta_{SORC\,CHPG} = \frac{P_{net} + Q_{DHW} + Q_h}{G(\tau).\,A_{sc}(\tau)}.\,100 \quad (18)$$

2.2.4. Heat exchanger modeling

The size of heat exchangers plays a vital role in the system cost of SORC CHPG. To predict the area of heat exchangers of the SORC CHPG, an average logarithmic temperature difference (LMTD) method was used. It is expressed in the following formula (Rajput, 2012):

$$Q_i = U_i\,.\,A_i\,.LMTD_i \quad (19)$$

where U is the overall heat transfer coefficient (OHTC), W/(m^2.°C). A is the heat exchanger area m^2. LMTD$_i$ is the average logarithmic temperature difference °C. For counter flow, the LMTD is determined as follows (Çengel, 2004):

$$\left.\begin{aligned} LMTD_i &= \frac{T_{h,in} - T_{c,out} - T_{h,out} - T_{c,in}}{\ln\left(\dfrac{T_{h,in} - T_{c,out1}}{T_{h,out} - T_{c,in}}\right)} \\ \Delta T_1 &= T_{h,in} - T_{c,out} \\ \Delta T_2 &= T_{h,out} - T_{c,in} \end{aligned}\right] \quad (20)$$

where ΔT_1 and ΔT_2 represent the temperature difference between two fluids at the two ends (inlet and outlet) of the heat exchanger. The values of OHTC for the evaporator, condenser, and heat exchanger for heating were taken as average depending on representative values in (Çengel, 2004). They are tabulated in Table 5.

Table 5. Average representative values of OHTC

Heat exchanger type for SORC CHPG	U, W/(m^2.°C)
Evaporator	300
Condenser	650
Heat exchanger for heating	225

3. RESULTS AND DISCUSSION

The main findings of the study regarding the desired working conditions are presented in Table 6.

Table 6. Results of the study

Parameter	Value
Heat rate in the evaporator (Q_{evap})	93.45 kW
Heat rejection in the condenser (Q_{cond})	78.62 kW
Work turbine (P_{ele})	15 kW
Work pump (W_P)	1.035 kW
Mass flow rate of the working fluid (m_{wf})	0.4223 kg/s
Mass flow rate of cooling water (m_w)	0.6241 kg/s
Mass flow rate of HTF (m_{HTF})	1.8 kg/s
Volumetric flow rate of the working fluid at the input of the expander (V_3)	0.002031 m^3/s
Volumetric flow rate of the working fluid at the outlet expander (V_4)	0.0003332 m^3/s
Net power output (P_{net})	13.97 kW
Thermal efficiency of the ORC (η_{ORC})	14.94 %
Energy efficiency of the SORC SA ($\eta_{SORC\,SA}$)	17.84 %
Total Energy efficiency of the SORC CHPG ($\eta_{SORC\,CHPG}$)	79.14 %
Area of ORC evaporator (A_{evap})	11.6 m^2
Condenser area (A_{cond})	2.6 m^2
Heat exchanger area for heating (A_{HEH})	4.81 m^2
Solar collector area of the SORC SA (A_{sc})	21.4 m^2
Solar collector area of the SORC CHPG (A_{sc})	90 m^2
Heat storage tanks volume (V_{HST})	1.125 m^3

3.1. Influence of vapor temperature

The temperature of the heat source plays an important role in the performance of the solar plant. The high temperature of HTF in the solar collector under conditions of Baghdad city leads to a higher vapor temperature at the turbine inlet of the SORC and, consequently, high energy efficiency. The efficiency is enhanced as the working fluid temperature increases at the turbine inlet. The thermal efficiency of SORC SA varies from 7.25 % to 14.94 % depending on the temperature, as shown in Figure 3.

The volumetric flow rate of R-245fa at the turbine outlet is crucial and affects the system cost and size. It decreases as the temperature increases, as shown in Figure 4.

Figure 5 shows the change in the mass flow rate of the working fluid depending on the temperature at the turbine inlet. The mentioned rate decreases following a rise in the temperature at the turbine inlet due to an increase in enthalpy difference. The temperature of the condensation affects the efficiency adversely, as presented in Figure 6.

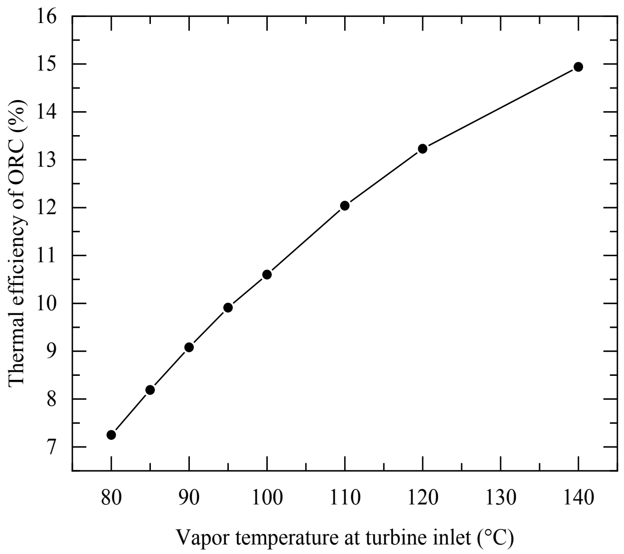

Figure 3. Influence of vapor temperature at the turbine inlet on the thermal efficiency of the ORC

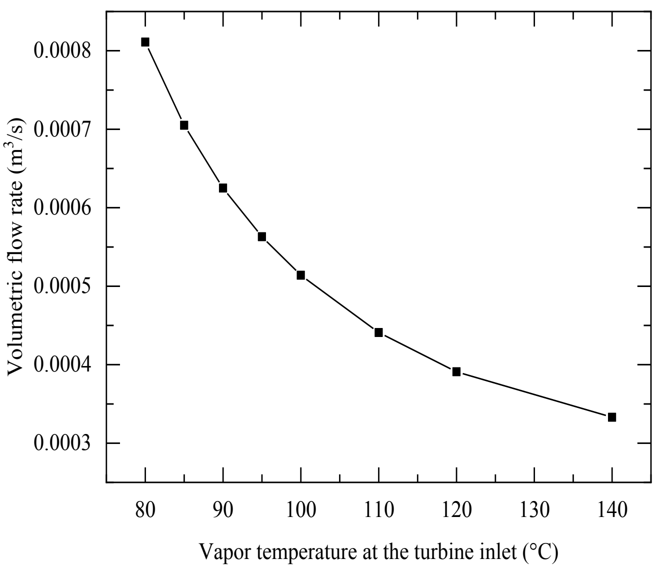

Figure 4. Influence of vapor temperature at the turbine inlet on the volumetric flow rate

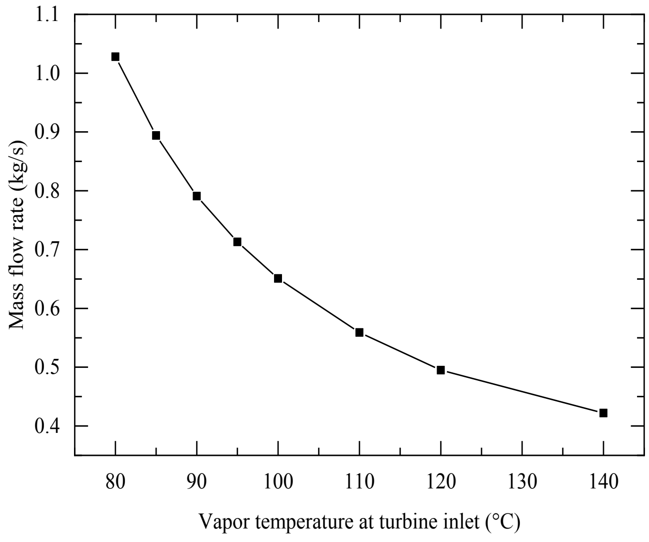

Figure 5. Influence of vapor temperature at the turbine inlet on the mass flow rate

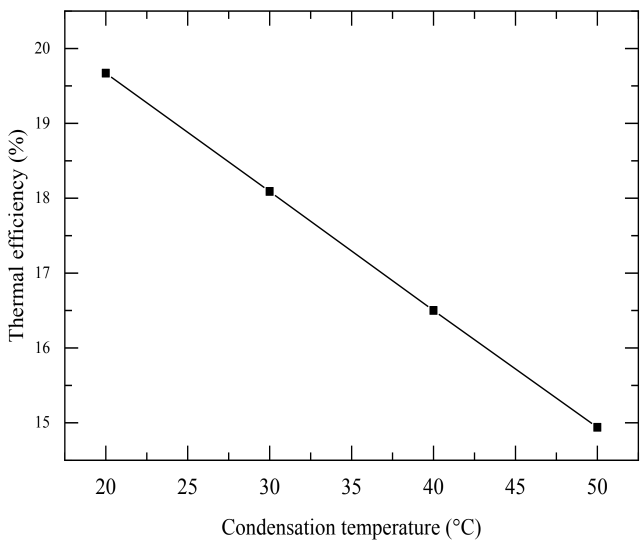

Figure 6. Influence of condenser temperature on the thermal efficiency of the ORC

3.2. Effect of pressures

To ensure the optimum system performance, the working pressure range of the working fluid must be determined along with its thermophysical properties when exposed to a certain temperature. High working pressure requires reliability and strength for the evaporator. The performance of SORC SA increases with an elevation of evaporation pressure, as illustrated in Figure 7.

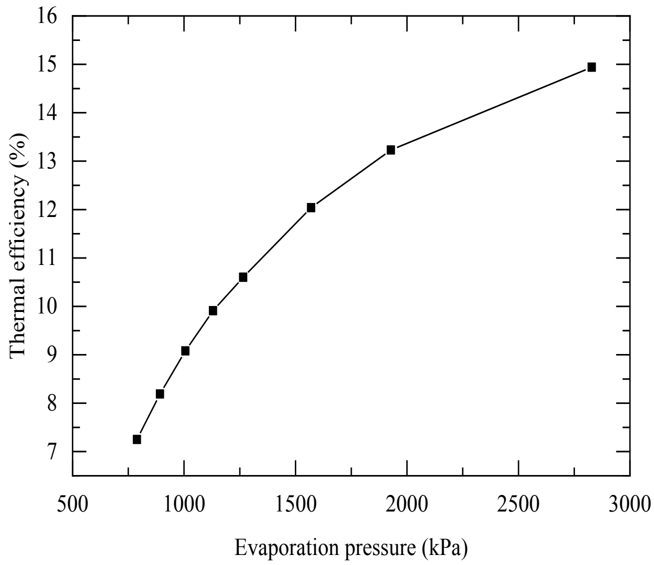

Figure 7. Influence of evaporation pressure on the performance of the ORC

3.3. Effect of solar radiation on Baghdad city

The area of the solar collector strongly depends on the intensity of solar radiation in the place of construction of the solar power plant. The high incident solar radiation, long periods of brightness, and high temperature in Baghdad reduce the solar collector area and subsequently, the cost of the system minimizes. The maximum and minimum values of the collector area for SORC SA and SORC CHPG range from 7.937 to 2.857 m^2 and 33.33 to 12 m^2, respectively, as shown in Figure 8.

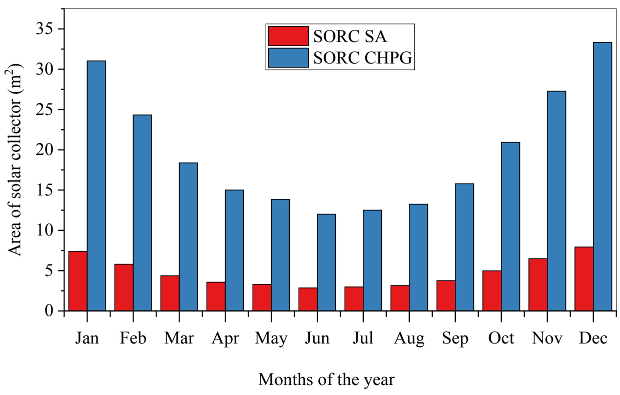

Figure 8. Variation of solar collector area with AGSR

The collector efficiency of the proposed SORC CHPG changes with the intensity of the Hourly Solar Radiation (HSR) and ambient temperature. The highest collector efficiency was 74.38 % when the recorded maximum value of HSR was 870 W/m^2 on the 15th day of July for Baghdad, as illustrated in Figure 9.

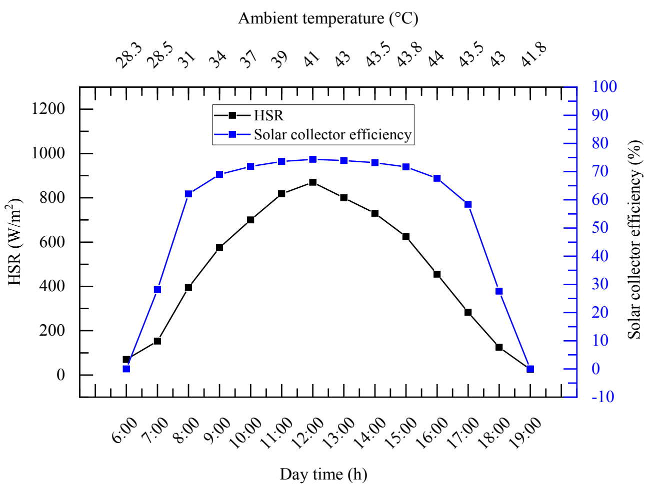

Figure 9. Variation of solar collector efficiency with the HSR and ambient temperature

Figure 10 shows the variation of the energy produced by both SORC SA and the novel SORC CHPG with HSR on the 15th day of July for Baghdad city. The maximum electric energy generated by SORC SA and the total energy (electric and heat demand) obtained by SORC CHPG reached 13.77 kW and 54.81 kW, respectively, when the HSR value was at its highest value of 870 W/m^2, as illustrated in Figure 10.

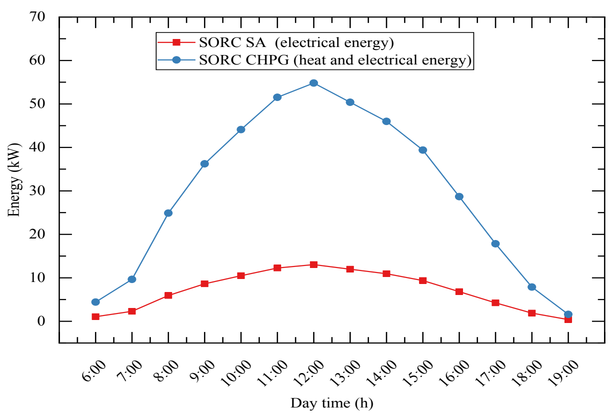

Figure 10. Daily energy generation by the hour

The maximum energy generated by both SORC SA and SORC CHPG was 118.1 and 472.5 kW, respectively, when the recorded AGSR of Baghdad was 7.5 kWh/m2/day in June, as presented in Figure 11.

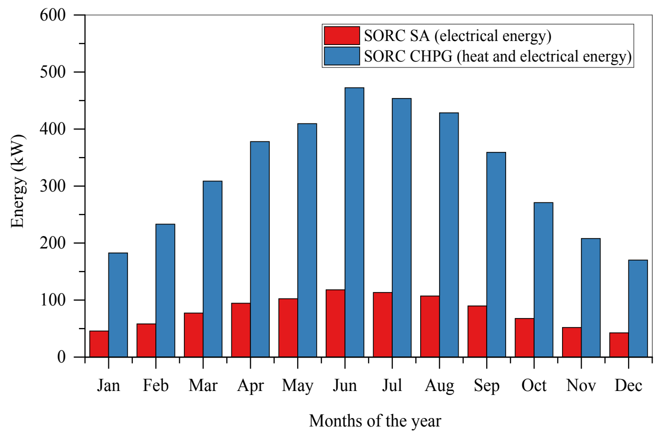

Figure 11. Variation of energy generated in different months of the year

3.4. Energetic efficiency enhancement

In the proposed developed design of SORC CHPG, many scenarios of energy generation can be achieved. The energy efficiency and its improvement for multi-generation are shown in Figure 12. The optimal efficiency and enhancement reached 79.1 % and 68.1 %, respectively, when the HSR was at the highest value of 870 W/m^2 in July. In the new model, the rate of heat transferred for DHW and heating purposes was taken into account; as a result, the total energy efficiency increased significantly.

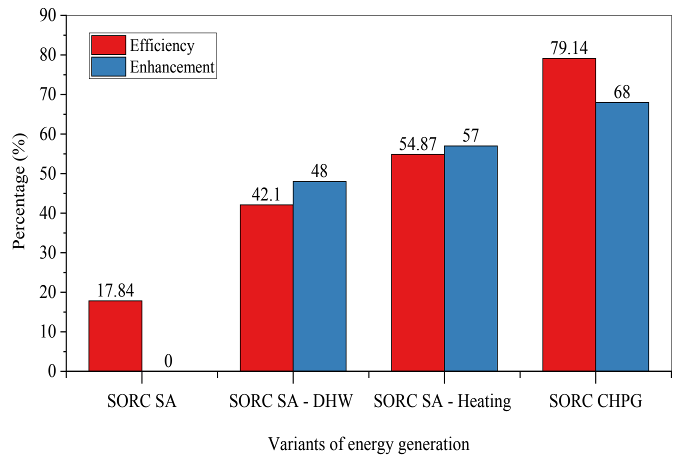

Figure 12. Comparison of the energy efficiency and improvements for different variants of energy generation

4. ECONOMIC ASPECTS AND COST ESTIMATION

It is important to investigate the economic aspects of the proposed energy supply system. The feasibility study of SORC CHPG was carried out for electric power of 15 kW, DHW demand of 19 kW, and heating load of 29 kW. The method of Payback Period (PP) and way of Net Present Cost (NPC) were employed to examine the feasibility of applying the SORC CHPG under the current state of energy in Iraq (Garcia-Saez et al., 2019; Gomaa et al., 2020). The cost of the solar collector was taken as 150–200 \$/m^2 (Gomaa et al., 2020). The cost of fittings, oil, and pipes was neglected in the current work given their minor contribution to the total cost of the system (Aghaziarati and Aghdam, 2021). Table 7 presents the economic assumptions used in the feasibility study. The Investment Capital Cost (ICC) and Operation and Maintenance (O & M) costs are calculated, as presented in Table 8.

Table 7. Economic input parameters

Parameters	Value
Price of kWh by the Iraqi government, (C_{ele})	0.024 \$/kWh (https://www.globalpetrolprices.com/)
Price of kWh from the SORC system, (C_{SORC})	8 cent/kWh (0.08 \$/kWh) (Muslim et al., 2018)
The lifetime of the SORC system, (LT)	20 years (Baral et al., 2015)
Interest rate, (r)	5 % (Garcia-Saez et al., 2019)
Operating time of solar plant per day, OT_{sp}	10-22 h

Table 8. Estimated cost of major components of SORC CHPG (Garcia-Saez et al., 2019; Gomaa et al., 2020; Baral et al., 2015)

No.	Parameter	ICC, \$	O & M costs (\$ for 20 years)	TICC (\$)
1	Solar collector	175 \$/m^2	(15 %.ICC_{sc}).LT	ICC_{sc} + O & M_{sc}
2	Expander/turbine	$4750.(P_{ele})^{0.75}$	(2 %.ICC_{ele}).LT	ICC_{ele} + O & M_{ele}
3	Evaporator	$150.(A_{evap})^{0.8}$	(4 %.ICC_{evap}).LT	ICC_{evap} + O & M_{evap}
4	Condenser	$150.(A_{cond})^{0.8}$	(4 %.ICC_{cond}).LT	ICC_{cond} + O & M_{cond}
5	Heat exchanger for heating	$150.(A_{HEH})^{0.8}$	(4 %.ICC_{HEH}).LT	ICC_{HEH} + O & M_{HEH}
6	Working fluid pump	$3500.(W_p)^{0.47}$	(2 %.ICC_p).LT	ICC_p + O & M_p
7	Heat storage tank	$1380.(V_{HST})^{0/4}$	(1 %.ICC_{HST}).LT	ICC_{HST} + O & M_{HST}
Total investment capital cost				$\sum TICC$ (\$)

The associated revenues from the new installation include electricity bill, savings for heating, and DHW. The number of years required to recover the TICC can be calculated using the following formula (Gomaa et al., 2020):

$$PP = \frac{TICC}{S_y} \tag{21}$$

where TICC is the total cost of the SORC CHPG, including O & M costs (Table 8). S_y is the annual saving per year, \$, and is calculated as the sum of the following:

$$S_y = C_{DHW} + C_h + C_{sp} \tag{22}$$

where C_{DHW} is the cost of DHW supply from an electric water heater, which runs on electricity supplied by the Iraqi government, and given as follows:

$$C_{DHW} = P_{ewh} \times OT \times C_{ele} \tag{23}$$

where P_{ewh} is the power consumed by the electric water heater, kWh. OT is the operating time, h. C_{ele} is the cost of kWh in Iraq established by the government, \$/kWh. C_h is the cost of electricity consumption for heating devices run on the local grid in winter and can be determined using the following formula:

$$C_h = P_{hd} \times OT \times C_{ele} \tag{24}$$

where P_{hd} is the electric power of heating devices, kWh. In the case of using the proposed SORC system to supply DHW and home heating, the costs that are spent on heating and hot water supply from the local network are considered savings for the consumer/investor; therefore, they are used in the payback period equation as benefits. C_{sp} represents the cost of electric power generated by the SORC system and is determined using the following formula (Muslim et al., 2018):

$$C_{sp} = P_g \times C_{SORC} \tag{25}$$

where C_{SORC} is the price of electricity unit generated by the SORC system, \$/kWh. P_g is the actual generation of electricity by the SORC system, kWh, and is determined via Eq. (26):

$$P_g = OT_{sp} \times 340 \times P_{ele} \tag{26}$$

where OT_{sp} is the daily actual operating time, 340 days is the real number of days that the system operates, and 25 days for rest and maintenance purposes. NPC reflects investment performance better. For regular savings per year, it can be calculated as follows:

$$NPC = \left[S_y . \frac{1-(1+r)^{-LT}}{r} \right] - TICC \tag{27}$$

NPC is calculated depending on the lifetime of SORC CHPG. The benefits of applying the SORC CHPG for a 20-year LT can be calculated by the following formula:

$$S_{LT} = (S_y \; . \; 20) - TICC \tag{28}$$

The payback period for the total costs of the solar plant decreases upon increasing the operating time. It is 10 years when the operating time is 18 h, as shown in Figure 13. In addition, a positive net present value was obtained at an operating time of 18h, as presented in Figure 14. Table 9 illustrates the findings of the economic investigation for the proposed SORC CHPG.

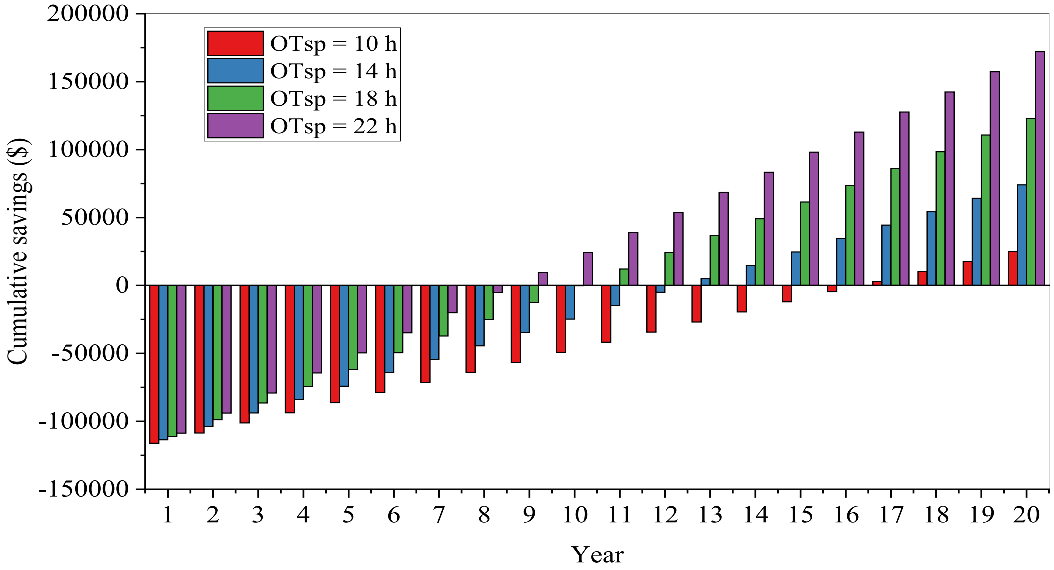

Figure 13. Variation in the payback period with operating time of SORC CHPG system

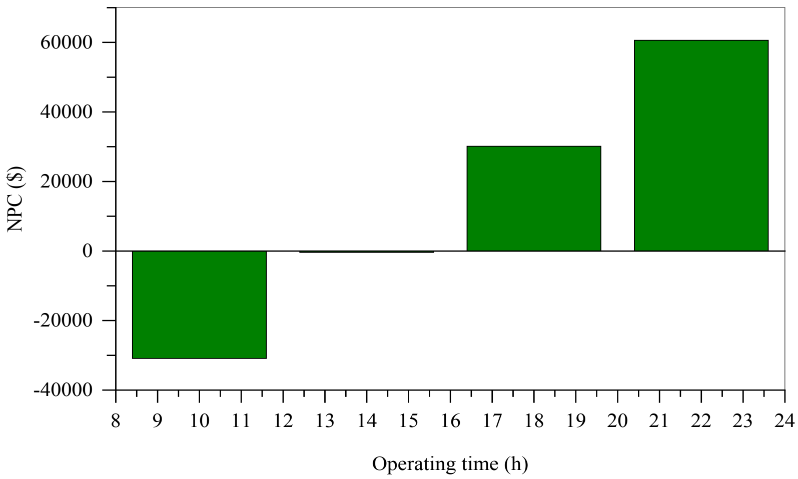

Figure 14. Variation in net present cost with the operating time of SORC CHPG system

Table 9. Outcomes of the economic investigation

Indicators	Value
Cost of the proposed SORC CHPG, (TICC)	123477 $
Net present cost, (NPC)	30112.7 $
Payback period, (PP)	10 years
Annual benefits, (S_y)	12324.4 $
Benefits for a 20-year lifetime from SORC CHPG, (S_{LT})	123011.7 $

5. CONCLUSIONS

In the present work, a thermo-economic assessment of improved solar ORC was carried out for supplying electrical energy and thermal energy in the form of hot water for domestic needs and heating purposes for a residential home under conditions of Baghdad city. A comparative study between the new design of SORC CHPG and conventional SORC SA was conducted concerning the thermal efficiency and energy generated. Parametric research and debating were conducted on key parameters of the proposed solar plant to determine optimal performance. The thermal energy storage unit was integrated for continuous and stable operation during climatic changes. The following conclusions can be derived from the study results:

1. The energetic efficiency of SORC CHPG was calculated as 79.14 %, compared to 17.84 % of SORC SA, which was 61.3 % higher than the thermal efficiency of SORC SA when the temperature of the solar heat source was in the range of 100 to 150 °C and solar radiation of 870 W/m^2 on the 15th day of July for Bagdad city.

2. The results of mathematical modeling showed that the optimal heat and electric energy produced by SORC CHPG was 54.81 kW when the HSR was approximately 870 W/m^2 at noon on the 15th day of July.

3. The total maximum energy (power and heat) obtained was 472.5 kW when the AGSR was at a higher value of 7.5 kWh/m^2/day in June under the climatic conditions of Baghdad.

4. The study of the influence of solar radiation proved that upon increasing solar radiation, the area of the solar collector decreased and, consequently, the energy efficiency of the system improved.

5. To obtain the high temperature of hot water, it could be provided directly from the solar collector.

6. From an economic point of view, the costs related to the solar field are reduced with increase in the potential of solar energy in Baghdad.

7. The economic investigation provided in this research showed that the payback period, net present cost, and annual benefits were 10 years, 30112.7 $, and 12324.4 $/year, respectively, at an operating time of 18 h. They significantly depended on the operating time of the solar power plant. Following the increased reliance on the proposed system, the economic indicators rose in value.

8. Compared to the power cost of an ordinary standard grid, the price of producing electricity with ORC was higher, which was about 3-8 cents per kWh. The proposed new design of SORC CHPG could be improved based on distributed off-grid applications, and the results might significantly enhance performance and lower costs. Despite the higher cost of SORC CHPG, it can be appealing for a variety of off-grid and waste heat recovery applications. To improve ORC system and reduce the costs, the trend of thermal performance and turbine size had meaningful relations with the temperature of vapor and mass flow rates of the working fluid. SORC CHPG or multi generation are variants that enhanced the total energy efficiency and reduce the costs. Solar ORC with tri generation seems to be implemented more cost-effectively than photovoltaic power generation system.

According to the results obtained from the study, the use of the SORC system in the cogeneration of electricity and hot water for a residential building illustrated the attractiveness of applying it for energy conservation, reduction of CO_2 emission, and solving of the acute shortage of energy supply in Baghdad, Iraq. The further research opportunities are theoretical and experimental studies of the SORC system for combined cooling, heating, and power generation under Iraqi climatic conditions with thermal energy storage units based on phase change materials.

6. ACKNOWLEDGEMENT

The author would like to thank the Department of Energy Supply for Enterprise and Thermal Engineering, Tambov State Technical University for supporting us. The researcher would like to express great appreciation of Dr. Sergei Kuzmin for providing remarkable support for this study.

NOMENCLATURE

P_{ele}	Electrical power (kW)
P_{net}	Net output power, (kW)
T	Temperature (°C)
m	Mass flow rate (kg/s)
h	Enthalpy (kJ/kg)
Q	Heat flow rate (kW)
G	Solar radiation (W/m^2)
A	Area (m^2)
C	Specific heat (kJ/kg.°C)
a_1, a_2	Coefficient of heat loss (W/(m^2.°C))
v	Specific volume (m^3/kg)
V	Volumetric flow rate (m^3/s)
U	Overall heat transfer coefficient (W/(m^2.°C))
LMTD	Logarithmic mean temperature difference (°C)
P	Pressure (kPa)
ICC	Investment capital cost ($)
TICC	Total investment capital cost ($)
S_y	Benefits/Savings per year ($)
S_{LT}	Benefits/savings during the lifetime of a system ($)
r	Interest rate (%)
C_{DHW}	Cost of domestic hot water supply ($)
C_h	Cost of heating ($)
P_{ewh}	Power of the electric water heater (kW)
OT	Operating time (h)
OT_{sp}	Daily actual operating time (h)
C_{ele}	Cost of kWh in Iraq ($)
C_{sp}	Cost of electric power generated by the SORC ($)
C_{SORC}	Cost of kWh by the SORC ($)
P_{hd}	Electric power of heating devices (kWh)
P_g	Actual generation of electricity by the SORC (kWh)
NPC	Net present cost ($)
O & M	Operation and maintenance ($)
Greek letters	
η	Efficiency (%)
τ	Time interval (h)
Subscripts	
ele	Electric
sc	Solar collector
HTF	Heat transfer fluid
out	Outlet
in	Inlet
HST	Heat storage tank
h	Heating
o	Optical
av	Average
am	Ambient
DHW	Domestic hot water
p	Pump
g	Generator, generation
e	Expander
evap	Evaporator
cond	Condenser
wf	Working fluid
w	water
sp	Solar plant
y	Year Lifetime
LT	Lifetime
Acronyms	
ORC	Organic Rankine cycle
SORC	Solar organic Rankine cycle
SORC SA	Solar organic Rankine cycle standalone
SORC CHPG	Solar organic Rankine cycle for combined heat and power generation
DHW	Domestic hot water
HFC	Hydrofluorocarbon
sc	Solar collector
spp	Solar power plant
NPC	Net present cost
EES	Engineering Equation Solver
PP	Payback period
ICC	Investment capital cost
LT	Lifetime

REFERENCES

1. Aghaziarati, Z., & Aghdam, A.H. (2021). Thermoeconomic analysis of a novel combined cooling, heating and power system based on solar organic Rankine cycle and cascade refrigeration cycle. *Renewable Energy*, *164*, 1267-1283. https://doi.org/10.1016/j.renene.2020.10.106
2. Akram Al-Khazzar, A.K. (2017). A comparative study of the available measured global solar radiation in Iraq. *Journal of Renewable Energy and Environment (JREE)*, *4*(2&3), 47-55. https://doi.org/10.30501/jree.2017.86011
3. Al-Kayiem, H.H., & Mohammad, S.T. (2019). Potential of renewable energy resources with an emphasis on solar power in Iraq: An outlook. *Resources*, *8*(1), 1-20. https://doi.org/10.3390/resources8010042
4. Al-Hamdani, N.I. (2017). Solar energy applications in Iraq. *International Journal of Scientific Engineering and Science*, *1*(9), 30-39. http://ijses.com/wp-content/uploads/2017/10/174-IJSES-V1N9.pdf
5. Al-Obaidi, M.Q., Hamid, T.G., & Derbel, N. (2020). *Design of solar powered water pumping system for domestic use in Erbil.* Proceedings of the 17th International Multi-Conference on Systems, Signals and Devices, SSD 2020 (pp. 272-278), Tunisia. https://doi.org/10.1109/SSD49366.2020.9364196
6. Baral, S., & Kim, K.C. (2014). Thermodynamic modeling of the solar organic rankine cycle with selected organic working fluids for cogeneration. *Distributed Generation and Alternative Energy Journal*, *29*(3), 7-34. https://doi.org/10.1080/21563306.2014.10879015
7. Bellos, E., & Tzivanidis, C. (2017). Parametric analysis and optimization of a solar driven trigeneration system based on ORC and absorption heat pump. *Journal of Cleaner Production*, *161*, 493-509. https://doi.org/10.1016/j.jclepro.2017.05.159
8. Bigerna, S., Bollino, C.A., & Polinori, P. (2021). Convergence in renewable energy sources diffusion worldwide. *Journal of Environmental Management*, *292*, 112784. https://doi.org/10.1016/j.jenvman.2021.112784
9. Bouvier, J.-L. (2016). Experimental study of a micro combined heat and power system with a solar parabolic trough collector. *Solar Energy*, *134*, 180-192. https://doi.org/10.1016/j.solener.2016.04.028
10. Chaichan, M.T., & Kazem, H.A. (2018). *Generating Electricity Using Photovoltaic Solar Plants in Iraq*. Springer Cham, Switzerland. https://doi.org/10.1007/978-3-319-75031-6
11. Çengel, Y.A. (2004). *Heat Transfer, A Practical Approach* (2nd ed.). McGraw-Hill. https://doi.org/10.5408/0022-1368-4.2-2.83
12. F-Chart Software, Engineering equation solver (EES). (https://fchartsoftware.com/ees/). (Accessed: 20 July 2022).
13. Freeman, J., Guarracino, I., Kalogirou, S.A., & Markides, C.N. (2017). A small-scale solar organic Rankine cycle combined heat and power system with integrated thermal energy storage. *Applied Thermal Engineering*, *127*, 1543-1554. https://doi.org/10.1016/j.applthermaleng.2017.07.163
14. Garcia-Saez, I., Méndez, J., Ortiz, C., Loncar, D., Becerra, J.A., & Chacartegui, R. (2019). Energy and economic assessment of solar organic Rankine cycle for combined heat and power generation in residential applications. *Renewable Energy*, *140*, 461-476. https://doi.org/10.1016/j.renene.2019.03.033
15. Global petrol prices, Iraq electricity prices, (https://www.globalpetrolprices.com/Iraq/electricity_prices/). (Accessed: 26 July 2022).
16. Gomaa, M.R., Mustafa, R.J., Al-Dhaifallah, M., & Rezk, H. (2020). A low-grade heat organic Rankine cycle driven by hybrid solar collectors and a waste heat recovery system. *Energy Reports*, *6*, 3425-3445. https://doi.org/10.1016/j.egyr.2020.12.011
17. Gupta, P.R., Tiwari, A.K., & Said, Z. (2022). Solar organic Rankine cycle and its poly-generation applications – A review. *Sustainable Energy Technologies and Assessments*, *49*(October 2021), 101732. https://doi.org/10.1016/j.seta.2021.101732
18. Habka, M., & Ajib, S. (2016). Performance estimation of mixtures in solar organic Rankine cycle with two mini cogeneration options for improvement purpose. *Sustainable Energy Technologies and Assessments*, *16*, 174-189. https://doi.org/10.1016/j.seta.2016.06.002
19. Hassan, Q., Abbas, M.K., Abdulateef, A.M., Abulateef, J., & Mohamad, A. (2021). Assessment the potential solar energy with the models for optimum tilt angles of maximum solar irradiance for Iraq. *Case Studies in Chemical and Environmental Engineering*, *4*(October), 100140. https://doi.org/10.1016/j.cscee.2021.100140
20. Herath, H.M.D.P., Wijewardane, M.A., Ranasinghe, R.A.C.P., & Jayasekera, J.G.A.S. (2020). Working fluid selection of organic Rankine cycles. *Energy Reports*, *6*, 680-686. https://doi.org/10.1016/j.egyr.2020.11.150
21. Hossin, K., & Mahkamov, K. (2015). *Performance evaluation for a 10 kW solar organic Rankine cycle power system to operate in the UK climate conditions*. The Third European Conference on Sustainability, Energy & the Environment, ECSEE2015 (p. 16). UK. https://doi.org/10.13140/RG.2.1.4135.4721
22. Kazem, H.A., & Chaichan, M.T. (2012). Status and future prospects of renewable energy in Iraq. *Renewable and Sustainable Energy Reviews*, *16*(8), 6007-6012. https://doi.org/10.1016/j.rser.2012.03.058
23. Malwe, P., Gawali, B., Shaikh, J., Deshpande, M., Dhalait, R., Kulkarni, S., Shindagi, V., Panchal, H., & Sadasivuni, K.K. (2021). Exergy assessment of an organic Rankine cycle for waste heat recovery from a refrigeration system: A review. *Chemical Engineering Communications*, 837-865. https://doi.org/10.1080/00986445.2021.1980396
24. Manufacturer of heat transfer fluids Polyester, Heat carrier TLV-330, (https://termolan.ru/tlv-330m/). (Accessed: 24 July 2022).
25. Martins, F., Felgueiras, C., Smitkova, M., & Caetano, N. (2019). Analysis of fossil fuel energy consumption and environmental impacts in european countries. *Energies, 12*(6), 1-11. https://doi.org/10.3390/en12060964
26. Mohammed Ali, S.A. (2020). Energy efficiency assessment of solar organic Rankine cycle for production of heat and electrical energy in the climatic conditions of Iraq., [MA dissertation, Tambov State Technical University]. https://www.tstu.ru/. (In Russian).
27. Muslim, H.N., Alkhazraji, A., & Salih, M.A. (2018). Feasibility study of using 2kWp residential PV system comparing with 2.5kVA gasoline generator (Case study: Baghdad city). *International Journal of Energy and Environment (IJEE)*, *9*(1), 2076-2909. https://www.ijee.ieefoundation.org/vol9/issue1/IJEE_05_v9n1.pdf
28. Oyekale, J., & Emagbetere, E. (2022). A review of conventional and exergetic life cycle assessments of organic Rankine cycle plants exploiting various low-temperature energy resources. *Heliyon*, *8*(7), e09833. https://doi.org/10.1016/j.heliyon.2022.e09833
29. Rajput, E.R.K. (2012). *Heat and Mass Transfer*. Fifth Edit, S. Chand & Company Ltd., New Delhi. http://referenceglobe.com/kpsslp/support/upload_videos/Heat%20and%20Mass%20Transfer%20%20rajput_1586515462.pdf
30. Rajput. R.K. (2007). *Engineering Thermodynamics* (3rd ed). LAXMI Publications Ltd. New Delhi-110002. https://deewanbittal.files.wordpress.com/2017/11/thermo-rk-rajput.pdf
31. Rayegan, R., & Tao, Y.X. (2011). A procedure to select working fluids for solar Organic Rankine Cycles (ORCs). *Renewable Energy*, *36*(2), 659-670. https://doi.org/10.1016/j.renene.2010.07.010
32. Razmi, A., Soltani, M., & Torabi, M. (2019). Investigation of an efficient and environmentally-friendly CCHP system based on CAES, ORC and compression-absorption refrigeration cycle: Energy and exergy analysis. *Energy Conversion and Management, 195*, 1199-1211. https://doi.org/10.1016/j.enconman.2019.05.065
33. Saeed, I.M., Ramli, A.T., & Saleh, M.A. (2016). Assessment of sustainability in energy of Iraq, and achievable opportunities in the long run. *Renewable and Sustainable Energy Reviews, 58*, 1207-1215. https://doi.org/10.1016/j.rser.2015.12.302
34. Singh, H., & Mishra, R.S. (2018). Performance analysis of solar parabolic trough collectors driven combined supercritical CO_2 and organic Rankine cycle. *Engineering Science and Technology, an International Journal*, *21*(3), 451-464. https://doi.org/10.1016/j.jestch.2018.03.015
35. Solarin, S.A. (2020). Towards sustainable development in developing countries: Aggregate and disaggregate analysis of energy intensity and the role of fossil fuel subsidies. *Sustainable Production and Consumption*, *24*, 254-265. https://doi.org/10.1016/j.spc.2020.07.011
36. Solarin, S.A. (2020). An environmental impact assessment of fossil fuel subsidies in emerging and developing economies. *Environmental Impact Assessment Review, 85*(July), 106443. https://doi.org/10.1016/j.eiar.2020.106443
37. Baral, S., Kim, D., Yun, E., & Kim, C.K. (2015). Energy, exergy and performance analysis of small-scale organic Rankine cycle systems for electrical power generation applicable in rural areas of developing countries. *Energies*, *8*, 684-713. https://doi.org/10.3390/en8020684
38. Tchanche, B.F., Papadakis, G., Lambrinos, G., & Frangoudakis, A. (2009). Fluid selection for a low-temperature solar organic Rankine

cycle. *Applied Thermal Engineering*, *29*(11–12), 2468-2476. https://doi.org/10.1016/j.applthermaleng.2008.12.025

39. Wang, Z., Zhou, N., & Jing, G. (2012). Performance analysis of ORC power generation system with low-temperature waste heat of aluminum reduction cell. *Physics Procedia*, *24*, 546-553. https://doi.org/10.1016/j.phpro.2012.02.080

40. Yang, J., Li, J., Yang, Z., & Duan, Y. (2019). Thermodynamic analysis and optimization of a solar organic Rankine cycle operating with stable output. *Energy Conversion and Management*, *187*(March), 459-471. https://doi.org/10.1016/j.enconman.2019.03.021

41. Yüksel, Y.E. (2018). Thermodynamic assessment of modified organic Rankine cycle integrated with parabolic trough collector for hydrogen production. *International Journal of Hydrogen Energy*, *43*(11), 5832-5841. https://doi.org/10.1016/j.ijhydene.2017.09.164

JREE: Vol. 10, No. 3, (Summer 2023) 51-58

Journal of Renewable Energy and Environment

Journal Homepage: www.jree.ir

Materials and Energy Research Center

MERC

Research Article

Techno-Economic and Environmental Analyses of Digestate Treatment after Anaerobic Digestion Process

Ali Nazari, Morteza Hosseinpour *, Mahdi Rezaei

Department of Renewable Energy Research, Niroo Research Institute (NRI), Tehran, Iran.

PAPER INFO

Paper History:
Received: 22 June 2022
Revised: 11 August 2022
Accepted: 12 September 2022

Keywords:
Anaerobic Digestion,
Biogas,
Sustainability,
Liquid Dairy Manure,
Aspen Plus

ABSTRACT

In this study, the impact of digestate treatment after Anaerobic Digestion (AD) process in two scenarios is analyzed in the case of an industrial diary unit in the United States. The first scenario involves production of liquid fertilizer and compost, while the second scenario lacks such a treatment process. Aspen Plus is used to simulate the AD process and evaluate the general properties of biogas and digestate. The results of technical analysis show insignificant changes in the net power production from the CHP unit in Scenario 1. The economic analysis, however, indicates the necessity of digestate treatment for AD systems to be profitable. Furthermore, the results of environmental analysis indicate the mitigation of about 93.4 kilotonnes of greenhouse gas (GHG) emissions in Scenario 1, while AD in Scenario 2 saves only 12 kilotonnes of GHG emissions. In other words, digestate treatment has a more significant environmental impact than the power production and its profitability from CHP unit. The reason could be attributed to the enormous consumption of energy during the production of chemical fertilizers where the digestate treatment process (scenario 1) offsets the utilization of chemical fertilizers in the agriculture industry.

https://doi.org/10.30501/jree.2022.347330.1390

1. INTRODUCTION

Global industrialization and population growth greatly contribute to higher energy consumption and environmental pollution. The dairy industry has great impact on the environment given its significant expansion throughout the world (David et al., 2021; Houston et al., 2014; Nandhini et al., 2022; Pham et al., 2022). Such an ever-increasing growth results from the income and population growth as well as changes in lifestyle and diet; in this respect, predictions indicate a global 2.5 % annual growth in animal waste (Lukuyu et al., 2019; Outlook for Biogas and Biomethane, 2020). Therefore, mismanaging the treatment of this type of waste causes a series of irreversible damages to water and soil. These damages range from creating environmental contaminations to dispersion of pathogens, accumulation of toxic ingredients, ammonia acidification, and Greenhouse Gas (GHG) emissions (methane (CH_4), oxide nitrogen, and ammonia (NH_3)) (Kozłowski et al., 2019; Thelen et al., 2010; Zeb et al., 2017). Farm-based management approaches can reduce these issues in dairies. Anaerobic Digestion (AD) is one of the most prominent ways based on environmental regulations to reduce the impacts the organic waste caused by different industries (Adiloğlu et al., 2012; Marin-Batista et al., 2020; Rajasimman et al., 2017). One of the main products of AD operation is biogas, which can be used as a fuel for energy production. AD has four stages and in each stage of operation, a group of microorganisms degrade primary substrates and leave them to the next stage of microorganisms (Adiloğlu et al., 2012). Any degradable and organic material can be used as the feedstock of AD. The composition and ingredients of feedstock significantly affect the efficiency of instruments producing the biogas (Outlook for Biogas and Biomethane, 2020; Vindis et al., 2009). Biogas as a product contains two major components: CH_4 and carbon dioxide (CO_2), which are the main causes of global warming with CH_4 consisting of 50 to 60 vol. % and CO_2 consisting of 20 % to 45 % (Karakurt et al., 2012; Moestedt et al., 2013). It is reported that CH_4 has 34 times more potential than CO_2 in the field of GHG emissions. Thus, incineration of CH_4 biogas and CO_2 generation from this phenomenon reduce the effect of GHG emissions of organic wastes (Flesch et al., 2011; Thi Nguyen et al., 2019). Based on the methane volume percentage, biogas Low Heating Value (LHV) varies between 16 to 28 MJ/m^3 (Outlook for Biogas and Biomethane, 2020).

However, AD cannot turn all of its feedstock into biogas and a by-product is produced in digester called digestate (Thi Nguyen et al., 2019). Digestate can be improved by various processes in which bio-fertilizers and composts are produced (Algapani et al., 2019). These products can be utilized in agriculture, aquaculture, and horticulture and their usage not only prevents the over-usage of chemical fertilizers that reduce the fertility of the soil. Further, it can reduce the

*Corresponding Author's Email: mhosseinpour@nri.ac.ir (M. Hosseinpour)
URL: https://www.jree.ir/article_158808.html

Please cite this article as: Nazari, A., Hosseinpour, M., & Rezaei, M. (2023). Techno-economic and environmental analyses of digestate treatment after anaerobic digestion process. *Journal of Renewable Energy and Environment (JREE), 10*(3), 51-58. https://doi.org/10.30501/jree.2022.347330.1390.

2423-7469/© 2023 The Author(s). Published by MERC. This is an open access article under the CC BY license (https://creativecommons.org/licenses/by/4.0/).

amount of pesticides as well as carbon emissions from the agricultural industry (Ersek, 2021). Moreover, digestate treatment methods for producing compost and bio-fertilizer is a well-known process that satisfies the concept of the circular economy (D'Adamo et al., 2021; Rasapoor et al., 2020).

Due to their physical properties, organic components, and abundance, dairy manures are known as the best type of biomass and feed for biogas units, especially in developing countries (Kaparaju & Rintala, 2011). Carbohydrates, proteins, and lipids are the main compositions of dairy manures (Møller et al., 2004). This type of waste is very attractive due to high water content (acting as a solvent) and low price (Al Seadi et al., 2008). Implementation and simulation of AD is a scientific and complicated process. Hence, many studies have been carried out on the simulation of this process. Betwan et al. developed ADM1, which is a precise and thorough Aspen Plus model over the information, reactions, and kinetic calculations of AD (Batstone & Keller, 2003). Several researches have investigated the economic effects of using a digestate treatment process (Gebrezgabher et al., 2010; Herbes et al., 2020). However, a comprehensive analysis of the environmental aspects of using bio-fertilizers and the composts produced by AD of dairy manure as well as economic effects of the presence of a digestate treatment unit has not been conducted.

Hence, the aim of this study is to investigate the feasibility of integrated management of dairy waste produced in livestock farms and production of value-added streams, including biogas and digestate. Moreover, the economic and environmental impacts of using digestate for further usage are investigated, as well.

2. MATERIAL AND METHOD

2.1. Case study description

An industrial dairy farm is the proposed case study for the integrated management of livestock-made dairy manures. This farm is located in the United States and has 1932 livestock, including cattle and dairy cows. The average weight of cows is around 670 kg, and each one produces approximately 0.048 m^3 manure daily. The keeping system is based on free stalls and the flushed-water system, which consumes 0.01 m^3 of water per animal, is used for waste collection, washing, and sand scratching. It should be noted that before storing the wastes, solid-liquid separation is needed because the solid particles derived from the bed of livestock can create many problems during the pumping of waste and dislocation. Hence, their concentration through time can decrease the capacity of the waste storage system. Also, mechanical separators can facilitate the recycling of wastes and land applications. More information about this diary is illustrated in Table 1.

Table 1. Animal husbandry information

Total number of livestock (head)	1932
Kind of keeping and washing system	Freestall-flushed water system
Bed type	Sand
Daily manure produced per animal (m^3/day)	0.048
Water consumption by animal (m^3/day)	0.01
Yearly produced waste (m^3/year)	40900.4

2.2. Process design and scenarios

The Aspen Process (V10) design was studied in detail in our previous paper (Hosseinpour et al., 2022). Two scenarios are considered to find the effects of using a digestate treatment process. In Scenario 1, the digestate treatment process produces compost and liquid fertilizer, while in the second scenario, Scenario 2, such a unit is omitted (Figure 1). For both cases, there is a Combined Heat and Power (CHP) generation system that generates heat and electrical power from the biogas produced in digester, as well.

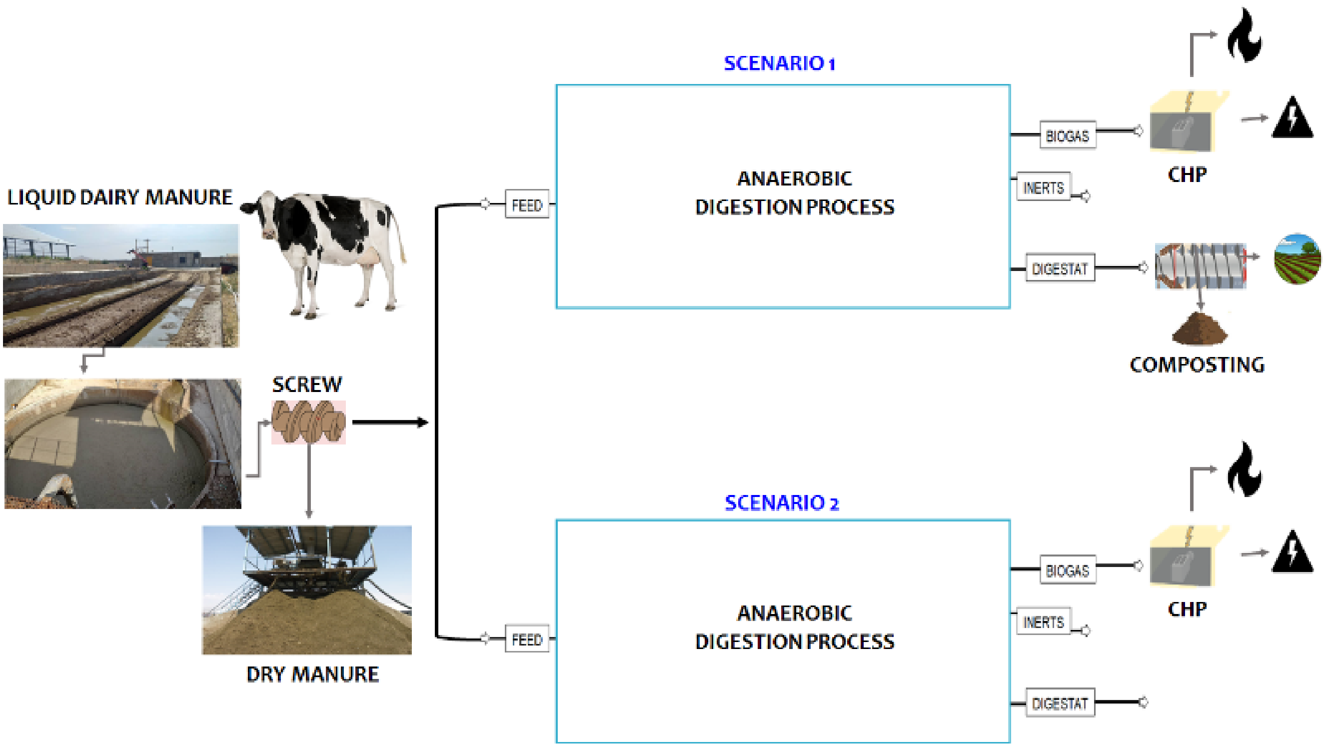

Figure 1. Aspen Plus model for the anaerobic digestion process

Feedstock characteristics, components, and materials in solid fraction are shown in Table 2 (Batstone & Keller, 2003; Ersek, 2021). Since the degradation of lignin is highly difficult and time-consuming, it is considered an inert component. Furthermore, process parameters of AD such as temperature, pressure, load rate, and retention time are illustrated in Table 2 (Pham et al. 2022). Temperature of the digester is in the thermophilic condition, which leads to better digestibility of the feedstock (Labatut et al., 2014).

Table 2. Characteristics of liquid manure and operation parameters of AD process

Liquid dairy manure characteristics	Unit of calculation	Amount
Total solids (TS)	Percentage of feedstock (%)	9.5 [7]
Volatile solid	Percentage of feedstock (%)	4.5 (Rico et al., 2011)
Carbohydrates (cellulose, hemicellulose, lignin, starch)	Percentage of total solids (% TS)	90.2 (Rico et al., 2011)
Fat	% TS	1.5 (Rico et al., 2011)
Cellulose	% TS	20.4 (Rico et al., 2011)
Hemicellulose	% TS	8.6 (Rico et al., 2011)
Glucose	% TS	25.7 (Rico et al., 2011)
Protein (Glycine)	% TS	8.3 (Rico et al., 2011)
Triolein	% TS	1.5 (Rico et al., 2011)
Others	% TS	35.5 (Rico et al., 2011)
Operational condition of the AD process		
Reactor temperature	°C	55 (Labatut et al., 2014)
Reactor pressure	atm	1
Hydraulic retention time	day	15
Load rate	Volumetric m^3 per day	112.056

Digestate treatment process and its impact on the economic situation of AD process are studied by modeling this section. During the digestion process, the majority of organic matter, especially nitrogen, is mineralized and is readily available for plants for their growth. In practice, the digestion rate of dairy waste is about 40 % (Al Seadi et al., 2008). The mineralization process involves the decomposition of carbon bonds and organic acids, resulting in a homogeneous digestate with enhanced nitrogen and phosphorus balance and a lower carbon-to-nitrogen ratio (Ali et al., 2020). Table 3 illustrates the amount of the biogas and digestate used in this research. Moreover, Table 4 shows the composition of the biogas and the digestate used in this research, as well. Biogas methane composition is in good agreement with the results from the experimental research conducted by Kaparaju et al. (Kaparaju et al., 2009) and the model developed by Kozlowski et al. (Kozłowski et al., 2019).

Table 3. Technical results of Aspen Plus model of the previous research

General parameters	Unit	Amount
Feedstock total mass	kilotonne/year	36.500
Biogas generation	million m^3/year	1.2
Digestate production	kilotonne/year	35.300

In the digestate treatment process, solid and liquid fractions of digestate are separated, and the effluent obtained from the AD process comes into the screw press machine for dewatering and separation. Non-Random Two-Liquid model (NRTL) is used as the fluid model in Aspen Plus simulation. The solid phase can be used as compost in agriculture and the liquid phase as the liquid fertilizer (de Baere, 2010). Figure 2 illustrates the digestate treatment process. After digestate production by the digester reactor, it enters a centrifugal pump, which is used for transporting digestate to the screw press unit.

Table 4. Biogas and digestate components and characteristics used for further steps

Compound	Composition (vol%)
Biogas	
CH_4	54
CO_2	37
NH_3	5
H_2O	0.9
H_2S	0.3
C_2H_5OH	0.4
H_2	0.2
Digestate	
Carbon dioxide	1
Glucose	4
Cellulose	1
Hemicellulose	0.6
Ethanol	0.8
Protein	0.1
Ammonia	0.1
Others	6

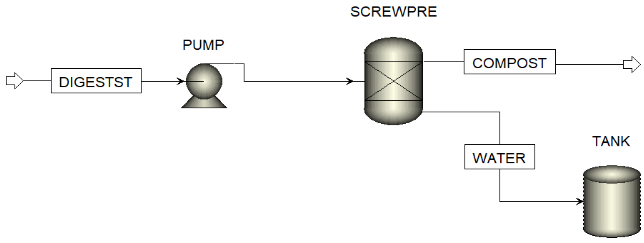

Figure 2. Aspen Plus model for the digestate treatment process (Scenario1)

Figure 3 illustrates the general concept of the CHP unit. In both scenarios, there is a CHP unit using the biogas derived from the digestion of liquid dairy manure and producing electricity and heat. In both scenarios of this research, the heat generated in the CHP unit is used for digester heating as well as other heating purposes in the diary complex. However, in the scenario involving digestate treatment, a portion of the electricity generated in the CHP unit is used for THE digestate treatment process, while the rest of electricity is sold to the general grid for further profitability. In the scenario without digestate treatment process, the entire electricity is sold to the general grid. To have a thorough analysis from the CHP unit, the catalog of the United States Department of Energy (U.S. DOE) is used for modeling the CHP unit (United States Department of Energy, 2016). For the CHP unit of this study, a reciprocating engine is chosen for its operation.

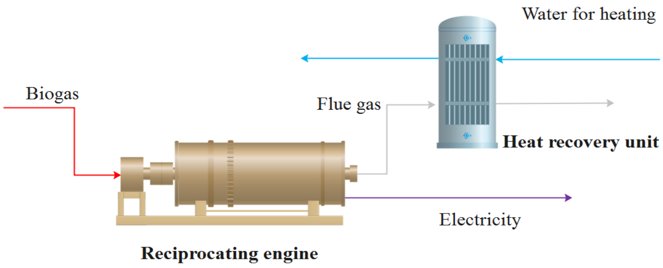

Figure 3. Structure of the combined heat and power unit

2.3. Economic analysis

There are two scenarios considered in this research. In the first scenario, digestate goes through the treatment process, which has been modeled in the previous section of this research. In the second scenario, digestate is untreated and not used for the economic aspect of AD. It is notable that the interest rate is considered to be simple and will not change by the year of operation. To provide the required energy for livestock by the AD process, viable business models are identified with stakeholder consultation. The stakeholders are research organizations, industry, financial institutions, and the government. The heat generated by the CHP unit is used for heating purposes such as maintaining the digestion temperature constant and meeting the thermal needs of the livestock. Table 5 shows the elements of the business model used in this research.

In the case of economic analysis in this research, Seider et al (Seider et al., 2016) considered different economic parameters based on sets of valuable sources and reasonable assumptions concerning economic issues. There are two categories for costs: Capital costs and production costs. There are 4 parameters considered for the capital costs. Direct Permanent Investments (DPI), Total Depreciable Costs (TDC), Total Permanent Investments (TPI), and Total Capital Investments (TCI). All of these parameters are calculated in which the described economic parameters are calculated as a requirement for further parameters to determine TCI for both scenarios. DPI of CHP unit is calculated based on the catalog of U.S. DOE, which covers economic issues of CHP unit ((United States Department of Energy, 2016) in the first step. It is assumed that it takes 50 % of this category of AD operations based on the previous research by Morelli et al. (Morelli et al., 2019). Therefore, DPI of the AD process can be calculated. Since the first scenario involves a digestate treatment unit, DPI of this part has to be calculated and be added to DPI of the AD process whose method of calculation has already been explained, as well. DPI of the digestate treatment unit was calculated by Seider et al. (Seider et al., 2016). Following the calculation of DPI for both scenarios, TDC, TPI, and TCI in both scenarios were calculated and the method of calculation for each element is shown in Table 6.

Table 5. Definition of the business model

Investment	Digester-CHP unit-separator (screw press)
Input	Liquid dairy manure
Output	Electricity-heat-compost-liquid fertilizer

For calculating the production costs of both scenarios, different sets of parameters are considered including maintenance costs, operation costs, depreciation, general expenses, overhead for maintenance and operation cost, and property taxes. Since the first scenario involves an additional unit compared to the second scenario, it requires higher production costs. In the first scenario, there are five operators who work in the complex, while in the second scenario, only 3 operators are present for the AD complex. In the next part of the economic analysis, the sources of income for both scenarios are shown. It is notable that there will be no source of income from compost and liquid fertilizer that can be produced from digestate separation unit in the second scenario. In the next part of the analysis, economic rates including tax rate, inflation rate, and interest rate are required for calculating the level of profitability for both scenarios. Levels of income in each year of operation for both scenarios are deduced by the production costs according to yearly costs of the AD complex. Finally, payback period is measured for both scenarios by considering the effects of the TCI, the results regarding the incomes and production costs of the AD complex, and economic rates. Table 6 presents the calculation method for the production costs, sources of income, and profitability indicators. The basis of the economic assumptions and calculations was derived from the study of Seider et al., in which economic issues were adequately covered (Seider et al., 2016).

Table 6. Parameterization of the business model (Seider et al., 2016)

Cost category	Parameter	Unit	Quantity
Capital costs	DPI	$	-
	TDC	$	115 % of DPC

	TPI	$	107 % of TDC
	TCI	$	115 % of TPI
Production costs	Maintenance cost (M)	$/year	4.5 % of TDC
	Operation costs (O)	$/operator.h	5
	Power plant lifetime	year	25
	Depreciation	$/year	3.4 % of TDC
	General expenses	$/year	5.25 % of incomes
	Property taxes and insurance	$/year	2 % of TDC
	Operation & maintenance overhead	$/year	5 % of M&O
	Operation hour per year	h	7800
Sources of income	Electricity price	$/kWh	0.1
	Heating price	$/kWh	0.02
	Compost price	$ /tonne	70
	Liquid fertilizer price	$/tonne	60
Economic rates	Interest rate	%	5
	Inflation rate	%	4
	Opportunity cost rate	%	3
	Tax rate	%	25

2.4. Environmental analysis

As mentioned in the previous sections, the use of liquid bio-fertilizers and composts in agricultural activities contributes to the intensity of global warming. Therefore, environmental analysis is performed for both scenarios and the impacts of digestate use are considered in this research based on the review and study of valuable resources. However, for establishing a reasonable analysis, carbon emissions should be analyzed through different concepts. In this research, GHG emission savings in both scenarios are studied as in the following three categories:

1- Emission savings achieved by preventing methane emissions from methane use in CHP unit;

2- Prevention of using natural gas for CHP units; and

3- Prevention of emissions caused by producing organic fertilizers and reducing emissions from chemical fertilizer production.

Emission saving achieved by the prevention of methane emission is calculated on the basis that methane has 34 times greater impact than GHG effects (Demirel & Scherer, 2011) and that its incineration inside the CHP unit prevents any methane leak while emitting only CO_2 which is caused by methane incineration. The amount of emissions saved by CHP unit are calculated by the catalog of the U.S DOE for both scenarios (United States Department of Energy, 2016). Since the CO_2 emitted by the CHP unit is renewable unlike natural gas, it is considered as a section for carbon savings. Statistics indicate that 1.2 % of the energy consumption in the world is caused by fertilizer production industry (Ammonia Production: Moving towards Maximum Efficiency and Lower GHG Emissions, 2014). Moreover, 36.4 billion tonnes of CO_2 was emitted in 2019 from the sources that consume much energy (Tiseo, 2023). Additionally, 190 million tonnes (Mt) of fertilizers were consumed in 2019 (Fernández, 2021). Based on the above information, 2.298 tonnes of CO_2 was emitted by the production of chemical fertilizers and it formed the basis of evaluation of GHG emissions in regard to digestate for both scenarios. Although GHG emission from the use of organic fertilizers instead of chemical fertilizers in agriculture can be studied as well, only the emissions caused by activities in AD complex and their impacts are the main issues of this research because of several uncertainties regarding the use of chemical and organic fertilizers (Havukainen et al., 2018). Therefore, this case of investigation is not considered.

3. RESULTS AND DISCUSSION

3.1. General results

In the first step, the general parameters of the AD complex must be measured and then, be used for further required analysis. The amount of produced biogas and digestate effluent affects the scale of the CHP unit as well as economy. Table 7 presents the values of general parameters in this research. According to a report provided by the European Biogas Association, the solid phase accounts for about 8 % of total digestate (de Baere, 2010). This part demonstrates the validity of the Aspen Plus simulation.

Table 7. Technical results of the business model

General parameters	Unit	Amount
Electricity production	GWh/year	1.94
Heat production	GWh/year	2.6
Compost production	kilotonne/year	2.824
Liquid fertilizer production	kilotonne/year	32.476

3.2. Efficiency and power generation analysis

In this section, the economic evaluation of both scenarios is presented. In Scenario 1, investment costs not only increase but also reduce the amount of income that can be earned from electricity production. However, production of compost and liquid fertilizer can offset these points. For calculating the efficiency of CHP unit, the catalog presented by the U.S. Energy Department is consulted to ensure higher precision (United States Department of Energy, 2016). Figure 4a shows the efficiency levels for all parts of CHP unit. As anticipated, CHP enhances the level of efficiency in comparison to the mere power generation. In addition, considering the heating requirements of the dairy industry, the economic aspects of this industry have been improved by reducing or eliminating the need for purchasing natural gas.

It is important to consider that the screw-press unit consumes a portion of electricity generated in the CHP unit.

Figure 4b shows the net amount of electricity produced in the AD complex. Regarding the electricity consumption of the screw-press unit, the results indicate that the screw-press unit does not have a significant effect on the net amount of electricity production of AD complex.

3.3. Economic analysis

Figure 5a shows the impacts of adding a screw-press unit to the total capital costs of AD complex. Results show that the addition of a screw-press unit leads to a 20 % increase in the capital costs of the AD complex as total. However, this figure is not enough to meet the requirement of economic analysis.

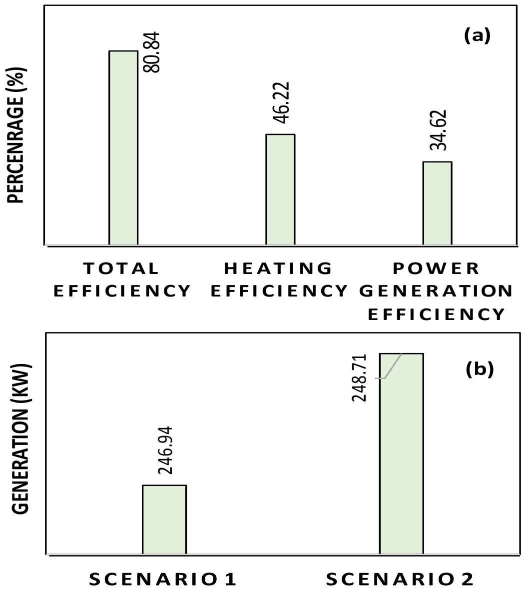

Figure 4. (a) The level of efficiency for the combined heat and power unit for both scenarios and (b) net power production for both scenarios

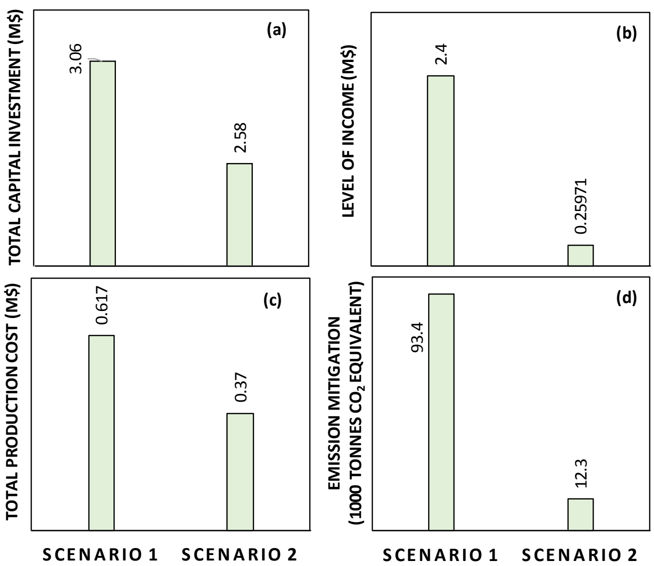

Figure 5. (a) Total capital investment (TCI), (b) level of income, (c) total production costs, and (d) Greenhouse gas emission per annual prevention of both scenarios

Figure 5b and Figure 5c illustrate the levels production costs and incomes of both scenarios. Although the figures show that use of a screw-press unit has a significant effect on the costs of production in AD complex, its positive impact on the incomes of the AD complex is far greater than its impact on the costs of AD complex. Ironically, these results indicate that the absence of a digestate treatment process and, consequently, lacking a stable income from such units cause a negative net economic outcome for the AD complex. However, the AD complex can use subsidies through carbon taxation programs and other governmental subsidies because of its role in reducing health impacts caused by dairy manure. Due to the benefit of the digestate treatment unit, it is profitable enough to eliminate the need for governmental subsidies. Therefore, using a digestate treatment process is of necessity for AD complexes to have an economic outcome for AD. Since incomes of the second scenario could not cover its production costs, the first scenario has another advantage in regard to profitability. However, the profitability of the first scenario is calculated. With the assumption of operation to the full potential of AD complex from the beginning of the operation, the payback period is 2.5 years for the first scenario, while the second scenario does not have a payback period since the level of incomes cannot cover the production costs. Results indicate that the use of a digestate treatment unit in AD complexes ensures profitability while reducing dependency on the governmental help.

3.4. Environmental analysis

AD enjoys various advantages in comparison to other treatment methods for organic-based materials. Its ability to kill pathogens present in the diary manure and the ability of methane for electricity generation are well-established concepts that prove AD efficiency in environmental issues. However, the use of the digestate treatment process and the production of solid and liquid fertilizer is the concept that facilitates further reduction of carbon emissions in the agriculture sector due to the prevention of chemical fertilizers that require energy production from fossil fuels. Figure 5d shows the carbon emission saving levels for different parts as already mentioned. Results indicate that the use of digestate treatment process has a far greater impact on GHG emission reduction than the CHP unit which uses biogas in both scenarios. The reason could be attributed to the production of fertilizers as an energy-intensive industry. Since much of the feedstock from AD turns into digestate, a considerable amount of fertilizer and compost is produced, which reduces the need for chemical fertilizers in agricultural industries (Ammonia Production: Moving towards Maximum Efficiency and Lower GHG Emissions, 2014).

4. CONCLUSIONS

In this research, the techno-economic performance of an AD unit for the treatment of a dairy farm was studied by selecting an industrial livestock unit as a case study using Aspen Plus as a simulation tool. Two scenarios were considered in which different effects of the use of digestate treatment process along the AD system were analyzed in the fields of electricity generation, economy, and environmental issues through these two scenarios to illustrate the true effects of such a unit in the AD process. AD process was implemented at a thermophilic temperature of 55 °C and pressure of 1 atm. According to the results, 3381 m^3 of biogas and 105 tonnes of digests were produced daily under specified operating conditions. In addition, the results of investigating the effects of the digestate treatment process application demonstrate that it does not reduce the net amount of electricity produced on a massive scale, while it significantly improves the economic and environmental aspects of AD systems. Results of this research indicate that the application of a digestate treatment process is necessary for the profitability of the AD complex and the usage of a digestate treatment process eliminates the need for subsidies for the profitability of this technology while reducing the tax burdens on citizens in the case of wastewater management processes. Moreover, while the usage of biogas in CHP systems improves the environmental aspects of the AD process by preventing methane emission, data analysis indicates that a digestate treatment process and the use of bio-fertilizers produced in this unit save 93.4 kilotonnes of GHG emissions by reducing dependence on chemical fertilizer production, which is an energy-intensive industry, while the CHP unit only saves about 12.3 kilotonnes of GHG emissions. Therefore, GHG saving in the scenario containing a digestate treatment unit for bio-fertilizer production is far superior to the one without such a unit. Moreover, the existence of this unit is crucial to an AD complex.

5. ACKNOWLEDGEMENT

The authors wish to acknowledge Niroo Research Institute (NRI) as the scientific supporter of this publication.

NOMENCLATURE

GHG	Greenhouse Gas
AD	Anaerobic Digestion
CHP	Combined Heat and Power
DPI	Direct Permanent Investments
TDC	Total Depreciable Costs
TPI	Total Permanent Investments
TCI	Total Capital Investments

REFERENCES

1. Achinas, S., Martherus, D., Krooneman, J., & Euverink, G.J.W. (2019). Preliminary assessment of a biogas-based power plant from organic waste in the North Netherlands. *Energies*, *12*(21), 4034. https://doi.org/10.3390/en12214034

2. Adiloğlu S.I., Yu, C., Chen, R., Li, J.J., Drahansky, M., Paridah, M., Moradbak, A., Mohamed, A., Owolabi, F., Li, H., Taiwo, A., Asniza, M., Abdul Khalid, S.H., Sharma, T., Dohare, N., Kumari, M., Singh, U.K., Khan, A.B., Borse, M.S., Patel, R., Paez, A., Howe, A., Goldschmidt, D., Corporation, C., Coates, J., & Reading, F. (2012). We are IntechOpen, the world's leading publisher of open access books built by scientists, for scientists TOP 1 %. Intech i:13.

3. Akbulut, A. (2012). Techno-economic analysis of electricity and heat generation from farm-scale biogas plant: Çiçekdaği{dotless} case study. *Energy*, *44*(1), 381-390. https://doi.org/10.1016/j.energy.2012.06.017

4. Algapani, D.E., Qiao, W., Ricci, M., Bianchi, D.M. Wandera, S., Adani, F., & Dong, R. (2019). Bio-hydrogen and bio-methane production from food waste in a two-stage anaerobic digestion process with digestate recirculation. *Renewable Energy*, *130*, 1108-1115. https://doi.org/10.1016/j.renene.2018.08.079

5. Ali, M.M., Ndongo, M., Bilal, B., Yetilmezsoy, K., Youm, I., & Bahramian, M. (2020). Mapping of biogas production potential from livestock manures and slaughterhouse waste: A case study for African countries. *Journal of Cleaner Production*, *256*. https://doi.org/10.1016/j.jclepro.2020.120499

6. Al-Rubaye, H., Karambelkar, S., Shivashankaraiah, M.M., & Smith, J.D. (2019). Process simulation of two-stage anaerobic digestion for methane production. *Biofuels*, *10*(2), 181-191. https://doi.org/10.1080/17597269.2017.1309854

7. Al Seadi, T., Rutz, D., Prassl, H., Kottner, M., Finsterwalder, T., & Silke Volk, R.J. (2008). https://www.lemvigbiogas.com/BiogasHandbook.pdf

8. *Ammonia production: Moving towards maximum efficiency and lower GHG emissions*. (2014). https://issuu.com/ifa-fertilizer/docs/2014_ifa_ff_ammonia_emissions_july

9. Batstone, D.J., & Keller, J. (2003). Industrial applications of the IWA anaerobic digestion model No. 1 (ADM1). *Water Science and Technology*, *47*(12), 199-206. https://doi.org/10.2166/wst.2003.0647

10. D'Adamo, I., Falcone, P.M., Huisingh, D., & Morone, P. (2021). A circular economy model based on biomethane: What are the opportunities for the municipality of Rome and beyond? *Renewable Energy*, *163*, 1660-1672. https://doi.org/10.1016/j.renene.2020.10.072

11. David, C., Ganduri, J., Ragunathan, V., & Natarajan, R. (2021). Characterization of pellets manufactured from plant waste and farm waste residues blended with distillery sludge as a prospective alternative fuel source. *Applied Nanoscience*. https://doi.org/10.1007/s13204-021-01982-6

12. de Baere, L. (2010). *The Dranco Technology: A unique digestion technology for solid organic waste*. Organic Waste Systems (OWS) Pub. Brussels, Beligium, 1-8. http://www.ows.be/wp-content/uploads/2013/02/The-DRANCO-technology-2012.pdf

13. Demirel, B., & Scherer, P. (2011). Trace element requirements of agricultural biogas digesters during biological conversion of renewable biomass to methane. *Biomass and Bioenergy*, *35*(3), 992-998. https://doi.org/10.1016/j.biombioe.2010.12.022

14. Ersek, K. (2021). *8 Advantages And Disadvantages Of Using Organic Fertilizer*. Holganix https://www.holganix.com/blog/8-advantages-and-disadvantages-of-using-organic-fertilizer

15. Fernández, L. (2021). *Global consumption of agricultural fertilizer by nutrient from 1965 to 2019*. Statista. https://www.statista.com/statistics/438967/fertilizer-consumption-globally-by-nutrient/

16. Flesch, T.K., Desjardins, R.L., & Worth, D. (2011). Fugitive methane emissions from an agricultural biodigester. *Biomass and Bioenergy*, *35*(9), 3927-3935. https://doi.org/10.1016/j.biombioe.2011.06.009

17. Gebrezgabher, S.A., Meuwissen, M.P.M., Prins, B.A.M., & Lansink, A.G.J.M.O. (2010). Economic analysis of anaerobic digestion—A case of Green power biogas plant in The Netherlands. *NJAS - Wageningen Journal of Life Sciences*, *57*(2), 109-115. https://doi.org/10.1016/j.njas.2009.07.006

18. Havukainen, J., Uusitalo, V., Koistinen, K., Liikanen, M., & Horttanainen, M. (2018). Carbon footprint evaluation of biofertilizers (Open access). *International Journal of Sustainable Development and Planning*, *13*, 1050-1060. https://doi.org/10.2495/SDP-V13-N8-1050-1060

19. Herbes, C., Roth, U., Wulf, S., & Dahlin, J. (2020). Economic assessment of different biogas digestate processing technologies: A scenario-based analysis. *Journal of Cleaner Production*, *255*, 120282. https://doi.org/10.1016/j.jclepro.2020.120282

20. Hosseinpour, M., Norouzi, F., & Talebi, S. (2022). Analysis of biogas recovery from liquid dairy manure waste by anaerobic digestion. *Journal of Renewable Energy and Environment (JREE)*, *10*(2), 125-132. https://doi.org/10.30501/jree.2022.336371.1354

21. Houston, C., Gyamfi, S., & Whale, J. (2014). Evaluation of energy efficiency and renewable energy generation opportunities for small scale dairy farms: A case study in Prince Edward Island, Canada. *Renewable Energy*, *67*, 20-29. https://doi.org/10.1016/j.renene.2013.11.040

22. Kaparaju, P., Ellegaard, L., & Angelidaki, I. (2009). Optimisation of biogas production from manure through serial digestion: Lab-scale and pilot-scale studies. *Bioresource Technology*, *100*(2), 701-709. https://doi.org/10.1016/j.biortech.2008.07.023

23. Kaparaju, P, & Rintala, J. (2011). Mitigation of greenhouse gas emissions by adopting anaerobic digestion technology on dairy, sow and pig farms in Finland. *Renewable Energy*, *36*(1), 31-41. https://doi.org/10.1016/j.renene.2010.05.016

24. Karakurt, I., Aydin, G., & Aydiner, K. (2012). Sources and mitigation of methane emissions by sectors: A critical review. *Renewable Energy*, *39*(1), 40-48. https://doi.org/10.1016/j.renene.2011.09.006

25. Kozłowski, K., Pietrzykowski, M., Czekała, W., Dach, J., Kowalczyk-Juśko, A., Jóźwiakowski, K., & Brzoski, M. (2019). Energetic and economic analysis of biogas plant with using the dairy industry waste. *Energy*, *183*, 1023-1031. https://doi.org/10.1016/j.energy.2019.06.179

26. Labatut, R., Angenent, L., & Scott, N. (2014). Conventional mesophilic vs. thermophilic anaerobic digestion: A trade-off between performance and stability? *Water Research*, *53C*, 249-258. https://doi.org/10.1016/j.watres.2014.01.035

27. Lukuyu, J.M., Blanchard, R.E., & Rowley, P.N. (2019). A risk-adjusted techno-economic analysis for renewable-based milk cooling in remote dairy farming communities in East Africa. *Renewable Energy*, *130*, 700-713. https://doi.org/10.1016/j.renene.2018.06.101

28. Marin-Batista, J.D., Villamil, J.A., Qaramaleki, S.V, Coronella, C.J., Mohedano, A.F., & Rubia, M.A. de la. (2020). Energy valorization of cow manure by hydrothermal carbonization and anaerobic digestion. *Renewable Energy*, *160*, 623-632. https://doi.org/10.1016/j.renene.2020.07.003

29. Moestedt, J., Påledal, S.N., Schnürer, A., & Nordell, E. (2013). Biogas production from thin stillage on an industrial scale-experience and optimisation. *Energies*, *6*(11), 5642-5655. https://doi.org/10.3390/en6115642

30. Møller, H.B., Sommer, S.G., & Ahring, B.K. (2004). Methane productivity of manure, straw and solid fractions of manure. *Biomass and Bioenergy*, *26*(5), 485-495. https://doi.org/10.1016/j.biombioe.2003.08.008

31. Morelli, B., Cashman, S., Arden, S., Ma, C., Turgeon, J., Garland, J., & Bless, D. (2019). *Life Cycle Assessment and Cost Analysis of Municipal Wastewater Treatment Expansion Options for Food Waste Anaerobic Co-Digestion*. https://cfpub.epa.gov/si/si_public_record_report.cfm?Lab=NRMRL&dirEntryId=346479

32. Nandhini, R., Berslin, D., Sivaprakash, B., Rajamohan, N., & Vo, D.V.N. (2022). Thermochemical conversion of municipal solid waste into energy and hydrogen: A review. *Environmental Chemistry Letters*. https://doi.org/10.1007/s10311-022-01410-3

33. Outlook for biogas and biomethane. (2020). https://doi.org/10.1787/040c8cd2-en

34. Pham, C.Q., Siang, T.J., Kumar, P.S., Ahmad, Z., Xiao, L., Bahari, M.B., Cao, A.N.T., Rajamohan, N., Qazaq, A.S., Kumar, A., Show, P.L., & Vo, D.-V.N. (2022). Production of hydrogen and value-added carbon materials by catalytic methane decomposition: A review. *Environmental Chemistry Letters*. https://doi.org/10.1007/s10311-022-01449-2

35. Rajasimman, M., Babu, S.V., & Rajamohan, N. (2017). Biodegradation of textile dyeing industry wastewater using modified anaerobic sequential batch reactor – Start-up, parameter optimization and performance analysis. *Journal of the Taiwan Institute of Chemical Engineers*, *72*, 171-181. https://doi.org/10.1016/j.jtice.2017.01.027

36. Rasapoor, M., Young, B., Brar, R., Sarmah, A., Zhuang, W.Q., & Baroutian, S. (2020). Recognizing the challenges of anaerobic digestion: Critical steps toward improving biogas generation. *Fuel*, *261*. https://doi.org/10.1016/j.fuel.2019.116497

37. Rico, C., Rico, J.L., Tejero, I., Muñoz, N., & Gómez, B. (2011). Anaerobic digestion of the liquid fraction of dairy manure in pilot plant for biogas production: Residual methane yield of digestate. *Waste Management*, *31*(9–10), 2167-2173. https://doi.org/10.1016/j.wasman.2011.04.018

38. Seider, W.D., Lewin, D.R., Seader, J.D., Widagdo, S., Gani, R., & Ng, K.M. (2016). *Product and Process Design Principles: Synthesis, Analysis and Evaluation*. Wiley. US.

39. Thelen, K.D., Fronning, B.E., Kravchenko, A., Min, D.H., & Robertson, G.P. (2010). Integrating livestock manure with a corn–soybean bioenergy cropping system improves short-term carbon sequestration rates and net global warming potential. *Biomass and Bioenergy*, *34*(7), 960-966. https://doi.org/10.1016/j.biombioe.2010.02.004

40. Thi Nguyen, M.-L., Lin, C.-Y., & Lay, C.-H. (2019). Microalgae cultivation using biogas and digestate carbon sources. *Biomass and Bioenergy*, *122*, 426-432. https://doi.org/10.1016/j.biombioe.2019.01.050

41. Tiseo, I. (2023). *Annual CO_2 emissions worldwide from 1940 to 2020*. Statista. https://www.statista.com/statistics/276629/global-co2-emissions/

42. United States Department of Energy. (2016). *Reciprocating Engines*. https://www.energy.gov/eere/amo/articles/reciprocating-engines-doe-chp-technology-fact-sheet-series-fact-sheet-2016

43. Vindis, P.B.M., Marjan, J., & F.C. (2009). The impact of mesophilic and thermophilic anaerobic digestion on biogas production. *Journal of Achievements in Materials and Manufacturing Engineering*, *36*. https://citeseerx.ist.psu.edu/document?repid=rep1&type=pdf&doi=05b6450b15729d6a0d5c5031aae9c3bcc0606c0b

44. Zeb, I., Ma, J., Frear, C., Zhao, Q., Ndegwa, P., Yao, Y., & Kafle, G.K. (2017). Recycling separated liquid-effluent to dilute feedstock in anaerobic digestion of dairy manure. *Energy*, *119*, 1144-1151. https://doi.org/10.1016/j.energy.2016.11.075

JREE: Vol. 10, No. 3, (Summer 2023) 59-66

Journal of Renewable
Energy and Environment

Journal Homepage: www.jree.ir

Materials and Energy
Research Center
MERC

Research Article

Numerical Simulation of a Solar Cooling System Based on Variable-Effect NH_3-Water Absorption Chiller using TRNSYS

Abir Hmida [a], Abdelghafour Lamrani [b], Mamdouh El Haj Assad [c*], Yashar Aryanfar [d], Jorge Luis Garcia Alcaraz [e]

[a] Applied Thermodynamics Research Laboratory, National Engineering School of Gabes, University of Gabes, Zrig Eddakhlania 6029, Gabes, Tunisia.
[b] Mohamed Rougui's Lab, Mohammadia School of Engineers, University of King Mohammed V., Rabat, Morocco.
[c] Department of Sustainable and Renewable Energy Engineering, University of Sharjah, Sharjah, United Arab Emirates.
[d] Department of Electric Engineering and Computers Sciences, Autonomous University of Ciudad Juarez, Ciudad Juárez 32310, Chih, Mexico.
[e] Department of Industrial Engineering and Manufacturing, Autonomous University of Ciudad Juarez, Ciudad Juárez 32310, Chih, Mexico.

P A P E R I N F O

Paper History:
Received: 09 February 2022
Revised: 18 June 2022
Accepted: 23 June 2022

Keywords:
Absorption Systems,
Solar Collectors,
Simulation,
Energy Efficiency,
TRNSYS

A B S T R A C T

Around the globe, a 60 % increase in energy demand is predicted to occur by the end of the year 2030 due to the ever-increasing population and development. With a registered temperature up to 50 °C in August 2020, which is classified as one of the hottest regions in the world, the demand for cool temperatures in Gabes-Tunisia to achieve the thermal comfort of people ensuring the product storage has become more and more intense. Removing heat from buildings represents the most extensive energy consumption process. In this paper, an absorption-refrigeration system driven by solar energy is proposed. A parametric simulation model is developed based on the TRNSYS platform. A comparison between different models for global radiation calculation and experimental meteorological data was carried out. It has been proven that the Brinchambaut model seems to be the most convenient in describing the real global radiation, with an error of up to 3.16 %. An area of 22 m² of evacuated tube solar collector ensures the proper functioning of the generator and achieves a temperature up to 2 °C in the cold room.

https://doi.org/10.30501/jree.2022.326640.1318

1. INTRODUCTION

Despite a 3.8 % fall in worldwide energy demand due to the Covid-19 lockout and an 8 % decline in global coal demand Global Energy and CO_2 Emissions in 2020 – Global Energy Review 2020 – Analysis - IEA, cooling and heating in buildings continue to be the leading energy consumers. With an ever-growing population, industrial development, and human life enhancement (Almutairi et al., 2022; Pan et al., 2020), with many parts of the world experiencing record-breaking temperatures, the need for cooling to ensure people's comfort and food storage is expanding significantly and has tripled since 1990 (Global Energy and CO2 Emissions in 2020 – Global Energy Review 2020 – Analysis - IEA; Sudhakar et al., 2019). In many countries, the primary cooling source is electrical power (Asim & Kanan, 2016; Shoaib et al., 2018). According to the IEA, space cooling accounted for over 8.5 % of total final electricity consumption in 2019 and approximately 15 % of peak electricity demand on hot days (Cooling – Analysis - IEA). The majority of electrical systems rely on fossil fuels (Shoaib et al., 2018), resulting in a rise in emissions to around 1 Gt of CO_2 in 2019 and at ambient temperature as well (Cooling – Analysis - IEA), contributing to global warming and ozone depletion concerns (Pan et al., 2020).

As a result, efforts to combat climate change must place a premium on decarbonizing energy technologies. Environmentally friendly and energy-efficient technology must be developed to mitigate the environmental impact of cooling required in the building industry while keeping costs reasonable (Gebreslassie et al., 2012; Hmida et al., 2018). Harmful emissions and fossil fuel consumption can be significantly reduced using renewable energy (Shoaib et al., 2018). Thus, solar cooling systems are a viable alternative for reducing primary energy use and are an excellent solution for today's energy challenges (Dhindsa, 2020; Li et al., 2019) and as Tiwari et al. stated, solar energy is a clean, unlimited and environmentally-friendly energy source (Tiwari et al., 2020). Solar cooling systems are of particular importance when the cooling load of a building is compared to the intensity of solar radiation. Due to the system's reliance on thermal energy for cold production, solar energy for industrial and domestic applications continues to be the greatest technology for refrigeration and air conditioning, particularly in hotter areas (Cascetta et al., 2017; Salilih et al., 2020). Two common types of solar cooling systems do exist. The first type converts sunlight directly into heat using solar thermal collectors driven

*Corresponding Author's Email: massad@sharjah.ac.ae (M. El Haj Assad)
URL: https://www.jree.ir/article_155116.html

Please cite this article as: Hmida, A., Lamrani, A., El Haj Assad, M., Aryanfar, Y., & Garcia Alcaraz, J.L. (2023). Numerical simulation of a solar cooling system based on variable-effect NH_3-water absorption chiller using TRNSYS. *Journal of Renewable Energy and Environment (JREE), 10*(3), 59-66. https://doi.org/10.30501/jree.2022.326640.1318

2423-7469/© 2023 The Author(s). Published by MERC. This is an open access article under the CC BY license (https://creativecommons.org/licenses/by/4.0/).

by the solar ejector, desiccant, adsorption, or absorption systems (Salilih et al., 2020; Ullah et al., 2013). The second category involves a photovoltaic module that powers the system (Ullah et al., 2013), thermoelectric refrigeration (TEC), and PV compression refrigeration (Salilih et al., 2020). Since compression systems require high-grade energy, alternative cooling systems such as absorption cooling systems are receiving greater attention than ever (Altun & Kilic, 2020).

Solar cooling absorption systems are a reliable and cost-effective alternative to other thermally operated refrigeration cycles because they can be powered by low-grade thermal energy, have a low total cost, and enjoy a higher performance coefficient than other thermally operated refrigeration cycles (Mazzei et al., 2014; Shoaib et al., 2018). Additionally, solar absorption refrigeration systems utilize ammonia, water, and lithium bromide as environmentally-friendly refrigerants, have no global warming potential, do not contribute to ozone layer depletion, and operate at a lower temperature than other vapor compressor refrigerants (Dhindsa, 2020; Gebreslassie et al., 2012).

Numerous studies and investigations in solar thermal cooling have been conducted experimentally and theoretically, examining a variety of situations, including solar thermal collectors, and demonstrating each system's efficiency and technical viability (Li et al., 2019; Lugo et al., 2019). (Kalogirou et al., 2016) conducted an exergy analysis of a solar cooling system using Flat Plate Collectors (FPCs). Zambolin and Del Col (Zambolin & Col, 2012) examined the same system using Evacuated Tubular Collectors (ETCs), and (Li et al., 2013) studied also the same system using Compound Parabolic Concentrating collectors (CPCs). Altun and Kilic concluded through TRNSYS simulation and the use of evacuated tube solar collectors (ETC) instead of flat plate collectors (FPC), a decrease in auxiliary energy consumption and an increase in the useful energy can be gained from collectors. (Altun & Kilic, 2020).

(Figaj et al., 2021) investigated a solar dish-concentrating system with thermal collectors experimentally and numerically using a dynamic simulation of solar cooling installation. The TRNSYS program was used to perform a computer simulation of the dynamic operation of the solar heating and cooling system. The goal of this study was to determine the amount of heat formed by sorption chillers that are used for heating and cooling. Numerous configurations, locations, and periods were studied to determine the energy and economic performance of the system.

Jalalizadeh et al. researched "Building Integrated Photovoltaic Thermal Collector (BIPVT)", a technology to simultaneously generate heat and electricity for the building. They concluded that integration of PVT with the building increased the Space Cooling (SC) load by 5 % and decreased the space heating (SH) load by 3 % (Jalalizadeh et al., 2021).

Tashtoush et al. also developed a simulation program using TRNSYS-EES software to design the solar collector system components and evaluate the performance of solar ejector cooling systems. To produce 7 kW for the cooling system, an evacuated tube solar collector was chosen with an area of 60-70 m^2 and a solar fraction of 0.52-0.542 (Tashtoush et al., 2015). Space cooling has been a focus of many researchers using solar energy for air conditioning systems (Rahman et al., 2019), geothermal energy for powering single-effect water/lithium bromide absorption chiller (El Haj Assad et al., 2021), and solar vapor compression refrigeration cycle (Aryanfar et al., 2022).

Numerous experimental research studies on solar thermal technologies have evaluated and designed them. Nonetheless, numerical simulation was used to optimize the system as several scenarios might be examined due to its cost. According to (Lugo et al., 2019), the creation of simulation software enables the identification of the behavior of various variables under various operating situations.

This paper aims to develop a model to determine the feasibility of a solar refrigeration system for a low-temperature room with a cooling capacity of 11 kW using an evacuated solar collector (ETC). The system maintains a constant temperature of 2 °C in the cold room. To predict the performance of the cooling thermally driven system for various climatic and seasonal changes in the year, a configuration model based on TRNSYS (Transient Simulation Program) is constructed and simulated. The components and connections from the standard TRNSYS library are used. The performance of the ETC under the climatic conditions of Gabes, Tunisia (33°53'N, 10°6'E) has been evaluated. The optimal collector tilt for the ETC collector was determined to be around 30°-45° (ETC), and other effects of operating parameters were evaluated and presented in the paper.

2. SYSTEM DESCRIPTION

Absorption refrigeration machines are the most used thermally driven cooling systems (Asim et al., 2016). The most used combination of fluids for low-temperature applications in absorption systems is ammonia-water (NH_3-H_2O). The absorbent (H_2O) on the low-pressure side absorbs the evaporating refrigerant (NH_3). An 8-kW solar-powered absorption system provides the cooling energy required for a cold room under different weather conditions in the region of Gabes. The cycling fluid in the system is the NH_3-H_2O. Figure 1 represents the schematic view of the model where the absorption system is the main system of the model, and it is interconnected with three subsystems: the first is the solar subsystem that consists of solar collectors and the storage tank where the ETC receives solar irradiation and is converted into thermal heat energy, which can be used to supply heat for the water tank. The second is the hot fluid subsystem, where the storage tank supplies the absorption chiller with hot water to heat the generator. The third is the load subsystem connecting the absorption chiller to the cold room (Altun & Kilic, 2020).

Low-pressure NH_3 vapor from the evaporator is dissolved in H_2O in the absorber (10) under an intermediate temperature up to 45 °C. Then, using an ordinary liquid pump (1), the resulting solution is pumped to high pressure (2, 3). The additional heat provided by the solar collector separates the NH_3 from the solution in the generator (120 °C) and then, directs it to the condenser (45 °C) (7). In this way, the NH_3 vapor is thermally compressed. Liquified refrigerant getting out from the condenser can then be expanded from this high-pressure zone (around 20 bars) (8) to the low-pressure evaporator (around 4 bars) (9). The energy required for refrigerant evaporation is extracted from the environment to be cooled. The refrigerant is then directed to the absorber (10) (Hmida et al., 2018).

On the other hand, the weak solution (with a low percentage of ammonia) is returned to the absorber (4) through a heat exchanger to recover the heat (5).

This study concentrates on the first subsystem. The thermodynamic study of the absorption chiller, as well as the cold room design, was conducted in previous studies (Hmida et al., 2017, Hmida et al., 2018, Hmida et al., 2019).

3. Modeling in TRNSYS

The model is implemented into the TRNSYS software environment, as presented in Figure 2. TRNSYS (Transient System Simulation) is an application used to model and simulate the behavior and performance of systems in a transient manner. The first step in TRNSYS simulation is identifying the individual components that better describe the performance of the whole system (Altun & Kilic, 2020; Tiwari et al., 2020).

The TRNSYS solver performs several iterations until the inputs to all of the "Types" remain stable at each time step of the simulation.

The components used in the TRNSYS model are explained below. In order to achieve greater efficiency, the tube collectors (Type 538) evacuated from the "Tess library" were selected for the system, and then the collector circulating pump was chosen as Type 3b. An auxiliary heater (Type 4a) was used to supply hot water when solar irradiation becomes insufficient, and typical meteorological year (Type 109-TMY2) data of the region of Gabes were used from the Meteonorm database of the TRNSYS library.

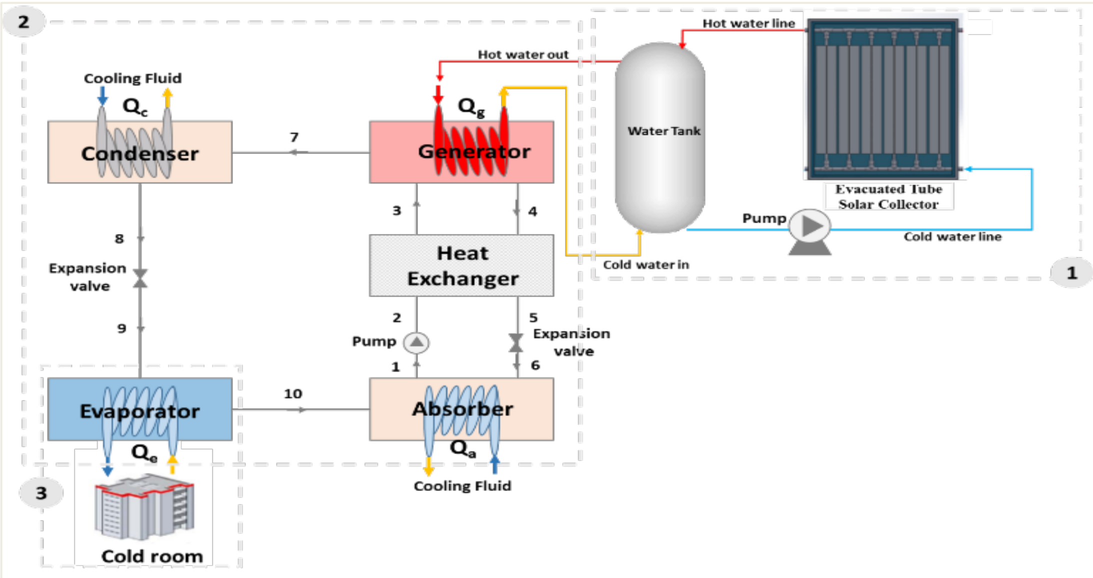

Figure 1. The schematic diagram of the solar absorption machine

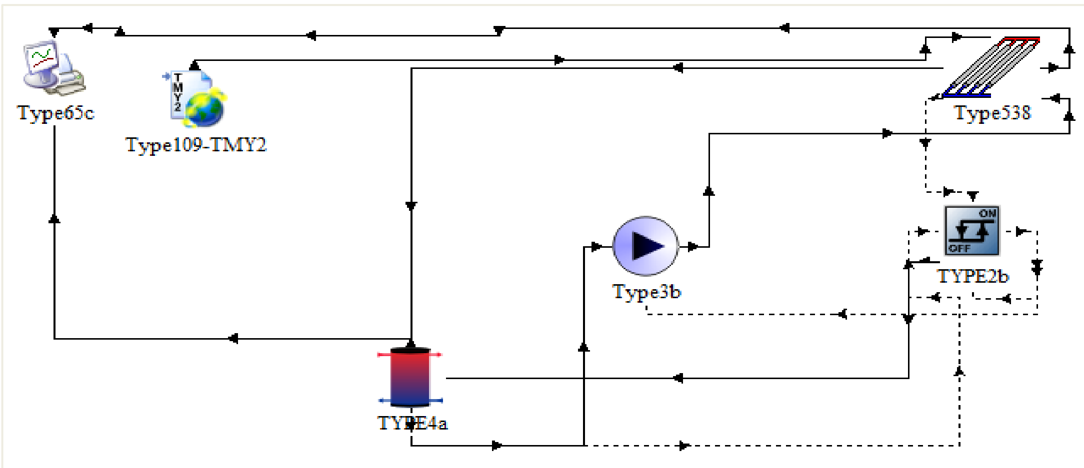

Figure 2. The solar installation with TRNSYS

4. SOLAR COLLECTOR DESIGN

4.1. Determination of the surface

Knowing that the helpful power of the solar collector depends on its surface and the local-global radiation, the needed area of the solar collector is determined using Eq. (1) to provide heat for the generator (Dezfouli et al., 2022).

$$A_c = \frac{P_u}{G \times \beta - G \times K \times (T_{fm} - T_e)} \quad (1)$$

$$P_u = 1.1 \times Q_g \quad (2)$$

where:
P_u: Useful power (kW)
Q_g: Heat absorbed by the generator (kW)
K: Heat loss coefficient (between 1.5 and 3 W/m² °C)
β: Optical coefficient for evacuated tube collector (between 0.5 and 0.8)
G: Global radiation (W/m²).

The global radiation is extracted from the climatic information of the study site. The absence of meteorological measuring stations requires establishing computational models based on empirical methods to estimate solar flux on a local scale. These models can only be applicable after comparing and validating the experimental data during all the year's seasons.

4.2. Global radiation

4.2.1. Capderou model

The well-known Capderou model was proposed to calculate the direct and diffuse radiation received on a plane (Hamed et al., 2014). On the horizontal plane, the global radiation was given as the direct radiation and the diffuse radiation sum:

$$G_h = I_h + D_h \tag{3}$$

The following equations, respectively, give direct light-sky radiation and diffuse radiation on a horizontal plane:

$$I_h = C\alpha \sin(h)\exp\left(-FTL\left(0{,}9+\frac{9{,}4}{0{,}89^z}\sin(h)\right)^{-1}\right) \tag{4}$$

$$D_h = C\exp\left(-1+1{,}06\log(\sin(h))+a-\sqrt{a^2+b^2}\right) \tag{5}$$

4.2.2. Eufrat model

Eufrat proposed other equations for the calculation of direct (I_i), diffuse (D_i), and global radiation (G_i) received on an inclined plane (Hamed et al., 2014). It can be obtained as:

$$I_i = C\alpha\times\exp\left(-\frac{AM\times FTL}{0{,}9\,AM+9{,}4}\right) \tag{6}$$

$$G_i=\alpha(1270-56\,FTL)(\sin(h))^{\left(\frac{FTL+36}{33}\right)} \tag{7}$$

$$D_i = G_i - I_i\sin(h) \tag{8}$$

where:
C: Solar constant (1367 W / m²)
FTL: Linke's trouble factor
AM: Atmospheric mass
h: Height of the sun
α: Correction of the distance between earth and sun.

4.2.3. Perrin Brinchambaut model

Perrin Brinchambaut proposed the following equations for the calculation of direct (I_i), diffuse (D_i), and global radiations (G_i) received on an inclined plane as follows (Hamed et al., 2014):

$$D_i = A'\cos(\theta)\exp\left(-\frac{1}{B'\sin(h+2)}\right) \tag{9}$$

$$I_i = \left(\frac{1+\cos(\beta)}{2}\right)D_h + \left(\frac{1-\cos(\beta)}{2}\right)\rho G_h \tag{10}$$

The direct radiation I_h, global radiation G_h, and the albedo ρ for a horizontal plane are respectively expressed as follows:

$$I_h = A''(\sin(h))^{0{,}4} \tag{11}$$

$$G_h = A'''(\sin(h))^{B''} \tag{12}$$

$$\rho \begin{cases} = 0.9 \text{ to } 0.8 \text{ snow} \\ = 0.8 \text{ to } 0.4 \text{ Clair ground} \\ = 0.4 \text{ to } 0.2 \text{ greeneries} \end{cases} \tag{13}$$

where A', A'', A''', B', and B'' are constants depending on the state of the atmosphere given in Table 1.

Table 1. Values of constants according to the nature of the sky

Nature of the sky	A' (W/m²)	B'	A'' (W/m²)	A''' (W/m²)	B''
Major blue	1300	6	87	1150	1.15
Light blue	1230	4	125	1080	1.22
Milky blue	1200	2.5	187	990	1.25

To assess the accuracy of these correlations, two statistical tests were used: the relative deviation (or error) (ER) and the average relative deviation (ERM). Low values of ER and ERM are desirable; they are calculated by the following relationships (Hamed et al., 2014):

$$ER(\%) = 100\times\left(\frac{Experimental.Value - Theoretical.Value}{Experimental.Value}\right) \tag{14}$$

$$ERM(\%) = \left(100\times\sum_k^n\left|\frac{Experimental.Value_k - Theoretical.Value_k}{Experimental.Value_k}\right|\right)\Big/ n \tag{15}$$

5. RESULTS AND DISCUSSION

5.1. Site study

This study was elaborated to produce cold for 109 m^3 room to preserve food (Hmida et al., 2019). The refrigeration system was driven by an absorption machine and installed in Gabes, a southern region of Tunisia (33°53'N, 10°6'E) with high solar potential and a long insolation period, particularly in June, July, and August months. In this period, refrigeration reaches its peak demand. Figure 3 exhibits the insolation data of the region of Gabes for twelve months based on the data provided by Meteonorm software. As seen, the summer season (June, July, and August) has the longest months with an average of 12 hours of sunshine and average radiation of 215kWh/m², as depicted in Figure 4, reaching an average temperature of 35 °C in July (Figure 5).

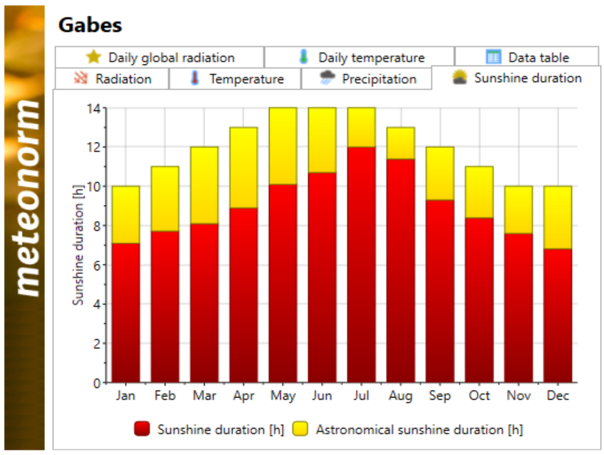

Figure 3. Sunshine period in the region of Gabes by Meteonorm 8

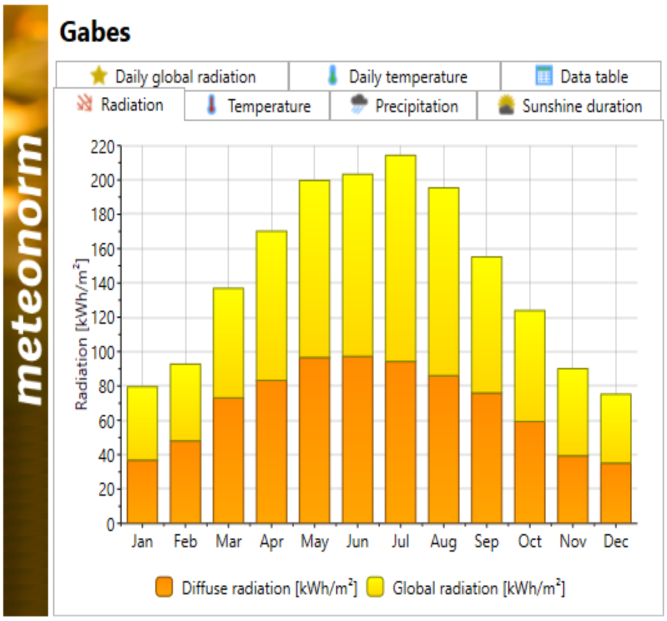

Figure 4. The region of Gabe's radiation by Meteonorm 8

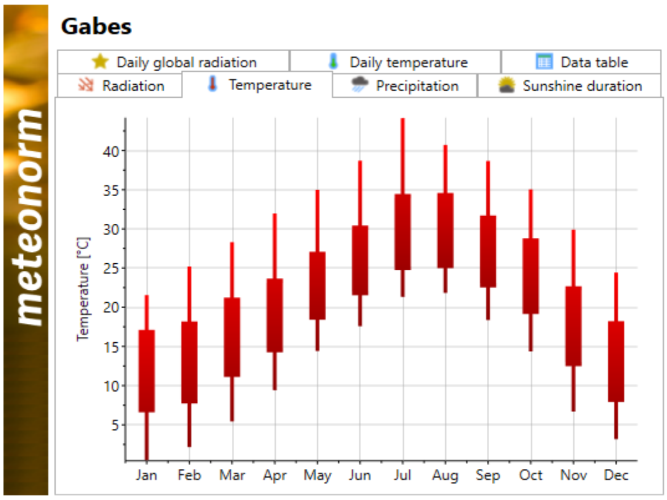

Figure 5. The average temperature of the region of Gabes by Meteonorm 8

Figure 6 shows the flowchart used in the calculation for the proposed solar/cooling system.

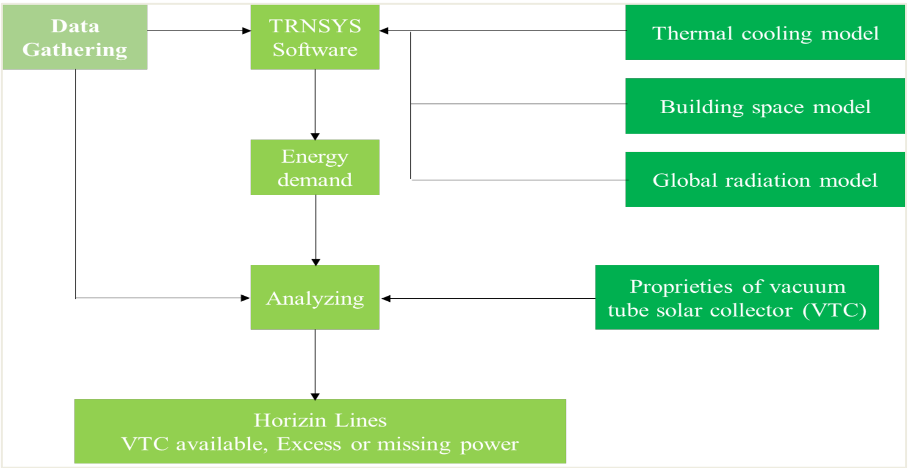

Figure 6. The flowchart of the study

The heat provided to the generator of the absorption machine is related to the ETC surface, which depends on the available global radiation. A comparison between the presented models for global radiation calculation (Eqs. 3-13) and the data provided by the National Institute of Meteorology in Tunisia (INM) was conducted.

Even though the experimental results of the global radiation for the year 2020 were not stable, as shown in Figure 7, the Brinchambaut model seems to be the most convenient in describing the real global radiation with an error of up to 3.16 % compared to 17.4 % and 20 % for the Eufrat and Capderou models, respectively.

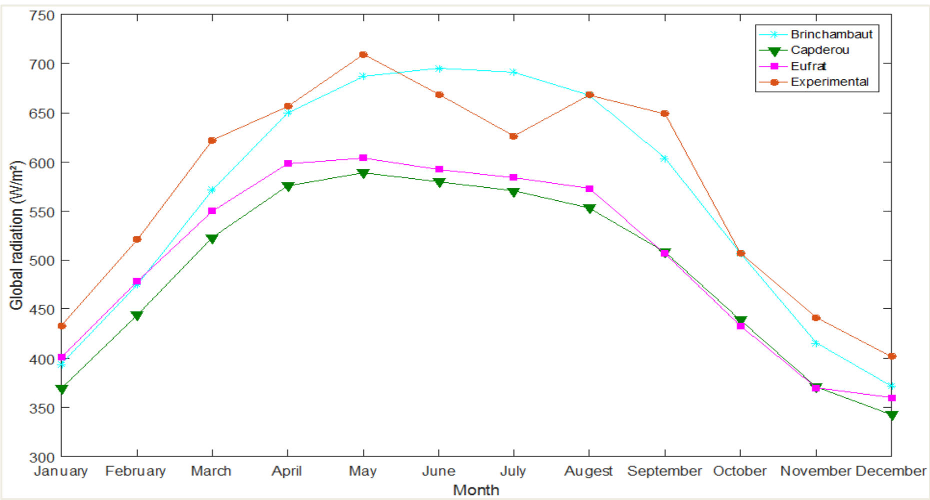

Figure 7. Comparison between the numerical models of the global radiation determination and the experimental data of the INM

5.2. TRNSYS simulation of the solar installation

The global radiation of the region of Gabes has allowed running the TRNSYS simulation. The system was simulated during the period of refrigeration need, that is, between the first of March (hour number 1416) and the last day of October (hour number 6421). As presented in Table 2, the technical characteristics of the solar system were chosen as follows: water as a heat transfer fluid (HTF) with a flow rate of 117 kg/h, the solar collector area is 21 m², producing 11 kW useful power and an average temperature on the surface up to 130 °C.

The temperature fluctuation presented in Figure 8 was due to the variation of the global radiation measured on the surface of the ETC, as presented in Figure 9. oriented to the South with a tilt equal to 45°, and 3 m²/collector as a solar collector area.

Table 2. Technical characteristics of the solar collector

VTC Parameters	
Collector area (m²)	3
Number of solar collectors in series	7
HTF Flowrate (kg/h.m²)	117
Efficiency slope (kJ/hr.m².°K)	15

In order to validate the simulation results using TRNSYS, the needed surface area using solar collector characteristics available in the market was calculated. As shown in Table 3, the needed surface area for VITSOL 200T, THERMOMAX HP100/200, and THERMOMAX DF100 is between 21 m² and 22 m², which is the surface found with TRNSYS simulation with a relative error up 2.8 %.

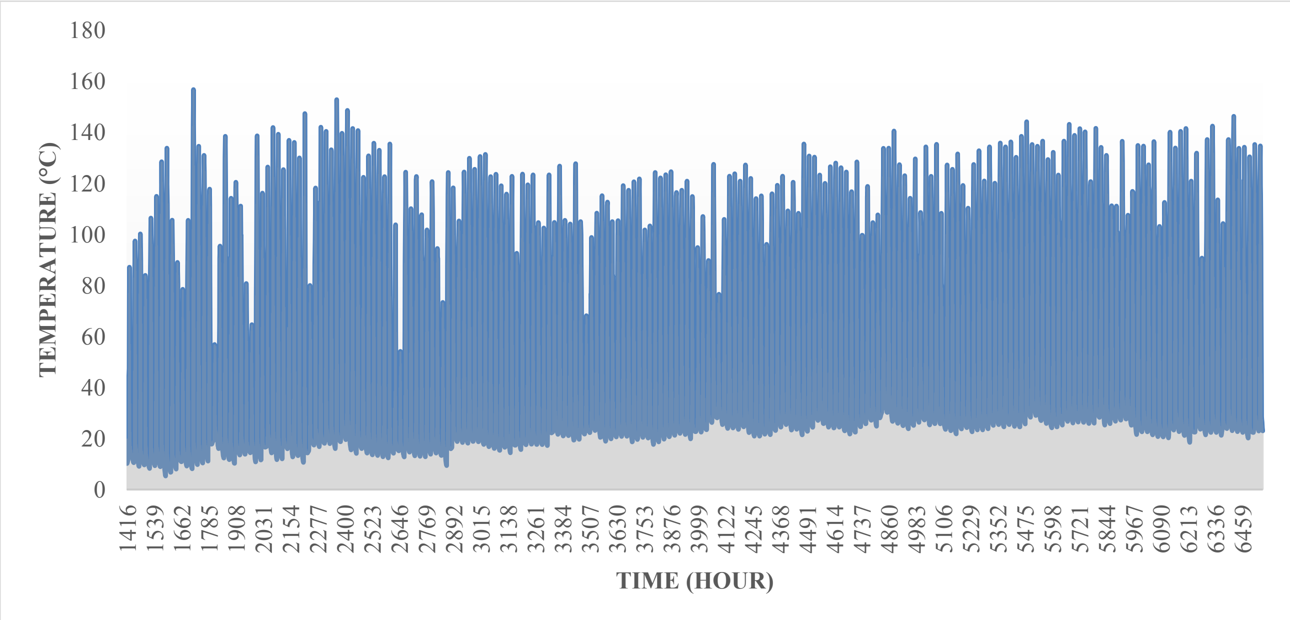

Figure 8. Hourly Temperature variation registered on the surface of the VTC

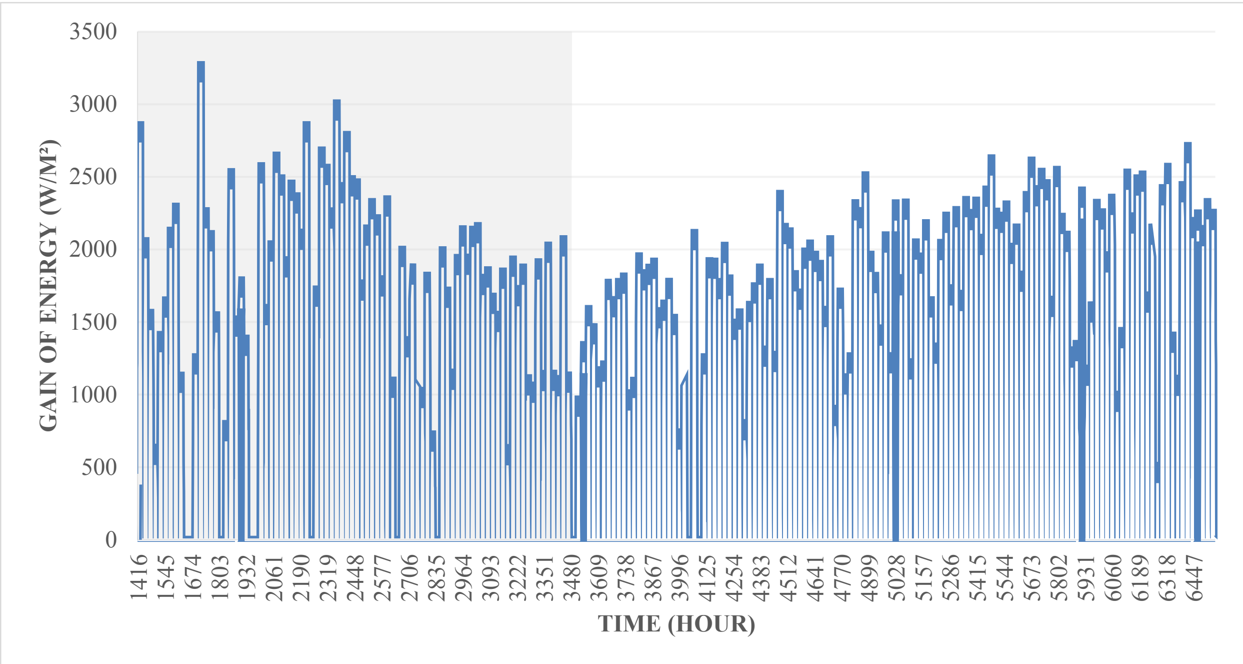

Figure 9. Global radiation fluctuation on the surface of the ETC

Table 3. Collector area and number

Collector type	Availability (m²)	K	β	S (m²)	N
Vitsol 200T	1,26	1,522	0.785	21.47	17
	1,51	1.443	0.801	20.59	14
	3,03	1.103	0.801	19.3	7
Thermomax HP100	3	1	0.739	20.85	7
Thermomax HP200	2	1.36	0.761	21.62	11
	3	1.36	0.761	21.62	7
Thermomax DF100	2	1.45	0.773	21.59	11
	3	1.45	0.773	21.59	7

6. CONCLUSIONS

Due to environmental problems, this study attempted to find a solution for better food storage using an available and renewable heat source. Since a good solar potential characterized the South of Tunisia, solar energy was chosen as the heat generator for the absorption machine. A simulation using TRNSYS software of a solar-based single-effect NH_3-H_2O absorption refrigeration system in a low-temperature room having a cooling capacity of 11 kW was carried out. The cold room temperature was kept at 2 °C. The weather data of the region of Gabes at latitude 33.53 N and longitude 10.6 E, collected in the year 2020, were used in the simulation.

Solar collector type, area, storage tank, and the flow rate through the cycle were investigated.

The performance of the solar collector was assessed to meet the desired outlet temperature adequate to run 11 kW cooling cycle to meet the cooling load demand. The energy requirements of 11 kW cooling system are best met with an evacuated tube solar collector having an area of 21 m^2 and a flow rate of 117 kg/h to provide heat for the generator in the refrigeration system.

The simulation result demonstrated that the temperature on the collector surface varied between 120 °C and 170 °C due to the global radiation fluctuation at the peak solar radiation in July. The required area of the ETC was found to be 21 m^2. This number can be reduced when considering the solar radiation of the summer months. The application of the sun as a heat source makes such systems economically alternative.

Other studies can follow this research by designing more environmentally-friendly buildings that meet the standards. With harmless cooling and heating load, those buildings tend to grant people comfort. In this context, simulations for air conditioning and heating systems applied to green buildings are established.

7. ACKNOWLEDGEMENT

This work was supported by the Applied Thermodynamics Research Laboratory (LR 18ES33), the University of Gabes, Tunisia. The authors would like to exspress their acknowledgment to the Ministry of Higher Education and Scientific Research of Tunisia.

NOMENCLATURE

AM	Atmospheric mass
C	Solar constant
CPCs	Parabolic concentrating collectors
D	Diffuse radiation (W/m²)
ETCs	Evacuated tubular collectors
FPCs	Flat plate collectors
FTL	Linke's trouble factor
G	Global radiation (W/m²)
$GtCO_2$	Gigaton of carbon diode
h	Height of the sun
HWST	Hot water storage tanks
I	Direct radiation (W/m²)
K	Heat loss coefficient (W/m^2 °C)
NH_3	Ammonia
P_u	Useful power (W)
PV	Photovoltaic panel
Q_g	Heat absorbed by the generator (W)
SAC	Solar adsorption cooling system
TRNSYS	Transient System Simulation TOOL
VTC	Vacuum Tube Collector
Greek letters	
α	Correction of the distance earth-sun
β	Optical coefficient for evacuated tube collector
ρ	The albedo
Subscripts	
h	Horizontal plane
i	Inclined plane

REFERENCES

1. Almutairi, K., Alhuyi, M., & Salem, M. (2022). A review on applications of solar energy for preheating in power plants. *Alexandria Engineering Journal*, *61*(7), 5283-5294. https://doi.org/10.1016/j.aej.2021.10.045
2. Altun, A.F., & Kilic, M. (2020). Economic feasibility analysis with the parametric dynamic simulation of a single effect solar absorption cooling system for various climatic regions in Turkey. *Renewable Energy*, *152*, 75-93. https://doi.org/10.1016/j.renene.2020.01.055
3. Aryanfar, Y., Assad, M.E.H., Khosravi, A., Atiqure, R.S.M., Sharma, S., Alcaraz, J.L.G., & Alayi, R. (2022). Energy, exergy and economic analysis of combined solar ORC-VCC power plant. *International Journal of Low-Carbon Technologies*, *17*, 196-205. https://doi.org/10.1093/ijlct/ctab099
4. Asim, M., & Kanan, S. (2016). TRNSYS simulation of a solar cooling system for the hot climate of Pakistan. *Energy Procedia*, *91*, 702-706. https://doi.org/10.1016/j.egypro.2016.06.233
5. Cascetta, F., Lorenzo, R. Di, Nardini, S., & Cirillo, L. (2017). A TRNSYS simulation of a solar-driven air refrigerating system for a low-temperature room of an agro-industry site in the Southern of Italy. *Energy Procedia*, *126*, 329-336. https://doi.org/10.1016/j.egypro.2017.08.259
6. *Cooling – Analysis - IEA*. Retrieved February 3, 2022, from https://www.iea.org/reports/cooling
7. Dezfouli, M.M.S., Sopian, K., & Kadir, K. (2022). Energy and performance analysis of solar solid desiccant cooling systems for energy efficient buildings in tropical regions. *Energy Conversion and Management: X*, *14*(November 2021), 100186. https://doi.org/10.1016/j.ecmx.2022.100186

8. Dhindsa, G.S. (2020). Review on performance enhancement of solar absorption refrigeration system using various designs and phase change materials. *Materials Today: Proceedings*, *37*, 3332-3337. https://doi.org/10.1016/j.matpr.2020.09.125

9. El Haj Assad, M., Sadeghzadeh, M., Ahmadi, M.H., Al-Shabi, M., Albawab, M., Anvari-Moghaddam, A., & Bani Hani, E. (2021). Space cooling using geothermal single-effect water/lithium bromide absorption chiller. *Energy Science and Engineering*, *9*(10), 1747-1760. https://doi.org/10.1002/ese3.946

10. Figaj, R., Zo, M., & Coil, F. (2021). Experimental and numerical analysis of hybrid solar heating and cooling system for a residential user. *Renewable Energy*, *172*, 955-967. https://doi.org/10.1016/j.renene.2021.03.091

11. Gebreslassie, B.H., Groll, E.A., & Garimella, S.V. (2012). Multi-objective optimization of sustainable single-effect water/Lithium Bromide absorption cycle. *Renewable Energy*, *46*, 100-110. https://doi.org/10.1016/j.renene.2012.03.023

12. *Global energy and CO_2 emissions in 2020 – Global energy review 2020 – Analysis – IEA*. (2022). Retrieved February 3, 2022, from https://www.iea.org/reports/global-energy-review-2020/global-energy-and-co2-emissions-in-2020

13. Hamed, M., Fellah, A. & Ben Brahim, A. (2014). Parametric sensitivity studies on the performance of a flat plate solar collector in transient behavior. *Energy Conversion and Management*, *78*, 938-947. https://doi.org/10.1016/j.enconman.2013.09.044

14. Hmida, A., Chekir, N., & Ben Brahim, A. (2017). Solar absorption refrigerator. *International Conference on Green Energy and Conversion Systems, GECS 2017,* IEEE, Hammamet, Tunisia. https://doi.org/10.1109/GECS.2017.8066193

15. Hmida, A., Chekir, N., & Ben Brahim, A. (2018). Performance of an absorption refrigerator using a solar thermal collector. *International Journal of Energy and Power Engineering*, *12*(10), 787-792. https://doi.org/10.5281/zenodo.1475032

16. Hmida, A., Chekir, N., Laafer, A., El Amine Slimani, M. & Ben Brahim, A. (2019). Modeling of cold room driven by an absorption refrigerator in the south of Tunisia : A detailed energy and thermodynamic analysis. *Journal of Cleaner Production*, *211*, 1239-1249. https://doi.org/10.1016/j.jclepro.2018.11.219

17. Jalalizadeh, M., Fayaz, R., Delfani, S., & Jafari, H. (2021). Dynamic simulation of a trigeneration system using an absorption cooling system and building integrated photovoltaic thermal solar collectors. *Journal of Building Engineering*, *43*(March), 102482. https://doi.org/10.1016/j.jobe.2021.102482

18. Kalogirou, S.A., Karellas, S., Braimakis, K., & Stanciu, C. (2016). Exergy analysis of solar thermal collectors and processes. *Progress in Energy and Combustion Science*, *56*, 106-137. https://doi.org/10.1016/j.pecs.2016.05.002

19. Li, X., Dai, Y.J., Li, Y., & Wang, R.Z. (2013). Comparative study on two novel intermediate temperature CPC solar collectors with the U-shape evacuated tubular absorber. *Solar Energy*, *93*, 220-234. https://doi.org/10.1016/j.solener.2013.04.002

20. Li, X., Lin, A., Young, C., Dai, Y., & Wang, C. (2019). Energetic and economic evaluation of hybrid solar energy systems in a residential net-zero energy building. *Applied Energy*, *254*(May), 113709. https://doi.org/10.1016/j.apenergy.2019.113709

21. Lugo, S., García-Valladares, O., Best, R., Hernández, J., & Hernández, F. (2019). Numerical simulation and experimental validation of an evacuated solar collector heating system with gas boiler backup for industrial process heating in warm climates. *Renewable Energy*, *139*, 1120-1132. https://doi.org/10.1016/j.renene.2019.02.136

22. Mazzei, M.S., Mussati, M.C., & Mussati, S.F. (2014). NLP model-based optimal design of LiBr-H_2O absorption refrigeration systems. *International Journal of Refrigeration*, *38*(1), 58-70. https://doi.org/10.1016/j.ijrefrig.2013.10.012

23. Pan, Q., Peng, J., & Wang, R. (2020). Application analysis of adsorption refrigeration system for solar and data center waste heat utilization. *Energy Conversion and Management*, *228*, 113564. https://doi.org/10.1016/j.enconman.2020.113564

24. Rahman, S., Issa, S., Said, Z., El Haj Assad, M., Zadeh, R., & Barani, Y. (2019). Performance enhancement of a solar powered air conditioning system using passive techniques and SWCNT /R-407c nano refrigerant. *Case Studies in Thermal Engineering*, *16*., 100565 https://doi.org/10.1016/j.csite.2019.100565

25. Salilih, E.M., Birhane, Y.T., & Abu-hamdeh, N.H. (2020). Performance prediction of a solar refrigeration system under various operating pressure of evaporator and condenser. *Solar Energy*, *209*(March), 485-492. https://doi.org/10.1016/j.solener.2020.09.033

26. Shoaib, M., Khan, A., Waheed, A., Talha, T., Wajahat, M., & Sarfraz, F. (2018). Configuration based modeling and performance analysis of single e ff ect solar absorption cooling system in TRNSYS. *Energy Conversion and Management*, *157*(September 2017), 351–-63. https://doi.org/10.1016/j.enconman.2017.12.024

27. Sudhakar, K., Jenkins, M.S., Mangal, S., & Priya, S.S. (2019). Modelling of a solar desiccant cooling system using a TRNSYS-MATLAB co- simulator : A review. *Journal of Building Engineering*, *24*(February), 100749. https://doi.org/10.1016/j.jobe.2019.100749

28. Tashtoush, B., Alshare, A., & Al-rifai, S. (2015). Hourly dynamic simulation of solar ejector cooling system using TRNSYS for Jordanian climate. *Energy Conversion and Management*, *100*, 288-299. https://doi.org/10.1016/j.enconman.2015.05.010

29. Tiwari, A.K., Gupta, S., Joshi, A.K., Raval, F., & Sojitra, M. (2020). TRNSYS simulation of flat plate solar collector based water heating system in Indian climatic condition. *Materials Today: Proceedings*, *46,* 5360-5365. https://doi.org/10.1016/j.matpr.2020.08.794

30. Ullah, K.R., Saidur, R., Ping, H.W., Akikur, R.K., & Shuvo, N.H. (2013). A review of solar thermal refrigeration and cooling methods. *Renewable and Sustainable Energy Reviews*, *24*, 499-513. https://doi.org/10.1016/j.rser.2013.03.024

31. Zambolin, E. and Del Col, D. (2012). An improved procedure for the experimental characterization of optical ef fi ciency in evacuated tube solar collectors. *Renewable Energy*, *43*, 37-46. https://doi.org/10.1016/j.renene.2011.11.011

JREE: Vol. 10, No. 3, (Summer 2023) 67-80

Journal of Renewable Energy and Environment

Journal Homepage: www.jree.ir

Materials and Energy Research Center

MERC

Technical Note

Analysis and Evaluation of the Formation of a Heat Island in Tehran During Three Decades

Mohammad Javad Amiri*, Ali Sayyadi

Faculty of Environment, College of Engineering, University of Tehran, Tehran, Iran.

P A P E R I N F O

Paper History:
Received: 13 July 2022
Revised: 04 September 2022
Accepted: 09 September 2022

Keywords:
Land Use Map,
NDVI,
LST,
Remote Sensing

A B S T R A C T

The rising temperature of the earth's surface and the formation of heat islands in megacities have become two of the biggest environmental threats. This compound problem affects urban climatology, including urban vegetation and air pollution, human health, and the environment, including the group of vulnerable members of the society and public health, leading to the growing death rate. Hence, the purpose of this study is to investigate the leading causes of temperature changes and the development of a thermal island in the city of Tehran following the expansion of this metropolis in recent decades. This research uses thermal remote sensing and GIS techniques to analyze information from Landsat satellite images in (TM-ETM-TIRS) sensors from 1984 to 2020. The results of the research indicated that the surface temperature of the city of Tehran during the years 1984 to 1996, 1998 to 2008, and 2010 to 2020 experienced a relative increase in the summer and winter seasons. In the first decade, the average temperature of the green layer was -7, while the temperature of the magenta and red layers were 20 and 25 degrees, respectively. In the second decade, the average temperatures of the green and dark green classes were -1 and 3 while they were 23 and 27 degrees for the magenta and red classes, respectively. In the third decade, the average temperatures of the green and dark green classes were -1 and 3, and thost of the magenta and red layers increased to 28 and 31 degrees, respectively. Furthermore, the analysis of vegetation cover based on the NDVI index pointed to the continuing reduction of vegetation in the studied years. Regarding the direct correlation between the heat island and vegetation and the concentration of the heat island in the city center, further measures must be taken and the vegetation cover should be increased to reduce the heat island. The city center needs to be decentralized as part of the remedy via proper urban design and planning.

https://doi.org/10.30501/jree.2022.349418.1396

1. INTRODUCTION

Urban heat island is a situation that occurs in cities or metropolises primarily due to human-made changes on the earth's surface when urban areas experience higher temperatures than their rural areas (Mendez-Astudillo et al., 2021). Continuous extension of artificial surface including road constructions and building constructions as well as changes in radiation flux and climate have already intensified urban heat and formed urban hot spots (Tepanosyan et al., 2021). The expansion of artificial phenomena causes the creation of urban heat islands (El-Hadidy, 2021). Urban materials such as buildings, roads, and other asphalted areas are replaced by natural vegetation that leads to heat islands (Macintyre et al., 2021; Kabano et al., 2021). This temperature increase starts from 2 degrees and can be increased to several degrees (Harun et al., 2020).

The heat island causes irreversible damage to human life and our existing environment; the urban heat island is the most significant contributing factor affecting urban climatology, including urban vegetation and air pollution (Li et al., 2022), including vulnerable groups, human health, and nature. It affects society (Wang et al., 2021) and public health (Sekertekin & Zadbagher, 2020; Vasenev et al., 2021) and increases death toll (Koopmans et al., 2021).

Land Surface Temperature (LST) is a key factor related to the earth's surface used at different scientific levels, such as weather forecast, hydrology, agriculture, public health, environmental science, etc. (Wei et al., 2021). It is also an important factor in global climate change, energy flux between the earth's surface and the atmosphere system, and the water cycle; therefore, its association with the environment has been widely studied (Ye et al., 2021; Gupta et al., 2019). LST is a key factor that controls physical, chemical, and biological processes at the interface between the earth and the atmosphere and greatly affects the state of vegetation and soil water (Chi et al., 2020).

Remote sensing is one of the main sources for estimating the amount of solar energy and preparing a map of LST in case of a lack of weather stations, specifically in land areas, oceans, and arid and semi-arid regions (Chi et al., 2020). The spatial resolution of sensors and the algorithms used to calculate solar

*Corresponding Author's Email: mjamiri@ut.ac.ir (M.J. Amiri)
URL: https://www.jree.ir/article_158621.html

Please cite this article as: Amiri, M.J., & Sayyadi, A. (2023). Analysis and evaluation of the formation of a heat island in Tehran during three decades. *Journal of Renewable Energy and Environment (JREE)*, *10*(3), 67-80. https://doi.org/10.30501/jree.2022.349418.1396.

2423-7469/© 2023 The Author(s). Published by MERC. This is an open access article under the CC BY license (https://creativecommons.org/licenses/by/4.0/).

radiation variables, vegetation indices, and land surface temperature are all factors measured using GIS remote sensing data (Al-Masaodi & Al-Zubaidi, 2021). Remote Sensing (RS) is a suitable method for directly acquiring experimental data and an effective means for environmental improvement, management, and monitoring urbanization dynamics. Geographical Information System (GIS) provides a spatial analysis, modeling, and mapping method. Many researchers have combined RS with GIS (Liu et al., 2021). Remote sensing satellites provide a simple way to investigate thermal differences between urban and rural areas, LST retrieval, and urban heat islands (Ahmed, 2017). The development of thermal remote sensing offers a good solution to the shortcomings observed in the conventional monitoring of urban heat islands. Such techniques can effectively quantify the distribution characteristics of urban heat islands and periodic and dynamic environmental changes (Wang et al., 2019). Today, a new generation of thermal remote sensing sensors such as MODIS (Medium Resolution Imaging Spectrometer), AVHRR (Very Advanced Resolution Radiometer), and ASTER (Medium Resolution Sensors) is used. Also, Landsat is practically free, and the oldest records in the archive have been used since the 1970s (Gadrani et al.,2018). The capital of Iran has experienced rapid urban development since the 1990s. Tehran is a key center for production, residence, trade, distribution, and transportation in Iran with a population of about 12 million people and is the first and most populous city in Iran (Mousavi-Baygi et al., 2010). The accelerated urban development of Tehran and lack of proper planning have important effects on its thermal environment. The political and geographical conditions of Tehran city and the damage of the heat island to humans and the environment have caused this research to investigate the process of the heat island using remote sensing.

1.1. Literature review

A review of the relevant literature and records shows that the term heat island was first proposed by Howard about a century ago, in 1833. Followed by further research, urbanization has caused significant changes in the meteorological parameters and features of the earth's surface and, as a result, has caused many changes in the local weather and climate. Mousavi et al. (2010); Akbari (2000); Weng (2009); Amiri et al (2009); Oke (1973) and Oke (1982) concluded in their studies that the island effect of heat was quite high on temperature than other meteorological quantities. They also stated that in a clear sky, weak wind and whirlwind presence could create suitable conditions for establishing a relatively intense heat island. In a study conducted in London between 1931 and 1960, the annual changes in air temperature were investigated. The average annual air temperature in this city, suburbs, and the surrounding rural areas was 11, 3, and 6 degrees Celsius, respectively, proving the existence of heat island in this city (Barry & Chorley, 1987). The first studies that attempted to investigate urban thermal landscapes using infrared thermal data used NOAA AVHRR sensor data. The areas in all these studies were 1.1 km, being suitable only for preparing a small map of the temperature on a city scale. Later, thermal infrared data of Landsat ETM, TM, and ASTER with spatial resolutions of 90, 60, and 120 meters, respectively, provided the possibility of extracting the surface temperature of the earth and a more accurate study of urban heat islands (Rizwan et al., 2008). Among the studies carried out in recent years, those studies that use multi-temporal thermal images are more critical, because it is possible to discover the spatial-temporal changes of heat islands. A significant portion of the studies that have attempted to identify the spatio-temporal changes of heat islands used classical statistical methods (Rajeshwari & Mani, 2014). In another study conducted in Beijing, China, the values of the surface radiation temperature were extracted from a TM image of the Landsat satellite, and the creation of a heat island in this city was confirmed (Lam, 1990).

Recent studies for the city of Tehran show that minimum temperatures in Tehran have increased compared to the Varamin station, which indicates the release of much more thermal energy in Tehran than in its suburbs (Akbari, 2000). Studies related to Tehran's thermal island show that the effect of Tehran's thermal island has become more evident and along with the growth and development of the metropolis of Tehran, the spatial and temporal characteristics of the thermal island have changed. The spatial structure of the ground surface temperature, the effects of Tehran's thermal island, and the methods of obtaining temperature in hot and polluted areas are of particular importance (Sadeghinia et al., 2013). No study has evaluated the thermal trend components in the metropolis of Tehran so far, especially over period of 40 years. Yet, some research has been carried out without considering the influencing factors and the thermal island variations in the city and that these pieces of research sufferred the limitation of short time period. To this end, considering the current challenges of the research including increase in the surface temperature of the city of Tehran and the emergence of a thermal island in this metropolis, it seems crucial to investigate the factors influencing the emergence of this problem. A spatial-spatial and biological environment view can be the way forward for this research. Therefore, in this research, the use of modern and practical technologies like remote sensing (thermal remote sensing), which has a general and spatial view of the city (the studied area of the city Tehran), and Geographic Information Systems (GIS), having the ability to perform various types of mapping and modeling and combining layers, the biological and environmental problems related to Tehran and the reasons for the emergence of a heat island in this city are investigated. For this purpose, this research aims to investigate the surface temperature of the city and its influencing factors and components in Tehran using remote sensing technology as well as Landsat satellite images and thermal bands from 1984 to 2020. Moreover, this study investigates and compares the trend of changes in the thermal component of Tehran over the last 40 years and three decades of study.

2. METHOD

2.1. The location of the study area

Tehran is the largest and most important city in Iran. The capital greatness and its particular political, economic, cultural, and geographical position and the concentration of information (compared to other parts of the country) have caused many people (for work, education, treatment, administrative affairs, buying or selling goods, and entertainment) to come to this city and settle gradually. With its current needs and development issues, this metropolis is run by about 24 government or public institutions. The municipality primarily organizes city issues and promotes citizen participation and satisfaction. The metropolis consists of 22 districts. The location of Tehran, along with the divisions of the districts, can be seen in Figure 1.

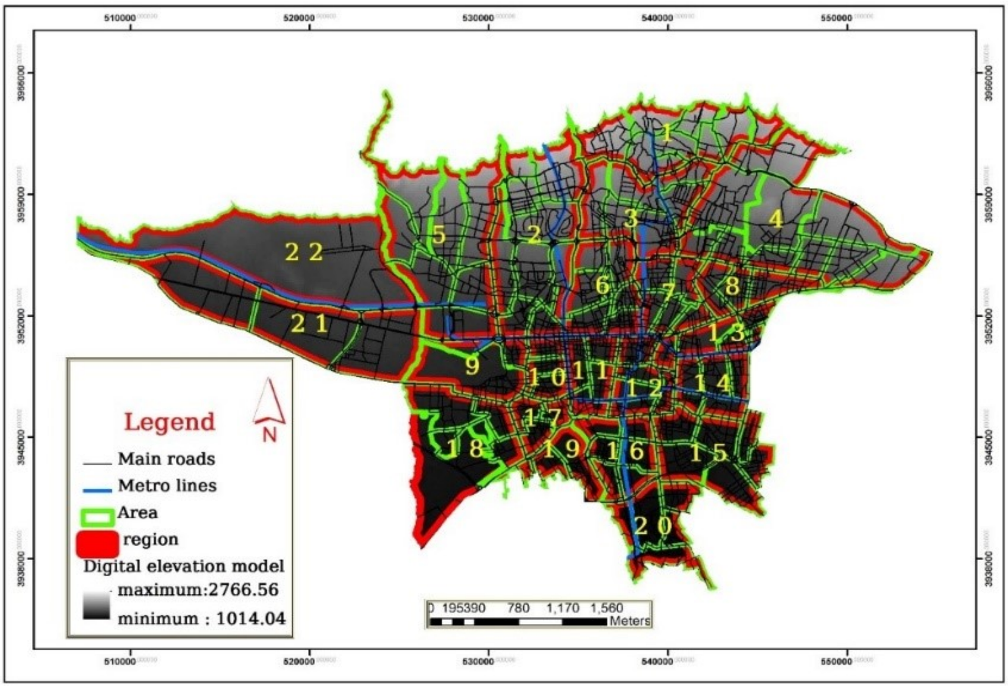

Figure 1. The geographical location of 22 districts of Tehran

2.2. Methodology

This is a descriptive-analytical and applied study in terms of purpose. In this study, Landsat satellite images are used for environmental and spatial analysis of Tehran. To this end, Landsat satellite images in TM, ETM+, and TIRS sensors from 1984 to 2020 are derived from the United States Geological Survey (USGS) and NASA website. This study aims to investigate (a) the changes in the climate and temperature of Tehran over the last 40 years and (b) the formation of a heat island in the city. One of the most important factors is the increase in LST which, as mentioned, is measured using thermal RS in summer and winter. Another factor is the study of vegetation in the area from 1984 to 2020 using the Normalized Difference Vegetation Index (NDVI) and Landsat Images.

Raw RS data collected from the land surface by various sensors are subject to shortcomings and errors. Therefore, deficiencies must be compensated and errors eliminated using satellite imagery.

ARC Gis 10.5 software is used here to generate output. IMAGIN ERDAS, Envi5.2, and IDRISI software are employed to process and analyze Landsat images and determine land use and thermal maps (Table 1). Table 1 shows the Landsat satellite imagery, sensors, and thermal bands used in this study. Landsat 5 and TM sensors were utilized from 1984 to 1998, Landsat 7 and ETM+ sensors were employed from 2000 to 2014, and Landsat 8 and OLI and TIRS sensors were applied from the year 2016 to 2020. Moreover, Band 6 and Bands 10 and 11 were utilized for ETM+ and TM sensors and TIRS sensors, respectively.

Table 1. Landsat satellite imagery specifications

Date of taking the image	Satellite	Sensor	PATH	ROW	Thermal band	Coordinate system
1984-04-25	LANDSAT_5"	"TM"	164	035	6	"WGS84"UTM_ZONE = 39
1984-11-19	LANDSAT_5"	"TM"	164	035	6	"WGS84"UTM_ZONE = 39
1987-07-07	LANDSAT_5"	"TM"	164	035	6	"WGS84"UTM_ZONE = 39
1987-01-12	LANDSAT_5"	"TM"	164	035	6	"WGS84"UTM_ZONE = 39
1990-07-31	LANDSAT_5"	"TM"	164	035	6	"WGS84"UTM_ZONE = 39
1990-12-22	LANDSAT_5"	"TM"	164	035	6	"WGS84"UTM_ZONE = 39
1992-01-26	LANDSAT_5"	"TM"	164	035	6	"WGS84"UTM_ZONE = 39
1992-08-05	LANDSAT_5"	"TM"	164	035	6	"WGS84"UTM_ZONE = 39
1994-01-15	LANDSAT_5"	"TM"	164	035	6	"WGS84"UTM_ZONE = 39
1994-08-27	LANDSAT_5"	"TM"	164	035	6	"WGS84"UTM_ZONE = 39
1996-08-23	LANDSAT_5"	"TM"	164	035	6	"WGS84"UTM_ZONE = 39

1996-10-10	LANDSAT_5"	"TM"	164	035	6	"WGS84"UTM_ZONE = 39
1998-01-26	LANDSAT_5"	"TM"	164	035	6	"WGS84"UTM_ZONE = 39
1998-08-06	LANDSAT_5"	"TM"	164	035	6	"WGS84"UTM_ZONE = 39
2000-01-16	"LANDSAT_7"	"ETM"	164	035	6	"WGS84"UTM_ZONE = 39
2000-08-11	"LANDSAT_7"	"ETM"	164	035	6	"WGS84"UTM_ZONE = 39
2002-01-13	"LANDSAT_7"	"ETM"	164	035	6	"WGS84"UTM_ZONE = 39
2002-08-09	"LANDSAT_7"	"ETM"	164	035	6	"WGS84"UTM_ZONE = 39
2004-01-19	"LANDSAT_7"	"ETM"	164	035	6	"WGS84"UTM_ZONE = 39
2004-08-14	"LANDSAT_7"	"ETM"	164	035	6	"WGS84"UTM_ZONE = 39
2006-02-25	"LANDSAT_7"	"ETM"	164	035	6	"WGS84"UTM_ZONE = 39
2006-08-04	"LANDSAT_7"	"ETM"	164	035	6	"WGS84"UTM_ZONE = 39
2008-01-14	"LANDSAT_7"	"ETM"	164	035	6	"WGS84"UTM_ZONE = 39
2008-08-09	"LANDSAT_7"	"ETM"	164	035	6	"WGS84"UTM_ZONE = 39
2010-01-03	"LANDSAT_7"	"ETM"	164	035	6	"WGS84"UTM_ZONE = 39
2010-08-15	"LANDSAT_7"	"ETM"	164	035	6	"WGS84"UTM_ZONE = 39
2012-01-25	"LANDSAT_7"	"ETM"	164	035	6	"WGS84"UTM_ZONE = 39
2012-08-04	"LANDSAT_7"	"ETM"	164	035	6	"WGS84"UTM_ZONE = 39
2014-01-14	"LANDSAT_7"	"ETM"	164	035	6	"WGS84"UTM_ZONE = 39
2014-08-10	"LANDSAT_7"	"ETM"	164	035	6	"WGS84"UTM_ZONE = 39
2016-02-03	"LANDSAT_8"	"OLI_TIRS"	164	035	11-10	"WGS84"UTM_ZONE = 39
2016-08-15	"LANDSAT_8"	"OLI_TIRS"	164	035	11-10	"WGS84"UTM_ZONE = 39
2018-01-25	"LANDSAT_8"	"OLI_TIRS"	164	035	11-10	"WGS84"UTM_ZONE = 39
2018-08-05	"LANDSAT_8"	"OLI_TIRS"	164	035	11-10	"WGS84"UTM_ZONE = 39
2020-01-15	"LANDSAT_8"	"OLI_TIRS"	164	035	11-10	"WGS84"UTM_ZONE = 39
2020-08-10	"LANDSAT_8"	"OLI_TIRS"	164	035	11-10	"WGS84"UTM_ZONE = 39

2.3. Parameters affecting LST

2.3.1. Land use

One factor affecting the temperature increase in Tehran is changes in land use. Examples include changes in land use, excessive space use, building densities, and urban areas. Changes in the type of land use and society’s tendency to intervene in space reflect the structure of the space economy in cities. The space economy in Tehran is based on developing high-price and high-quality urban lands in the affluent areas of the city. The predominant trends included residential, commercial, office, and tourism spaces. The most significant demand involves changing the use of green space, residential spaces, and development reserve lands.

Studies show that the space economy in Tehran is based on the development of high-price and high-quality urban lands in the affluent areas of this city. The high concentration of these interventions can be seen at Districts 1, 2, and 3. Trends in land-use interventions and changes in Tehran are not balanced. The spatial distribution pattern of land use and spatial autocorrelation indicate that the predominant trend involves residential, commercial, office, and tourism uses and that a tremendous demand for land-use change is changing the use of green space residential spaces and development reserve lands. Continuation of this process has caused excessive use of building surfaces instead of vegetation and garden and, consequently, an increase in temperature at the districts of Tehran. Remote sensing, which aims to identify and separate land phenomena and classify them, and Landsat satellite imagery from 1984 to 2020 are used to study these changes. Band composition in Landsat images is one of the methods used to obtain a land-use map before classification. In this study, the 2-3-4 band combination is used for TM and ETM+ while the 2-3-5 band composition is applied to the TIRS sensor. In this combination, Band 4 is the infrared band, with the vegetation having the highest reflectance. Band compositions for preparing land-use maps for Tehran from 1984 to 2020 can be seen in Figures 2 and 3. As seen in the figure, the study area is divided into five classes (green space and vegetation in green, urban land use in pink, barren and abandoned lands in white, poor lands or mountains in purple, and roads in black). Land-use changes for studying the heat island in Tehran are quite evident with further expansion of the thermal island due to reduced vegetation and increased urban land use. According to Figure 2, from 1984 to 2004, Tehran was divided into 2 parts, the urban part at the center and the outside where barren and inferior lands covered with vegetation lie. Over time, poor quality of land and life along with useless vegetation have transformed into the city (residential areas and roads). Based on Figure 3, from 2006 to 2020, the green part (vegetation) changed to pink (city) and the vegetation was reduced a lot in 2018 and 2020, being one of the factors in increasing the temperature of the earth's surface.

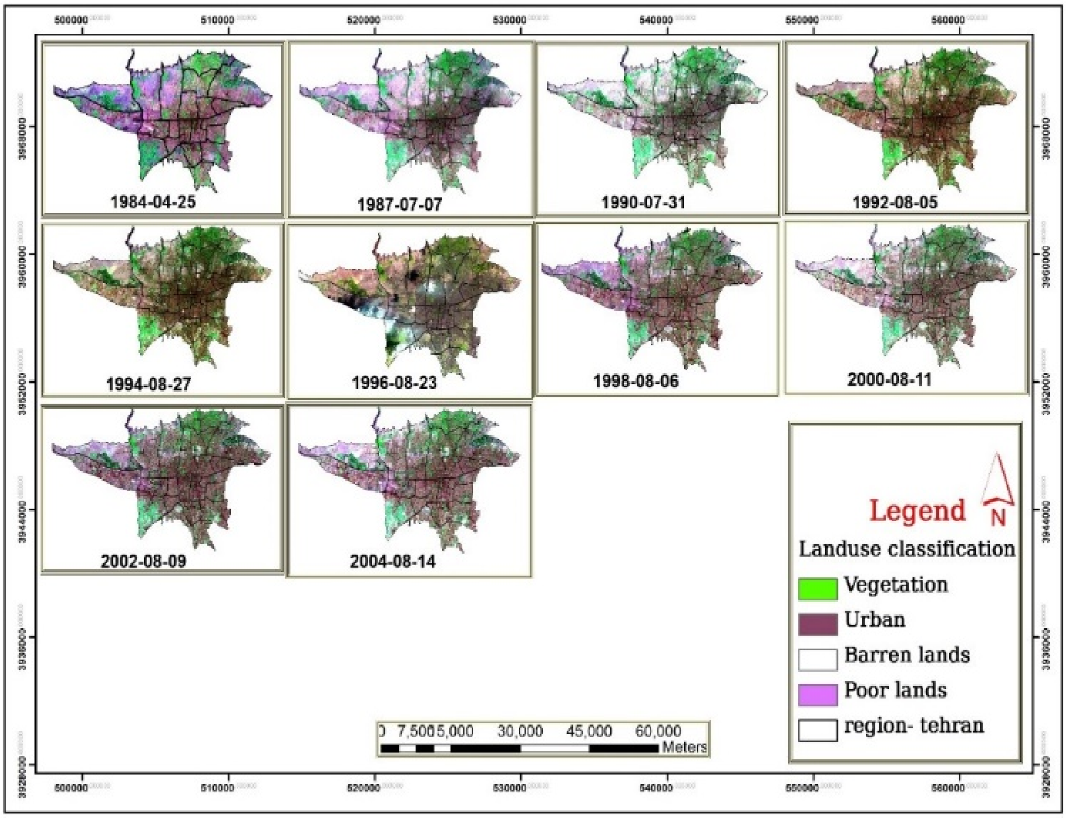

Figure 2. Land-use map of Tehran from 1984 to 2004

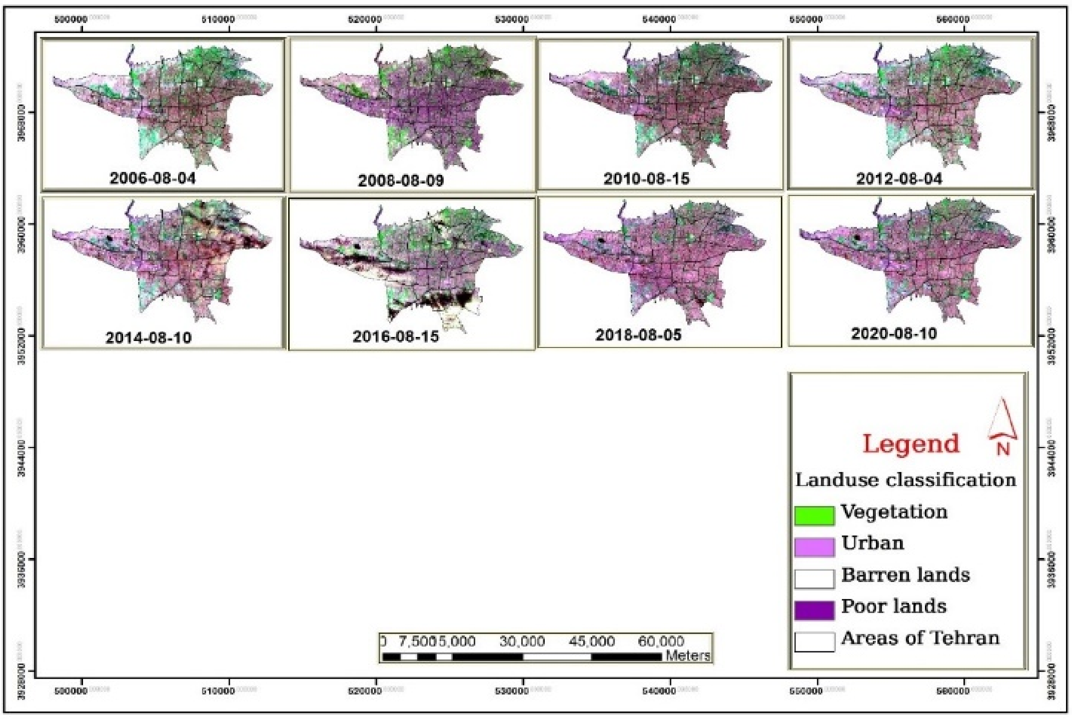

Figure 3. Land-use map of Tehran from 2006 to 2020

2.3.2. Land Surface Temperature (LST)

One of the most critical factors affecting the increase in temperature of Tehran is LST, which is obtained using the thermal bands of Landsat satellite in TM, ETM+, and TIRS sensors. The pixels of the images must first be processed to obtain correct information to prepare a thermal map of the city. All of these are called image pre-processing or image correction. One of the most critical corrections made to image pixels is radiometric. One part of radiometric corrections of the images is spectral correction performed on digital numbers (DN) or the pixel such that when the image is taken, it has DN. These DNs contain information about land surface phenomena. However, the initial data contain basic information (uncorrected) and cannot represent the parameters of the land surface, such as temperature, humidity, vegetation, etc. The DN of the satellite imagery must be corrected to apply the values of the ground surface parameters to the desired satellite imagery. The DN of each image must be converted into radiance and reflectance. This form of correction is referred to as spectral correction. Several models and methods for converting DN of satellite images into radiance and reflectance are given in the following. Equation (1) (Chander et al., 2009) converts raw image values into radiance for Landsat TM and ETM images.

$$L\lambda = \left(\frac{\mathrm{LMAX}-\mathrm{LMIN}}{\mathrm{Qcalmax}-\mathrm{Qcalmin}}\right)(\mathrm{Qcal}-\mathrm{Qcalmin})+\mathrm{LMIN} \quad (1)$$

where Lλ is the spectral radiance in the sensor, Qcal is the pixel value (DN) in the desired band, Qcalmin is the minimum pixel value (DN), Qcalmax is the maximum pixel value (DN), and LMIN and LMAX are minimum and maximum spectral radiances, respectively, in the sensor.

$$p\lambda = \frac{\pi \times L\lambda \times d^2}{\mathrm{ESUN}\ \lambda \times \cos\theta s} \quad \text{(2) (Chander et al., 2009)}$$

where pλ is the reflectance coefficient, π = 3.1459, Lλ is the spectral radiance in the sensor, d is the distance between the earth and the sun (astronomical unit), ESUN is the average of the sun's rays, and θ is the angle of the sun's rays (degrees).

Equation (3) (Chander et al., 2009) is employed to obtain the spectral radiance in the OLI sensor:

$$L\lambda = \mathrm{ML} * \mathrm{Qcal} + \mathrm{AL} \quad (3)$$

where Lλ is the radiance above the atmosphere (watts/m^2*srad*μm), ML is the multiplicative conversion factor, Qcal includes the pixel values (DNs) of 10 and 11, and AL is the aggregate conversion factor.

2.3.3. Obtaining the brightness temperature

Thermal band data can be converted from spectral radiance in the sensor into brightness temperature, assuming that the earth is a black body and includes the effects of the atmosphere (absorption and radiance). The brightness temperature for Landsat satellite sensors is calculated using Equation (4) (Rajeshwari & Mani, 2014).

$$T = \frac{K2}{\mathrm{Ln}\left(\frac{K1}{L\lambda}+1\right)} \quad (4)$$

where T is the temperature affecting the brightness in the sensor in Kelvin, K2 is the calibration coefficient 2 in Kelvin, K1 is the calibration coefficient 1 in W (m st μm), and Lλ is the spectral radiance in the sensor. The coefficients K1 and K2 are calculated according to Table 2.

Satellite images of Tehran are calibrated and the necessary corrections are made. The mentioned algorithms are used to prepare thermal maps and the thermal zoning map of Tehran is compiled covering the years 1984 to 2020.

Table 2. Coefficients K1 and K2 for Landsat satellite

Sensor coefficient (band)	Calibration coefficient 1	Calibration coefficient 2 (in K)
L5-TM B6	607.76	1260.56
L7-ETM+B6	666.09	1282.71
L8-OLI B10	777.89	1321.08
L8-OLI B11	480.89	1201.14

2.3.4. Vegetation

One of the other factors affecting the temperature increase in Tehran is its vegetation density, which is obtained using Landsat satellite images and NDVI.

One of the most well-known, simplest, and most widely used indices in vegetation studies is NDVI. It has a simple computational process and has higher dynamic power than other indices. This index has the highest sensitivity to vegetation changes and is less sensitive to the effects of weather and soil, except in cases where vegetation is low. NDVI is calculated using Equation (5) (Van de Griend & Owe, 1993):

$$\mathrm{NDVI} = \frac{\mathrm{NIR}-\mathrm{RED}}{\mathrm{NIR}+\mathrm{RED}} \quad (5)$$

where NIR and RED are the reflectance and reflectance at the infrared and red bands, respectively. Although theoretically, the value of this index is in the range of -1 to 1, in practice, it is less than 1 and more than -1. The values of this index for dense vegetation tend to be 1, but negative values characterize clouds, snow, and water. In addition, the rocks and barren soils with similar spectral reactions used at the two bands are seen with values close to zero. Based on this index, typical soil is considered equal to 1. The higher the pixel distance from the soil size, the denser the vegetation. In this regard, NDVI is applied to Landsat images, and the vegetation map of Tehran is prepared from 1984 to 2020 in five classes: very light red, relatively light orange, medium-density yellow, relatively high light green, and very high-density dark green.

3. RESULTS AND DISCUSSION

One of the most critical factors affecting the increase in temperature in Tehran is LST. This study prepared a thermal zoning map based on Landsat thermal images in ETM and TM sensors at Band 6 and TIRS sensors at Bands 10 and 11 in winter and summer from 1984 to 2020. The thermal zoning map of Tehran was divided from minimum to maximum temperature into eight classes, including green, dark green, blue, light blue, yellow, orange, pink, and red in three time periods 1984 to 1996, 1998 to 2008, and 2010 to 2020, each of which is explained separately.

3.1. Thermal zoning map of Tehran from 1984 to 1996

The thermal zoning map of Tehran from 1984 to 1996 can be seen in Figure 4. According to the figure, the largest zones belong to the yellow, coral, and magenta classes, while the lowest zones belong to the green, sea green, and cyan classes.

LST is divided into eight classes in Table 3. According to the table, the minimum temperature of -5 °C belongs to the year 1984, while the maximum temperature of 51 °C belongs to the year 1987. Figure 5 shows the average LST of -7 °C for the green class from 1984 to 1996 and the average LST of 20 and 25 °C for the magenta and red classes, respectively.

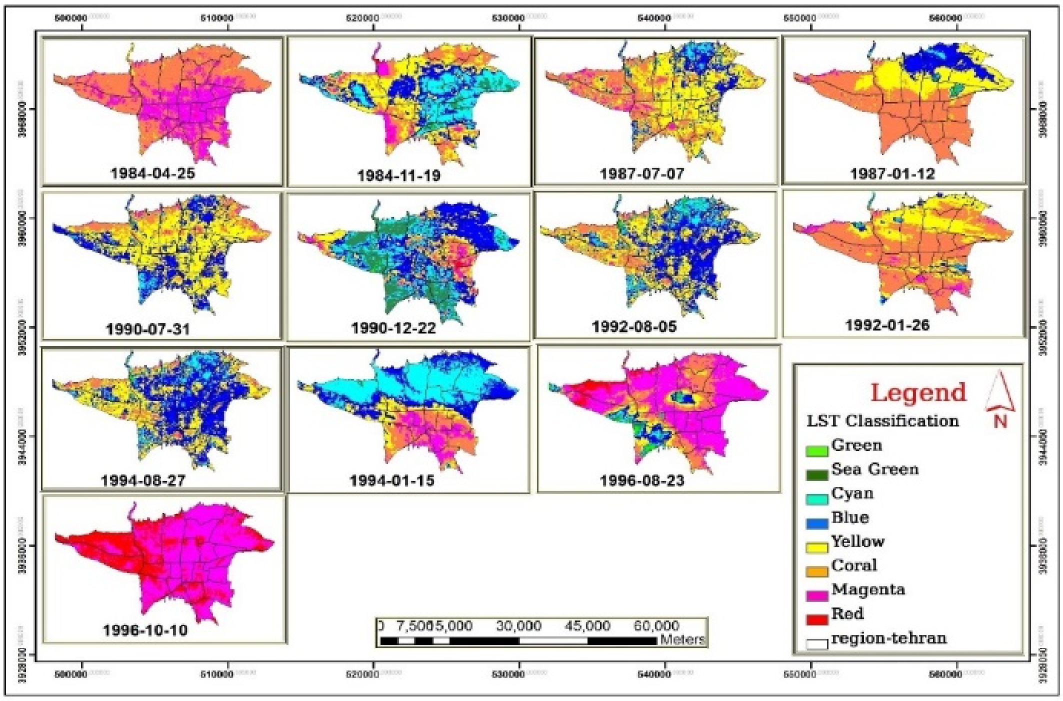

Figure 4. LST map of Tehran from 1984 to 1996

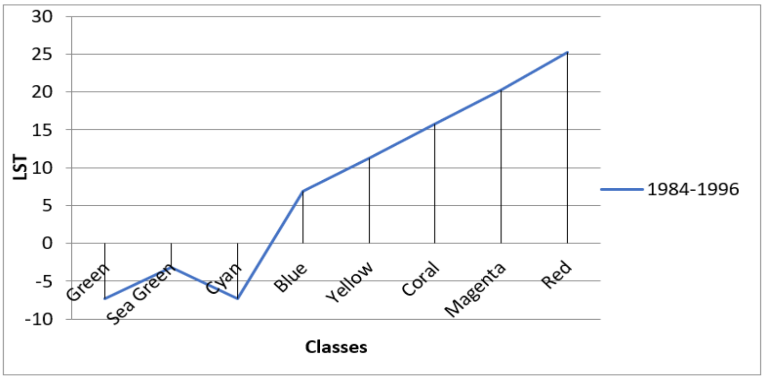

Figure 5. Average LST in Tehran from 1984 to 1996

Table 3. LST in Tehran from 1984 to 1996

Year	Class temperature (°C)							
	Green	Sea Green	Cyan	Blue	Yellow	Coral	Magenta	Red
1984-04-25	-05 - -0	-0 - 04	04 - 09	09 - 14	14 - 19	19 - 24	24 - 29	29 - 34
1984-11-19	-27 - -25	-25 - -22	-22 - -20	-20 - -18	-18 - -15	-15 - -13	-13 - -11	-11 - -08
1987-07-07	23 - 26	26 - 30	30 - 33	33 - 37	37 - 40	40 - 44	44 - 47	47 - 51
1987-01-12	-18 - -23	-18 - -13	-13 - -08	-08 - -02	-02 - 02	02 - 07	07 - 12	12 - 18
1990-07-31	19 - 23	23 - 26	26 - 30	30 - 33	33 - 37	37 - 41	41 - 44	44 - 48
1990-12-22	-20 - -17	-17 - -14	-14 - -11	-11 - -08	-08 - -05	-05 - -03	-03 - -0	-0 - 02
1992-01-26	-26 - -21	-21 - -17	-17 - -13	-13 - -09	-09 - -04	-04 - -0	-0 - -03	03 - 07
1992-08-05	22 - 25	25 - 27	27 - 30	30 - 32	32 - 35	35 - 37	37 - 40	40 - 43
1994-01-15	-15 - -12	-12 - -08	-08 - -05	-05 - -02	-02 - 0	0 - 03	03 - 07	07 - 10
1994-08-27	23 - 26	26 - 29	29 - 32	32 - 34	34 - 37	37 - 40	40 - 43	43 - 46
1996-08-23	-14 - -06	-06 - 01	01 - 08	08 - 16	16 - 24	24 - 32	32 - 39	39 - 47
1996-10-10	-71 - -57	-57 - -44	-44 - -30	-30 - -16	-16 - -03	-03 - 10	10 - 24	24 - 37

The trend of LST classes from 1984 to 1996 can be seen in Figure 6.

Figure 7 shows changes in LST classes from 1984 to 1996.

3.2. Thermal zoning map from 1998 to 2008

The thermal zoning map of Tehran from 1998 to 2008 can be seen in Figure 8. As can be seen, the highest thermal zones belong to the yellow, coral, and magenta classes.

LST classes (8 classes) can be seen in Table 4. According to the table, the average LST of green and sea green classes included -1 and 3 °C respectively, and the average LSTs of magenta and red classes were 23 and 27 °C, respectively, from 1984 to 1996. Figure 9 shows average LST in Tehran from 1998 to 2008. Changes in LST classes from 1998 to 2008 can be seen in Figure 10.

Figure 11 shows the changes in LST classes in Tehran from 1998 to 2008.

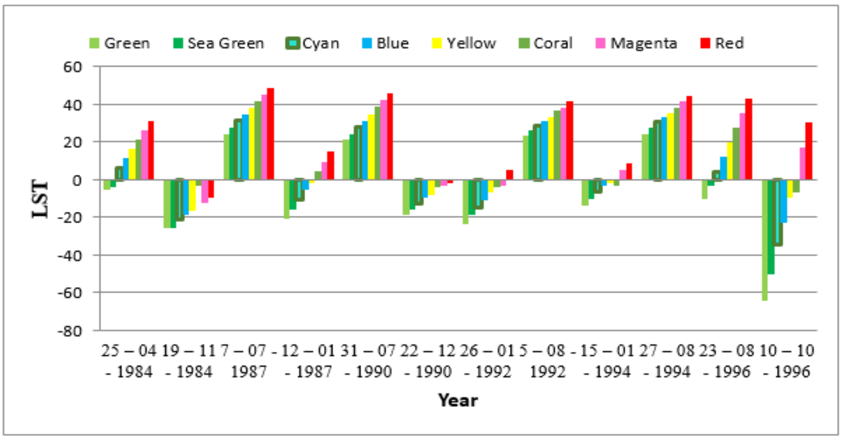

Figure 6. LST classes in Tehran from 1984 to 1996

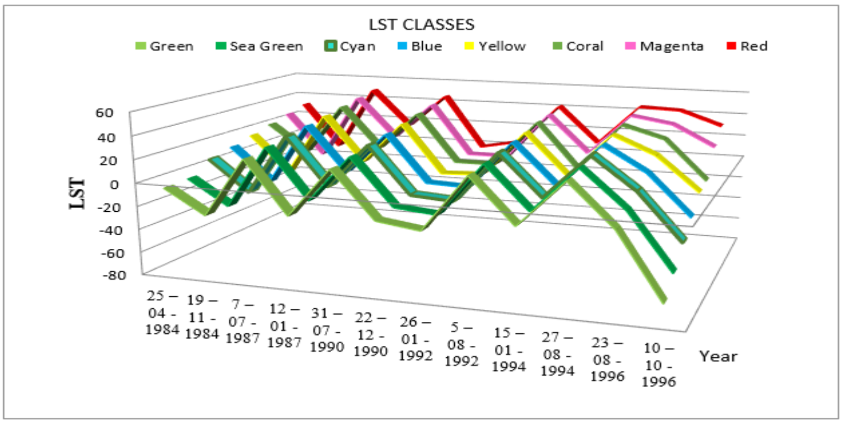

Figure 7. The trend of changes in LST classes in Tehran from 1984 to 1996

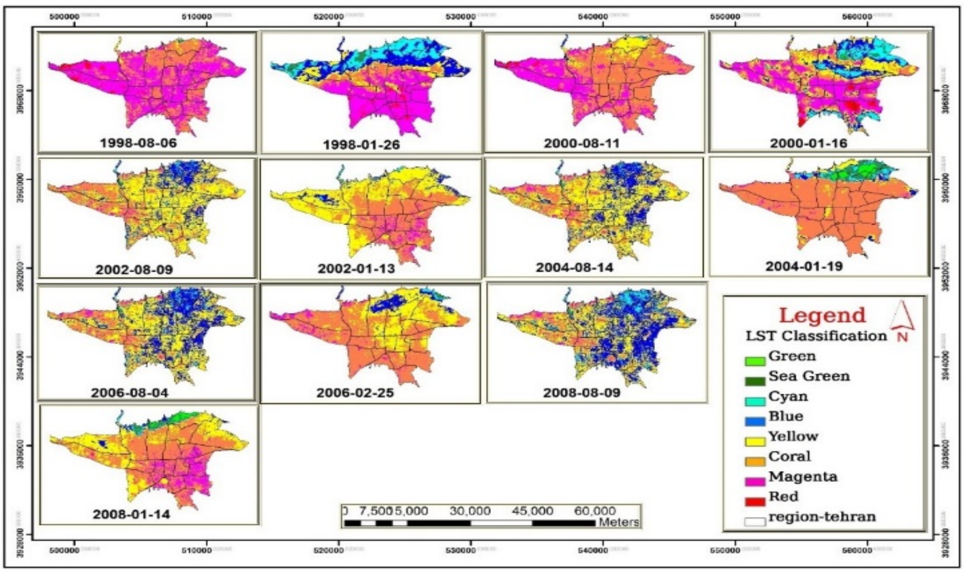

Figure 8. LST map of Tehran from 1998 to 2008

Table 4. LST in Tehran from 1998 to 2008

Year	Classes							
	Green	**Sea Green**	**Cyan**	**Blue**	**Yellow**	**Coral**	**Magenta**	**Red**
1998-01-26	-29 - -24	-24 - -19	-19 - -13	-13 - -08	-08 - -03	-03 - 02	02 - 07	07 - 12
1998-08-06	02 - 07	07 - 12	12 - 17	17 - 22	22 - 27	27 - 32	32 - 36	36 - 41
2000-01-16	-29 - -27	-27 - -25	-25 - -23	-23 - -21	-21 - -18	-18 - -16	-16 - -14	-14 - -12
2000-08-11	05 - 09	09 - 14	14 - 18	18 - 22	22 - 27	27 - 31	31 - 36	36 - 40
2002-01-13	-17 - -13	-13 - -10	-10 - -07	-07 - -04	-04 - -01	-01 - 01	01 - 04	04 - 07
2002-08-09	25 - 29	29 - 33	33 - 37	37 - 41	41 - 46	46 - 50	50 - 54	54 - 58
2004-01-19	-23 - -17	-17 - -11	-11 - -05	-05 - -0	-0 - 05	05 - 11	11 - 17	17 - 23
2004-08-14	21 - 25	25 - 28	28 - 32	32 - 35	35 - 39	39 - 42	42 - 46	46 - 50
2006-02-25	-17 - -11	-11 - -05	-05 - 0	0 - 07	07 - 13	13 - 19	19 - 25	25 - 31
2006-08-04	23 - 26	26 - 29	29 - 33	33 - 36	36 - 40	40 - 43	43 - 47	47 - 50
2008-01-14	-22 - -19	-19 - -15	-15 - -12	-12 - -08	-08 - -05	-05 - -01	-01 - 01	01 - 04
2008-08-09	24 - 27	27 - 30	30 - 33	33 - 36	36 - 39	39 - 42	42 - 45	45 - 48

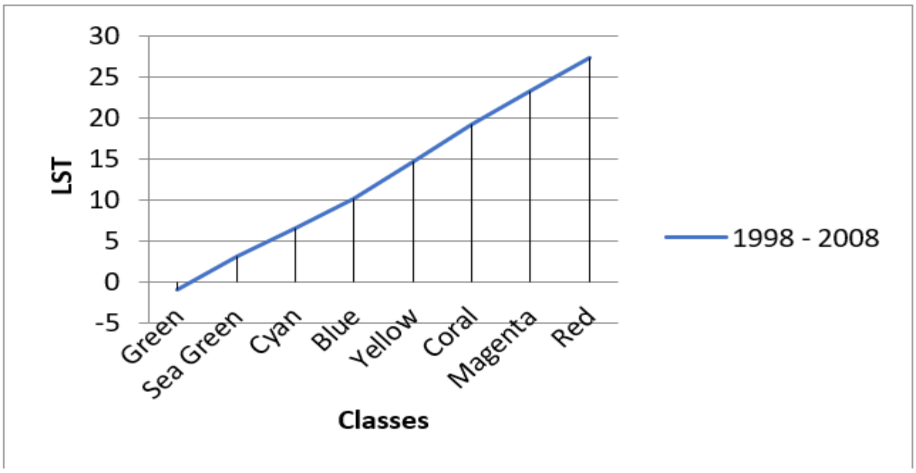

Figure 9. Average LST in Tehran from 1998 to 2008

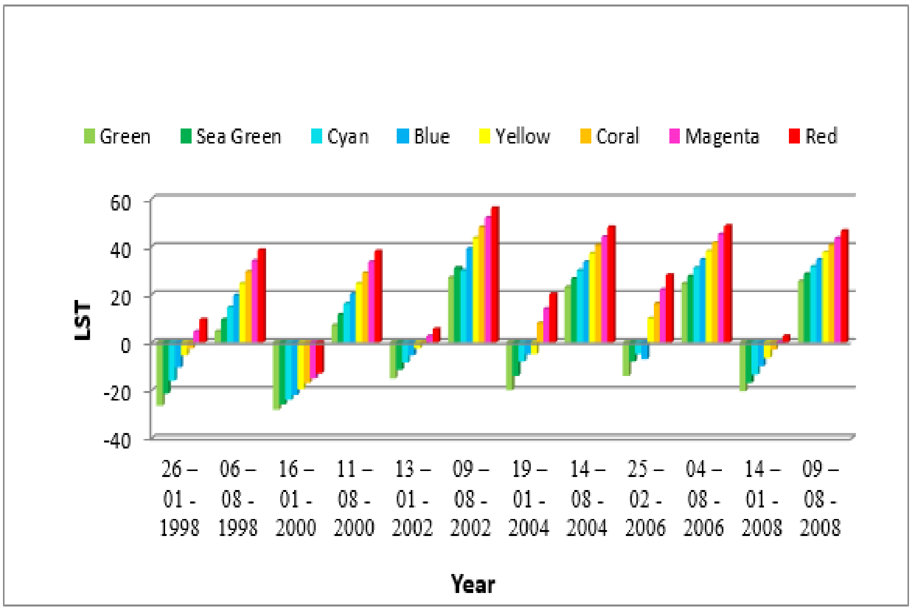

Figure 10. Changes in LST classes in Tehran from 1998 to 2008

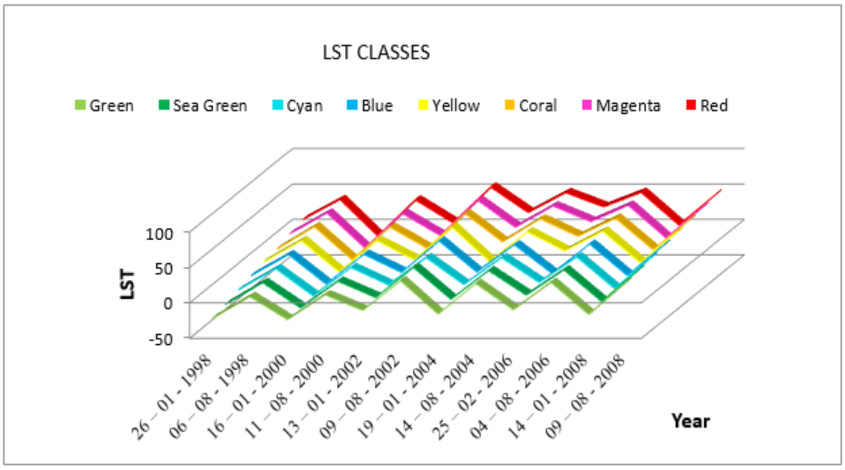

Figure 11. The trend of changes in LST classes in Tehran from 1998 to 2008

3.3. Thermal zoning map of Tehran from 2010 to 2020

Figure 12 shows the thermal zoning map of Tehran from 2010 to 2020. As can be seen, the highest thermal zones belong to the yellow, blue, and magenta classes.

Table 5 shows the LST classes (eight classes). The average LST of -1 and 3 °C for the green and sea green classes, respectively, and the average LST of 28 and 31 °C for the magenta and red classes, respectively, from 2010 to 2020 can be seen in Figure 13.

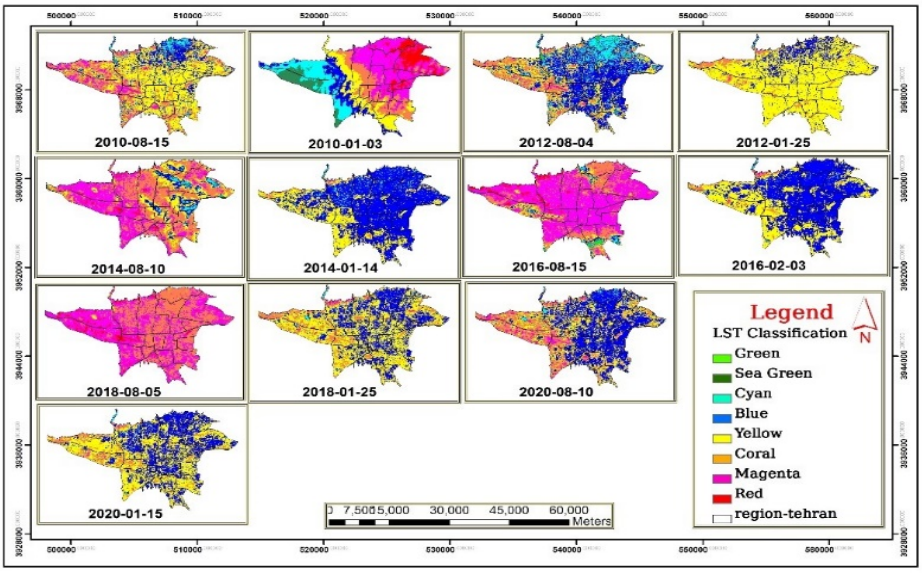

Figure 12. LST map of Tehran from 2010 to 2020

Table 5. LST in Tehran from 2010 to 2020

Year	Classes							
	Green	Sea green	Cyan	Blue	Yellow	Coral	Magenta	Red
2010-01-03	-48 - -42	-42 - -35	-35 - -29	-29 - -22	-22 - -16	-16 - -09	-09 - -03	-03 - 03
2010-08-15	19 - 22	22 - 25	25 - 29	29 - 32	32 - 35	35 - 38	38 - 41	41 - 44
2012-01-25	-17 - -12	-12 - -07	-07 - -02	-02 - 02	02 - 07	07 - 12	12 - 17	17 - 22
2012-08-04	22 - 25	25 - 28	28 - 31	31 - 34	34 - 37	37 - 40	40 - 43	43 - 46
2014-01-14	-09 - -05	-05 - -01	-01 - 03	03 - 07	07 - 11	11 - 15	15 - 20	20 - 24
2014-08-10	-02 - 04	04 - 11	11 - 18	18 - 25	25 - 32	32 - 39	39 - 46	46 - 53
2016-02-03	26 - 27	27 - 27	27 - 28	28 - 28	28 - 29	29 - 29	29 - 30	30 - 31
2016-08-15	-12 - -05	-05 - 02	02 - 09	09 - 17	17 - 24	24 - 32	32 - 39	39 - 47
2018-01-25	-05 - -01	-01 - 02	02 - 06	06 - 10	10 - 14	14 - 18	18 - 22	22 - 26
2018-08-05	-05 - 01	01 - 08	08 - 15	15 - 22	22 - 30	30 - 37	37 - 44	44 - 51
2020-01-15	-14 - -10	-10 - -06	-06 - -01	-01 - 02	02 - 06	06 - 11	11 - 15	15 - 20
2020-08-10	16 - 20	20 - 24	24 - 28	28 - 33	33 - 37	37 - 41	41 - 45	45 - 49

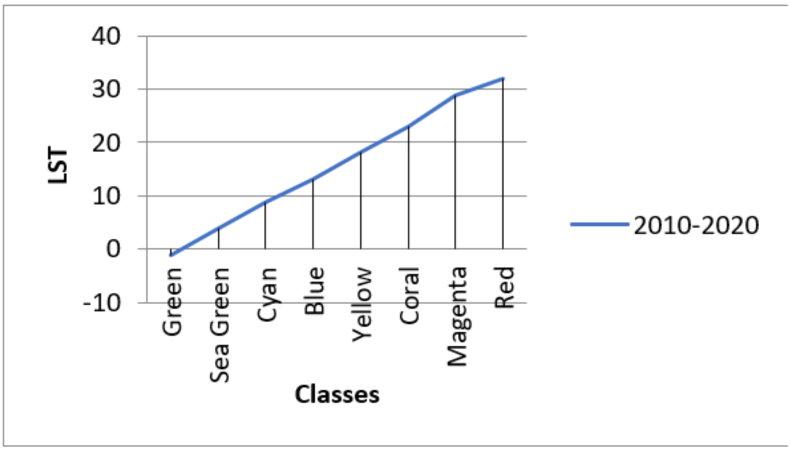

Figure 13. Average LST in Tehran from 2010 to 2020

Figure 14 shows the changes in LST classes in Tehran from 2010 to 2020.

The trend of changes in LST classes in Tehran from 2010 to 2020 can be seen in Figure 15.

According to the thermal zoning map, figures, and tables, the temperature in Tehran over the last 40 years and within the interval of three periods from 1984 to 1996, 1998 to 2008, and 2010 to 2020 in winter and summer has increased significantly. If this trend continues, there will be no winters or cold seasons in Tehran in the future and hot weather will replace colder weather. NDVI was also used to study the vegetation trend in Tehran. The index was prepared for Landsat images from 1984 to 2020. It was classified into four classes: Very low density in red, relatively low density in coral, medium density in green, and very high density in sea green. The results of the NDVI maps show the declining trend of vegetation over the last 40 years (Figures 16 and 17).

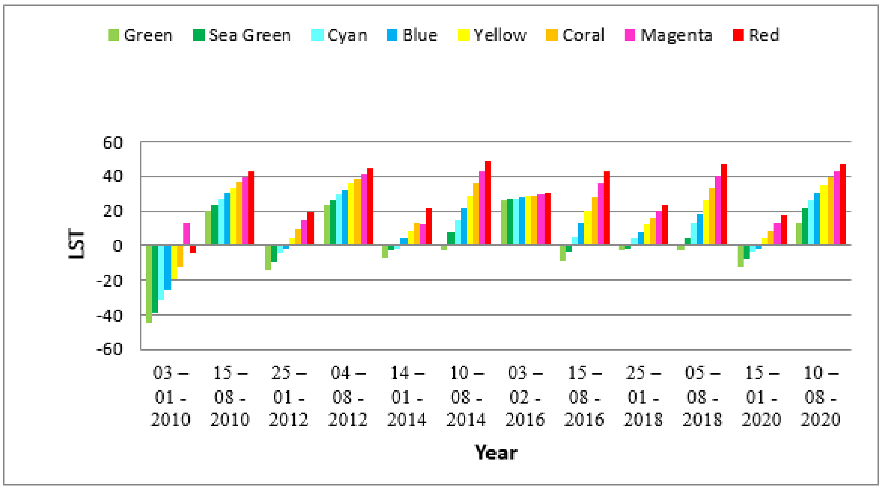

Figure 14. LST classes in Tehran from 2010 to 2020

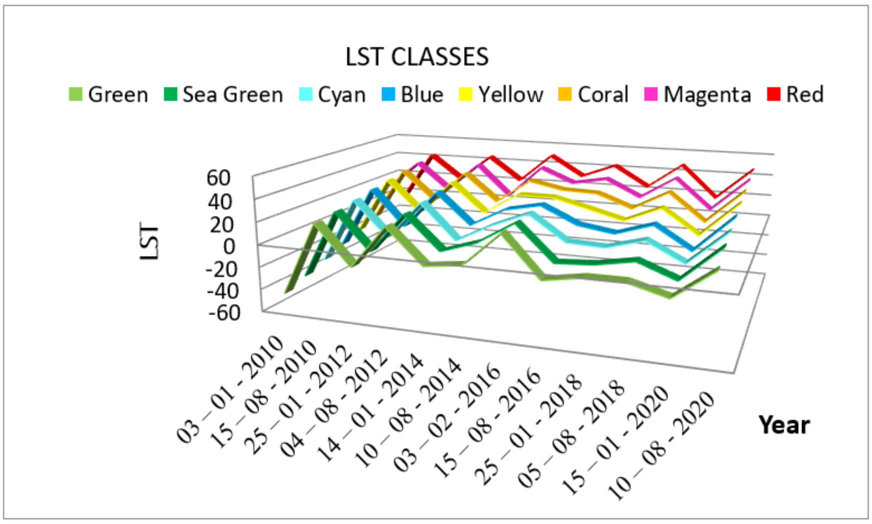

Figure 15. The trend of changes in LST classes from 2010 to 2020

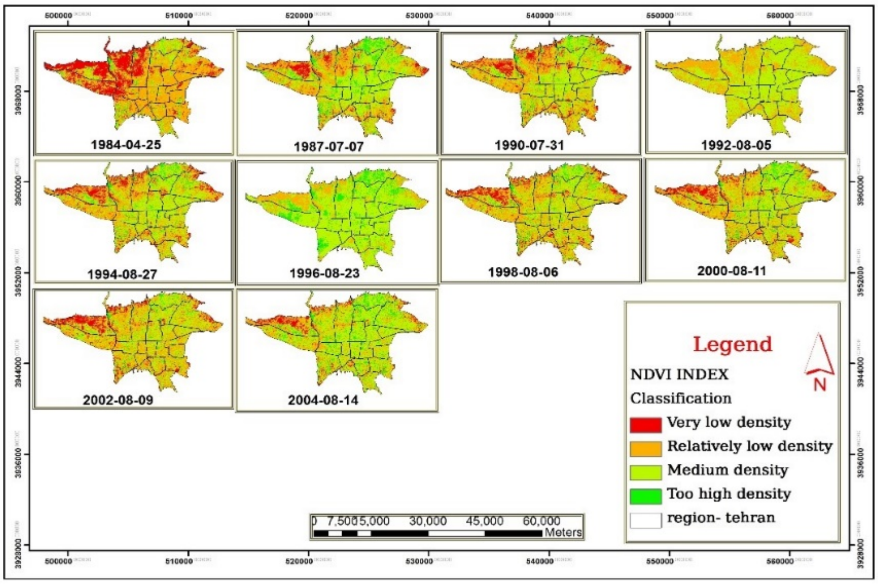

Figure 16. NDVI map of Tehran from 1984 to 2004

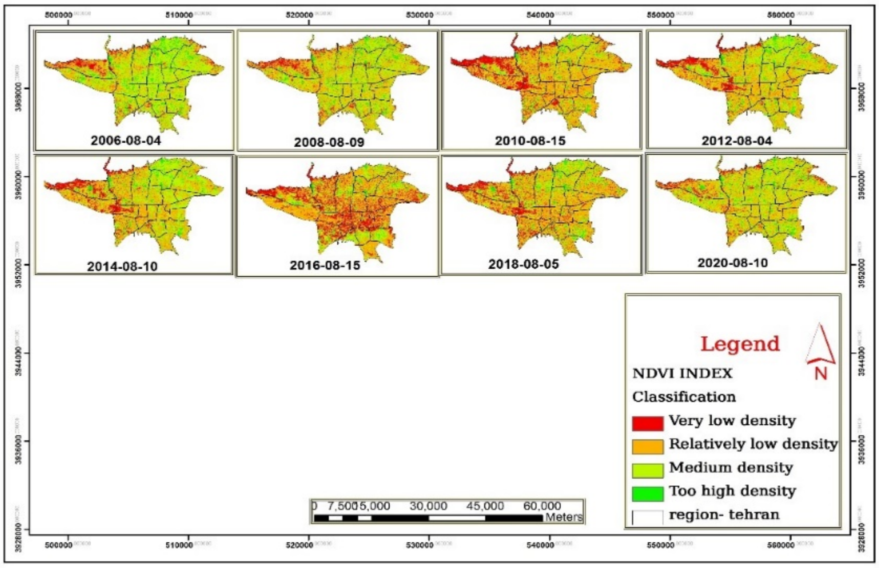

Figure 17. NDVI map of Tehran from 2008 to 2020

4. CONCLUSIONS

The increase in temperature and heat islands directly impacts urban vegetation and air, human health, and the environment and causes increased mortality. In the process of controlling and monitoring the heat island, one should keep in mind that the thermal change and increase depend on many factors. Mousavi et al (2010); Akbari (2000); Weng (2009) and Amiri et al (2009) realized that these many factors were uncontrollable climatic ones including solar radiation, wind intensity, etc. However, other factors are controllable and include human activities in the environment, changing the state of the earth's natural surface, and replacing vegetation with urban materials such as buildings, roads, and other asphalt areas, which can cause an increase in temperature. According to the stated problems and the possibility of controlling the second category of factors, the main goal of this research is to investigate the temperature changes in the city and the components and factors influencing its formation. Considering that no research has implemented the unique evaluation process of the thermal component of Tehran metropolis over the last 40 years, or perhaps there are some studies that faied to consider the influencing factors, a survey of the land surface temperature, vegetation, and temperature in Tehran seems to be necessary.

The Use-Land survey demonstrated that Tehran was divided into two parts: the urban part located at the center and the outside covering barren lands, lowlands, and vegetation. Nevertheless, in recent decades, the barren lands and vegetation have been urbanized and transformed (residential areas and roads). The survey (LST) illustrated that the minimum and maximum temperatures were -5 °C and 51 °C in 1984 and 1987, respectively. The LST recorded in each decade has changed from 20 and 25 to 23 and 27. In the last decade, LST has changed from 23 and 27 to 28 and 31 degrees. NDVI survey showed that NDVI had had a decreasing trend in the last 40 years. The review of Tehran temperature over the years indicates that Tehran's temperature increases significantly in the winter and summer. If this trend continues, there will be no winter and cold season in Tehran in the future. Based on the results and evident factors, the rising trend of temperature in Tehran continues and will cause irreparable damage.

Heat islands can be controlled by proper city designing and vegetation management (increasing green roofs, parks, etc.), and heat flow at the center of the city should be managed, which requires urban planning and use of remote sensing in design and use. In the end, it is recommend that future research be examined regionally according to the size of the city. Besides, the impact of the relationship between the types of structures and roads on the increase of heat islands be examined.

5. ACKNOWLEDGEMENT

The authors would like to acknowledge the valuable comments and suggestions of the reviewers, which have improved the quality of this paper.

REFERENCES

1. Ahmed, S. (2017). Assessment of urban heat islands and impact of climate change on socioeconomic over Suez Governorate using remote sensing and GIS techniques. *The Egyptian Journal of Remote Sensing and Space Sciences*, *21*(1), 15-25. https://doi.org/10.1016/j.ejrs.2017.08.001
2. Akbari, H. (2000). Consideration of temperature distribution pattern of Tehran using Landsat TM thermal data [MA dissertation, Tarbiat Modarres University]. https://ganj.irandoc.ac.ir (In Persian).
3. Al-Masaodi, H.J.O., & Al-Zubaidi, H.A.M. (2021). Spatial-temporal changes of land surface temperature and land cover over Babylon Governorate, Iraq. *Materials Today: Proceedings*. https://doi.org/10.1016/j.matpr.2021.05.179
4. Amiri, R., Weng, Q., Alimohammadi, A., & Alavipanah, S.K. (2009). Spatial-temporal dynamics of land surface temperature in relation to fractional vegetation cover and land use/cover in the Tabriz urban area, Iran. *Remote Sensing of Environment*, *113* (12, 15), 2606-2617. https://doi.org/10.1016/j.rse.2009.07.021
5. Barry, R., & Chorley, R.J. (1987). Atmosphere, weather and climate. London: Methuen and co. Ltd. https://www.routledge.com/Atmosphere Weather-and-Climate/Barry-Chorley/p/book/9780415465700
6. Chander, G., Markham, B., & Helder, D. (2009). Summary of current radiometric calibration coefficients for Landsat MSS, TM, ETM+, and EO-1 ALI sensors". *Remote Sensing of Environment*, *113*(5), 893-903. https://doi.org/10.1016/j.rse.2009.01.007
7. Chi, Y., Sun, J., Sun, Y., Liu, Sh., & Fu, Zh. (2020). Multi-temporal characterization of land surface temperature and its relationships with normalized difference vegetation index and soil moisture content in the Yellow River Delta, China. *Global Ecology and Conservation*, *23*, Article Number: (e01092). https://doi.org/10.1016/j.gecco.2020.e01092
8. El-Hadidy, Sh.M. (2021). The relationship between urban heat islands and geological hazards in Mokattam plateau, Cairo, Egypt. *The Egyptian Journal of Remote Sensing and Space Sciences*, *24*(3, Part 2), 547-557. https://doi.org/10.1016/j.ejrs.2021.02.004
9. Gadrani, L., Lominadze, G., & Tsitsagi, M. (2018). F Assessment of landuse/landcover (LULC) change of Tbilisi and surrounding area using remote sensing (RS) and GIS. *Annals of Agrarian Science* , *16* (2), 163-169. https://doi.org/10.1016/j.aasci.2018.02.005
10. Gupta, N., Mathew, A., & Khandelwal, S. (2019). Analysis of cooling effect of water bodies on land surface temperature in the nearby region: A case study of Ahmedabad and Chandigarh cities in India. *The Egyptian Journal of Remote Sensing and Space Sciences*, *22*(1), 81-93. https://doi.org/10.1016/j.ejrs.2018.03.007
11. Harun, Z., Reda, E., Abdulrazzaq, A., Amer Abbas, A., Yusup, Y., & Zaki, Sh.A. (2020). Urban heat island in the modern tropical Kuala Lumpur: Comparative weight of the different parameters. *Alexandria Engineering Journal*, *59*(6), 4475-4489. https://doi.org/10.1016/j.aej.2020.07.053
12. Kabano, P., Lindley, S., & Harris, A. (2021). Evidence of urban heat island impacts on the vegetation growing season length in a tropical city. *Landscape and Urban Planning*, *206*, Article Number: 103989. https://doi.org/10.1016/j.landurbplan.2020.103989
13. Koopmans, S., Heusinkveld, B.G., & Steeneveld, G.J. (2020). A standardized physical equivalent temperature urban heat map at 1-m spatial resolution to facilitate climate stress tests in the Netherlands. *Building and Environment*, *181*(15), Article Number: (106984). https://doi.org/10.1016/j.buildenv.2020.106984
14. Lam, N.S.N. (1990). Description and measurement of Landsat TM images using fractals. *Photogrammetric Engineering and Remote Sensing*, *56*, 187-195. https://www.asprs.org/wp-content/uploads/pers/1990journal/feb/1990_feb_187-195.pdf
15. Li, H., Zhou, Y., Jia, G., Zhao, K., & Dong, J. (2022). Quantifying the response of surface urban heat island to urbanization using the annual temperature cycle model. *Geoscience Frontiers* , *13*(1). Article Number: 101141. https://doi.org/10.1016/j.gsf.2021.101141
16. Liu, Ch., Yang, M., Hou, Y., Zhao, Y., & Xue, X. (2021). Spatiotemporal evolution of island ecological quality under different urban densities: A comparative analysis of Xiamen and Kinmen Islands, Southeast China. *Ecological Indicators*, *124*, Article Number: 107438. https://doi.org/10.1016/j.ecolind.2021.107438
17. Macintyre, H.L., Heaviside, C., Cai, X., & Phalkey, R. (2021). The winter urban heat island: Impacts on cold-related mortality in a highly urbanized European region for present and future climate. *Environment International*, *154*, Article Number: 106606. https://doi.org/10.1016/j.envint.2021.106530
18. Mendez-Astudillo, J., Lau, L., Tang, Y.T., & Moore, T. (2021). A new Global Navigation Satellite System (GNSS) based method for urban heat island intensity monitoring. *International Journal of Applied Earth Observations and Geoinformation*, *94*, Article Number: 102222. https://doi.org/10.1016/j.jag.2020.102222
19. Mousavi-Baygi, M., Ashraf, B., & Miyanabady, A. (2010). The Investigation of Tehran's heat island by using the surface ozone and temperature data. *International Journal of Applied Environmental Sciences*,5(2),189-200. https://www.researchgate.net/publication/268327877_The_Investigation_of_Tehran%27s_Heat_Island_by_using_the_Surface_Ozone_and_Temperature_Data
20. Oke, T.R. (1979). City size and the urban heat island. *Atmospheric Environment Pergamon Press*, 7, 769-779. https://www.patarnott.com/pdf/Oke1979CitySizeAndHeatIsland.pdf
21. Oke, T.R. (1982). The energetic basis of urban heat island. *Journal of the Royal Meteorological Society* , *108*, 1-24. https://www.patarnott.com/pdf/Oake1982_UHI.pdf
22. Rajeshwari, A., & Mani, N.D. (2014). Estimation of land surface temperature of Dindigul district using Landsat 8 data. *International Journal of Research in Engineering and Technology*, *3*,122-126. https://ijret.org/volumes/2014v03/i05/IJRET20140305025.pdf
23. Rizwan, A.M., Dennis, L.Y., & Liu, C. (2008). A review on the generation, determination and mitigation of urban heat island. *Journal of Environmental Sciences*, *20*(1), 120-128. https://doi.org/10.1016/S1001-0742(08)60019-4
24. Sadeghinia, A., Alijani, B., Ziaeian, P., & Khaledi, S. (2013). Application of spatial autocorrelation techniques in the analysis of the thermal island of Tehran. *Applied Research in Geographical Sciences* , *13*(30), 67-90. https://www.sid.ir/en/Journal/ViewPaper.aspx?ID=354812 (In Persian).
25. Sekertekin, A., & Zadbagher, E. (2021). Simulation of future land surface temperature distribution and evaluating surface urban heat island based on impervious surface area. *Ecological Indicators*, 122 ,Article Number: 107230. https://doi.org/10.1016/j.ecolind.2020.107230
26. Tepanosyan, G., Muradyan, V., Hovsepyan, A., Pinigin, G., Medvedev, A., & Asmaryan, Sh. (2021). Studying spatial-temporal changes and relationship of land cover and surface Urban Heat Island derived through remote sensing in Yerevan. *Armenia Building and Environment*, *187*, Article Number: 107390. https://doi.org/10.1016/j.buildenv.2020.107390
27. Van de Griend, A., & Owe, M. (1993). On the relationship between thermal emissivity and the normalized difference vegetation index for natural surfaces. *International Journal of Remote Sensing*, *14*(6), 1119-1131. https://doi.org/10.1080/01431169308904400
28. Vasenev, V., Varentsova, M., Konstantinov, P., Romzaykina, O., Kanareykina, I., Dvornikov, V., & Manukyana, Y. (2021). Projecting urban heat island effect on the spatial-temporal variation of microbial respiration in urban soils of Moscow megalopolis. *Science of the Total Environment*,786(10), Article number: (147457). https://doi.org/10.1016/j.scitotenv.2021.147457

29. Wang, W., Liu, K., Tang, R., & Wang, Sh. (2019). Remote sensing image-based analysis of the urban heat island effect in Shenzhen. *China Physics and Chemistry of the Earth*, *110*, 168-175. https://doi.org/10.1016/j.pce.2019.01.002

30. Wang, Y., Yi, G., Zhou, X., Zhang, T., Bie, X., Li, J., & Ji, B. (2021). Spatial distribution and influencing factors on urban land surface temperature of twelve megacities in China from 2000 to 2017. *Ecological Indicators*, *125*, Article Number: 107533. https://doi.org/10.1016/j.ecolind.2021.107533

31. Wei, B., Bao, Y., Yu, Sh., Yin, Sh., & Zhang, Y. (2021). Analysis of land surface temperature variation based on MODIS data a case study of the agricultural pastural ecotone of northern China. *International Journal of Applied Earth Observations and Geoinformation*, *100*, Aarticle number: 102342. https://doi.org/10.1016/j.jag.2021.102342

32. Weng, Q. (2009). Thermal infrared remote sensing for urban climate and environmental studies: Methods, applications, and trends. *ISPRS Journal of Photogrammetry and Remote Sensing* , *64*(4), 335-344. https://doi.org/10.1016/j.isprsjprs.2009.03.007

33. Ye, X., Ren, H., Liang, Y., Zhu, J., Guo, J., Nie, J., Zeng, H., Zhao, Y., & Qian, Y. (2021). Cross-calibration of Chinese Gaofen-5 thermal infrared images and its improvement on land surface temperature retrieval. *International Journal of Applied Earth Observations and Geoinformation*, 101, Article number: 102357. https://doi.org/10.1016/j.jag.2021.102357

JREE: Vol. 10, No. 3, (Summer 2023) 81-98

Journal of Renewable
Energy and Environment

Journal Homepage: www.jree.ir

Materials and Energy
Research Center
MERC

Research Article

Investigation of Wind Speed to Generate Energy Using Machine Learning Algorithms Approach Over Selected Nigerian Stations

Francis Olatunbosun Aweda [a*], Segun Adebayo [b], Adetunji Ayokunnu Adeniji [a], Timothy Kayode Samson [c], Jacob Adebayo Akinpelu [a]

[a] *Physics Programme, College of Agriculture Engineering and Science, Bowen University, P.M.B. 284, Iwo, Nigeria.*
[b] *Mechatronics Engineering Programme, College of Agriculture Engineering and Science, Bowen University, P. M. B. 284, Iwo, Nigeria.*
[c] *Statistics Programme, College of Agriculture Engineering and Science, Bowen University, P. M. B. 284, Iwo, Nigeria.*

P A P E R I N F O

Paper History:
Received: 03 August 2022
Revised: 19 October 2022
Accepted: 28 October 2022

Keywords:
Meteorological Data,
Machine Learning,
Neural Network,
Statistical Models

A B S T R A C T

Wind energy has been identified as a critical component in the growth of all countries throughout the world. Nigeria has been identified as having energy issues as a result of poor maintenance of hydro and thermal energy generating stations. As a result, the current study uses some machine learning approaches over wind speed data for energy generation in the country. Machine learning models were employed for wind speed using selected meteorological parameters. Little research was done using some meteorological data and machine learning to investigate wind speed across Nigerian sub-stations, resulting in the need for further research. This research, on the other hand, focuses on a neural network for forecasting, a Long Short-Term Memory (LSTM) network model based on several fire-work algorithms (FWA). The data for this study came from the archive of the Modern-Era Retrospective analysis for Research and Applications, Version 2 (MERRA-2) Web service, which was modeled. The LSTM predicts the wind speed model based on the FWA, which used hyper-parameter optimization and was based on a real-time prediction model that was dependent on the change and dependence of the neural network. The study data was split into two categories: test and training. According to the validation technique, the sample data was reviewed, and the first 80 % of the data was utilized for training, as revealed by the (LSTM) network model. The remaining 20 % of the data was used as forecast data to ensure that the model was accurate. The normalization of the data for the wind speed range of 0 to 1 which illustrates the process data, the high peak in 1985 (a = 0.12 m/s, b = 0.11 m/s, c = 0.13 m/s, d = 0.08 m/s, e = 0.06 m/s, f = 0.10 m/s) was discovered. However, the summary result of the performances of different 11 Machine Learning algorithms of regression type for each of the seven locations in Nigeria has different values. As a result, it is recommended that this study will facilitate the prediction of wind speed for energy generation in Nigeria.

https://doi.org/10.30501/jree.2022.354698.1422

1. INTRODUCTION

Energy challenges have been an issue for decades around the world; however, wind energy is quickly gaining acceptance for the development of any country around the world through economic and commercial use for technological development. According to (Staff, 2012), a more equitable number of people have not benefitted from their national grid all over the world, particularly in the African sub-region. These challenges have grown fast in Nigeria due to the low supply of the national grid to its populace, thus attenuating the industrialization and development of the nation due to low or no power supply for the nation. Research has shown that wind energy has been known to be one of the major sources of energy (Dhunny et al., 2014; Pobočíková & Sedliačková, 2014; Salahaddin, 2013), which contributes to electricity production (Dhunny et al., 2014; Pobočíková & Sedliačková, 2014; Salahaddin, 2013) and has been considered by so many countries across the world (Dhunny et al., 2014; Pobočíková & Sedliačková, 2014; Salahaddin, 2013). However, (Pishgar-Komleh et al., 2015) reported that wind energy distribution was shown as a power generation, which contributed to Weibull distribution among other forms of energy generation. More so, (Agbo et al., 2021) reported that Nigeria's energy production could benefit from the use of wind energy. It was reported that, on average, wind energy velocity prediction contributed to the rotation of wind energy turbines in wind farms and, thus, this energy generation played a role in the development of any nation (Salahaddin, 2013). Authors in (Aliyu et al., 2015; Oyedepo, 2014) suggested methods for promoting the utilization of wind energy in Nigeria that are equally applicable to other sub-Sahara African countries; however, the major factors militating against the wind energy deployment

*Corresponding Author's Email: aweda.francis@bowen.edu.ng (F.O. Aweda)
URL: https://www.jree.ir/article_161023.html

Please cite this article as: Aweda, F.O., Adebayo, S., Adeniji, A.A., Samson, T.K., & Akinpelu, J.A. (2023). Investigation of wind speed to generate energy using machine learning algorithms approach over selected Nigerian stations. *Journal of Renewable Energy and Environment (JREE)*, *10*(3), 81-98. https://doi.org/10.30501/jree.2022.354698.1422.

2423-7469/© 2023 The Author(s). Published by MERC. This is an open access article under the CC BY license (https://creativecommons.org/licenses/by/4.0/).

in most of these countries are lack of government clear policies on wind energy and the economy of technologies. Authors in (Asiegbu, 2007; Munteanu et al., 2008; Ohunakin & Akinnawonu, 2012) found that the estimation of wind energy helped form several methods (Asiegbu, 2007; Munteanu et al., 2008; Ohunakin & Akinnawonu, 2012) for the generation of wind energy. This also shows that the usage of statistical analysis (Asiegbu, 2007; Munteanu et al., 2008; Ohunakin & Akinnawonu, 2012) to describe wind energy (Asiegbu, 2007; Munteanu et al., 2008; Ohunakin & Akinnawonu, 2012) adds to some good research (Asiegbu, 2007; Munteanu et al., 2008; Ohunakin & Akinnawonu, 2012) about wind energy generation (Chang, 2011a, 2011b; Justus et al., 1978; Kaoga et al., 2014; Martin et al., 1999; Mert & Karakuş, 2015; Waewsak et al., 2011). However, the authors of this study prefer to investigate wind energy using a machine learning approach. There is universal agreement that reliable and environmentally acceptable energy sources are critical to meeting rising energy demand (Asiegbu, 2007; Munteanu et al., 2008; Ohunakin & Akinnawonu, 2012), which is increasing at a faster rate than previously (Asiegbu, 2007; Munteanu et al., 2008; Ohunakin & Akinnawonu, 2012), due to high population growth (Asiegbu, 2007; Munteanu et al., 2008; Ohunakin & Akinnawonu, 2012), technological advancements, and development, among other factors (Antor & Wollega, 2020; Oyewole et al., 2019). Airstream and lunar energy bases appear to be viable options for renewable energy sources (Antor & Wollega, 2020). On the other hand, predicting the output of renewable energy sources is extremely challenging (Antor & Wollega, 2020). Different authors have worked on wind; some of them uses Sentinel 1 satellite image analysis by SNAP software (Majidi Nezhad et al., 2022) to conduct wind source potential assessment; a new forecasting model is based on machine learning in Sardinia. However, the authors in (Neshat et al., 2022) used quaternion convolutional long short-term memory neural model and adaptive decomposition method for wind speed forecasting in the north Aegean islands. Moreover, in (Majidi Nezhad et al., 2022), researchers investigated the sites that prioritize offshore wind energy potential and mapping for installation of wind forms in an Iranian Island. Furthermore, this study (Majidi Nezhad et al., 2020; Majidi Nezhad et al., 2022) worked on Mediterranean Sea offshore wind classification using MERRA-2 and machine learning models. However, for this research, the author uses MERRA-2 data to investigate wind speed for energy generation using a machine learning algorithm approach over selected Nigerian stations. However, because of the scarcity of electricity in Nigeria, this study was conducted.

This research aims to investigate wind speed using a machine learning algorithm approach over selected Nigeria stations. However, Machine Learning (ML) algorithms require effective training and testing to make correct predictions. Many datasets are utilized for various purposes to develop an algorithm that will generate predictions and judgments based on data from the real world according to different authors, as shown in Table 1.

Table 1. The use of multi-criteria decision-making methods by multiple studies

Methods	Description	Location	References
CEEMDAN, VMD technique, and LSTM	Application of hybrid model	China	(Ma et al., 2020)
LSTM neural network and optimal input sets	wind speed forecasting	Iran	(Memarzadeh & Keynia, 2020)
Hybrid model and LSTM	Multi-step wind speed forecasting	Brazil	(Moreno et al., 2020)
Hybrid Laguerre neural network	Wind power forecasting	China	(Wang et al., 2020)
Machine learning in biomedical datasets	Training and testing process	Turkey	(Uçar et al., 2020)
ANN	Prediction of wind speed and wind direction	Brazil	(Khosravi et al., 2018)
Predictive model	Stepwise regression and grid search	Nigeria	(Olubi et al., 2021)
ANN	Wind power density forecasting	Spain	(Rodríguez et al., 2020)
ANN	Forecasting of wind power generation	Greece	(Zafirakis et al., 2019)
ANN	Wind speed distribution	Saudi Arabia	(Brahimi et al., 2019)
ANN	Wind speed prediction	India	(Navas et al., 2020)
Wind speed prediction model	Wind speed prediction	Nigeria	(Lawan et al., 2020)
high-frequency wind power prediction	Wind speed prediction	United Kingdom	(Lin et al., 2020)
ANN	Wind turbine power prediction	Sri Lanka	(Nielson et al., 2020)
Hybrid Approach	E-mail spam	Iran	(Hassani et al., 2020)
Hybrid renewable energy system	Renewable energy system	Chennai	(Venkatakrishnan et al., 2021)
LSTM prediction	Wind speed prediction	China	(Zhang et al., 2019)
Neural network approach	Wind speed forecasting	China	(Liu et al., 2020)
Wind turbine based	Control of pitch angle	Iran	(Hosseini et al., 2022)
A numerical analysis using WT	Wind turbine power regulation	United Kingdom	(Maheri et al., 2022)

2. Network architecture with long-short time memory (LSTM)

The LSTM layer captures the temporal dependence of prior wind speed on future wind speed (Zhang et al., 2019). The information of the nonlinear correlation has a linear and maximal correlation coefficient according to Pearson's correlation. The LSTM network reveals that in the nearby gate dataset, there is a need to compare the performance of huge datasets with previously published larger predictors.

According to many studies, the gate of the input dataset undergoes sigmoid variation, resulting in the tanh of the data function. This function displays the weight value that falls within the range of -1 to 1, as given in the formulae below:

$$i_t = \sigma(w_i [h_{(t-1)}, x_t] + b_i) \tag{1}$$

$$c_t = \tanh(w_c [h_{(t-1)}, x_t] + b_c) \tag{2}$$

$$f_t = \sigma(w_f [h_{(t-1)}, x_t] + b_f) \tag{3}$$

The examined state ($h_{(t-1)}$) has a significant value in the input ($x_{(t)}$) and the outnumber of the state cell ($c_{(t-1)}$) where the value is shown to be zero. The decided gate forgot using the sigmoid input function that varied from different networks, showing that the examined state ($c_{(t-1)}$) has a significant value in the input($x_{(t)}$) and the outnumber of the state cell ($c_{(t-1)}$). This value is occasionally left out of the actual value 1 that is retained. However, the architectural output that passed through the sigmoid function gate revealed a value of 0 to 1 (Asiegbu, 2007; Munteanu et al., 2008; Ohunakin & Akinnawonu, 2012). However, the function tanh returns the weight reflection level of the output sigmoid function's crucial multiple (Adebayo et al., 2013; Shao et al., 2021).

$$o_{(t)} = \sigma(w_o [h_{(t-1)}, x_t] + b_o) \tag{4}$$

$$h_{(t)} = o_{(t)} \times \tanh(c_t) \tag{5}$$

2.1. Network of Recurrent Neural Networks (RNN)

The feed-forward network displays information from the forward direction with the input node, which could be a ring or a sequence network (Shao et al., 2021; Yin et al., 2017). There have been some decisions that have been made based on the predictions of some future events that are relevant to the current input. The feed-forward network is a severe problem to deal with since it resulted in a succession of data with no memory timeline. The recurrent neural network illustrates that the feed-forward network allows for the aforementioned output, which is based on the data input. The internal state memory of the recurrent neural network displays a sequence of input datasets. This network shows that the architectural design and application of the neural network have a significant impact on the processing of some learning languages in machines (Yin et al., 2017). This network can be mathematically represented as follows:

$$h_{(t)} = f_c(h_{(t-1)}, x_{(t)}) \tag{6}$$

where f_c is the parameterized function, $h_{(t-1)}$, $x_{(t)}$ is the input vector at time step t and is the previous state. When you use the activation function, you get:

$$h_{(t)} = \tanh(w_{hh} h_{(t-1)} + w_{xh} x_{(t)}) \tag{7}$$

and the output state is described as follows:

$$y_{(y)} = w_{hy} h_{(t)} \tag{8}$$

W indicates that the hidden vector for a unit neuron is the input weight, h. The prior weight is known as w_{hh}, whereas the present weight is known as w_{xh}. The Recurrent Neural Network (RNN) is stated to be divided into several categories. Multiple single output data (MISOD), multiple outputs, multiple inputs data (MOMID), single input, single, single output data (SISOD), and single input, multiple outputs data (SIMOD) are among these classes; however, the RNN, which is heavily influenced by some of the affected gradients, vanishes as a result of the significant problem encountered.

The Fireworks Algorithm (FWA) (Tan & Zhu, 2010) is a swarm intelligence algorithm that selects a set of random points constrained by some distance metrics in the hope that one or more of them will produce promising results (Zheng et al., 2013), allowing for a more focused search and, thereby, exploring a very large solution space in this way. The algorithm (Zheng et al., 2013) demonstrated that promising result (Salahaddin, 2013) in solutions to complex problem (Li & Tan, 2019) in a large data space (Zhang et al., 2015).

Furthermore, FWA was combined (Aliyu et al., 2015) with LSTM to improve the performance of the time series model of weather data (Pei et al., 2012).

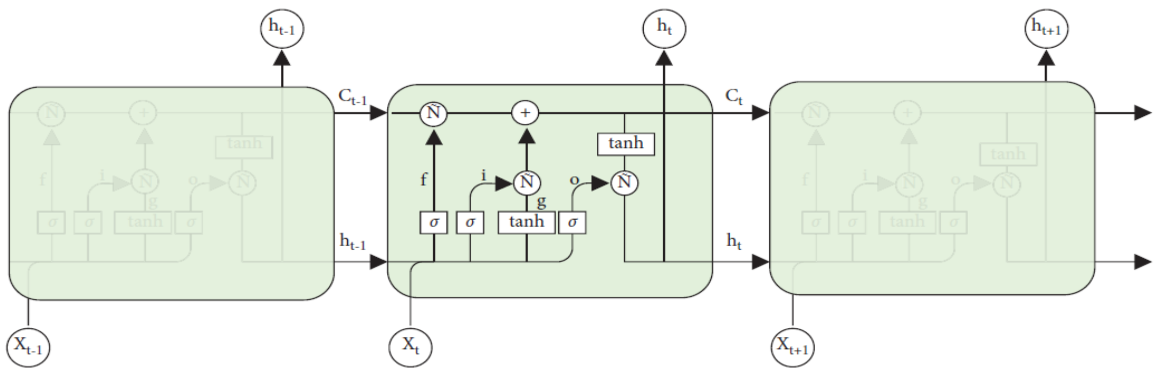

Figure 1. The LSTM's fundamental principle

3. EXPERIMENTAL

3.1. Model used for the research

For this research, the model used is based on the Artificial Neural Network and 11 different machine learning methods employed in this study; however, the data was submitted to different percentages: for example, 80 % of the data was trained while 20 % of the data was tested using Artificial Neural Network (ANN). The accuracy of machine learning algorithms in predicting wind speed in seven Nigerian cities (Sokoto, Maiduguri, Ilorin, Ikeja, Port Harcourt, and Abuja) is compared in this study, but it has a direct impact on wind generation at each location. For testing the algorithms, data samples of over 324,120 hours with 20 predictors (i.e. factors) for the wind speed response variables were obtained from the Solar Data Analysis (SoDa) website archive. The research data is derived from meteorological database parameters. Clustering data were employed to examine the dataset to get insight into it and to facilitate data simplification, which may be necessary before further processing, and this followed what was reported by (Adebayo et al., 2013; Aweda et al., 2022). However, the refractivity index of the meteorological dataset on the use of neural networks was retrieved for dataset training and testing for forecasting. Furthermore, the model evaluation and validation were matched to the statistically created model for the analysis. Thus, the performance of the proposed model was evaluated utilizing a variety of methodologies, including Mean Average Error (MAE), Root Mean Square Error (RMSE), and R-square.

Consequently, this study focused on wind energy for Nigeria's growth. Nigeria, on the other hand, has been noted as having energy challenges due to poor maintenance of hydro and thermal energy-generating units. In addition, the current research questions are as follows: to determine energy for human consumption, determine statistical analysis for energy generation, determine the performance of the LSTM and bi-LSTM for training and testing datasets, and determine data visualization of other meteorological parameters.

As a result, the current study employs several machine learning algorithms over wind speed data for energy generation in the country in order to tackle the country's energy problem using wind speed data. However, due to insufficient maintenance of hydro energy generating and poor water storage for electricity generation in the country, the study, on the other hand, focuses on a forecasting neural network, a Long Short-Term Memory (LSTM) network model based on several Fire-Work Algorithms (FWA). However, the key advantage of using LSTM models based on FWA models to tackle the country's energy crisis is that the energy generation is based on machine learning, which reduces the country's whole reliance on hydro energy generation and threatens its economy.

3.3. Data collection and description

The authors used Solar Data of Modern-Era Retrospective analysis for Research and Applications, Version 2 (MERRA-2) meteorological re-analysis for the collection of monthly air temperature, air pressure, relative humidity, wind speed, and direction for nine tropical regions of African stations (Aweda et al., 2020; Aweda et al., 2021; Gelaro et al., 2017). The data was evaluated on January 15th, 2022. From 1985 to 2021, the data was collected in Comma-Separated Value (CSV) format as a monthly average for January to December of each year. The dataset includes the name of the city, latitude and longitude coordinates, and the date of the observation (Figure 2).

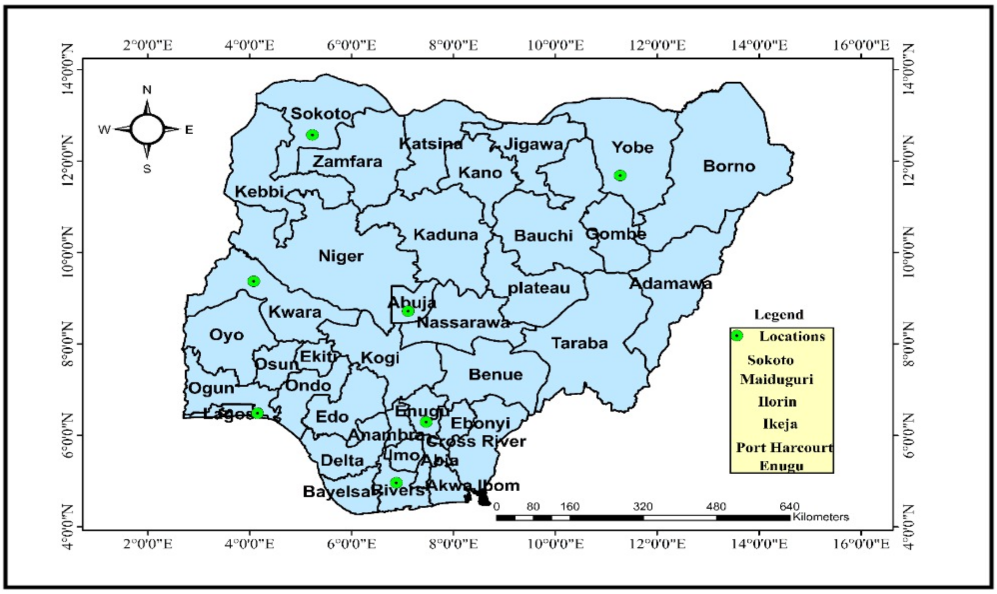

Figure 2. The stations depicted on the map

3.4. The subject of research

The following stations were employed in this study: Abuja, Ilorin, Ikeja, Damaturu, Port Harcourt, and Sokoto. These stations were chosen from throughout the country (Table 2). The effect of meteorological data across the country is demonstrated by dividing these stations into different climate areas.

3.5. Metrics for statistical accuracy

The study employed performance metrics to compute R-Squared, RMSE, and MAE by calculating data training and testing. To determine different machine learning parameters for the analysis, 80 % of the data was trained and 20 % of the data tested. However, from the standpoint of machine learning, data processing, feature selection, modeling, and testing were performed based on the nature of the data and available models for analysis. The prediction error that is related to the model performance of the wind speed dataset was investigated using statistical parameter (R-Squared, RMSE, MAE, MSE). The MAE (mean absolute error) that was employed in this study shows the difference between the expected and actual values. Mean Squared Error (MSE), on the other hand, displays the average value of a dataset by squaring the difference between real and predictable values. Furthermore, when compared to the value of the original dataset, the root means square error reveals that the coefficient of determination (R-squared) reproduces the outcome of the matches in the togetherness. In this case, the percentage and range are presumed to be between 0 and 1. In contrast, it demonstrates that the higher the value of any model, the better the outcome.

Table 2. The stations used and their locations

Stations	Longitude ^{0}N	Latitude ^{0}E
Abuja	9.07	7.49
Ilorin	6.46	7.55
Ikeja	6.61	3.35
Damaturu	11.75	11.97
Port-Harcourt	4.78	17.01
Sokoto	13.01	5.25

$$\mathrm{MAE} = \frac{1}{N}\sum_{t=1}^{N}\left|y_i - \hat{y}\right| \tag{9}$$

$$\mathrm{MSE} = \frac{1}{N}\sum_{t-1}^{N}\left(y_i - \hat{y}\right)^2 \tag{10}$$

$$\mathrm{RMSE} = \sqrt{\mathrm{MSE}} = \sqrt{\frac{1}{N}\sum_{t-1}^{N}\left(y_i - \hat{y}\right)^2} \tag{11}$$

$$R^2 = 1 - \frac{\sum\left(y_i - \hat{y}\right)^2}{\sum\left(y_i - \overline{y}\right)^2} \tag{12}$$

where $\hat{y}$ – the predicted value of y, $\overline{y}$ – mean value of y.

2.6. Normalization of wind speed processes

$$X_{nor} = \frac{X - X_{min}}{X_{max} - X_{min}} \tag{13}$$

Equation 12 is the normalization formula used in the study. X_{nor} represents the normalization, X_{max} the maximum value of the wind speed data, and X_{min} the minimum value of the wind speed data used in the study.

4. RESULTS AND DISCUSSION

The following stations are labeled based on the results reported in the manuscript as shown in Figure 3 (a to f) as in a-Abuja, b-Ilorin, c-Ikeja, d-Maiduguri, e-Port-Harcourt and f-Sokoto. This displays the wind speed data after the machine learning method has filled in the nulls. The findings indicate that practically every considered station has an almost similar pattern. This demonstrates that all stations in Nigeria have the same wind speed pattern.

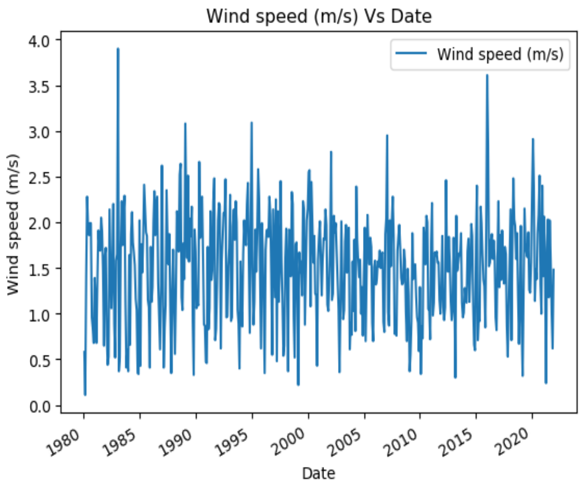

(a)

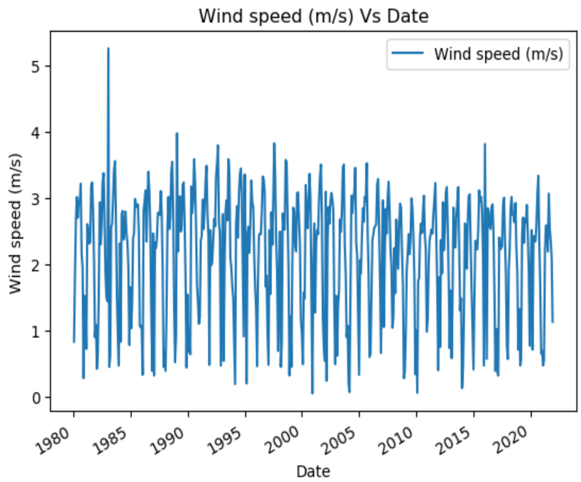

(b)

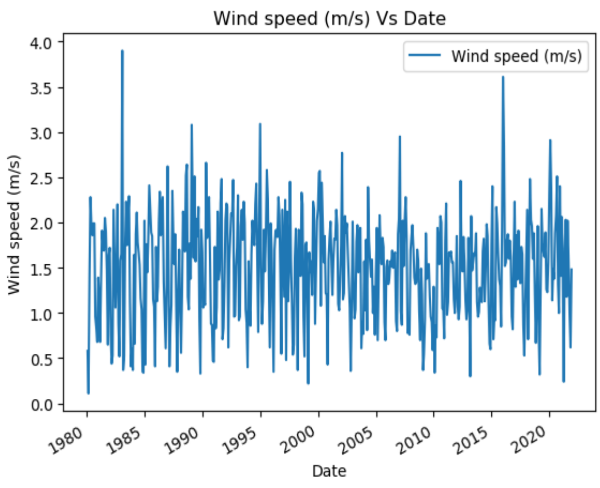

(c)

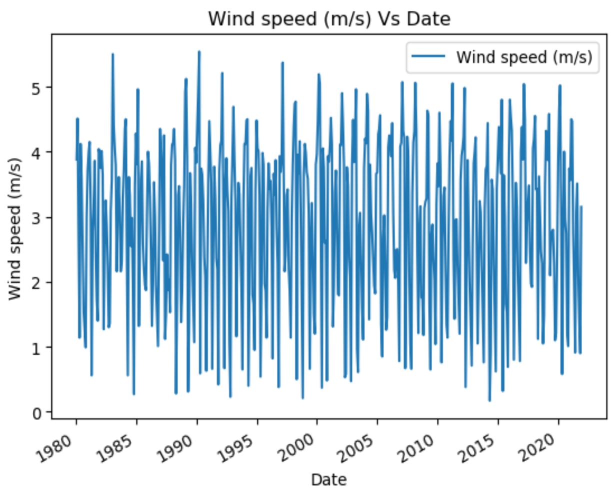

(d)

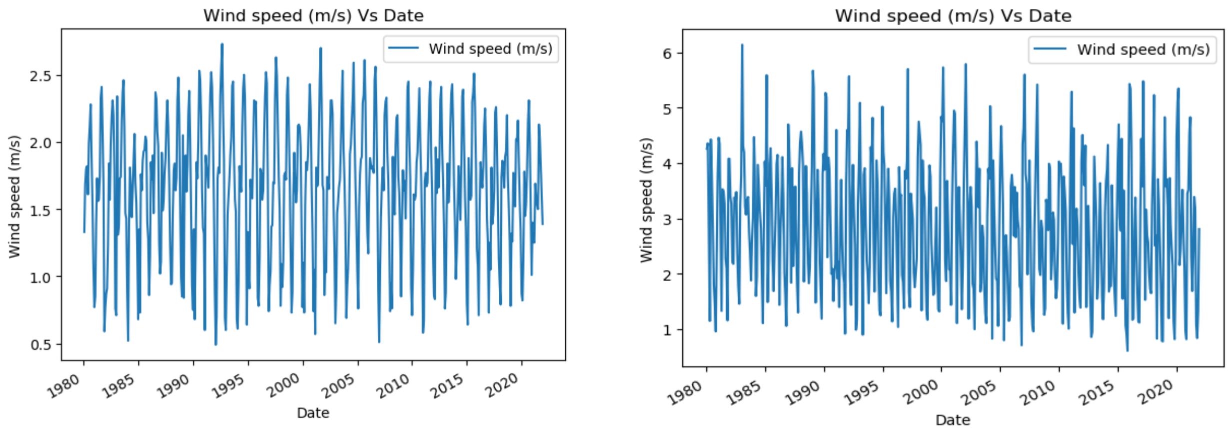

(e) (f)

Figure 3. Wind speed after the machine learning method has filled in the nulls

The result in Figure 3 (a to f) demonstrates that the pattern of wind speed at each station is nearly identical, indicating that the wind speed at the chosen station moves at a similar pace, which can increase the production of wind energy across the entire nation. However, during the period when energy output from wind is increasing, short-term wind speed predictions are crucial. Furthermore, Figure 3 (a to f) shows the wind speed vs date for the stations under investigation. The maximum wind speed for the stations was found to be between (6.5-2.6 m/s), while the minimum wind speed was found to be between (0.2-1.0 m/s). This demonstrates that the wind speed for energy generation in the reported stations is low.

Figure 4 (a to f) shows the dataset split ratio into trained and tested, demonstrating that 80 % of the dataset is used for training and the remaining 20 % for the purpose test set. However, several writers have stated that the test and trained data are critical when using machine learning to model wind speed. The trained data for this study covers the years 1985 to 2014, whereas the test data covers the years 2015 to 2021; this equates to 30 years of training and 7 years of testing. However, the training of the data set takes longer than the testing. Furthermore, if the numerical value of the samples was adequate, the sampling techniques for this research dataset would be balanced. According to authors (Junior & do Carmo Nicoletti, 2019; Rojas, 2009), if approaches like Boosting and AdaBoost are employed for any study, the number of data sets used will be sufficient. Each of the samples utilized, however, participates in the training and testing operations of the dataset, being separated into parts, and the other portions participate in the dataset training, as reported in (Junior & do Carmo Nicoletti, 2019; Rojas, 2009). By averaging the accuracy rates used to obtain each classification technique, the outcome validation for each piece of data testing at each phase may be done.

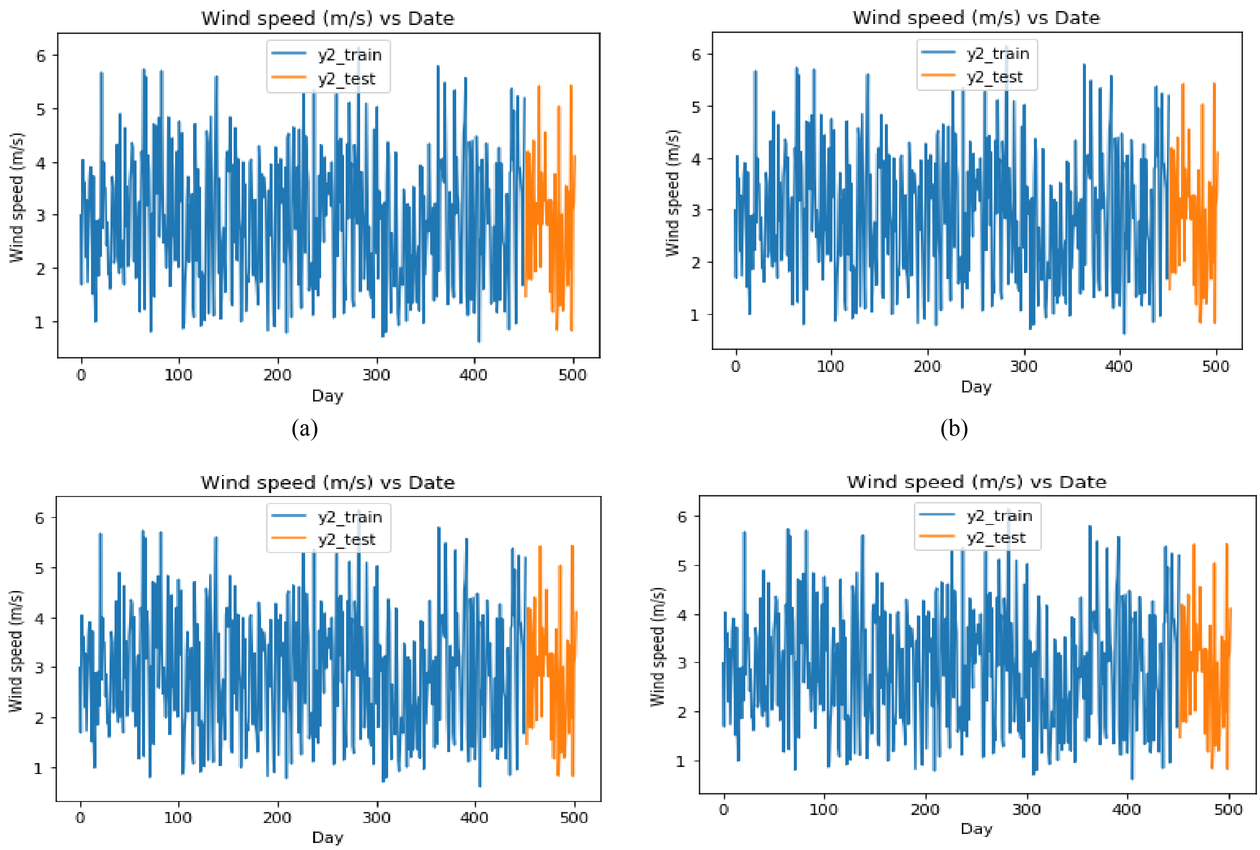

(a) (b)

(c) (d)

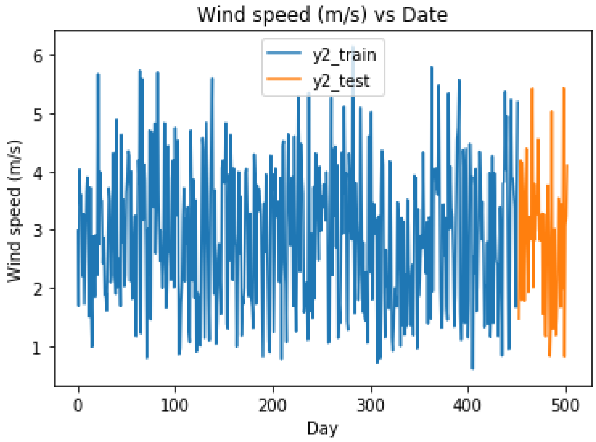

(e)

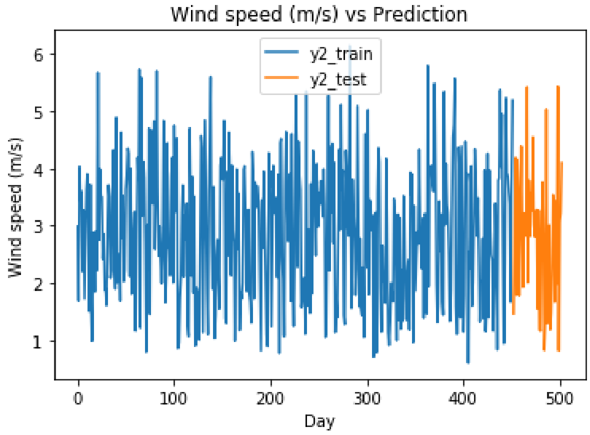

(f)

Figure 4. Training and testing of the wind speed over the selected stations

As shown in Figure 4 (a to f), the data for the study were divided into two sets: testing and training. The sample data was examined, and the first 80 % of the data was used for training, as revealed by the LSTM network model, according to the validation procedure. The remaining 20 % of the data was utilized as the prediction data to verify the model efficiency.

Results in Figure 4 show that the training data had more input than testing data. However, this demonstrates that the training data are more important than testing data. Moreover, the training data indicate that the wind speed performs better.

Figure 5 shows data normalization using Equation 12. This is used to process wind speed data (Junior & do Carmo Nicoletti, 2019; Rojas, 2009) for samples with values ranging from 0 to 1. Figure 5 depicts the process data, showing a high peak in 1985 (a = 0.12 m/s, b = 0.11 m/s, c = 0.13 m/s, d = 0.08 m/s, e = 0.06 m/s, f = 0.10 m/s). The results reported in Figure 4 (a to f) are based on training and testing data sets that span 36 years. However, the figure was plotted using 500 days. This is because the data was normalized. The train days were approximately 450 days, while the test data was approximately 50 days.

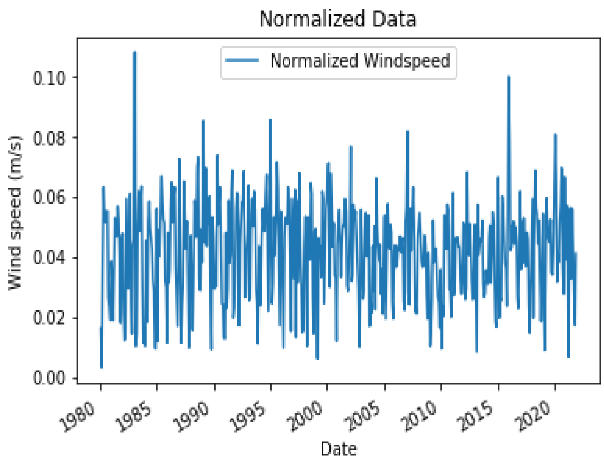

(a)

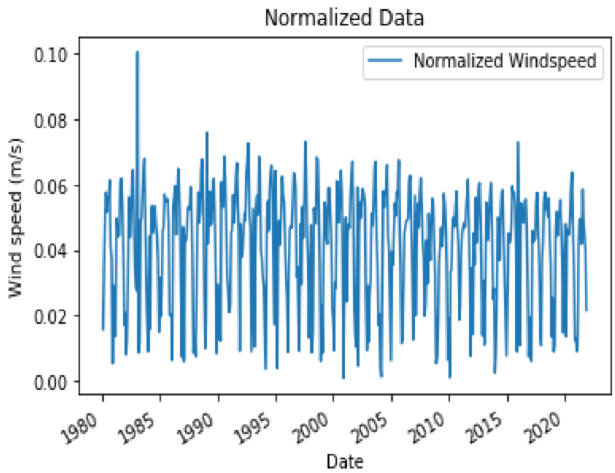

(b)

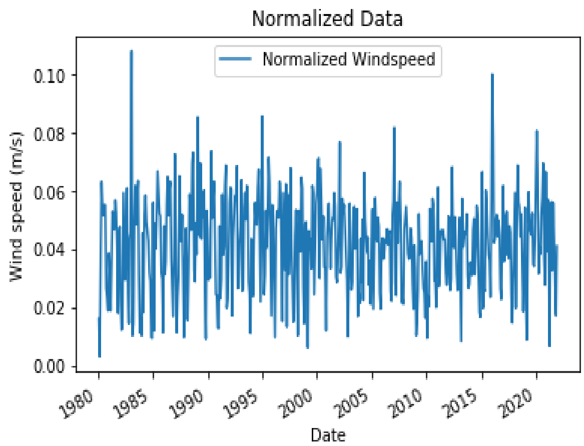

(c)

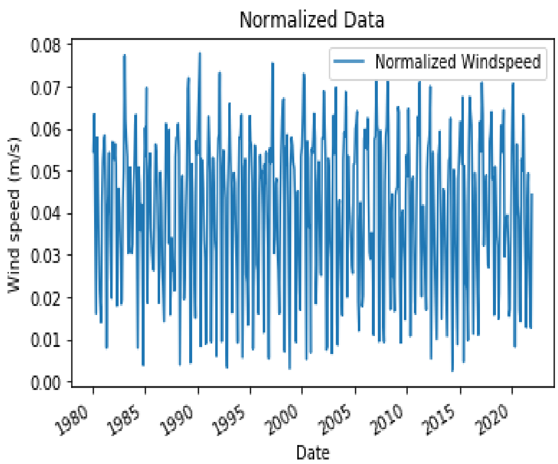

(d)

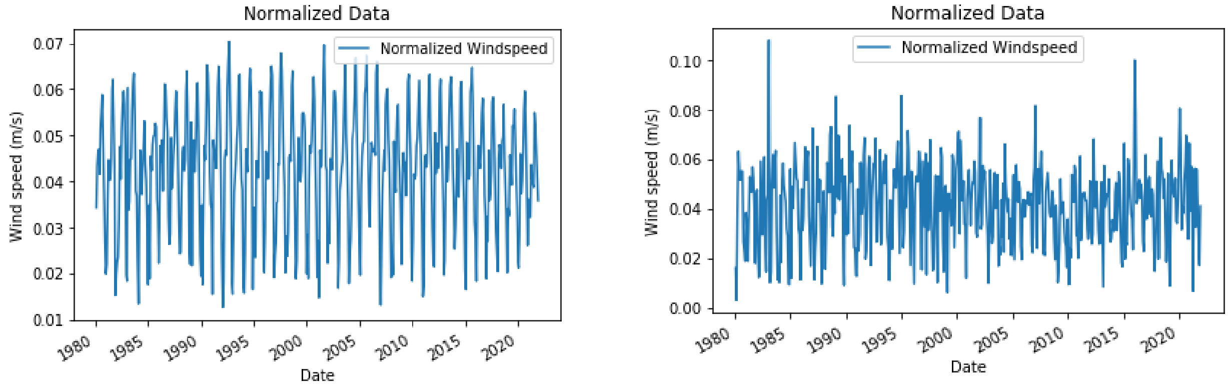

(e) (f)

Figure 5. Normalization of wind speed processes over selected stations

The range standardization process for wind speed data, which ranges from 0 to 1, is demonstrated by the data normalization and is based on the computation method used during the range standardization (Shao et al., 2021). However, as reported by authors in (Shao et al., 2021), the training of the LSTM network model and the first 80 % of the data are used as the training data. The remaining 20 % of the data are utilized as prediction data to assess the model effectiveness. The outcome thus demonstrates the significance of wind speed and direction in energy generation forecasting, which could result in the production of energy across the entire country. Wind speed normalization, in particular, demonstrates that the data are typically adjusted for the aim of energy production.

4.1. The theoretical frequency of wind speed

By exhibiting relative frequencies associated with the stations under investigation as shown in Figure 6 (a to f), the histogram shows that the dataset is standardized. The fraction of cases that fall into multiple categories is equal to 1 according to the findings. Abuja has a maximum frequency of 70 and a minimum frequency of around 8. Ilorin, on the other hand, has a maximum frequency of roughly 76 and a low frequency of around 3. Other stations, as indicated in Figure 6, appear to follow the same pattern. The reported results revealed that the frequency of wind speed was critical. The findings point to this conclusion that the categories of consecutive, non-consecutive, and non-overlapping variable intervals with categories (intervals) are contiguous, and they are all of the same size, as shown in the figures. Each of the indicators continuously has its original variables, as shown by the histogram rectangle. However, the result shows that none of the best numbers is bins, denoting different size bins, as some data reveals. The theoretical bin demonstrates that the optimal number of data bins is determined from various attempts. The bin with widths adequate for the experimentation of the dataset utilized in the result is denoted by the distribution dependence and the analysis purpose.

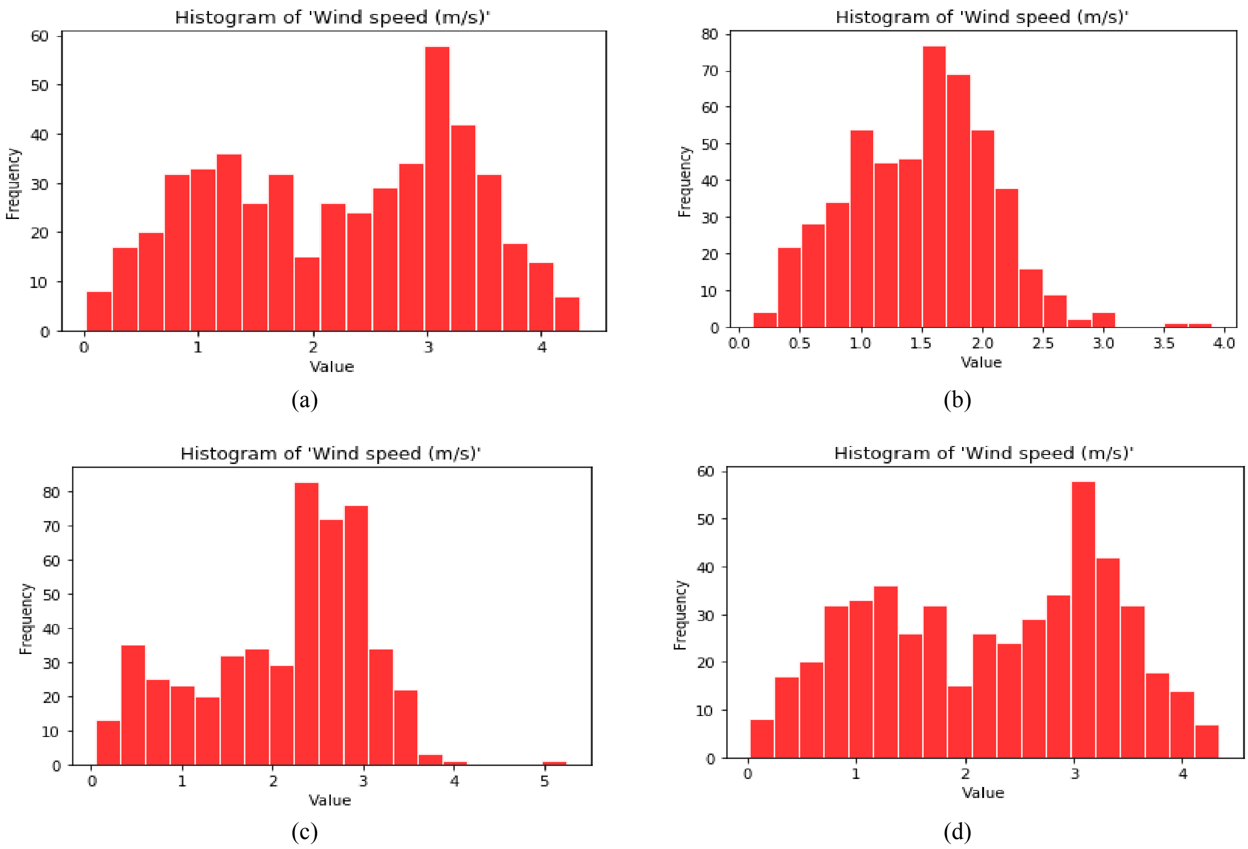

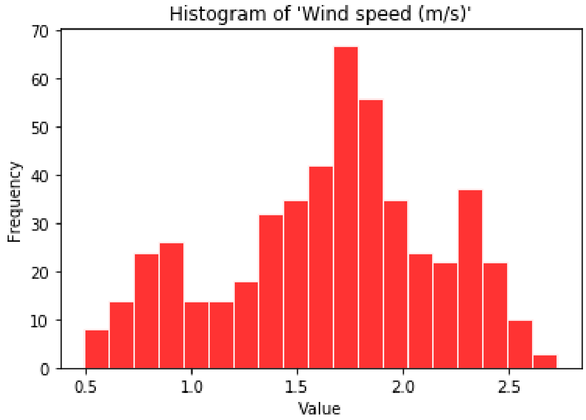

(e)

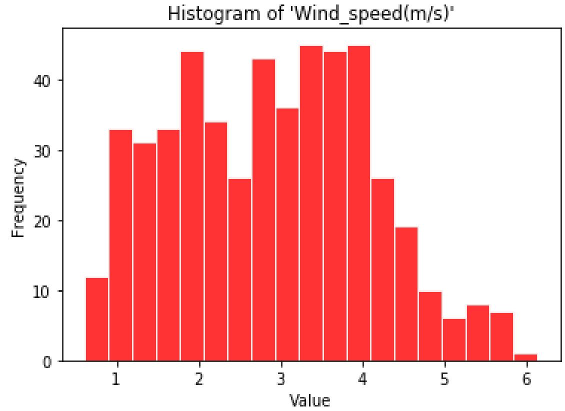

(f)

Figure 6. Frequency dataset of the wind speed

The frequency result of the wind speed data demonstrates that wind speed contributes significantly to the outcome of energy production. However, the frequency result demonstrates that good energy generation occurs when the data are well correlated, which will increase the country's overall energy production.

4.2. Wind speed prediction using basic LSTM

The core four layers of the LSTM model as shown in Figure 7 (a to f), each with one input layer and two hidden levels each with one output layer, are used to forecast wind speed. That is, the connection among the three layers of the LTSM is established by the 1st layer of the LTSM, which receives an input time step of variable 1, but has 64 neurons, as stated in (Shao et al., 2021). The input of the training data transforms into its output, which appears after the hidden layer as the 2nd layer used in this study. In addition, the input of the training transforms into its output, which appears after the hidden layer as the third layer used in this study. The number of neurons in this study indicates that the first layer has the same pattern as in Figure 7 and that the third layer (Dense) uses the first layer of the long short-term memory for the output layer of the third layer, as shown in the result. The output of the 2nd layer is similarly received by the 3rd layer, which is shown as input, and the connection is the result of the connected layer. The results of the studied stations show that a one-dimensional vector with a length of 150 output data sets is connected in the learning for the final output of future data sets. The output results provided 150 data points, as shown in Figure 7. The hidden layer is used to regularize the 2nd layer, as shown in the image, and the LSTM is used to validate the dropout layer of the data that was added to the 1st layer, confirming what was reported by the previous layer (Shao et al., 2021). According to the results of the tests, the accuracy of the training set with the greatest dropout of 0.2 s was discovered (Ma et al., 2021; Shao et al., 2021).

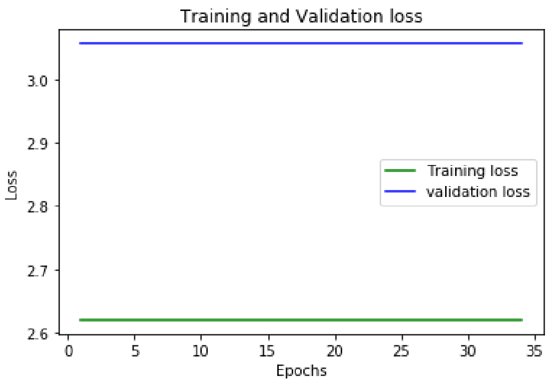

(a)

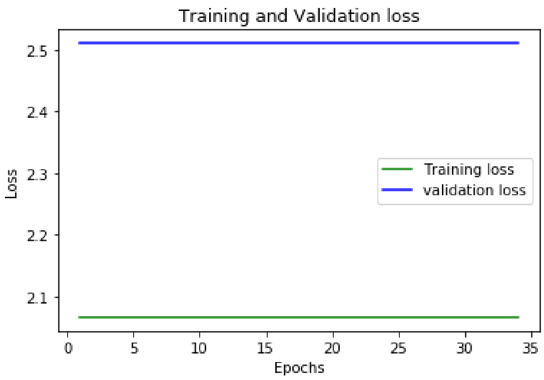

(b)

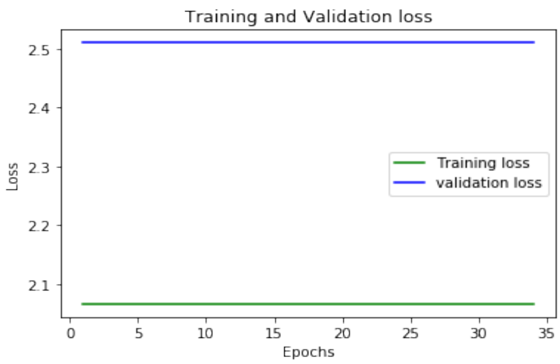

(c)

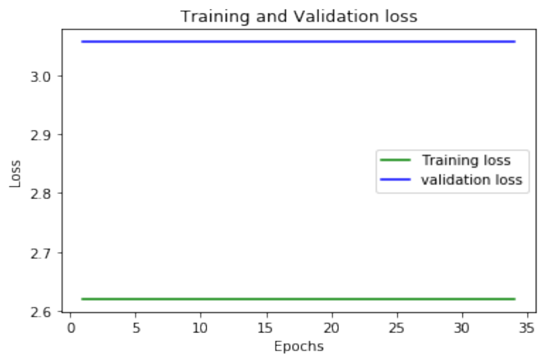

(d)

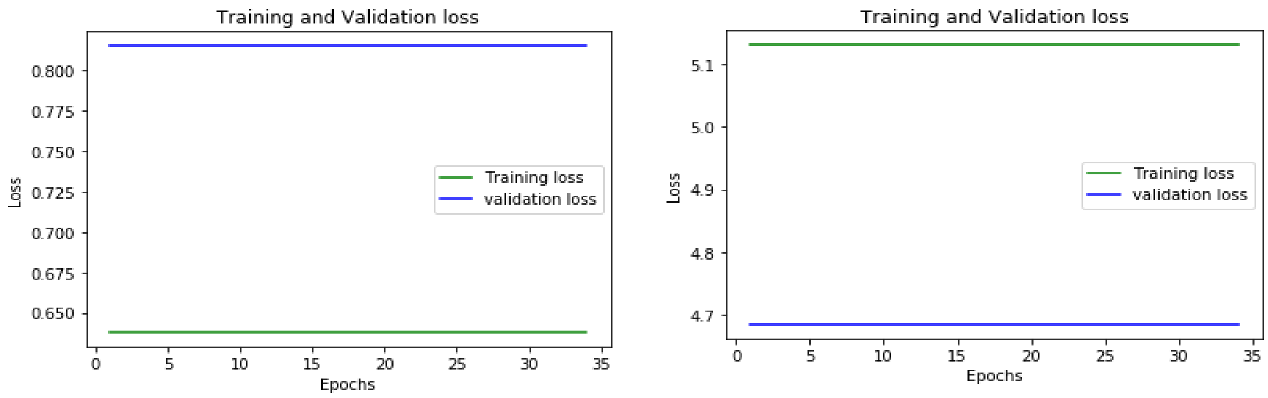

(e) (f)

Figure 7. The performance of the LSTM and bi-LSTM for training and testing datasets

The performance of the bidirectional long-short term memory (bi-LSTM) may be seen in this result, where the training and validation loss line is always close to one and the loss is virtually zero. The model, on the other hand, is of well-trained validation. The Recurrent Neural Network (RNN), LSTM, and bi-LSTM works were found useful in the investigation of wind speed validation and training in this study. As a result, each of the models employed in this study is unique. Finally, the step-by-step approach yielded a simple bi-LSTM model for text classification following what was reported by (Samadianfard et al., 2020). The data set, on the other hand, was idle for the categorization process, and most of the models demonstrate a real-life problem solution for the research of wind patterns at the specified study stations. More specifically, the model investigates what happened with the real-world wind speed data issue. As a result, it will text data, audio data, and time series data for the benefit of the outcome.

The LSTM and bi-LSTM research indicate that the wind energy forecast will increase product knowledge for the improvement of energy generation. If this is put to use, it will aid in the decrease of the energy problem that the entire nation is currently experiencing. Additionally, given that energy is a major problem throughout the world, LSTM and bi-LSTM will account for a significant energy generation to lessen the burden placed on hydroelectric energy output.

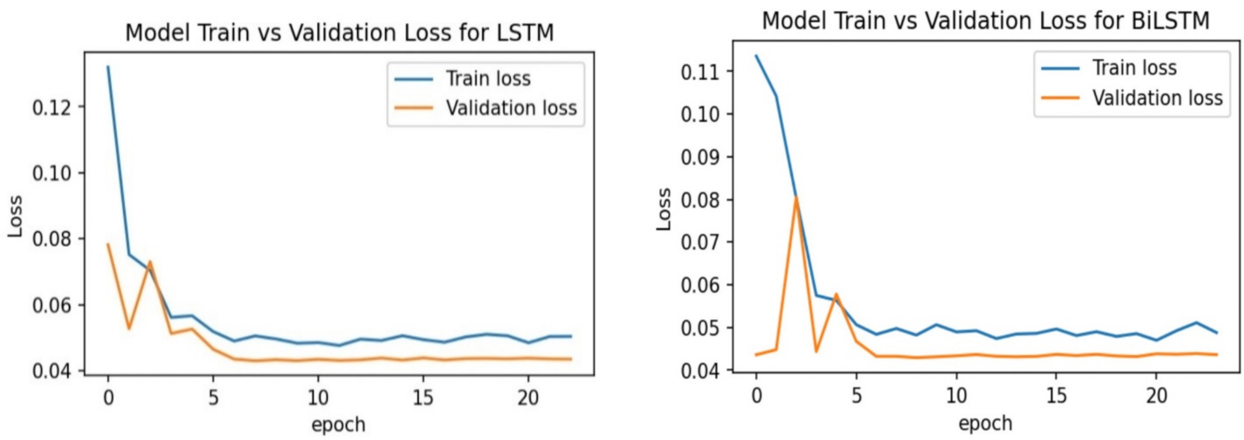

(a) (b)

Figure 8. Model training performance against validation loss

Figure 8 shows the difference in wind speed prediction performance among LSTM, BiLSTM, and GRU in terms of training and validation loss. The minimum training and validation cost (loss) functions are 0.04 and 0.045 at the 4^{th} epoch for BiLSTM, 0.043 and 0.046 at the 5^{th} epoch for LSTM, and 0.05 and 0.01 at the 6^{th} epoch for GRU. This demonstrates that although having the lowest cost function, the GRU model has a faster convergence time. To avoid model overfitting, the training process was terminated when the validation error trend shifted from dropping to climbing; this followed what was reported by authors in (Moghadasi et al., 2021).

4.3. The training algorithm's performance

Table 3 presents the summary result of the performances of the different 11 Machine Learning algorithms of regression type for each of the seven locations in Nigeria. For Abuja, Coarse Tree, Ensemble Bagged Trees, and Gaussian-Squared Exponential GPR show the highest R^2 of 0.44, while for Enugu, it was medium Tree (R^2 = 0.74). Result reveals that in Ikeja, Gaussian-Squared Exponential GPR and Rotational Quadratic GPR (R^2 = 0.37); for Ilorin, R^2 = Ensemble Boosted Trees; for Maiduguri, it was Narrow Neural Network; for Port-Harcourt, it was Medium Gaussian SVM (R^2 = 0.81), while for Sokoto, the Narrow Neural Network that gave the highest R^2 (R^2 = 0.68). This implies that these ML algorithms exhibit better fitness performance than other models. In terms of forecasting performance of these ML algorithms based on RMSE, the best forecasting Machine Learning model was Ensemble Bagged Trees for Ikeja (RMSE = 0.10299); Medium Tree for Enugu (RMSE = 0.0876); Gaussian-Squared Exponential GPR and Rotational Quadratic GPR for Ikeja (RMSE = 0.11969). Result reveals that Ensemble Boosted

Trees give the least RMSE for Ilorin (RMSE = 0.10651), Narrow Neural Network for Maiduguri (RMSE = 0.1029), Medium Gaussian SVM for Port-Harcourt (RMSE = 0.10115), and Ensemble Boosted Trees for Sokoto (RMSE = 0.1218), meaning that these ML algorithms outperformed other models.

Table 3. Summary result of the machine learning Algorithm (MLA) for wind speed data across selected stations in Nigeria

Different Models Used	**Abuja**			**Enugu**			**Ikeja**			**Ilorin**		
Machine Learning Algorithm	**R^2**	**RMSE**	**MAE**	**R^2**	**RMSE**	**MAE**	**R^2**	**RMSE**	**MAE**	**R^2**	**RMSE**	**MAE**
Medium Tree	0.40	0.10681	0.081377	0.74	0.087688	0.065278	0.31	0.12486	0.088858	0.79	0.11676	0.089249
Coarse Tree	0.44	0.10312	0.080436	0.55	0.11562	0.09035	0.33	0.12353	0.090195	0.75	0.12643	0.10061
Fine Gaussian SVM	0.33	0.11301	0.085718	0.68	0.097669	0.071186	0.31	0.12535	0.090072	0.77	0.12161	0.092987
Medium Gaussian SVM	0.40	0.10645	0.084072	0.63	0.1041	0.076264	0.31	0.12551	0.093378	0.77	0.1233	0.096499
Ensemble Boosted Trees	0.36	0.10974	0.08792	0.68	0.096728	0.071891	0.33	0.12295	0.090359	0.83	0.10651	0.082177
Ensemble Bagged Trees	0.44	0.10299	0.081808	0.67	0.098439	0.0747	0.36	0.12066	0.0936	0.77	0.12106	0.09426
Gaussian-Squared Exponential GPR	0.44	0.10312	0.080436	0.66	0.10076	0.077159	0.37	0.11969	0.087037	0.79	0.11705	0.0911044
Gaussian-Matern 5/2 GPR	0.38	0.10814	0.085041	0.66	0.10076	0.077127	0.36	0.12538	0.092184	0.79	0.1175	0.091995
Exponential GPR	0.37	0.10937	0.085171	0.67	0.099089	0.075147	0.31	0.12086	0.088137	0.79	0.11759	0.091529
Rotational Quadratic GPR	0.39	0.10736	0.084767	0.66	0.10082	0.077192	0.37	0.11969	0.08707	0.79	0.11723	0.091341
Narrow Neural Network	0.39	0.10764	0.08163	0.71	0.093159	0.067218	0.36	0.12493	0.095756	0.79	0.11665	0.090558
Bidirectional LSTM	-0.0024	0.5298	0.4141	-0.0002	0.8609	0.7271	-3.6399	9.6416	8.5489	-0.0243	0.8712	0.6876
LSTM	-0.0792	0.5497	0.4405	-0.0080	0.8642	0.7471	-3.5740	9.5729	8.4762	-0.0289	0.8731	0.6846
GRU	-0.0025	0.5298	0.4143	-0.0017	0.8615	0.7361	-3.5788	9.5778	8.4802	-0.0178	0.8684	0.6928
Different Models Used	**Maiduguri**			**Port-Harcourt**			**Sokoto**					
Machine Learning Algorithm	**R^2**	**RMSE**	**MAE**	**R^2**	**RMSE**	**MAE**	**R^2**	**RMSE**	**MAE**			
Medium Tree	0.78	0.10669	0.08342	0.80	0.10463	0.078763	0.62	0.12971	0.094396			
Coarse Tree	0.74	0.117	0.093373	0.68	0.13324	0.10785	0.56	0.1394	0.10293			
Fine Gaussian SVM	0.73	0.11877	0.087973	0.78	0.11094	0.082671	0.62	0.12885	0.091896			
Medium Gaussian SVM	0.67	0.13115	0.10104	0.81	0.10115	0.077071	0.56	0.13886	0.11089			
Ensemble Boosted Trees	0.78	0.10768	0.082073	0.77	0.1118	0.086639	0.66	0.1218	0.090333			
Ensemble Bagged Trees	0.75	0.1131	0.090676	0.80	0.10471	0.081664	0.59	0.13391	0.10418			
Gaussian-Squared Exponential GPR	0.77	0.10981	0.083424	0.80	0.110449	0.077995	0.66	0.12242	0.90771			

Gaussian-Matern 5/2 GPR	0.77	0.10925	0.084038	0.80	0.10422	0.077357	0.66	0.12208	0.089877
Exponential GPR	0.77	0.1086	0.083315	0.80	0.10463	0.077443	0.66	0.12276	0.090102
Rotational Quadratic GPR	0.77	0.10981	0.083424	0.80	0.10437	0.07769	0.66	0.12242	0.090771
Narrow Neural Network	0.80	0.1029	0.081107	0.79	0.10652	0.077358	0.68	0.12444	0.096222
Bidirectional LSTM	-0.0330	1.2208	1.0137	-0.0321	0.4111	0.3304	-0.0319	1.3147	1.0921
LSTM	-0.0691	1.2419	1.0248	-0.0470	0.4140	0.3323	-0.0283	1.3124	1.0904
GRU	-0.0882	1.2530	1.0305	-0.0139	0.4074	0.3293	-0.0351	1.3168	1.0936

Furthermore, the performance of LSTM, BiLSTM, and GRU models is shown in Table 3 using three assessment metrics: R^2, MAE, and RMSE. The neurons in the hidden layers, as well as the hyper-parameter turning, significantly affect the architecture of the models. The number of hidden layers was modified from two to five to achieve the best architecture, with each layer holding thirty neurons. The average coefficients of determination (R^2) for all the stations observed for LSTM, BiLSTM, and GRU with two layers are -0.548, -0.538, and -0.534, respectively. This demonstrates that the three models outperform the other models used. Furthermore, as the model complexity increases, so does its performance. The MAE and RMSE statistics show that as the number of neurons increases, GRU and BiLSTM tend to marginally reduce prediction errors in comparison to the LSTM neural network model. GRU outperformed both the BiLSTM and LSTM by a narrow margin. Table 4 further demonstrates that wind speed prediction using GRU with one hidden layer has the lowest MAE and RMSE.

The pair plots of meteorological data utilized for wind speed prediction are shown in the resulting Figure 9 (a to f). It was discovered that the tools swiftly investigated how to distribute the dataset and the relationships within it.

The sea born, on the other hand, demonstrates that the pair plot of the dataset is the easy default way. As seen in Figure 9, wind speed against temperature has a fragmented dataset for all of the stations studied. The customized extended pair grid, on the other hand, demonstrates that the dataset is a significant component of the value, which is derived not from showy machine learning but the visualization of the dataset. A pair plot is a powerful tool for analyzing large datasets. This aids in the display of the weather data.

Table 4 displays the descriptive statistics analysis of the variability of wind speed data for the chosen stations. The results show that the maximum wind speed recorded was 6.14 at Sokoto in January with a standard deviation of 0.74, while the minimum wind speed recorded was 0.10 at Ilorin in December, with a standard deviation of 0.61. However, this demonstrates that Sokoto is Iran's north, whereas Ilorin is Iran's centre. As a result, high wind speed in the north and low wind speed in the south of the country are given.

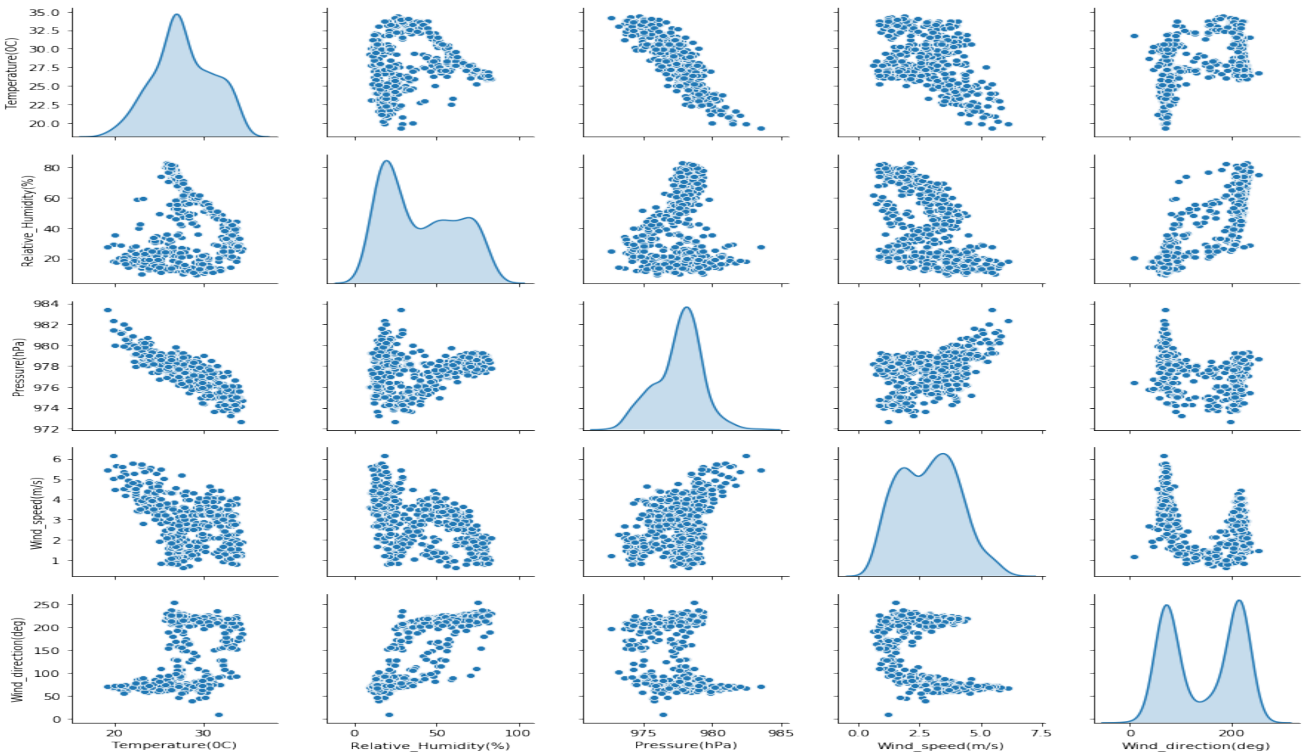

(a)

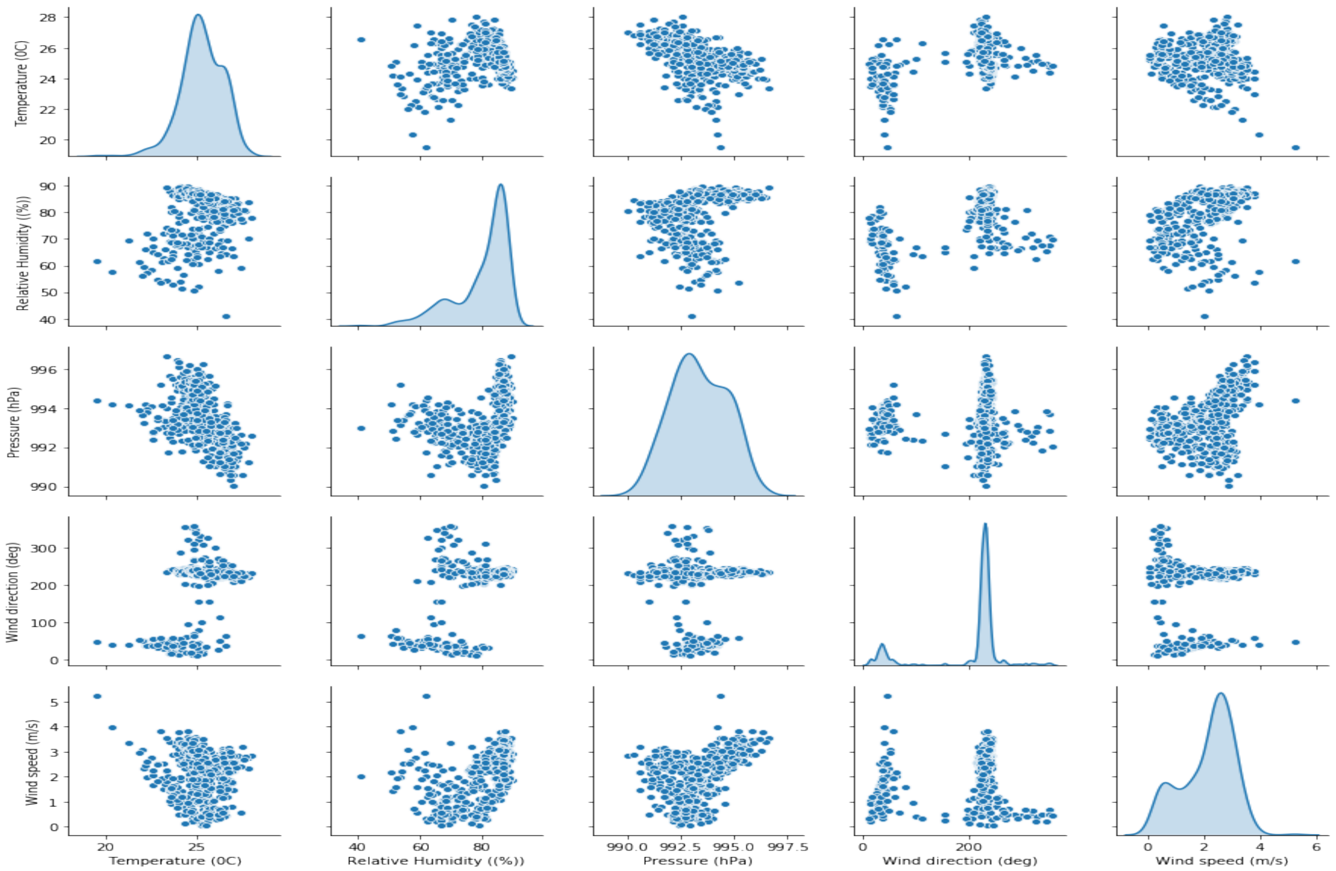
Temperature (0C)
Relative Humidity ((%))
Pressure (hPa)
Wind direction (deg)
Wind speed (m/s)

(b)

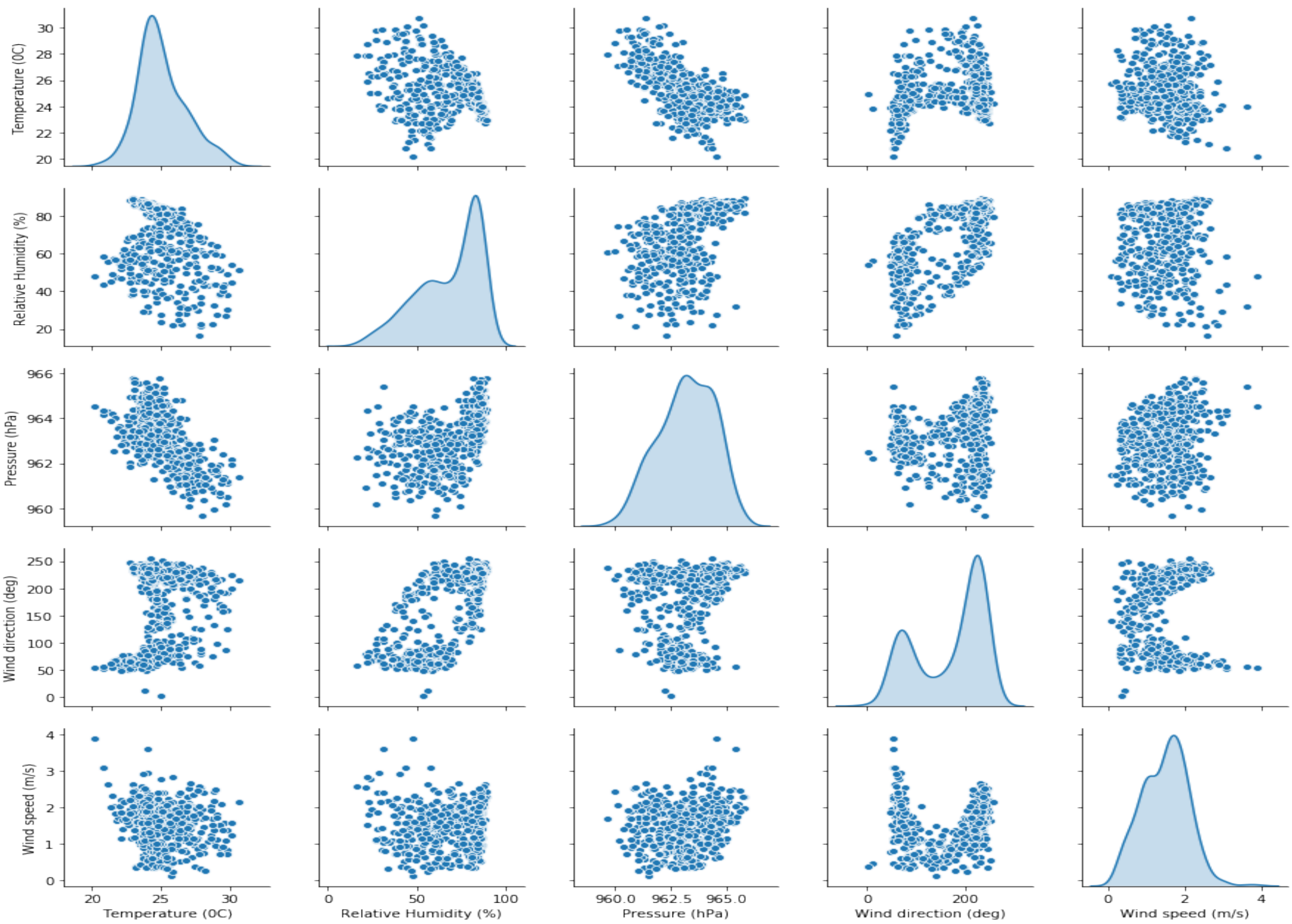
Temperature (0C)
Relative Humidity (%)
Pressure (hPa)
Wind direction (deg)
Wind speed (m/s)

(c)

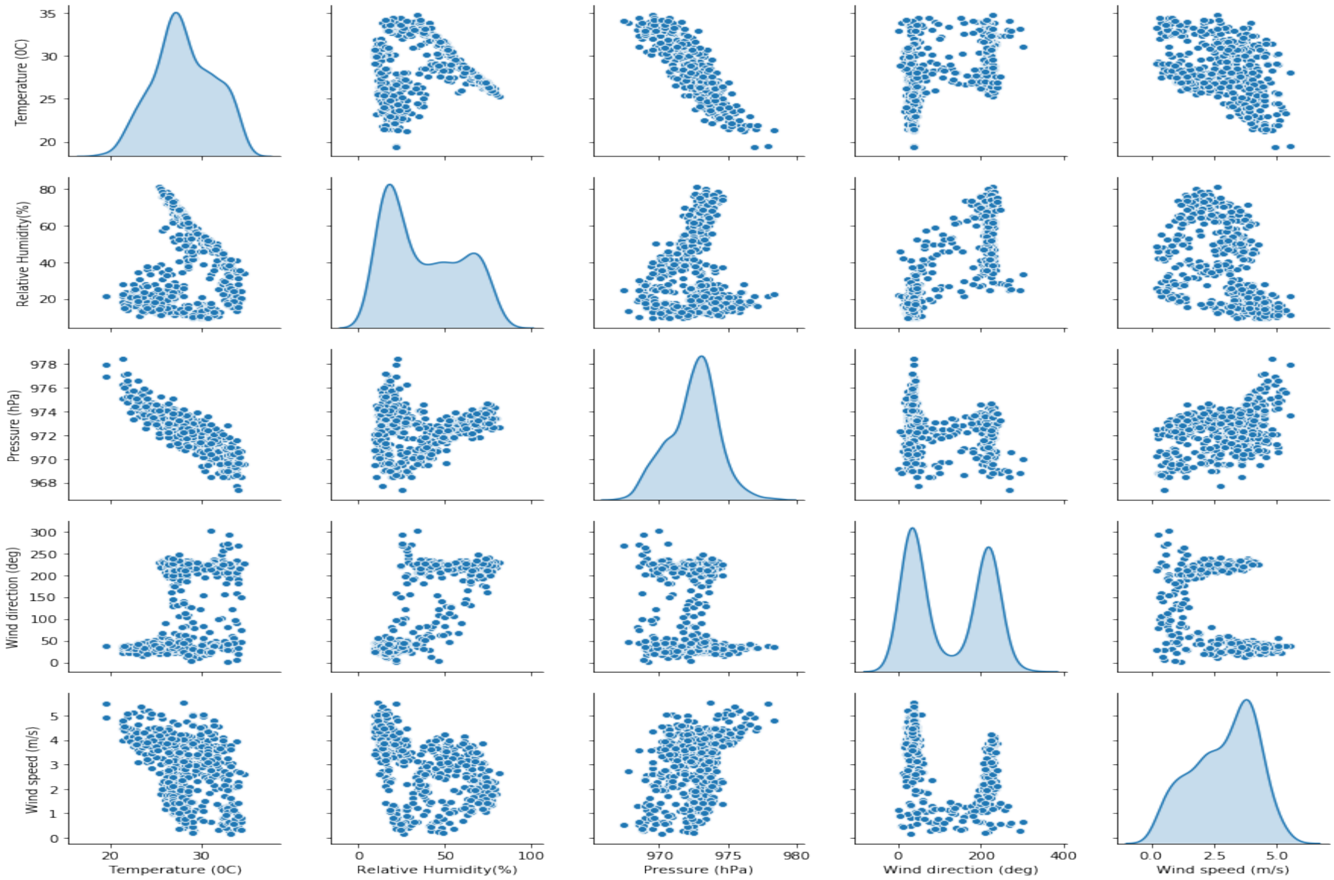
Temperature (0C)
Relative Humidity(%)
Pressure (hPa)
Wind direction (deg)
Wind speed (m/s)

(d)

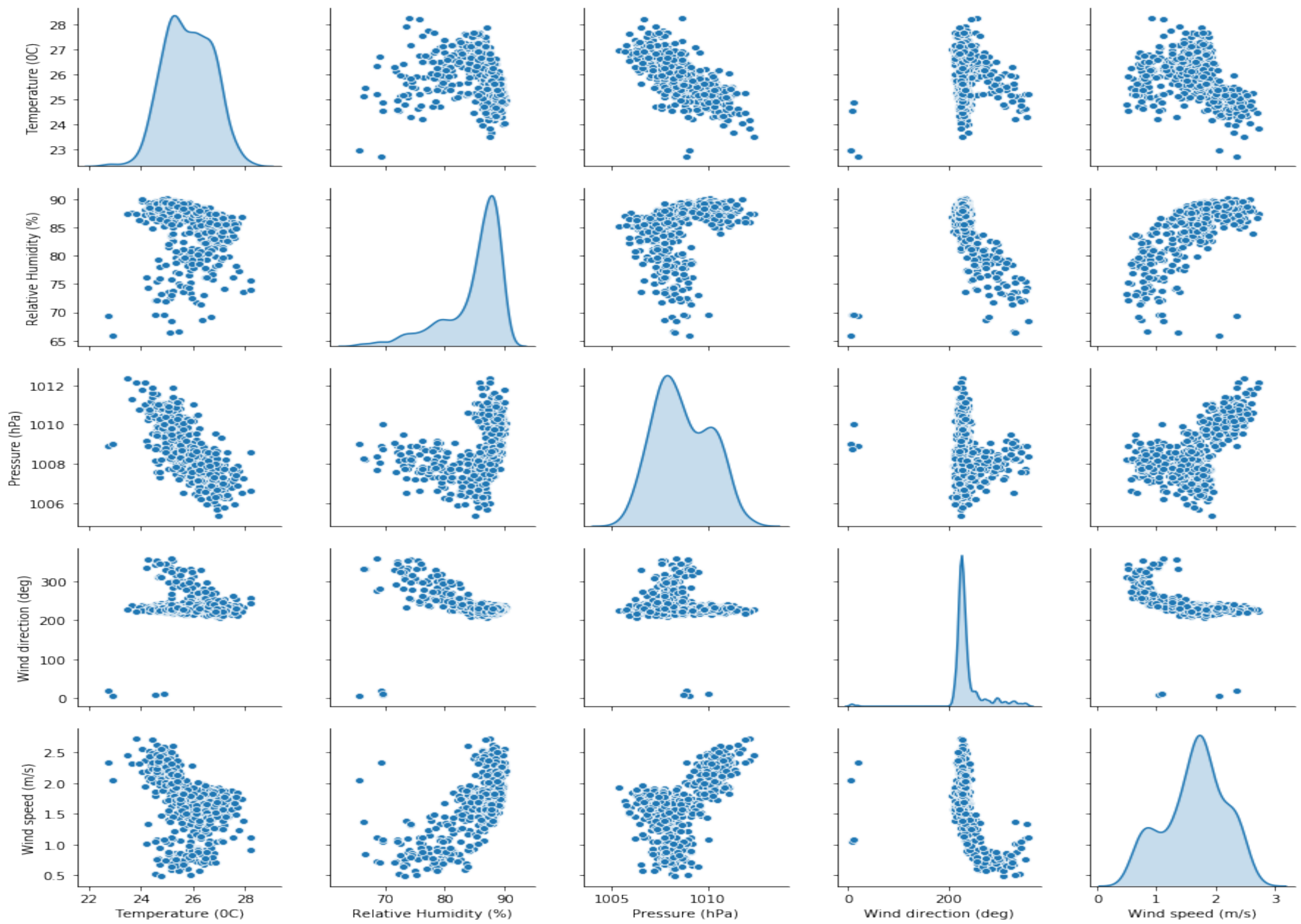
Temperature (0C)
Relative Humidity (%)
Pressure (hPa)
Wind direction (deg)
Wind speed (m/s)

(e)

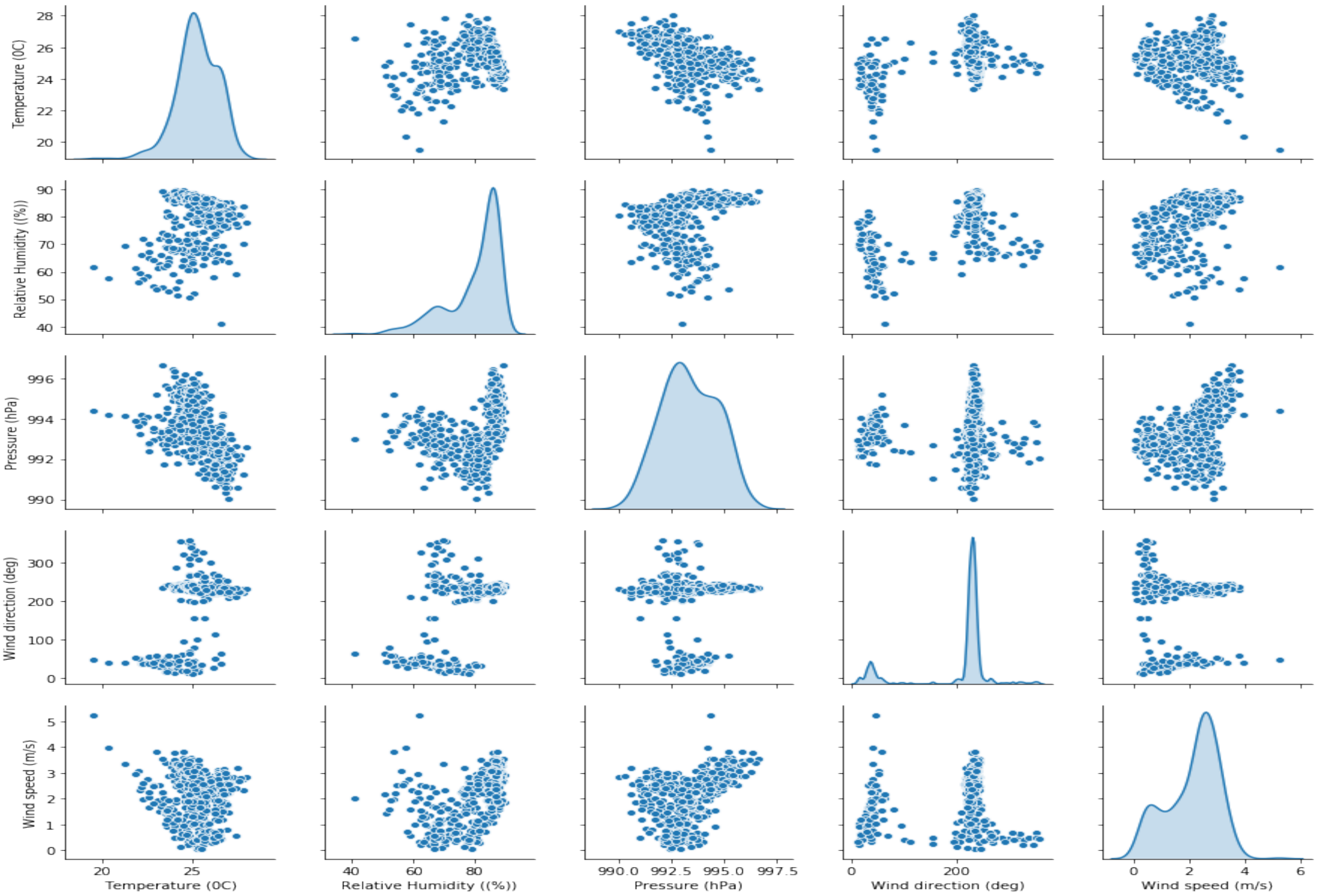

(f)

Figure 9. Data visualization of the meteorological parameters

Table 4. Summary result of the statistical evaluation for wind speed data across the selected stations in Nigeria

Months	Abuja				Enugu				Ikeja				Ilorin			
	Min	Max.	Mean	STD	Min	Max.	Mean	STD	Min	Max.	Mean	STD	Min	Max.	Mean	STD
Jan.	0.34	3.90	0.83	1.63	0.06	5.25	1.42	1.15	0.34	3.90	1.63	0.83	0.13	4.15	1.32	0.90
Feb.	0.11	2.57	0.65	1.10	0.07	2.80	1.35	0.79	0.11	2.57	1.10	0.65	0.02	3.07	1.44	0.82
Mar.	0.24	2.07	0.45	1.20	0.61	2.94	2.22	0.58	0.24	2.07	1.20	0.45	0.34	3.91	2.55	0.91
Apr	0.92	2.66	0.38	1.92	2.15	3.19	2.70	0.27	0.92	2.66	1.92	0.38	2.09	4.34	3.53	0.46
May	1.13	2.41	0.29	1.76	1.93	2.98	2.48	0.24	1.13	2.41	1.76	0.29	2.25	4.11	3.11	0.41
Jun.	1.06	2.18	0.27	1.68	2.19	3.32	2.72	0.26	1.06	2.18	1.68	0.27	2.31	3.57	2.92	0.35
Jul.	1.40	2.58	0.31	1.94	2.63	3.82	3.13	0.28	1.40	2.58	1.94	0.31	2.67	3.93	3.24	0.36
Aug.	1.16	2.64	0.38	1.86	2.47	3.79	3.18	0.28	1.16	2.64	1.86	0.38	2.31	4.16	3.21	0.48
Sept.	0.61	1.65	0.20	1.07	2.09	3.08	2.54	0.25	0.61	1.65	1.07	0.20	1.43	3.16	1.96	0.38
Oct.	0.33	1.48	0.27	0.77	1.06	2.46	1.80	0.31	0.33	1.48	0.77	0.27	0.77	2.19	1.28	0.32
Nov.	0.34	2.40	0.55	1.27	0.05	1.82	0.80	0.43	0.34	2.40	1.27	0.55	0.15	1.98	0.86	0.47
Dec.	0.37	3.61	0.55	1.76	0.13	3.81	1.32	0.76	0.37	3.61	1.76	0.55	0.10	3.31	1.32	0.61

Months	Maiduguri				Port-Harcourt				Sokoto			
	Min	Max.	Mean	STD	Min	Max.	Mean	STD	Min	Max.	Mean	STD
Jan.	3.28	5.50	1.63	0.83	0.49	2.34	1.05	0.37	2.79	6.14	4.38	0.74
Feb.	3.30	5.37	1.10	0.65	0.57	1.96	1.33	0.41	1.92	5.73	4.13	1.01
Mar.	1.32	5.54	1.20	0.45	1.12	1.92	1.68	0.19	1.17	5.19	2.93	1.02
Apr	0.17	4.80	1.92	0.38	1.39	1.91	1.71	0.13	0.80	4.44	1.76	0.77
May	0.32	4.12	1.76	0.29	1.42	1.98	1.66	0.14	1.55	4.43	3.06	0.75
Jun.	1.50	4.23	1.68	0.27	1.50	2.34	1.95	0.20	2.48	4.27	3.45	0.43
Jul.	2.42	4.16	1.94	0.31	1.86	2.63	2.27	0.16	2.36	3.64	2.98	0.35
Aug.	1.54	3.08	1.86	0.38	2.03	2.73	2.38	0.16	1.07	2.83	2.00	0.36

Sept.	1.05	2.62	1.07	0.20	1.70	2.44	2.07	0.18	0.79	2.40	1.52	0.40
Oct.	0.21	2.32	0.77	0.27	1.40	2.02	1.67	0.14	0.61	2.43	1.29	0.40
Nov.	2.18	4.11	1.27	0.55	0.59	1.64	1.19	0.26	1.94	4.34	3.10	0.60
Dec.	3.23	4.80	1.76	0.55	0.51	1.40	0.85	0.20	2.18	5.43	4.09	0.57

5. CONCLUSIONS

The application of wind speed prediction to energy production is of significant value, as wind power has a significant impact on the planning and stability of power energy around the world. This study demonstrates that different LSTM neural networks are used to optimize some hyper-parameters in the establishment of LSTM prediction models within the algorithm framework. When RMSE prediction is compared to certain empirical methods, it is discovered that some parameters and the double-layer LSTM of the wind speed dataset are extremely essential. In comparison to the impact of some neural networks and statistical model, the FWA-LSTM model produced some predictions in the generation of wind speed. However, the LSTM model of the wind speed experiment result showed that when compared to each other, that is, LSTM and FWA-LSTM methods, error in wind speed prediction was significantly reduced. As a result of the wind speed investigation, it was discovered that wind speed occurrence was more probable at stations like Damaturu, Sokoto, and Ikeja. This could result from the exposure of stations to tides and ocean currents.

As a result of this research, it was concluded that the investigation of wind speed energy using the improved active learning algorithm could be applied to the effective generalization of the larger validation of the data set, which would facilitate the prediction of wind energy optimization and its importance for power planning to reduce the pressure mounted on hydro energy generation because wind energy is also a renewable source of energy. Therefore, this research recommends that the government of the Federal Republic of Nigeria invest more funds in research to help solve Nigeria's power outage.

6. ACKNOWLEDGEMENT

The authors would like to express their heartfelt gratitude to the Modern-Era Retrospective analysis for Research and Applications, Version 2 (MERRA-2) Web service, for providing the data for this study. We are also appreciative of Bowen University for providing us with the opportunity to conduct this research.

7. DATA AVAILABILITY

The data used for this research were collected from the archive of the MERRA-2 website of Solar Data, (http://www.soda-pro.com).

NOMENCLATURE

ANN	Artificial Neural Network
Bi-LSTM	Bidirectional Long-Short Term Memory
CEEMDAN	Complete Ensemble Empirical Mode Decomposition with Adaptive Noise
CSV	Comma-Separated Value
FWA	Fire-Work Algorithms
GRU	Gated Recurrent Unit
LSTM	Long Short-Term Memory
MAE	Mean Average Error
MERRA-2	Modern-Era retrospective Analysis for Research and Applications, Version 2
MISOD	Multiple Single Output Data
MOMID	Multiple Outputs, Multiple Inputs Data
ML	Machine Learning
MLA	Machine Learning Algorithm
MSE	Mean Squared Error
RMSE	Root Mean Square Error
RNN	Recurrent Neural Network
R Square	Root Square
SISOD	Single, Single Output Data
SNAP	Sentinel Application Platform
VMD	Variational Mode Decomposition
WT	Wind Turbine

REFERENCES

1. Adebayo, S., Aweda, F.O., Ojedokun, I.A., & Olapade, O.T. (2022). Refractive index perception and prediction of radio wave through recursive neural networks using meteorological data parameters. *International Journal of Engineering, 35*(4), 810-818. https://doi.org/10.5829/IJE.2022.35.04A.21
2. Agbo, E.P., Edet, C.O., Magu, T.O., Njok, A.O., Ekpo, C.M., & Louis, H. (2021). Solar energy: A panacea for the electricity generation crisis in Nigeria. *Heliyon, 7*(5), e07016. https://doi.org/10.1016/j.heliyon.2021.e07016
3. Aliyu, A.S., Dada, J.O., & Adam, I.K. (2015). Current status and future prospects of renewable energy in Nigeria. *Renewable and Sustainable Energy Reviews, 48*, 336-346. https://doi.org/10.1016/j.rser.2015.03.098
4. Antor, A.F., & Wollega, E.D. (2020). *Comparison of machine learning algorithms for wind speed prediction.* Proceedings of the International Conference on Industrial Engineering and Operations Management. http://www.ieomsociety.org/detroit2020/papers/198.pdf
5. Asiegbu, A. (2007). Studies of wind resources in Umudike, South East Nigeria-An assessment of economic viability. https://medwelljournals.com/abstract/?doi=jeasci.2007.1539.1541
6. Aweda, F.O., Adebayo, S., Samson, T.K., & Ojedokun, I.A. (2021). Modelling net radiative measurement of meteorological parameters using merra-2 data in sub-sahara african town. *Iranian (Iranica) Journal of Energy & Environment, 12*(2), 173-180. https://doi.org/10.5829/IJEE.2021.12.02.10
7. Aweda, F.O., Olufemi, S.J., & Agbolade, J.O. (2022). Meteorological parameters study and temperature forecasting in selected stations in sub-sahara africa using merra-2 data. *Nigerian Journal of Technological Development, 19*(1), 80-91. https://doi.org/10.4314/njtd.v19i1.9
8. Aweda, F.O., Oyewole, J.A., Fashae, J.B., & Samson, T.K. (2020). Variation of the earth's irradiance over some selected towns in Nigeria. *Iranian (Iranica) Journal of Energy & Environment, 11*(4), 301-307. https://doi.org/10.5829/IJEE.2020.11.04.08
9. Brahimi, T., Alhebshi, F., Alnabilsi, H., Bensenouci, A., & Rahman, M. (2019). Prediction of wind speed distribution using artificial neural network: The case of saudi arabia. *Procedia Computer Science, 163*, 41-48. https://doi.org/10.1016/j.procs.2019.12.084
10. Chang, T.P. (2011a). Estimation of wind energy potential using different probability density functions. *Applied Energy, 88*(5), 1848-1856. https://doi.org/10.1016/j.apenergy.2010.11.010
11. Chang, T.P. (2011b). Performance comparison of six numerical methods in estimating weibull parameters for wind energy application. *Applied Energy, 88*(1), 272-282. https://doi.org/10.1016/j.apenergy.2010.06.018
12. Dhunny, A.Z., Lollchund, R.M., Boojhawon, R., & Rughooputh, S.D. (2014). Statistical modelling of wind speed data for mauritius. *International Journal of Renewable Energy Research. 4*(4), 1056-1064. https://doi.org/10.20508/ijrer.v4i4.1664.g6447
13. Gelaro, R., McCarty, W., Suárez, M.J., Todling, R., Molod, A., Takacs, L., Reichle, R. Wargan, K., Coy, L., Cullather, R., Draper, C., Akella, S., Buchard, V., Conaty, A., Silva, A.M.D., Gu, W., Kim, G.K., Koster, R., Lucchesi, R., Merkova, D., Nielsen, J.E., Partyka, G., Pawson, S., Putman, W., Rienecker, M., Schubert, S.D., Sienkiewicz, M., & Zhao,

B. (2017). The modern-era retrospective analysis for research and applications, version 2 (merra-2). *Journal of Climate, 30*(14), 5419-5454. https://doi.org/10.1175/JCLI-D-16-0758.1

14. Hassani, Z., Hajihashemi, V., Borna, K., & Sahraei Dehmajnoonie, I. (2020). A classification method for e-mail spam using a hybrid approach for feature selection optimization. *Journal of Sciences, Islamic Republic of Iran, 31*(2), 165-173. https://dx.doi.org/10.22059/JSCIENCES.2020.288729.1007444
15. Hosseini, E., Behzadfar, N., Hashemi, M., Moazzami, M., & Dehghani, M. (2022). Control of pitch angle in wind turbine based on doubly fed induction generator using fuzzy logic method. *Journal of Renewable Energy and Environment (JREE), 9*(2), 1-7. https://dx.doi.org/10.30501/JREE.2021.293546.1226
16. Junior, J.R.B., & do Carmo Nicoletti, M. (2019). An iterative boosting-based ensemble for streaming data classification. *Information Fusion, 45*, 66-78. https://doi.org/10.1016/j.inffus.2018.01.003
17. Justus, C., Hargraves, W., Mikhail, A., & Graber, D. (1978). Methods for estimating wind speed frequency distributions. *Journal of Applied Meteorology (1962-1982)*, *17*(3), 350-353. https://doi.org/10.1175/1520-0450(1978)017<0350:MFEWSF>2.0.CO;2
18. Kaoga, D.K., Raidandi, D., Djongyang, N., & Doka, S.Y. (2014). Comparison of five numerical methods for estimating weibull parameters for wind energy applications in the district of kousseri, cameroon. *Asian Journal of Natural & Applied Sciences, 3*(1), 72. http://www.ajsc.leena-luna.co.jp/AJSCPDFs/Vol.3%281%29/AJSC2014%283.1-08%29.pdf
19. Khosravi, A., Koury, R., Machado, L., & Pabon, J. (2018). Prediction of wind speed and wind direction using artificial neural network, support vector regression and adaptive neuro-fuzzy inference system. *Sustainable Energy Technologies and Assessments, 25*, 146-160. https://doi.org/10.1016/j.seta.2018.01.001
20. Lawan, S., Abidin, W., & Masri, T. (2020). Implementation of a topographic artificial neural network wind speed prediction model for assessing onshore wind power potential in Sibu, Sarawak. *The Egyptian Journal of Remote Sensing and Space Science, 23*(1), 21-34. https://doi.org/10.1016/j.ejrs.2019.08.003
21. Li, J., & Tan, Y. (2019). A comprehensive review of the fireworks algorithm. *ACM Computing Surveys (CSUR), 52*(6), 1-28. https://dl.acm.org/doi/fullHtml/10.1145/3362788
22. Lin, Z., Liu, X., & Collu, M. (2020). Wind power prediction based on high-frequency scada data along with isolation forest and deep learning neural networks. *International Journal of Electrical Power & Energy Systems, 118*, 105835. https://doi.org/10.1016/j.ijepes.2020.105835
23. Liu, X., Zhang, H., Kong, X., & Lee, K.Y. (2020). Wind speed forecasting using deep neural network with feature selection. *Neurocomputing, 397*, 393-403. https://doi.org/10.1016/j.neucom.2019.08.108
24. Ma, X., Chen, Y., Yi, W., & Wang, Z. (2021). Prediction of extreme wind speed for offshore wind farms considering parametrization of surface roughness. *Energies, 14*(4), 1033. https://dx.doi.org/10.3390/en14041033
25. Ma, Z., Chen, H., Wang, J., Yang, X., Yan, R., Jia, J., & Xu, W. (2020). Application of hybrid model based on double decomposition, error correction and deep learning in short-term wind speed prediction. *Energy Conversion and Management, 205*, 112345. https://doi.org/10.1016/j.enconman.2019.112345
26. Maheri, A., Wiratama, I.K., & Macquart, T. (2022). Performance of microtabs and trailing edge flaps in wind turbine power regulation: A numerical analysis using wtsim. *Journal of Renewable Energy and Environment (JREE), 9*(2), 18-26. https://dx.doi.org/10.30501/JREE.2021.291397.1220
27. Martin, M., Cremades, L., & Santabarbara, J. (1999). Analysis and modelling of time series of surface wind speed and direction. *International Journal of Climatology: A Journal of the Royal Meteorological Society, 19*(2), 197-209. https://doi.org/10.1002/(SICI)1097-0088(199902)19:2<197::AID-JOC360>3.0.CO;2-H
28. Memarzadeh, G., & Keynia, F. (2020). A new short-term wind speed forecasting method based on fine-tuned lstm neural network and optimal input sets. *Energy Conversion and Management, 213*, 112824. https://doi.org/10.1016/j.enconman.2020.112824
29. Mert, I., & Karakuş, C. (2015). A statistical analysis of wind speed data using burr, generalized gamma, and weibull distributions in Antakya, Turkey. *Turkish Journal of Electrical Engineering and Computer Sciences, 23*(6), 1571-1586. https://dx.doi.org/10.3906/elk-1402-66
30. Moghadasi, M., Ozgoli, H.A., & Farhani, F. (2021). Steam consumption prediction of a gas sweetening process with methyldiethanolamine solvent using machine learning approaches. *International Journal of Energy Research, 45*(1), 879-893. https://doi.org/10.1002/er.5979
31. Moreno, S.R., da Silva, R.G., Mariani, V.C., & dos Santos Coelho, L. (2020). Multi-step wind speed forecasting based on hybrid multi-stage decomposition model and long short-term memory neural network. *Energy Conversion and Management, 213*, 112869. https://doi.org/10.1016/j.enconman.2020.112869
32. Munteanu, I., Bratcu, A.I., CeangĂ, E., & Cutululis, N.-A. (2008). *Optimal Control of Wind Energy Systems: Towards a Global Approach* (Vol. 22). Springer. https://link.springer.com/book/10.1007/978-1-84800-080-3
33. Navas, R.K.B., Prakash, S., & Sasipraba, T. (2020). Artificial neural network based computing model for wind speed prediction: A case study of coimbatore, Tamil Nadu, India. *Physica A: Statistical Mechanics and its Applications, 542*, 123383. https://doi.org/10.1016/j.physa.2019.123383
34. Neshat, M., Nezhad, M.M., Mirjalili, S., Piras, G., & Garcia, D.A. (2022). Quaternion convolutional long short-term memory neural model with an adaptive decomposition method for wind speed forecasting: North aegean islands case studies. *Energy Conversion and Management, 259*, 115590. https://doi.org/10.1016/j.enconman.2022.115590
35. Nezhad, M.M., Heydari, A., Groppi, D., Cumo, F., & Garcia, D.A. (2020). Wind source potential assessment using sentinel 1 satellite and a new forecasting model based on machine learning: A case study Sardinia islands. *Renewable Energy, 155*, 212-224. https://doi.org/10.1016/j.renene.2020.03.148
36. Nezhad, M.M., Heydari, A., Neshat, M., Keynia, F., Piras, G., & Garcia, D.A. (2022). A mediterranean sea offshore wind classification using merra-2 and machine learning models. *Renewable Energy, 190*, 156-166. https://doi.org/10.1016/j.renene.2022.03.110
37. Nezhad, M.M., Neshat, M., Piras, G., & Garcia, D.A. (2022). Sites exploring prioritisation of offshore wind energy potential and mapping for wind farms installation: Iranian islands case studies. *Renewable and Sustainable Energy Reviews, 168*, 112791. https://doi.org/10.1016/j.rser.2022.112791
38. Nielson, J., Bhaganagar, K., Meka, R., & Alaeddini, A. (2020). Using atmospheric inputs for artificial neural networks to improve wind turbine power prediction. *Energy, 190*, 116273. https://doi.org/10.1016/j.energy.2019.116273
39. Ohunakin, O.S., & Akinnawonu, O.O. (2012). Assessment of wind energy potential and the economics of wind power generation in Jos, Plateau State, Nigeria. *Energy for Sustainable Development, 16*(1), 78-83. https://doi.org/10.1016/j.esd.2011.10.004
40. Olubi, O., Oniya, E., & Owolabi, T. (2021). Development of predictive model for radon-222 estimation in the atmosphere using stepwise regression and grid search based-random forest regression. *Journal of the Nigerian Society of Physical Sciences, 3*(2), 132-139. https://doi.org/10.46481/jnsps.2021.177
41. Oyedepo, S.O. (2014). Towards achieving energy for sustainable development in Nigeria. *Renewable and Sustainable Energy Reviews, 34*, 255-272. https://doi.org/10.1016/j.rser.2014.03.019
42. Oyewole, J.A., Aweda, F.O., & Oni, D. (2019). Comparison of three numerical methods for estimating weibull parameters using Weibull distribution model in Nigeria. *Nigerian Journal of Basic and Applied Sciences, 27*(2), 8-15. https://doi.org/10.4314/njbas.v27i2.2
43. Pei, Y., Zheng, S., Tan, Y., & Takagi, H. (2012). *An empirical study on influence of approximation approaches on enhancing fireworks algorithm.* Proceedings of the 2012 IEEE International Conference on Systems, Man, and Cybernetics (SMC). https://doi.org/10.1109/ICSMC.2012.6377916
44. Pishgar-Komleh, S., Keyhani, A., & Sefeedpari, P. (2015). Wind speed and power density analysis based on Weibull and Rayleigh distributions (A case study: Firouzkooh county of Iran). *Renewable and Sustainable Energy Reviews, 42*, 313-322. https://doi.org/10.1016/j.rser.2014.10.028
45. Pobočíková, I., & Sedliačková, Z. (2014). Comparison of four methods for estimating the Weibull distribution parameters. *Applied Mathematical Sciences, 8*(83), 4137-4149 https://www.researchgate.net/publication/309918562_Comparison_of_Four_Methods_for_Estimating_the_Weibull_Distribution_Parameters

46. Rodríguez, F., Florez-Tapia, A.M., Fontán, L., & Galarza, A. (2020). Very short-term wind power density forecasting through artificial neural networks for microgrid control. *Renewable Energy, 145*, 1517-1527. https://doi.org/10.1016/j.renene.2019.07.067

47. Rojas, R. (2009). Adaboost and the super bowl of classifiers a tutorial introduction to adaptive boosting. *Technical Report of Freie University, Berlin.* https://www.inf.fu-berlin.de/inst/ag-ki/adaboost4.pdf

48. Salahaddin, A.A. (2013). Comparative study of four methods for estimating Weibull parameters for Halabja, Iraq. *International Journal of Physical Sciences, 8*(5), 186-192. https://doi.org/10.5897/IJPS12.697

49. Samadianfard, S., Hashemi, S., Kargar, K., Izadyar, M., Mostafaeipour, A., Mosavi, A., Nabipour, N., & Shamshirband, S. (2020). Wind speed prediction using a hybrid model of the multi-layer perceptron and whale optimization algorithm. *Energy Reports, 6*, 1147-1159. https://doi.org/10.1016/j.egyr.2020.05.001

50. Shao, B., Song, D., Bian, G., & Zhao, Y. (2021). Wind speed forecast based on the lstm neural network optimized by the firework algorithm. *Advances in Materials Science and Engineering, 2021.* https://doi.org/10.1155/2021/4874757

51. Staff, International Energy Agency. (2012). *Energy Balances of Non-OECD Countries*: Organization for Economic. https://doi.org/10.1787/energy_bal_non-oecd-2012-en

52. Tan, Y., & Zhu, Y. (2010). *Fireworks algorithm for optimization.* Part 1, Proceedings of the Advances in Swarm Intelligence: First International Conference, ICSI, Beijing, China. https://doi.org/10.1007/978-3-642-13495-1_44

53. Uçar, M.K., Nour, M., Sindi, H., & Polat, K. (2020). The effect of training and testing process on machine learning in biomedical datasets. *Mathematical Problems in Engineering, 2020.* https://doi.org/10.1155/2020/2836236

54. Venkatakrishnan, G., Rengaraj, R., Sathish, K., Dinesh, R., & Nishanth, T. (2021). Implementation of modified differential evolution algorithm for hybrid renewable energy system. *Journal of the Nigerian Society of Physical Sciences*, *3*(3), 209-215. https://doi.org/10.46481/jnsps.2021.240

55. Waewsak, J., Chancham, C., Landry, M., & Gagnon, Y. (2011). An analysis of wind speed distribution at Thasala, Nakhon Si Thammarat, Thailand. *Journal of Sustainable Energy & Environment, 2*(2), 51-55. https://www.thaiscience.info/Journals/Article/JOSE/10889661.pdf

56. Wang, C., Zhang, H., & Ma, P. (2020). Wind power forecasting based on singular spectrum analysis and a new hybrid laguerre neural network. *Applied Energy, 259*, 114139. https://doi.org/10.1016/j.apenergy.2019.114139)

57. Yin, W., Kann, K., Yu, M., & Schütze, H. (2017). Comparative study of CNN and RNN for natural language processing. https://arxiv.org/abs/1702.01923

58. Zafirakis, D., Tzanes, G., & Kaldellis, J.K. (2019). Forecasting of wind power generation with the use of artificial neural networks and support vector regression models. *Energy Procedia, 159*, 509-514. https://doi.org/10.1016/j.egypro.2018.12.007

59. Zhang, B., Zheng, Y.-J., Zhang, M.-X., & Chen, S.-Y. (2015). Fireworks algorithm with enhanced fireworks interaction. *IEEE/ACM Transactions on Computational Biology and Bioinformatics, 14*(1), 42-55. https://doi.org/10.1109/TCBB.2015.2446487

60. Zhang, Z., Qin, H., Liu, Y., Wang, Y., Yao, L., Li, Q., Li, J., & Pei, S. (2019). Long short-term memory network based on neighborhood gates for processing complex causality in wind speed prediction. *Energy Conversion and Management, 192*, 37-51. https://doi.org/10.1016/j.enconman.2019.04.006

61. Zheng, S., Janecek, A., & Tan, Y. (2013). *Enhanced fireworks algorithm.* Proceedings of the 2013 IEEE congress on evolutionary computation. https://ieeexplore.ieee.org/document/6557813

JREE: Vol. 10, No. 3, (Summer 2023) 99-106

Journal of Renewable Energy and Environment

Journal Homepage: www.jree.ir

Materials and Energy Research Center

MERC

Research Article

Prediction of Anthropogenic Greenhouse Gas Emissions via Manure Management in Indonesia and Alternative Policies for Indonesian Livestock Development

Nur Aini [a*], Widi Hastomo [a], Ratna Yulika Go [b]

[a] Department of Management, Faculty of Economic and Business, Ahmad Dahlan Institute of Technology and Business, Indonesia.
[b] Department of Information Technology, Faculty of Computer Science, Universitas Indonesia, Indonesia.

PAPER INFO

Paper History:
Received: 05 August 2022
Revised: 08 October 2022
Accepted: 17 October 2022

Keywords:
GHG Emission,
Indonesia,
Livestock Policy,
Development,
Emission Prediction

ABSTRACT

The percentage of production and utilization of hydrocarbon resources from the livestock sector has raised concerns regarding the worldwide issue of global warming. A total of CH_4 emissions from enteric fermentation and waste management has been estimated at 78.3 %. Meanwhile, N_2O emissions are 75-80 % of total agricultural emissions. This raises questions about the extent of global warming due to increased CO_2 resulting in changes in weather and global warming. This research aims to predict Green House Gas (GHG) emissions from manure management and present policy alternatives for Indonesian livestock development. Secondary data was taken from a related website (fao.org) with coverage throughout Indonesia from 1961 to 2021, containing 12,480 rows and 5 column features including item, Element, Year, Unit, and Value emission. LSTM and GRU are used to predict the trend of emission from manure management to provide alternative policies on greenhouse gas mitigation in Indonesia. The results showed that based on 15 types of livestock that emit GHG emissions, 3 types of livestock produce the highest emissions from 1961 to 2021: (a) cattle, (b) cattle and non-dairy, and (c) poultry. Significant reduction in the emission of carbon dioxide (CO_2eq) in 2020 is indicated by reduced public consumption and hampered supply chains with large-scale social restrictions (covid-19 pandemic policy). Based on these results, fertilizer storage duration can be used as a policy to reduce CO_2eq emissions, hence it is desired that fertilizer management techniques can be properly regulated. Mitigation can also be accomplished by utilizing livestock waste as biogas and upgrading animal feed additives with chitosan or potassium nitrate.

https://doi.org/10.30501/jree.2022.354796.1423

1. INTRODUCTION

Livestock is one contributor among many to emissions from enteric fermentation of manure as excretory waste and methane as a byproduct of digestion (Broucek, 2014). Enteric fermentation of plant-eating animals is produced via the digestive process in the form of methane. The amount of methane released from animals depends on their weight, age, and quality and quantity of the consumed feed. For example, cattle and sheep are animals with moderate methane production compared to pigs and horses (Gitarskiy, 2019).

One of the largest contributors to the world's agricultural sector is the livestock sector. 78.3 % of total anthropogenic CH_4 emissions result from both enteric fermentation and waste management (FAOSTAT Agriculture Total Online Database, 2020). N_2O emissions represent 75-80 % of the total emissions from agriculture (Ambazamkandi et al., 2015). The percentage of production and utilization of hydrocarbon resources raises concerns about the issue of global warming (Whelan et al., 2013). This is evidenced by increase in CO_2 levels resulting in changes in weather and global warming.

Scholars and international organizations suggest implementing a carbon dioxide tax to reduce greenhouse gases. With the carbon tax, companies can control CO_2 emissions by changing prices. Its application can also be adapted to existing taxes so that correct positions can be provided to negotiate on climate change in the future (Zhao et al., 2013).

Various efforts such as the implementation of carbon taxes have been made so far to overcome global warming issues. With the carbon tax, the source of air pollution will be more controlled and energy consumption will be better (Fang et al., 2016). This long-term implementation can be carried out in stages and becomes a concern for international organizations from environmental, economic, and energy conservation perspectives (Zhao et al., 2013). The development of organic fertilizers and biogas is also an effort to develop an alternative energy to develop renewable energy (Anderson et al., 2016) so that it can reduce greenhouse gas emissions by regional development targets.

*Corresponding Author's Email: aini.nur1969@gmail.com (N. Aini)
URL: https://www.jree.ir/article_160786.html

Please cite this article as: Aini, N., Hastomo, W., & Go, R.I. (2023). Prediction of anthropogenic greenhouse gas emissions via manure management in Indonesia and alternative policies for Indonesian livestock development. *Journal of Renewable Energy and Environment (JREE)*, *10*(3), 99-106. https://doi.org/10.30501/jree.2022.354796.1423.

2423-7469/© 2023 The Author(s). Published by MERC. This is an open access article under the CC BY license (https://creativecommons.org/licenses/by/4.0/).

Previous research has mentioned that one of the efforts to reduce methane emissions is the provision of aloe vera waste supplements to the Bali cattle diet (Mahardika et al., 2011). In addition, feed plays an important role in meeting the energy needs of livestock. In its processing, adding chitosan to animal feed has been shown to reduce enteric methane emissions and change the rumen fermentation profile in a favorable direction (Harahap et al., 2020).

Several alternatives to reducing GHG emissions have been adopted by previous studies in terms of animal feed (Herawati, 2012; Ambazamkandi et al., 2015; Pachauri & Leo Meyer, 2014). It is implied that animal feed not only contributes to animal waste emissions but also plays a role in producing GHG emissions in other sectors such as agriculture, forestry, livestock farming, and transportation (Herawati, 2012; Le Quéré et al., 2020; Miranti Ariani, Ardiansyah, 2015; Utaminingsih & Hidayah, 2012). Research on GHG has not been widely carried out in Indonesia. Therefore, there has not been much discussion about GHG emission factors caused by animal waste and prediction methods (LSTM and GRU) have been employed to determine the level of GHG emissions in the future. LSTM and GRU are methods for predicting emissions that are popular and successful because they provide simulation results in the form of GHG emission predictions that have been quite accurate in previous studies (Chlingaryan et al., 2018).

Indonesia is currently committed to reducing GHG emissions by 29 % by 2030. As much as 60 % of GHG is produced in the forestry sector and 36 % in the energy sector (Limanseto, 2021). Livestock also contributes to national GHG emissions. Although the figure is still below 2 % of the total national GHG emissions, it will continue to increase in line with the increase in the livestock population (Widiawati et al., 2021).

Based on the explanation above, this research takes advantage of machine learning to predict manure management that has been carried out so far and proposes policies to regulate and reduce greenhouse gas emissions in Indonesia in the livestock sector.

2. MATERIAL AND METHODS

This study uses secondary manure management data from FAO (FAOSTAT Agriculture Total Online Database, 2020) with coverage throughout Indonesia. The annual data were derived, starting from the year 1961 to 2021, containing 12,480 rows. These raw data consist of 5 column features: (a) item, (b) Element, (c) Year, (d) Unit, (e) Value emission. The collected data were then divided into datasets. The datasets have value and time attributes as included in the time series data category, which can be used as input to machine learning. The datasets are divided into training datasets ranging from 70 % to 80 % of the total datasets. LSTM and GRU are used to predict GHG emission trends from manure management to provide alternative solutions for GHG emission mitigation in Indonesia.

2.1. Data management and data analysis

The data that have been collected are analyzed using descriptive methods and the results of the system prediction become the basis for policy formulation so that the conducted mitigation can properly reduce the impact of GHG emissions in Indonesia as intended. The tier 1 methodology was used to calculate CH_4 and N_2O emissions from the 2006 IPCC guidelines. This method was utilized because it could be tabulated based on temperature, type of animal, location, and manure management (Ambazamkandi et al., 2015).

In substance, the initial step of this experimentation begins with the input of the dataset and the next step is data cleansing that cleans up duplicate, missing, outlier, and null data, followed by pre-processing, namely the stationary transformation, differencing, polynomial, and decomposition processes. It is followed by autoregressive, moving average, graph, and RMSE processes. The next step is data analysis consisting of data training and data testing, by which the results are shown in graphical visualization and RMSE values. The experimental flow is shown in Figure 1.

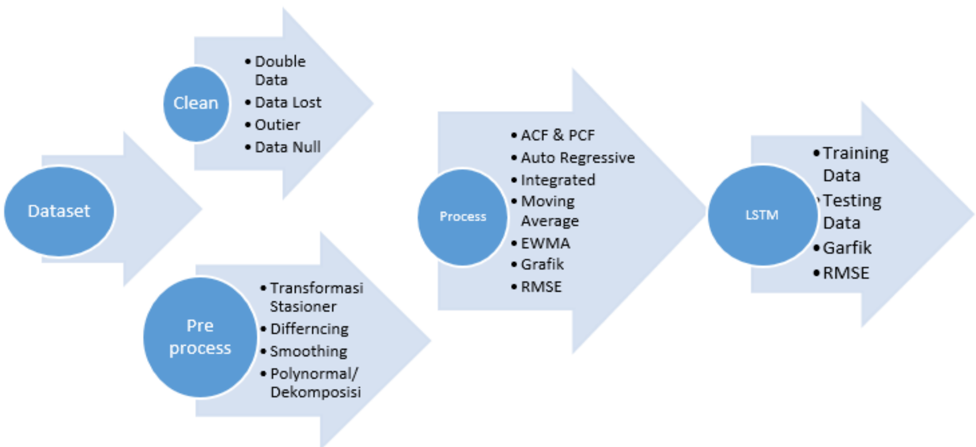

Figure 1. Experimental flow

2.2. Long Short-Term Memory (LSTM) method

This Long Short Term Memory (LSTM) method is usually used in combination with several learning architectures. The LSTM is a type of neural network that can predict time series (Van Houdt et al., 2020). Forget gate, input gate, and output gate are controlling the gates. Each gate has sigmoid and pointwise intervals [0..1]. This method can also read the input vector x = {x_1, x_2, . . . , x_t, . . .}, where $X_t \in R^m$ comes from the m-dimensional vector.

According to Figure 2, it can be seen that the LSTM formula is as follows:

$$h_t = O_t + \tanh(C_t) \quad (1)$$

where h_t is othe utput final, O_t othe utput gate, tanh the hyperbolic tangent function, and C_t value of the memory cell state. The output gate task controls the number of activations of each functional unit. Then, the LSTM can store the required information from each unit.

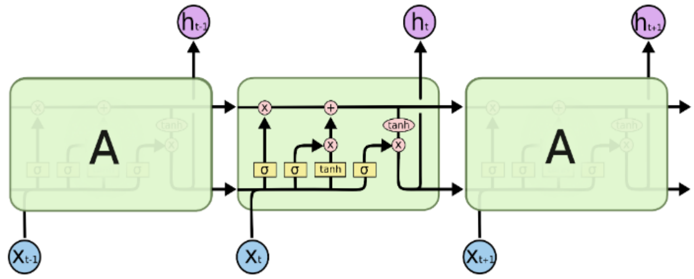

Figure 2. Four layers of activation in the LSTM cell

2.3. Gated Recurrent Unit (GRU) method

The Gated Recurrent Unit (GRU) consists of two gates: a reset r gate and a z gate. The output status contained at time (t) is calculated in the hidden state at time t-1, which is entered into the time series value at time t; the equation can be seen as follows (2).

$$h_t = f(h_{t-1}, x_i) \quad (2)$$

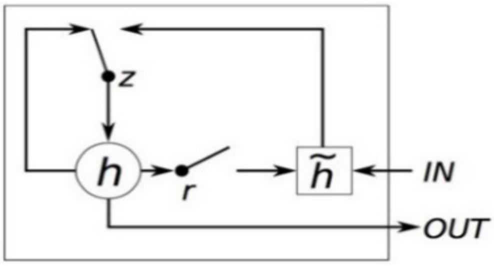

Figure 3. Illustration of GRU

2.4. Mean Squared Error (MSE) and Root Mean Squared Error (RMSE)

Root Mean Squared Error (RMSE) was used to see the difference between the estimated value and the actual value of the model parameters. Previously, the MSE calculation was carried out to check the error value in the prediction. Then, the result is the square root. The smaller or closer to zero the resulting number is, the more accurate the prediction results are. The formula of RMSE and MSE is as follows:

$$\text{RMSE} = \sqrt{\sum_{i=1}^{n} \frac{(y_1 - \widehat{y_1})^2}{n}} \quad \text{and} \quad \text{MSE} = \frac{1}{n}\sum_{i=1}^{n}(y_1 - \widehat{y_1})^2 \quad (3)$$

where $\widehat{y_1}, \widehat{y_2}, \ldots\ldots, \widehat{y_n}$ = values predicted, $y_1, y_2, \ldots, y_n$ = values observed and n = number of data sets observed.

3. RESULTS

The datasetw collected from the year 1961 to 2021 are used in machine learning to predict the level of greenhouse gas emissions. The datasets are divided into 'training datasets' ranging from 70 % to 80 % of the total data and 'test datasets' ranging from 20 % to 30 %. The results of the predicted test dataset measure the error value with respect to the value of the real testing dataset (target data). The obtained error value is used to update the weight value. The new weight value is applied to the prediction of the next iteration.

Based on the results of machine learning, it was found that for CO_2eq emissions that consist of 15 categories of livestock (Figure 4), three categories emit the highest emissions, namely (a) cattle, (b) cattle and non-dairy, (c) poultry (Figure 5).

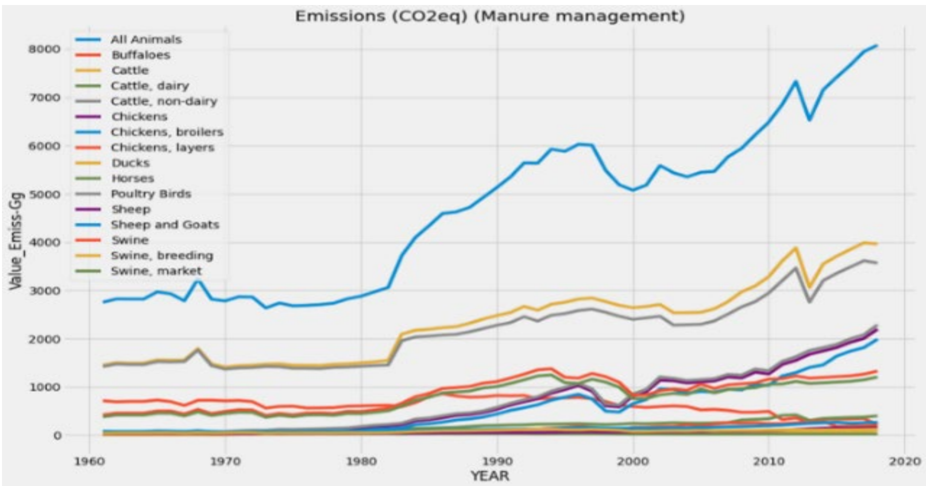

Figure 4. Training dataset of CO_2eq emission in Indonesia by livestock category

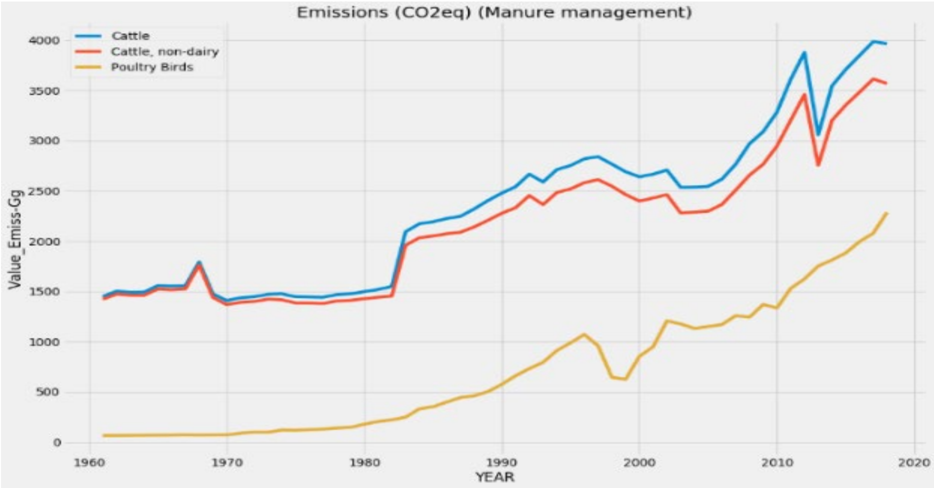

Figure 5. CO_2eq emission in Indonesia based on the highest emission

The results of manure management optimization in the three livestock categories with the highest emissions using machine learning are shown in Table 1. In the 10th epoch, the lowest RMSE of the cattle category is 4.25 %. Meanwhile, in the cattle non-dairy category, the RMSE is the lowest at 3.61 in the 15th epoch and 3.25 % in the polluter bird's category at the same epoch. This shows that the smaller the resulting RMSE value, the more accurate the prediction results will be.

Table 1. Combinatorial optimization of cattle hidden layer

Epoch	**RMSE**		
	Cattle (%)	Cattle, non-dairy (%)	Poultry Birds (%)
5	9.56	5.51	9.69
10	**4.25**	3.70	3.45
15	4.37	**3.61**	**3.25**
20	5.87	3.67	3.76

The graph of the predicted futures has a downward trend starting from the late 2019 and reaching the lowest point in 2021. This is because the pandemic entered Indonesia in 2020 and continued until 2021 as the second year of the pandemic. Among the factors are the decline in people's purchasing power during the pandemic due to the soaring price of beef and the increase in the rupiah exchange rate. Similar to the cattle category, GHG emission predictions in the non-cattle category begin to decline from the end of 2019 to 2020, reaching 50 % (Figures 6 and 7).

One example of the category of poultry is broilers. At the beginning of the pandemic, the price of broilers fell drastically, far below the cost of goods sold (COGS); the influencing factor was the large-scale social restriction that resulted in a drastic reduction in public consumption. This had an impact on reduction of CO_2eq emissions from the poultry sector. Consumption of broilers continues to rise from the end of 2021 to 2025.

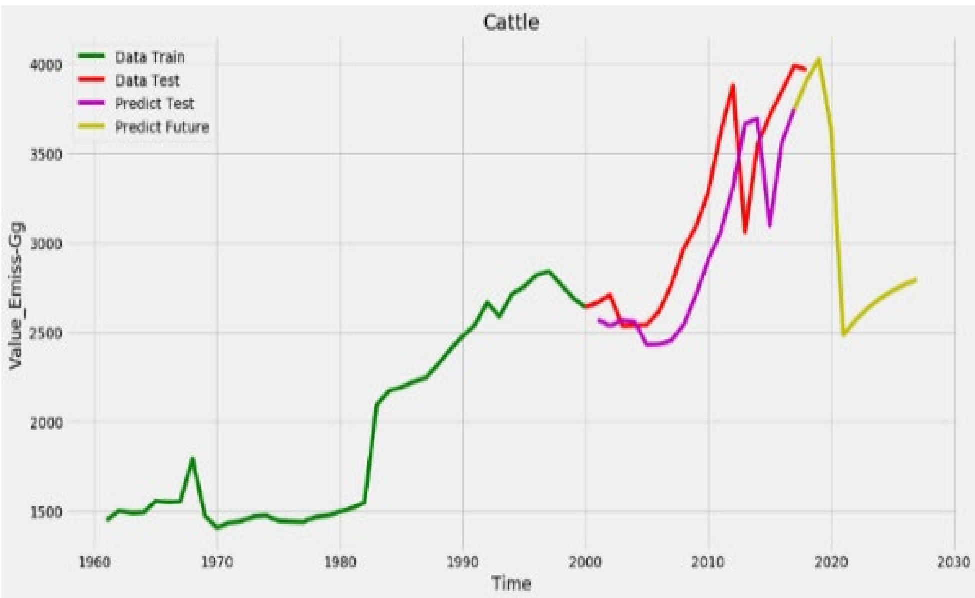

Figure 6. Prediction of future cattle

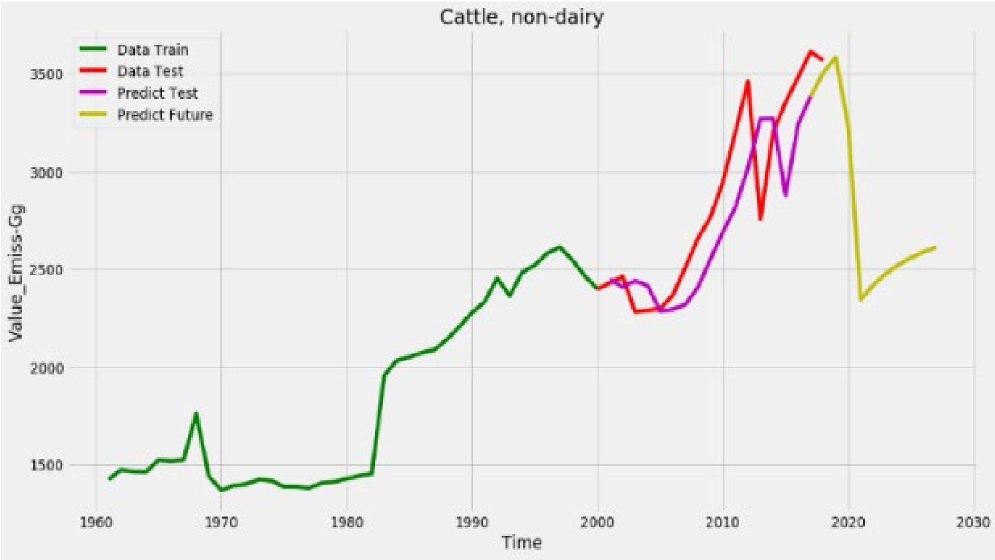

Figure 7. Prediction of future cattle, non-dairy

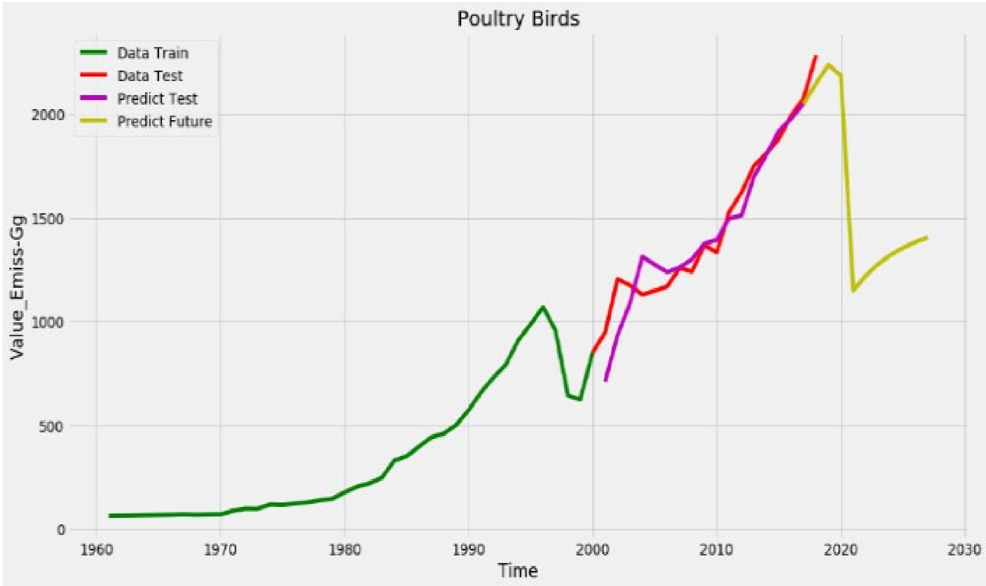

Figure 8. Prediction of future poultry

4. DISCUSSION

The LSTM method was also applied in (Hamrani et al., 2020) for optimization of 9 Machine Learning Methods; (1) LASSO, (2) Random Forest (RF), (3) SVM, (4) ExNN, (5) RBFNN, (6) FNN, (7) DBN, (8) LSTM, and (9) CNN. Using the LSTM model as another method of machine learning to predict GHG emissions can provide a new perspective on future assessments and decisions and generate the most suitable LSTM for predicting future CO_2 and N_2O. Another case study by (Chlingaryan et al., 2018) discussed the prediction of nitrogen emission status using a machine learning approach. Nitrogen (N) plays an important role in the process of photosynthesis, essential for plant health and development. At the same time, environmental and cost factors require a prudent application of N. Because of these factors, the problem of optimal N management has attracted the attention of many researchers.

The use of fossil fuels, deforestation, and land use change are all activities that increase anthropogenic GHG emissions. IPCC considers the effect of GHG emissions on climate change (Pachauri & Leo Meyer, 2014). Manure management is a source of N_2O and CH_4 emissions. Nitrogen oxide emissions are produced as part of the nitrogen-nitrification and denitrification cycle of organic nitrogen substances contained in manure. N_2O emissions are associated with the use of manure as fertilizer before added to the soil.

Manure management is produced from methane (CH_4) emissions during the anaerobic decomposition of manure. In the end, the basic element to consider is the limited livestock management facilities (Ambazamkandi et al., 2015). Greenhouse gas emissions of CO_2, CH_4, and N_2O have an important role as a major contributor to climate change because they are included in long-lived greenhouse gases (World Meteorological Organization & Atmosphere Watch Global, 2017).

Table 2. The atmospheric lifetime of greenhouse gases (Masson Delmotte et al., 2018)

Compound	Time (years)
CO_2	5-2.000
CH_4	12
N_2O	144

According to findings (Pachauri, Leo Meyer, 2014), Global Warming Potential (GWP) can be used to calculate greenhouse gases assocaited with CO_2. The value of GWP can be seen in the following table.

Table 3. Global warming potential value (Masson Delmotte et al., 2018)

Compound	Value
CO_2	1
CH_4	28
N_2O	265

Inventory of GHG emissions on agricultural land in Grobogan and Tanjung Jabung Timur regencies using the 2006 IPCC method for calculating N_2O & CH_4 emissions directly from the soil (2006-2017) shows that the main GHG emission source based on gas type is CH4 gas (wetland management, enteric fermentation, and manure management), which is > 50 % (in CO_2eq) (Miranti Ariani, Ardiansyah, 2015).

Based on research from (Anderson et al., 2016) states that the Pathway Scenario (RCP), RCP 2.6, and 8.5 determined greenhouse gas and aerosol emissions. Mitigation needs to be done by using renewable energy and nuclear power, which are the main ingredients, and using new technology in carbon storage. Meanwhile in Indonesia, to deal with the problem of greenhouse gas emissions, the Government is following up on the Copenhagen Accord agreement from the 15th Conference of Parties (COP-15) in Copenhagen and at the G-20 Pittsburgh, Indonesia commits to reducing greenhouse gas emissions by 26 %. This commitment was strengthened by the ratification of (Peraturan Presiden Republik Indonesia No 61 Tahun 2011 Tentang Rencana Aksi Nasional Penurunan Emisi Gas Rumah Kaca, 2011; Peraturan Presiden Republik Indonesia No. 71 Tahun 2011 Tentang Penyelenggaraan Inventarisasi Gas Rumah Kaca Nasional, 2011) points a and b concerning Reducing Greenhouse Gas Emissions. As stated in the attachment of Presidential Decree No. 61/2011 that the agricultural sector must reduce the level of GHG emissions by 0.008 Gt CO_2eq.

To minimize future GHG emissions, appropriate policies and decisions are needed. On this issue, the IPCC has prepared a special report (IPEC 2000) that will assist in making GHG mitigation policies (Missanjo & Kadzuwa, 2021). One of the proposed policies is to implement a carbon tax. With the addition of a carbon tax to the budget, the income can be used to assist the environmental tax reform process and help mitigate the regressive impact of price increases due to carbon taxes (if they occur) on low-income households and industries in the form of proportional reductions of other tax, so that the level of tax progressivity is maintained.

In addition, Government can direct Indonesia's economy to a low-carbon path by allocating a portion of revenue to research and development and providing investment support for renewable energy. Investments in biofuel-fueled public transportation and electric vehicle technology are also needed to encourage the reduction of energy consumption and carbon emissions. An alternative approach involves offering a lump sum direct discount, with or without conditions, to encourage emission reductions among low-income households, the elderly, and the unemployed (Ratnawati, 2016).

Another alternative to tackling the problem of greenhouse gas emissions lies in the transportation sector. The study (Le Quéré et al., 2020) illustrated that GHG emissions could be reduced by providing policy changes and economic shifts such as walking and cycling. These activities help reduce half of the world's CO_2 emissions. Large cosmopolitan cities such as Bogota, New York, Paris, and Berlin have implemented countermeasures by providing pedestrian and bicycle areas to stay safe.

In the livestock sector, several factors determine the amount of GHG emissions, namely livestock husbandry including housing, feeding, sanitation, and utilization of manure. Research (Herawati, 2012) was conducted in West Java (Cikole, Lembang, Canning, Ciampea, Cisarua, Bogor, Ciracas, and Cakung), Central Java (Semarang, Boyolali, and Magelang), and East Java (Batu, Pujon, Pasuruan, and Malang) as model locations for biogas production and the mitigation technique used to reduce methane emissions is the provision of supplements such as aloe vera waste as a feed supplement in Bali cattle. This practice reduces feed consumption and methane production, but increases metabolized energy and energy utilization efficiency and raises nitrogen uptake so that protein retention can be increased (Mahardika et al., 2011).

Processing of feed ingredients can reduce methane emission using the fermentation of feed. Potassium nitrate reduces methane production compared to the addition of urea. This effect persists for an incubation period of 6 to 48 days. If sulfur is added, reduction in methane production will be greater than that if only nitrate is added (Phuong et al., 2012).

Utilization of chitosan as a feed additive in ruminant diets can reduce enteric methane emissions and change the rumen fermentation profile in a favorable direction (Harahap et al., 2020). Chitosan changes the fatty acid profile of Volatile Fatty Acids (VFA) by increasing the concentration of propionate (C_3) and, thereby, reducing CH_4 production (Jayanegara et al., 2020). Furthermore, the addition of a chitosan source from black soldier flies at a 2 % concentration of feed substrate resulted in a sharp reduction in CH_4 emissions (Jayanegara et al., 2020).

The next method is composting and without realizing its effects and potentials, farmers have been utilizing it to reduce emissions. In addition, biogas production is one of the uses of “green energy”, which is associated with global warming and is an environmentally friendly activity. This form of green energy must be developed, considering that this type is a source of renewable fuel for alternative energy produced by livestock farmers (Herawati, 2012).

What is important and needs to be done is the socialization of GHG mitigation by providing appropriate directions such as fertilization, composting, biogas production, and sanitation to farmers. If the mitigation efforts can be implemented properly, it will generate economic value that incentivizes farmers such as composting, direct use of fertilizers, or gas production (Herawati, 2012).

In the forestry sector, interventions that cause a sustainable decline include reforestation and natural regeneration; protected area conservation; identification of diseases and pests; and biological control (Missanjo & Kadzuwa, 2021). Meanwhile, research on the cultivation aspect of reducing CO-eq emissions in the Mrican Kanan Irrigation Area of 13,102 ha indicates that the application of intermittent irrigation for rice cultivation can reduce emissions by 44.67 %

with CH_4 by 33.18 % compared to conventional rice cultivation (Utaminingsih & Hidayah, 2012).

5. CONCLUSIONS

The results show that machine learning using a combination of hidden layers can generally simulate and predict GHG emissions for GHG mitigation options in manure management. From a total of 15 livestock emiting GHG emissions, 3 livestock that emit the highest emissions from 1961 to 2021 were selected, namely (a) Cattle, (b) Cattle and non-dairy, and (c) Poultry. Significant reductions in CO_2eq emissions in 2020 were demonstrated through reduced public consumption and supply chain obstructions reinforced by large-scale social restrictions (Covid-19 pandemic policy). This experiment was expected to provide added value for developing better decision-making supporting tools and models to assess emission trends in the livestock sector as well as to reinforce the idea of developing CO_2eq emission mitigation strategies during manure storage, leading to more sustainable fertilizer management practices. The policy in the livestock sector regarding the mitigation of CO_2eq emissions remained viable during the storage of manure, leading to more sustainable fertilizer management practices. Mitigation to reduce methane emissions can also be done by utilizing livestock waste as biogas and improving livestock feed using chitosan or potassium nitrate.

The limitation of this study does not include the total number of 15 livestock in Indonesia that emit GHG emissions but only the selected three livestock that emitted the highest emissions from 1961 to 2021, namely (a) cattle, (b) cattle and non-dairy, and (c) poultry. Hence, in the future, the next researcher can predict 15 types of livestock to determine each emission released.

6. CONFLICT OF INTEREST

The author conveys that this research does not contain conflicts between organizations or individuals, both from finances or relationships with other people.

7. ACKNOWLEDGEMENT

The author would like to thank Pimpinan Pusat Muhammadiyah for supporting this research in the RISETMU Batch 5 Grant program with ID 2826.

NOMENCLATURE

CH_4	Methane
N_2O	Nitrous Oxide
CO_2	Carbon Dioxide

REFERENCES

1. Ambazamkandi, P., Thyagarajan, G., Sambasivan, S., Davis, J.R., Sankaralingam, S., & Joseph, B.A. (2015). *Shelter Design for Different Livestock from a Climate Change Perspective*. Springer, (pp. 399-424). https://doi.org/10.1007/978-81-322-2265-1_23
2. Anderson, T.R., Hawkins, E., & Jones, P.D. (2016). CO_2, the greenhouse effect and global warming: from the pioneering work of Arrhenius and Callendar to today's Earth System Models. *Endeavour*, *40*(3), 178-187. https://doi.org/10.1016/j.endeavour.2016.07.002
3. Broucek, J. (2014). Production of methane emissions from ruminant husbandry: A review. *Journal of Environmental Protection*, *05*(15), 1482-1493. https://doi.org/10.4236/jep.2014.515141
4. Chlingaryan, A., Sukkarieh, S., & Whelan, B. (2018). Machine learning approaches for crop yield prediction and nitrogen status estimation in precision agriculture: A review. *Computers and Electronics in Agriculture*, *151*(November 2017), 61-69. https://doi.org/10.1016/j.compag.2018.05.012
5. Fang, G., Tian, L., Fu, M., Sun, M., Du, R., & Liu, M. (2016). Investigation of carbon tax pilot in YRD urban agglomerations-analysis and application of a novel ESER system with carbon tax constraints. *Energy Procedia*, *88*(025), 290-296. https://doi.org/10.1016/j.egypro.2016.06.148
6. FAOSTAT Agriculture Total Online Database. (2020). *FAOSTAT Agriculture Total Online Database*. Fao.Org. http://www.fao.org/faostat/en/#data/GT
7. Hamrani, A., Akbarzadeh, A., & Madramootoo, C.A. (2020). Machine learning for predicting greenhouse gas emissions from agricultural soils. *Science of the Total Environment*, *741*, 140338. https://doi.org/10.1016/j.scitotenv.2020.140338
8. Harahap, R.P., Setiawana, D., Nahrowib, S., Suharti, S., Obitsud, T., & Jayanegara, A. (2020). Enteric methane emissions and rumen fermentation profile treated by dietary chitosan: A meta-analysis of in vitro experiments. *Tropical Animal Science Journal*, *43*(3), 233-239. https://doi.org/10.5398/tasj.2020.43.3.233
9. Herawati, T. (2012). Refleksi sosial dari mitigasi emisi gas rumah kaca pada sektor peternakan di Indonesia. *Wartazoa*, *22*(1), 35-46. https://repository.pertanian.go.id/server/api/core/bitstreams/b45033a2-b954-4f14-b967-27827982475a/content
10. Gitarskiy, M.L. (2019). The refinement to the 2006 ipcc guidelines for national greenhouse gas inventories. *Fundamental'naâ I Prikladnaâ Klimatologiâ*, *2*, 5-13. https://doi.org/10.21513/0207-2564-2019-2-05-13
11. Mahardika, I.G., Suryani, N.N., Mariani, N.P., Suarna, I.W., Duarsa, M., & Mudita, I.M. (2011). Pemanfaatan limbah lidah buaya sebagai feed supplemet pakan sapi bali dalam upaya mengurangi emisi metan. *Pastura : Jurnal Ilmu Tumbuhan Pakan Ternak*, *1*(2), 44-47. https://ojs.unud.ac.id/index.php/pastura/article/view/1596
12. Jayanegara, A., Haryati, R.P., Nafisah, A., Suptijah, P., Ridla, M. & Laconi, E.B. (2020). Derivatization of chitin and chitosan from black soldier fly (*hermetia illucens*) and their use as feed additives: An *in vitro* study. *Archives of Anesthesiology and Critical Care*, *8*(5), 472-477. http://dx.doi.org/10.17582/journal.aavs/2020/8.5.472.477
13. Le Quéré, C., Jackson, R.B., Jones, M.W., Smith, A.J.P., Abernethy, S., Andrew, R.M., De-Gol, A.J., Willis, D.R., Shan, Y., Canadell, J.G., Friedlingstein, P., Creutzig, F., & Peters, G.P. (2020). Temporary reduction in daily global CO_2 emissions during the COVID-19 forced confinement. *Nature Climate Change*, *10*(7), 647-653. https://doi.org/10.1038/s41558-020-0797-x
14. Limanseto, H. (2021, October). Kelola isu perubahan iklim, pemerintah manfaatkan strategi transformasi ekonomi melalui pembangunan hijau. *Kementerian Koordinator Bidang Perekonomian*. https://www.ekon.go.id/publikasi/detail/3386/kelola-isu-perubahan-iklim-pemerintah-manfaatkan-strategi-transformasi-ekonomi-melalui-pembangunan-hijau
15. Masson Delmotte, V., Zhai, P., Pörtner, H.-O., Roberts, D., Skea, J., Shukla, P.R., Pirani, A., Moufouma-Okia, W., Péan, C., Pidcock, R., Connors, S., Matthews, J.B.R., Chen, Y., Zhou, X., Lonnoy, E., Maycock, T., & Tignor, M. (2018). *Summary for Policymakers*. https://www.ipcc.ch/sr15/chapter/spm/
16. Miranti Ariani, M., & Ardiansyah, P.S. (2015). Inventarisasi emisi GRK lahan pertanian di kabupaten grobogan dan tanjung jabung timur dengan menggunakan metode IPCC 2006 dan modifikasinya. *Jurnal Sumberdaya Lahan*, *9*(1), 15-26. https://www.neliti.com/id/publications/132900/inventarisasi-emisi-grk-lahan-pertanian-di-kabupaten-grobogan-dan-tanjung-jabung
17. Missanjo, E., & Kadzuwa, H. (2021). Greenhouse gas emissions and mitigation measures within the forestry and other land use subsector in Malawi. *International Journal of Forestry Research*, *2021*(i). https://doi.org/10.1155/2021/5561162
18. Pachauri, R.K., & Leo Meyer, T.C.W.T. (2014). Contribution of working groups I, II and III to the fifth assessment report of the intergovernmental panel on climate change [core writing team, R.K. Pachauri and L. Meyer (eds)], *Intergovernmental panel on climate change* (pp. 155), IPCC, Geneva, Switzerland,. https://www.ipcc.ch/report/ar5/syr/
19. Peraturan Presiden Republik Indonesia No. 71 Tahun 2011 tentang Penyelenggaraan Inventarisasi Gas Rumah Kaca Nasional, (2011). https://peraturan.bpk.go.id/Home/Details/41187/perpres-no-71-tahun-2011.

20. Peraturan Presiden Republik Indonesia No 61 Tahun 2011 tentang Rencana Aksi Nasional Penurunan Emisi Gas Rumah Kaca, (2011). https://peraturan.bpk.go.id/Home/Details/41199/perpres-no-61-tahun-2011
21. Phuong L.T.B., Khang, D.N., & Preston, T.R. (2012). Effect of NPN source, level of added sulphur and source of cassava leaves on growth performance and methane emissions in cattle fed a basal diet of molasses. *Livestock Research for Rural Development*, *24*(4). http://www.lrrd.org/lrrd24/4/phuong24070.htm
22. Ratnawati, D. (2016). Carbon tax sebagai alternatif kebijakan untuk mengatasi eksternalitas negatif emisi karbon di indonesia. *Indonesian Treasury Review Jurnal Perbendaharaan Keuangan Negara Dan Kebijakan Publik*, *1*(2), 53-67. https://doi.org/10.33105/itrev.v1i2.51
23. Utaminingsih, W., & Hidayah, S. (2012). Mitigasi emisi gas rumah kaca melalui penerapan irigasi intermittent di lahan sawah beririgasi. *Jurnal Irigasi*, *7*(2), 132. https://doi.org/10.31028/ji.v7.i2.132-141
24. Van Houdt, G., Mosquera, C., & Nápoles, G. (2020). A review on the long short-term memory model. *Artificial Intelligence Review*, *53*(8), 5929-5955. https://doi.org/10.1007/s10462-020-09838-1
25. Whelan, B., Taylor, J., & Taylor, J.A.P. (2013). *Precision agriculture for grain production systems*. CSIRO. https://www.researchgate.net/publication/239731186_Precision_Agriculture_for_Grain_Production_Systems
26. Widiawati, R.A.Y., Tiesnamurti, B., Hdayat, C., Nurhayati, I.S., Wahyono, T., Krisnan, R., Rofiq, M.N., Shiddique, M.I., Ramadhan, B.A., Krishna, N.H., Anggraeny, Y.N., Ginting, S.P., & Munawaroh, I.S. (2021c). Emisi gas rumah kaca dari peternakan di indonesia dengan TIER 2 IPCC. In *Penerbit BRIN eBooks*. https://doi.org/10.55981/brin.461
27. World Meteorological Organization & Atmosphere Watch Global. (2017). *Greenhouse gas*. https://public.wmo.int/en/resources/library/wmo-greenhouse-gas-bulletin
28. Zhao, G., Miao, Y., Wang, H., Su, M., Fan, M., Zhang, F., Jiang, R., Zhang, Z., Liu, C., Liu, P., & Ma, D. (2013). A preliminary precision rice management system for increasing both grain yield and nitrogen use efficiency. *Field Crops Research*, *154*, 23-30. https://doi.org/10.1016/j.fcr.2013.07.019

JREE: Vol. 10, No. 3, (Summer 2023) 107-113

Journal of Renewable
Energy and Environment

Journal Homepage: www.jree.ir

Materials and Energy Research Center
MERC

Research Article

Feasibility Study of Energy Production from Small Archimedes Turbines on the Coast of Bandar Abbas and Calculation of Efficiency Optimization Parameters by Linear Programming

Majid Zarezadeh [a*], Hoda Mansouri [b], Alireza Eikani [c]

[a] *Department of Planning and Support, Administration Standard of Hormozgan, Iranian National Standard Organization, P. O. Box: 7919716839, Bandar Abbas, Hormozgan, Iran.*
[b] *Technical Director of Inspection, Nik Azmai Hormozgan Co., Bandar Abbas, Hormozgan, Iran.*
[c] *Department of Electrical Engineering, Amirkabir University of Technology, Tehran, Iran.*

PAPER INFO

Paper History:
Received: 09 June 2022
Revised: 14 August 2022
Accepted: 21 August 2022

Keywords:
Archimedes Turbine,
Linear Programming,
Feasibility Study,
Numerical Study,
Tidal Waves

ABSTRACT

In this study, in addition to assessing the conditions in the coastal region of Bandar Abbas, the feasibility of utilizing Archimedes torsional turbines for renewable energy production in this area was investigated through a combination of field measurements and numerical simulations. Field studies included the measurement of environmental conditions, depth, and vessel traffic. The determination of a safe depth was based on these measurements. Additionally, the current patterns were assessed in the field, measuring key parameters like salinity, electrical conductivity, and density. To further develop the results, a numerical simulation was conducted using the ROMS numerical model to establish the hydrodynamic current patterns in the target area. Upon reviewing the outcomes with the SOLVER program and employing linear programming methods, effective constraints derived from field monitoring were created. The study explored the optimal energy efficiency of Archimedes torsional turbines under different inclinations relative to the seabed and angular velocities. The research and simulations revealed that varying the tilt of the vertical axis of the turbine within the range of 5 to 15 degrees significantly impacted the turbine's efficiency. The highest efficiency, at 75 %, was achieved at a 15-degree angle with a turbine rotation speed of 150 rpm. This result is particularly notable, considering the low slope of the studied area.

https://doi.org/10.30501/jree.2022.345193.1383

1. INTRODUCTION

Fast depleting resources of fossils fuels and their environmental effects have forced humans to look away and seek renewable sources for sustainable development. Among all renewable sources, hydropower continues to be a promising source for energy generation and energy storage. This chapter covers advanced and emerging technologies related to hydropower plants by discussing plant classifications, turbine types, flow instabilities, and market optimization. It provides a detailed overview of the recent efforts to increase the operational range of hydraulic turbines in order to reach exceptional levels of flexibility.

Although Iran is one of the oil-rich countries in the world and has huge natural gas resources due to its high potential in the coastal areas, it can save a considerable amount of energy using the currents of waves and tides. Problems in the use of fossil fuels, as well as increasing environmental pollution, have led many developed countries to use these alternative energy sources. According to the International Renewable Energy Agency, from 2010 to 2020, the installation of renewable energy equipment from the sea and ocean has more than doubled (Figure 1). Iran has a huge maritime potential and high potential for renewable energy. Tidal energy, as one of the most important and suitable renewable sources of marine energy, can supply part of the country’s energy demand and be an alternative to reduce fossil energy consumption for electricity generation. Exploiting the tidal range in the coastal strip using barriers to block coastal waters, and estuaries in a high or low position and considering tidal cycles help harness this energy. The tidal range varies from region to region because it is dependent on the longitude and latitude of a location, the hydrodynamics of the region, and the type of seabed. One of the advantages of tidal energy is its predictability as well as its seasonal fluctuations, which will lead to sustainable energy production over the years. In recent years, tidal energy has become less common among renewable energies, which highlights the need for research and study in this area. Tidal power farms and sites off the coast of Europe are currently generating renewable energy.

*Corresponding Author’s Email: majid_zarezadeh_nu@yahoo.com (M. Zarezadeh)
URL: https://www.jree.ir/article_158807.html

Please cite this article as: Zarezadeh, M., Mansouri, H., & Eikani, M.R. (2023). Feasibility study of energy production from small Archimedes turbines on the coast of Bandar Abbas and calculation of efficiency optimization parameters by linear programming. *Journal of Renewable Energy and Environment (JREE)*, *10*(3), 107-113. https://doi.org/10.30501/jree.2022.345193.1383.

2423-7469/© 2023 The Author(s). Published by MERC. This is an open access article under the CC BY license (https://creativecommons.org/licenses/by/4.0/).

There are generally different ways to use tidal currents in energy production, including tidal turbines, Archimedes torsion, tidal dams, floating structures, tidal kites, and finally artificially intelligent turbines. In the Persian Gulf, due to the low speed of coastal currents and its shallow depth, the use of heavy equipment is not cost-effective and practical, but the use of small equipment such as Archimedes torsional turbines is feasible. This turbine is one of the oldest machines used in the past and continues to function today. This equipment is known as small-scale power plants and is now widely used on the coasts of different parts of the world to produce clean and renewable energy. Low maintenance costs and ease of working with this equipment are other advantages. Archimedes torsional turbines are less harmful to marine ecosystems due to their construction (Khan et al., 2019). Archimedes turbines are slow and perform well in low currents. Due to their symmetrical shape, they can generate energy in tidal currents and, if the optimal angle and tidal velocity are calculated, the efficiency reaches above 70 % (Khan et al., 2019). Due to its simpler design than other tidal energy generation methods, the construction of the Archimedes turbine is much less expensive than other types of turbines.

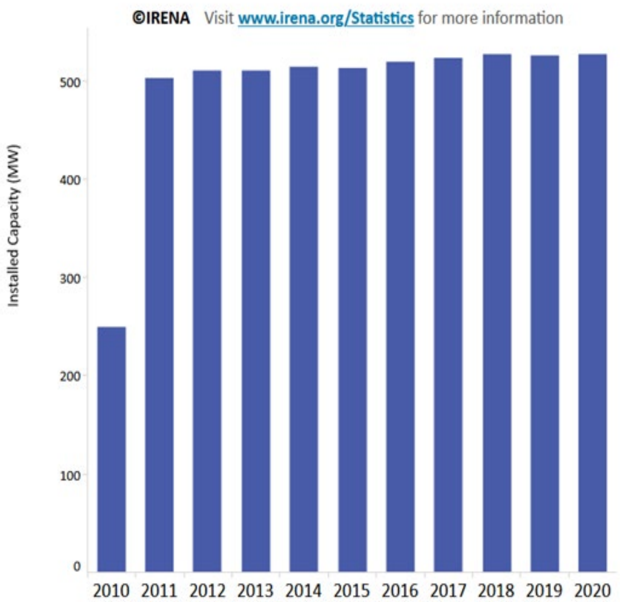

Figure 1. Installation process and use of renewable energy production equipment at sea and ocean from The International Renewable Energy Agency (IRENA)

2. BACKGROUND RESEARCH

Although the Archimedes turbine is capable of operating well in a wide range of flow values, the ability to operate at variable speeds increases this capability and leads to increased turbine efficiency (Borah, 2015). One of the good features of using this type of turbine is that its length can be determined in proportion to the installation location and flow rate by users, in addition, its flexibility brings about increased efficiency in different locations under various conditions.

In the construction of the Archimedes turbine, the parameters are divided into two categories: external and internal (Figure 2). Some of external parameters are external radius Ro, final length of pipe, and slope of the K screw. Internal parameters include the internal radius of the Ri cylinder, blade slope P, and number of blades (Saroinsong et al., 2016). The hydraulic power of the Archimedes wheel turbine in watts is obtained from Equation (1) (YoosefDoost & Lubitz, 2020):

$$P_{hyd} = \rho.g.Q.H = \rho.g.m.\Delta y \tag{1}$$

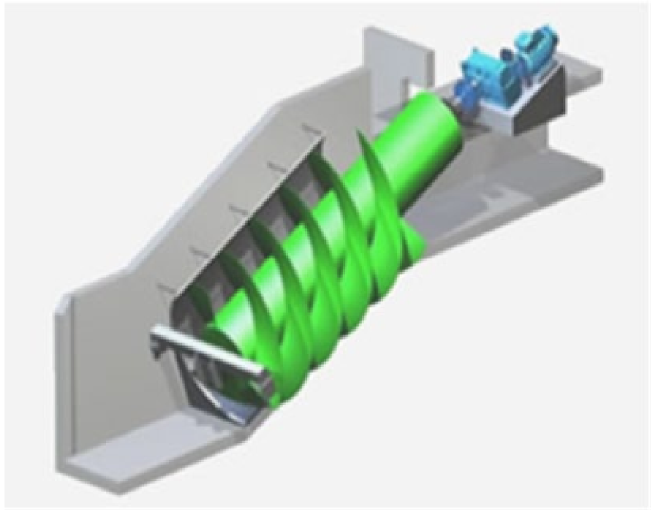

Figure 2. View of the Archimedes screw turbine (Saroinsong et al., 2016)

where ρ is water density, g gravity acceleration, Q flow rate, m number of turns, and Δy the difference in blade height on the slope. The power of a torsional turbine P is equal to the product of the torsion multiplied by T at the angular velocity of the rotation, ω, in watts, calculated by Equation (YoosefDoost & Lubitz, 2020):

$$P = T.\omega = T.\frac{2n\pi}{60} \tag{2}$$

Finally, the efficiency of the torsion turbine is (YoosefDoost & Lubitz, 2020):

$$\eta = \frac{P}{P_{hyd}}.100\ \% \tag{3}$$

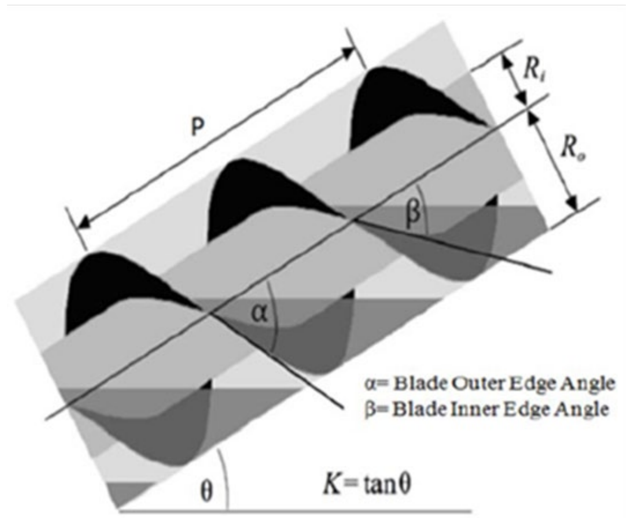

Figure 3. View of the inner and outer profiles of Archimedes turbine (Saroinsong et al., 2016)

Various researches and studies have been done on the conversion of currents, waves, and tides into energy.

Generally, the relevant studies done in Iran are of general and overview types while, in other parts of the world, they involve simulation, optimization, and improvement of the efficiency of Archimedes torsional turbines in a more specialized way. In a study, the feasibility of harnessing renewable energy from the Persian Gulf's sea has been explored. The utilization of the robust currents within the Persian Gulf is suggested as a pivotal factor (Kumar et al., 2016). In a separate study, a floating turbine was designed to leverage vertical and reciprocating tidal wave movements. Following the modeling phase, the energy production efficiency of this system was evaluated. The modeling results indicated that this turbine design exhibits commendable efficiency for energy generation on islands and adjacent coastlines (Seif Jahromi, 2016; Zabihian, 2004). To investigate the feasibility of wave energy absorption via the oscillator column system, proper modeling was used and it was found that if the height of the input waves increased by 10 %, the power of the device would increase by 40 %. In a study conducted in India, the Archimedes torsional turbine was considered as a small-scale power plant and its efficiency was improved by 85 % to 90 % upon performance enhancement (Katabdari, 2011). Another study scrutinized the relationship between external parameters impacting the efficiency of the Archimedes torsional turbine and its internal components, demonstrating that variables such as flow velocity and turbine blade thickness have a direct influence on the turbine's efficiency (Kumar et al., 2016; Suraya et al., 2015). Research on sustainable energy development using Archimedes turbines demonstrated that this type of turbine reduced sedimentation and erosion of the installation site of this equipment (YoosefDoost & Lubitz, 2020). A study on the orientation and angle of Archimedes turbines and their relationship with turbine efficiency concluded that orientation at a 22-degree angle would increase the efficiency of the 4W device by 1.4 % to 49 % (Borah, 2015).

3. METHOD AND MATERIAL

3.1. Basic studies

On the feasibility of using tidal energy, the most important point is to study the depth of the area to immerse the equipment and calculate the minimum safe depth, which is not in the path of the vessels. Moreover, the distance of dynamic systems from the shore is another important parameter in locating the equipment installation site (Kumar et al., 2016). The data required for the depth of the area were obtained from the GEBCO (General Bathymetric Chart of the Ocean) database as well as data from the surveying organization (Zarezadeh et al., 2021). Another important point to consider in examining the feasibility of equipment deployment is the distance of these tools from the habitats of birds and marine animals. Referring to Figure 4, on the eastern part of the coast, there is a gradual change in slope and depth. After covering a distance of 6 to 7 km, it reaches a depth of 8 meters. In contrast, on the western part, this depth is attained after only 1 to 2 km. The eastern coast of Bandar Abbas is predominantly influenced by the tidal zone and features a mild depth gradient.

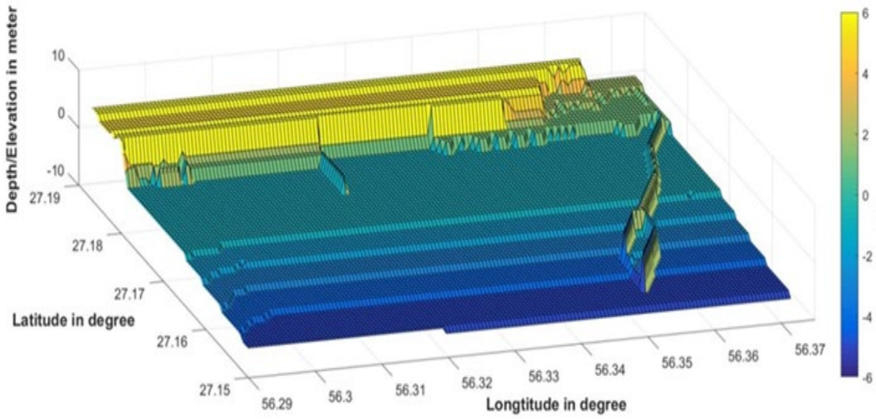

Figure 4. Bathymetry of the study area (Zarezadeh et al., 2021)

3.2. Field measurments

Field measurements are required to perform calculations related to current velocity and effective parameters in the leading study. As shown in Figure 5, for the measurement of current speed vectors and directions, the ADCP[2] device was positioned on the southern side of the pier, located at a distance of 500 meters from the shoreline. Additionally, another ADCP unit was placed on the eastern side of Bandar Abbas beach, precisely at 27.1 degrees latitude and 56.3 degrees longitude. To choose the right place to install the ADCP device, a place with suitable measuring conditions such as flat installation, distance from the post and height, a minimum flow rate of 8 cm/s, and the distance from electric and magnetic fields (Mueller & Wagner, 2013), was selected and ADCP was installed at a depth of 7 m in that location within 30 days, taking into account the presence of spring tide[3] and neap tide[4]. Based on the depth of the area and water level changes, the ADCP device with a frequency of 600 kHz was used (Mueller & Wagner, 2013). To record the current in both x and y directions, the settings of the ADCP device were configured at two time intervals in two layers with a thickness

[2] An acoustic doppler current profiler (ADCP) is a hydroacoustic current meter similar to a sonar and is used to measure water current velocities over a depth range using the Doppler effect of sound waves scattered back from particles within the water column.

[3] Tide around new moon and full moon when the Sun, Moon, and Earth form a line.

[4] Tide when the Moon is at first quarter or third quarter, the Sun and Moon are separated by 90° when viewed from the Earth.

of 2 meters. Over a 30-day measurement period, more than 4300 current velocity data were obtained. Of note, the values obtained for the current are average values at the time interval and the spatial interval specified in the device settings. The T-Tide software package is used to monitor and control tidal current data and eliminate potential outliers. Amplitude and phase of different harmonics were obtained at a confidence level of 95 %. According to the predictions, the main components of the semidiurnal and diurnal tides are M2, S2, K1, O1[5], each of which has a characteristic amplitude of oscillation and phase (Seif Jahromi, 2016). In addition to measuring inlet current velocity using ADCP, various parameters, including salinity, density, water turbidity, and temperature, were measured and monitored by CTD at 11 stations for verification and calibration. Outlier data and normality tests were conducted on this dataset. At a 95 % confidence level, the data showed no outliers and exhibited a normal distribution.

Figure 5. Position of field measurement of current and effective parameters and installation of ADCP device

3.3. ROMS simulation

Because field measurements were conducted at several stations, simulations were needed to survey the entire area. ROMS numerical model was used to simulate and study the tidal current pattern in the region. ROMS[6] is a model that is used dramatically by researchers around the world due to its algorithm type, high efficiency, and appropriate output results, and its wide application (Zarezadeh et al., 2021). As ROMS is an open-source model, it undergoes updates and algorithm improvements to align with the specific conditions of each region and adapt to new events. This iterative process enhances the model's stability, resulting in consistent and reliable output results. The model is analyzed and estimated using flow field data by Reynolds three-dimensional equations.

$$\frac{\partial}{\partial x}\left(\frac{\rho h^3}{12\mu}\frac{\partial p}{\partial x}\right)+\frac{\partial}{\partial y}\left(\frac{\rho h^3}{12\mu}\frac{\partial p}{\partial y}\right)=\frac{\partial y}{\partial x}\left(\frac{\rho h(u_a+u_b)}{2}\right)+\frac{\partial}{\partial y}\left(\frac{\rho h(v_a+v_b)}{2}\right)+\rho(w_a-w_b)-\rho u_a\frac{\partial h}{\partial x}-\rho v_a\frac{\partial h}{\partial y}+h\frac{\partial \rho}{\partial t} \quad (4)$$

where p is fluid film pressure, x and y are the bearing width and length coordinates, z is fluid film thickness coordinate, h is fluid film thickness, μ is fluid viscosity, ρ is fluid density, u, v, w are the bounding body velocities in x , y , z directions, respectively, and a and b are subscripts denoting the top and bottom bounding bodies, respectively.

In order to simulate the study area, a 5 km stretch of the beach in Bandar Abbas, along with a 9 km section perpendicular to the shore, was taken into account. Consequently, the model includes a dry boundary along Bandar Abbas beach and three open water boundaries. Given that field data were solely collected at open boundary 2, determining the currents at Boundaries 3 and 4 necessitated the initial model implementation for the entire Persian Gulf. After reaching a steady state, the ROMS model utilized tidal current data from T-Tide for other open boundaries. Depending on the specific area and the regions influenced by tides, a nested network was employed to simulate the entire area (Table 1). ADCP field measurement data were used to estimate the simulation accuracy in the study area (Zarezadeh et al., 2021). After setting the initial inputs of the model, it was calibrated and tidal data were employed to validate the results on open boundaries. After networking, delimitation, and boundary conditions, tidal data were generated and its information was incorporated into the ROMS model. The duration of the model is 30 days and in the study area, it is defined at time intervals of 600 seconds (Table 1). After defining all the required parameters, the model was implemented based on the output of current velocities u and v in the study area and on the coast of Bandar Abbas.

4. RESULTS AND DISCUSSION

4.1. Analysis of measurment and simulation monitoring results

Coastal tidal currents have different speeds and directions at different times. First, all the data are statistically analyzed, such that if there is outlier, this data is excluded from the calculations. For this purpose, the Grubb test was used at a 95 % confidence level, which indicated the absence of outliers in the measurement data. According to the simulated current pattern in the region, maximum velocity is 89.59 cm/s in the bed layer during the measuring month while the value of 93.81 cm/s is superficial. As expected, the maximum velocities occurred at intervals of new and full moons. WRplot software was employed to draw the rose current diagram, indicating the existence of two dominant streams (Figure 6). The mainstream is to the north, the coast of Bandar Abbas, and the tidal current is to the southwest. Considering the orientation and angle of the Nakhle Nakhoda pier towards the coast of Bandar Abbas, this direction of the mainstream is the main cause of sedimentation and erosion rates around the pier.

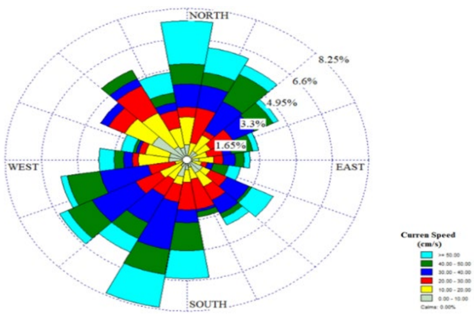

Figure 6. Diagram of the dominant rose current

---
[5] K1 and O1 are tidal diurnal harmonic; M2 and S2 are tidal simidiurnal harmonic.
[6] Regional Ocean Models (ROMS).

The time course of the velocities is in accordance with the tidal period of one month in the region. The study of asymmetry in the tidal current indicates the dominance of one of the currents, which is called the dominant tide or dominant wave. Figure 7 shows the directional distribution of tidal currents with respect to periodicity. The maximum flood tidal current is 93.81 cm/s and the maximum ebb tidal current is 81.60 cm/s. This difference due to the asymmetry of the tidal current velocity leads to a change in the balance of sediment transport and in the long run, the sediment transport will go to the bay and form sedimentary hills (Borah, 2015). Measurement of important data such as salinity, temperature, acidity, and density by CTD in the operation range shows that the data have a normal distribution (Table 2). These data can also be used to analyze the feasibility of using Archimedes torsional turbines.

Table 1. Variables in the nesting for ROMS simulation (Zarezadeh et al., 2021)

Nesting name	Longitude	Latitude	Time Resolution (Second)	Space Resolution(m)
Nesting 1	56.34E-56.36E	27.16N-27.18N	600	50
Nesting 2	56.28E-56.34E	27.14N-27.17N	600	500
Nesting 3	50.01E-56.61E	24.09N-30.11N	3600	10000

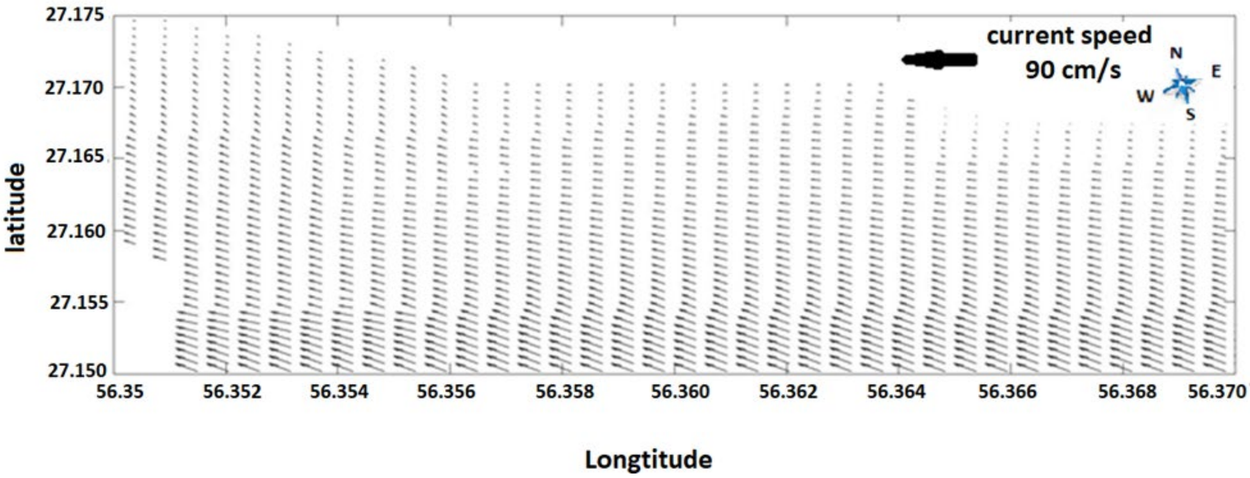

Figure 7. Current pattern simulated by ROMS in the study area

Table 2. Distribution of important parameters in the field measurement

Station number	Longitude	Latitude	Conductivity	Salinity	Dissolve oxygen	Oxygen	pH	chl-a	Turbidity
1	56.350	27.153	50.806	37.393	27.481	1.952	5.680	1.414	26.510
2	56.360	27.160	50.397	37.412	30.240	2.164	4.657	1.616	19.788
3	56.362	27.163	49.200	36.718	30.412	2.198	4.802	2.268	13.149
4	56.367	27.156	49.442	37.022	30.565	2.210	4.202	1.819	6.342
5	56.364	27.154	50.498	37.557	29.522	2.113	5.610	1.165	7.111
6	56.362	27.152	50.541	37.525	29.258	2.091	5.549	2.549	10.962
7	56.360	27.150	50.760	37.482	29.172	2.076	5.665	1.579	24.551
8	56.363	27.148	50.887	37.434	28.954	2.056	6.532	1.719	11.770
9	56.367	27.152	50.847	37.476	28.954	2.057	5.615	1.579	10.277
10	56.367	27.152	50.730	37.485	29.202	2.080	5.787	1.553	15.277
11	56.369	27.154	50.619	37.504	29.215	2.085	5.110	1.169	8.292
12	56.350	27.153	50.806	37.393	27.481	1.952	5.680	1.414	26.510
13	56.360	27.160	50.397	37.412	30.240	2.164	4.657	1.616	19.788
14	56.367	27.156	49.442	37.022	30.565	2.210	4.202	1.819	6.342
15	56.364	27.154	50.498	37.557	29.522	2.113	5.610	1.165	7.111
16	56.362	27.152	50.541	37.525	29.258	2.091	5.549	2.549	10.962
17	56.360	27.150	50.760	37.482	29.172	2.076	5.665	1.579	24.551
18	56.358	27.148	50.887	37.434	28.954	2.056	6.532	1.719	11.770
19	56.363	27.148	50.847	37.476	28.954	2.057	5.615	1.579	10.277
20	56.367	27.152	50.730	37.485	29.202	2.080	5.787	1.553	15.277
21	56.369	27.154	50.619	37.504	29.215	2.085	5.110	1.169	8.292

The uniformity of temperature, density, and salinity parameters in the measurement and simulation range and the normal distribution of this data at a 95 % confidence level indicate the correct choice of the study site.

4.2. Evaluation results for Archimedes screw turbine

The output of field measurement data as well as the output data of the model and parameters by CTD can be used to analyze and evaluate the feasibility of using the Archimedes torsional turbine. According to Relationships 1 to 3 and using the SOLVER program[7], important values are analyzed and suggestions are made about suitable values that have high efficiency. Based on Equations 1 and 2, different parameters are effective in determining the efficiency of the torsional turbine. Therefore, only a number of parameters are considered variable while others are constant. The efficiency of a torsional turbine depends on the geometry of the turbine and the changes in fluid flow (Saroinsong et al., 2016). A noteworthy point about torsional turbines is the combination of different parameters; therefore, the variation in the values of paramters affects each paramter. This mutual impact that parameters have on each other should be considered in optimizing their efficiency. It is not possible to modify all these parameters in the optimization process; thus, as a result of a large number of parameters and ambiguity in the optimization process, only some parameters are considered variable. In this research, the current velocity and the angular velocity of rotation will be selected as variable parameters.

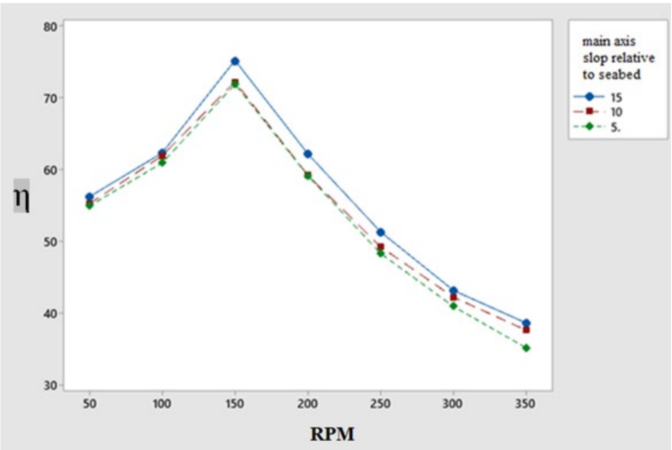

Figure 8. Comparison of efficiency changes in terms of turbine incline relative to beneath and rotational speeds (RPM)

Torsional turbine performance is calculated and estimated based on Equation 3. Figure 8 shows turbine efficiencies at three angles of 5 %, 10 %, and 15 %. According to this optimization, the maximum efficiency is at an angle of 15 degrees to the bed and 150 rpm.

5. CONCLUSIONS

The use of the output of the ROMS model in optimization calculations and finding the optimal value of RPM from coastal current data in an area with a gentle slope are the innovations of this research. The study area has not been explored enough for the use of renewable energy due to its gentle slope, high humidity, and high temperature. The primary hypothesis of this research was whether the coastal area of Bandar Abbas with a gentle slope and low current speed could be a proper place for the installation of the Archimedes turbine. Since this type of turbine is mainly used in canals and river beds, its use near the coast with constant coastal current remains the basic question of this research. Is it economical to use this type of turbine?

Due to the importance of energy consumption in the country and the relatively low cost of Archimedes turbines, this type of turbine can be used as a pilot on the coast of Bandar Abbas to generate limited energy. This turbine is not only eco-friendly but also inexpensive. These features help reduce damage to the environment, facilitate job creation, and contribute to appropriate research in this field. The diagram in Figure 9 shows the research process in summary.

Based on the findings from field data and simulations, it can be concluded that the gentle slope of the coastal area can be offset by modifying the speed of the tidal current.

Due to the shallow depth and gentle slope of the coastal region in Bandar Abbas, coupled with the low speed of the tidal current, the utilization of an Archimedes turbine is a cost-effective and appropriate choice for this area.

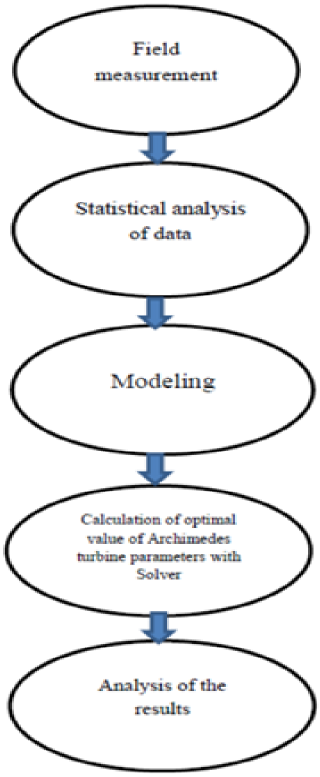

Figure 9. Flowchart to describe research steps

6. ACKNOWLEDGEMENT

We must thank and appreciate the cooperation and assistance of the Department and staff of the Persian Gulf Oceanographic Center, who were instrumental in the field measurement by ADCP equipment.

NOMENCLATURE

P	Water density (kg/m^3)
G	Gravity acceleration (m/s^2)

[7] Solver is a Microsoft Excel add-in program that can use for what-if analysis. Use Solver to find an optimal (maximum or minimum) value for a formula in one cell subject to constraints, or limits, on the values of other formula cells on a worksheet.

Q	Flow rate (m^3/s)
M	Number of turns
P	Power of a torsional turbine (w)
Ro	External radius (cm)
Ri	Internal radius (cm)
Greek letters	
Ω	Angular velocity of the rotation (Radian/s)
η	Efficiency of the torsion turbine (%)

REFERENCES

1. Borah, S., Gogoi, S., & Askary, Z. (2015). A theoretical study of design parameters of an Archimedean screw turbine. *Journal of Material Science and Mechanical Engineering (JMSME)*, *2*(14), 32-34. https://www.google.com/url?sa=t&rct=j&q=&esrc=s&source=web&cd=&cad=rja&uact=8&ved=2ahUKEwjPtKubi-b_AhU5m_0HHagyBPQQFnoECA4QAQ&url=http%3A%2F%2Fwww.energiazero.org%2Fidroelettrico%2Farchimede%2FArchimedean%2520Screw%2520Turbine.pdf&usg=AOvVaw1tqZnXx3b2X1ZDbmLfsKT-&opi=89978449
2. Katabdari, M.J., & Ahmadi, M.E. (2011). Feasibility study of energy absorption from sea waves in the Southern coasts of Iran with the help of numerical modeling. *Quarterly Journal of Marine Science and Technology*, *25*(90), 20-29. https://dorl.net/dor/20.1001.1.17355346.1390.15.60.3.1
3. Khan, A., Khattak, A., Ulasyar, A., Imran, K., & Munir, M. (2019). *Investigation of Archimedean screw turbine for optimal power output by varying number of blades*. Proceedings of the 2019 International Conference on Electrical, Communication, and Computer Engineering (ICECCE), Swat, Pakistan. https://doi.org/10.1109/ICECCE47252.2019.8940654
4. Kumar, U., Singh, P., & Tiwari, A. (2016). Suitability of Archimedes screws for micro hydro power generation in India. *International Journal of Thermal Technologies, 6*(3), 273-278. https://inpressco.com/suitability-of-archimedes-screws-for-micro-hydro-power-generation-in-india/
5. Mueller, D., & Wagner, C.R. (2013). Measuring discharge with acoustic Doppler current profilers from a moving boat. Chapter 22 of Section A: Surface-water techniques in Book 3: *Applications of Hydraulics*. https://doi.org/10.3133/tm3A22
6. Saroinsong, T., Soenoko, R., Wahyudi, S., & Sasongko, M.N. (2016). Performance of three-bladed Archimedes screw turbine. *ARPN Journal of Engineering and Applied Sciences, 11*(15), 9491-9495. https://www.researchgate.net/profile/Tineke-Saroinsong/publication/307568262_Performance_of_threebladed_Archimedes_screw_turbine/links/58d380b7458515e6d900d7bd/Performance-of-three-bladed-Archimedes-screw-turbine.pdf?origin=publication_detail
7. Seif Jahromi, M., & Souri, A. (2016). *Feasibility study of sea wave energy extraction.* Proceedings of the 10th National Conference on Renewable, Clean and Efficient Energy, Tehran, Iran. https://sid.ir/paper/833162/fa
8. Suraya, N., Nik Mutasim, M., & Jamaludin, U. (2015). The effect of substantive parameters on the efficiency of Archimedes screw microhydro power: A review. *IOP Conference Series: Materials Science and Engineering*, *100*, 012030. https://doi.org/10.1088/1757-899X/100/1/012030.
9. YoosefDoost, A., & Lubitz, W.D. (2020). Archimedes screw turbines: A sustainable development solution for green and renewable energy generation—A review of potential and design procedures. *Sustainability*, *12*(18). http://dx.doi.org/10.3390/su12187352
10. Zabihian, F. (2004). *Evaluation of the energy of the Iranian sea waves and construction and testing of a model for the extraction of this energy.* Proceedings of 19th International Conference on Electricity, Tehran, Iran. https://civilica.com/doc/20816/
11. Zarezadeh, M., Rahbani, M., Hamzeei, S., & Khosravi, M. (2021). Investigating the effect of Nakhle Nakhoda pier construction on current pattern and turbidity in the region. *Hydrophysics*, *7*(1), 47-58. https://www.hydrophysics.ir/article_248924.html

ABSTRACTS

Investigation of the Height Distribution Effect of Residential Complex Blocks on Optimization of Cooling and Heating Loads (Tehran, District 9)

Zeinab Ghasemi Sangi, Abbas Tarkashvand, Haniyeh Sanaieian *

Department of Building and Environment, School of Architecture and Environmental Design, Iran University of Science and Technology, P. O. Box: 1684613114, Tehran, Iran.

PAPER INFO

Paper History:
Received: 29 May 2022
Revised: 08 October 2022
Accepted: 13 October 2022

Keywords:
Energy Optimization,
Height Distribution,
Urban Blocks,
Residential Complex,
Layout,
Simulation

ABSTRACT

The height of buildings is one of the main features of urban configuration that affects energy consumption. However, to our knowledge, the complexity of relationships between the height parameters and energy use in urban blocks is poorly understood. In this context, the present study investigates the effect of the height distribution of buildings located in a residential complex on the energy consumption required for cooling and heating. This research simulates different possible layouts through computational software. For this purpose, first, the density of a residential complex was determined based on the rules and regulations of Tehran city and according to the site dimensions and certain site coverage. Then, the required building density was distributed in different layouts based on their diversity at different heights. The product of this stage involved 7 different layouts in which the height varied from 1 floor to the maximum number calculated in each part of the simulation. In the next step, the annual energy consumption for cooling and heating the complex was calculated for each of these layouts and compared with each other. The parametric generative model was created in the Grasshopper plugin from Rhino software, and the energy consumption was evaluated with the Honeybee plugin over one year. Also, the research findings were validated through DesignBuilder software using the EnergyPlus engine. The results of the energy simulation indicate that the height distribution of the blocks can have a significant effect on energy consumption. In the optimal case, proper layout reduces the annual cooling and heating energy consumption by 28 % and 13 %, respectively. Therefore, achieving an optimal value for each of the cooling and heating loads depends on the specific priorities and conditions of the design project. If the design project's priority is to reduce heating energy consumption, increasing the height and distributing the floors evenly between the blocks is a better answer. However, if the priority is to mitigate cooling energy consumption, the optimal layout can include low-rise blocks and a single very high-rise block.

https://doi.org/10.30501/jree.2022.344678.1380

2423-7469/© 2023 The Author(s). Published by MERC. This is an open access article under the CC BY license (https://creativecommons.org/licenses/by/4.0/).

چکیده

ارتفاع ساختمان‌ها، یکی از شاخصه‌های اصلی پیکربندی شهری می‌باشد که بر میزان مصرف انرژی مؤثر است. با این حال، طبق دانسته‌های ما، پیچیدگی روابط بین پارامترهای ارتفاعی و میزان مصرف انرژی در بلوک‌های شهری به خوبی درک نشده است. در این چارچوب، پژوهش حاضر، به بررسی تأثیر نحوه‌ی توزیع ارتفاعی ساختمان‌های واقع در یک مجموعه‌ی مسکونی، برمیزان مصرف انرژی مورد نیاز این مجموعه برای سرمایش و گرمایش پرداخته است. این پژوهش، با روش شبیه‌سازی چیدمان‌های مختلف ممکن، از طریق نرم‌افزارهای محاسباتی انجام شده است. برای این منظور، ابتدا تراکم یک مجموعه‌ی مسکونی، با توجه به ابعاد زمین، سطح اشغال معین و بر اساس ضوابط و قوانین شهر تهران، مشخص شده است. سپس، تراکم مورد نیاز، در چیدمان‌های مختلف، بر اساس تنوع آن‌ها در ارتفاع‌های متفاوت، توزیع شده است. محصول این مرحله، ۷ تیپ چیدمان مختلف بوده که ارتفاع در آن‌ها از ۱ طبقه تا حداکثر تعداد محاسبه شده در هر بخش از شبیه‌سازی، متغیر می‌باشد. در مرحله‌ی بعد، میزان مصرف انرژی سالانه جهت سرمایش و گرمایش مجموعه، برای هر یک از این چیدمان‌ها محاسبه و با یکدیگر مقایسه شده است. مدل مولد پارامتریک، در افزونه‌ی گرس‌هاپر از نرم‌افزار راینو ایجاد شده و ارزیابی میزان مصرف انرژی، با افزونه‌ی هانی‌بی، در یک بازه‌ی یک‌ساله انجام شده است. همچنین، یافته‌های پژوهش، از طریق نرم‌افزار دیزاین بیلدر، با استفاده از موتور انرژی‌پلاس اعتبارسنجی شده است. نتایج حاصل از شبیه‌سازی انرژی، حاکی از آن است که نحوه‌ی توزیع ارتفاعی بلوک‌ها، می‌تواند تأثیر چشم‌گیری بر میزان مصرف انرژی داشته باشد. در حالت بهینه، چیدمان مناسب، موجب کاهش میزان مصرف انرژی سرمایشی سالیانه تا ۲۸ ٪ و کاهش میزان مصرف انرژی گرمایشی تا حدود ۱۳ ٪ می‌شود. از این رو، دستیابی به مقدار بهینه برای هر یک از بارهای سرمایشی و گرمایشی، به اولویت‌ها و شرایط خاص پروژه‌ی طراحی بستگی دارد. درصورتیکه، اولویت پروژه طراحی با کاهش مصرف انرژی گرمایشی باشد، افزایش ارتفاع و توزیع طبقات میان بلوک‌ها به صورت برابر، پاسخ بهتری است. اما زمانیکه کاهش مصرف انرژی سرمایشی اولویت باشد، چیدمان بهینه می‌تواند شامل بلوک‌های کوتاه‌مرتبه و یک بلوک بسیار بلندمرتبه باشد.

Mitigating Energy Consumption of Educational Buildings Using a Novel Simulation Method (Case Study: Faculty of Oil and Petrochemical Engineering, Razi University, Iran)

Soheil Fathi [a], Abbas Mahravan [b*]

[a] Department of Architecture, Faculty of Architecture and Urbanism, Art University of Isfahan, Isfahan, Iran.
[b] Department of Architectural Engineering, Faculty of Engineering, Razi University, Kermanshah, Iran.

PAPER INFO

Paper History:
Received: 28 June 2022
Revised: 16 August 2022
Accepted: 28 August 2022

Keywords:
Educational Buildings,
Energy Retrofit,
Shading Devices,
Window,
Insulation

ABSTRACT

In many middle- and high-income countries, existing buildings will occupy the majority of building areas by 2050 and measures are needed to upgrade the mentioned buildings for a sustainable transition. This research proposes a method to mitigate the energy consumption of existing educational buildings using four energy efficiency measures (EEMs). The proposed method divides simulations into two main parts: simulations with and without using heating, ventilating, and air conditioning (HVAC) systems. Four passive EEMs are used, including window replacement, proposed shading devices, new insulations, and installing a new partition wall for the entrance part of the building. This research uses a simulation-based method to examine the effect of each EEM on the energy consumption of the building using DesignBuilder software. The steps of data collection and modeling in this research include collecting raw data related to the physical characteristics of the building experimentally and creating a basic model. Afterwards, simulation scenarios were defined based on the proposed method, and several simulations were carried out to examine the impact of each EEM on the energy performance of the building. Two environmental parameters of the simulation process, including indoor air temperature (IAT) and relative humidity (RH), were used. The measures reduced the heating and cooling demands in the building by 80.14 % and 15.70 %, respectively. Moreover, the results indicated that the total energy consumption of the building were reduced by 10.44 % after retrofitting measures.

https://doi.org/10.30501/jree.2022.349282.1394

2423-7469/© 2023 The Author(s). Published by MERC. This is an open access article under the CC BY license (https://creativecommons.org/licenses/by/4.0/).

چکیده

در بسیاری از کشورهای با درآمد بالا و متوسط ساختمان‌های موجود بیشترین سهم را تا سال ۲۰۵۰ به خود اختصاص خواهند داد، و راهکارهایی برای بهبود ساختمان‌های ذکر شده برای گذاری پایدار باید معرفی شوند. این تحقیق، روشی را برای کاهش مصرف انرژی ساختمان‌های آموزشی موجود با استفاده از چهار راهکار بهسازی انرژی پیشنهاد می‌دهد. این روش پیشنهادی شبیه‌سازی‌ها را به دو بخش عمده تقسیم می‌کند: شبیه‌سازی‌های بدون سیستم تهویه و شبیه‌سازی‌های با سیستم تهویه. چهار راهکار غیرفعال شامل تعویض پنجره، سایه‌اندازی پیشنهادی، عایق‌های جدید و نصب یک دیوار جداکننده برای بخش ورودی ساختمان استفاده شده‌اند. این تحقیق از روش مبتنی بر شبیه‌سازی با استفاده از نرم‌افزار دیزاین‌بیلدر برای بررسی تأثیر هر راهکار بهسازی انرژی بر مصرف انرژی ساختمان استفاده می‌کند. مراحل جمع‌آوری داده‌ها و مدل‌سازی در این تحقیق شامل جمع‌آوری داده‌های مربوط به خصوصیات فیزیکی ساختمان به شکل تجربی و ساخت یک مدل پایه اولیه است. سپس، سناریوهای شبیه‌سازی برا اساس روش پیشنهادی تعریف شدند و شبیه‌سازی‌های مختلفی برای بررسی تأثیر هر راهکار بهسازی انرژی بر عملکرد انرژی ساختمان تعریف شدند. دو متغیر محیطی فرآیند شبیه‌سازی، شامل دمای هوای داخل و رطوبت نسبی، استفاده شدند. این راهکارها نیاز گرمایشی و سرمایشی ساختمان را به ترتیب تا ۸۰/۱۴ ٪ و ۱۵/۷۰ ٪ کاهش دادند. همچنین، نتایج این تحقیق نشان دادند که مصرف انرژی ساختمان تا ۱۰/۴۴ ٪ پس از راهکارهای بهسازی کاهش پیدا کرده است.

Enhancement of 5-Hydroxymethylfurfural and 2,5-Furandicarboxylic Acid Extractions into Bio-Plastic Production from Renewable Sources

Payam Ghorbannezhad [a,b*], Behnam Dehbandi [c], Imtiaz Ali [d]

[a] *Department of Biorefinery, Faculty of New Technologies Engineering, Shahid Beheshti University, Tehran, Iran.*
[b] *Alliance for Biomass and Sustainability Research–ABISURE, National University of Colombia, Campus Robledo, M3-214, Medellín, Colombia.*
[c] *Department of Chemistry, Science and Research Branch, Islamic Azad University, Tehran, Iran.*
[d] *Department of Chemical and Materials Engineering, King Abudlaziz University, Rabigh, Suadia Arabia.*

PAPER INFO

Paper History:
Received: 28 July 2022
Revised: 08 October 2022
Accepted: 21 October 2022

Keywords:
5-Hydroxymethylfurfural (HMF),
2,5-Furandicarboxylic Acid (FDCA),
Renewable Sources,
Density Function Theory (DFT)

ABSTRACT

Furandicarboxylic acid (FDCA) is recognized as a valuable product of hydroxymethylfurfural (HMF) derived from cellulosic materials as an abundant renewable source. It could find future bioplastic application if a feasible separation process is developed. To find a commercially available solvent, FDCA should be selectively separated from HMF and the downstream process be supported by pyrolysis-gas chromatography-mass spectrometry experiments in line with density functional theory (DFT). Evaluation of the sigma potential and sigma surface analysis demonstrated that benzene and ethyl acetate enjoyed better extraction and HMF selectivity, whereas FDCA exhibited ideal behavior in the presence of DMF and DMSO solvents. It was proved that the hydrophobicity could be changed by improving the hydrogen-bonding interaction between them. Moreover, the up-down selection of classes of solvents based on the experimental data found by GC-MS revealed that polar molecular solvents (ethanol-water) were more compatible with carboxylic acids and alcohol compounds, while n-hexane was a desirable solvent for phenolic compounds. It was found that levoglucosan retained a significant fraction of water compared to other solvents, which need to be considered for further economic and environmental analysis under the multifaceted framework of biomass-derived products.

https://doi.org/10.30501/jree.2022.353576.1415

2423-7469/© 2023 The Author(s). Published by MERC. This is an open access article under the CC BY license (https://creativecommons.org/licenses/by/4.0/).

چکیده

فوران دی کربوکسیلیک اسید به عنوان یک ماده با ارزش مشتق شده از هیدروکسیل متیل فورفورال از مواد سلولزی به عنوان یک منبع تجدیدپذیر فراوان شناخته شده است. اگر یک فرآیند جداسازی مناسب توسعه یابد، این ماده می‌تواند برای کاربرد پلاستیک‌های زیستی در آینده استفاده شود. جهت یافتن حلال تجاری، انتخاب جداسازی فوران دی کربوکسیلیک اسید و هیدروکسی متیل فورفورال توسط روش آزمایشگاهی پیرولیز به همراه نظریه تابعی چگالی استفاده شده است. ارزیابی پتانسیل سیگما و آنالیز سطح سیگما نشان داده است که بنزن و اتیل استات حلال مناسب‌تری جهت استخراج هیدروکسی متیل فورفورال می‌باشد درصورتیکه فوران دی کربوکسیلیک اسید رفتار ایده‌آل‌تری برای حلال‌های دی‌متیل فرم‌آلدهید و دی‌متیل سولفوکساید نشان داده است. این اثبات شده است که قطبیت، توسط بهبود اثر متقابل پیوند هیدروژنی بین آن‌ها تغییر یافت. علاوه بر آن انتخاب بالا-پایین حلال‌ها بر اساس داده‌های آزمایشگاهی کروماتوگرافی طیف سنجی جرمی نشان داده است که حلال‌های قطبی (آب-اتانول) با اسیدهای کربوکسیلیک و ترکیبات الکلی سازگارترند، در حالیکه ان-هگزان برای ترکیبات فنلی مناسب‌تر است. همچنین لوگلوکوزان یک تجزیه معنی‌دار نسبت به آب در مقایسه با دیگر حلال‌ها دارد که نیاز است برای آنالیز اقتصادی و محیط‌زیستی تحت یک چارچوب چند بعدی از ترکیبات مشتق شده از زیست‌توده در نظر گرفته شود.

Energy Efficiency Assessment and Optimization of Solar Organic Rankine Cycle for Combined Heat and Power Generation for a Residential Building: Case Study of Baghdad City, Iraq

Mohammed Ali Sami Mahmood [a,b*], Sergei Kuzmin [a]

[a] *Department of Energy Supply for Enterprise and Thermal Engineering, Tambov State Technical University, Tambov, Russia.*
[b] *Department of Machines and Equipment Engineering Techniques, Al-Mussaib Technical College, Al-Furat Al-Awsat Technical University, Babil, Iraq.*

P A P E R   I N F O

Paper History:
Received: 07 September 2022
Revised: 22 October 2022
Accepted: 28 October 2022

Keywords:
Energy Efficiency Assessment,
Solar Organic Rankine Cycle,
CHP,
Baghdad,
Republic of Iraq

A B S T R A C T

Solar Organic Rankine Cycle (SORC) is a successful approach to sustainable development and exploiting clean energy sources. The research aims to improve and evaluate the energy efficiency of the SORC for combined heat and power generation for a residential home under the climatic conditions of Baghdad, Iraq. Thermoeconomic analysis was carried out for the proposed energy supply system. Refrigerant HFC-245fa was used as a working fluid in a solar organic Rankine cycle, and oil poly alkyl benzene (TLV-330) was suggested as a heat transfer fluid in the solar collector field. Parametric studies for some key parameters were conducted to examine the impact of various operating conditions on energy efficiency. The results showed a significant improvement in energy efficiency. The maximum efficiency of SORC CHPG reached 79.14 % when solar heat source temperatures were in the range of 100 to 150 °C and the solar radiation was at a maximum value of 870 W/m^2 at noon on the 15th day of July in Baghdad. The maximum energy produced by SORC CHPG was 472.5 kW when the optimal average value of global solar radiation was 7.5 kWh/m^2/day in June. The economic investigations revealed that the payback period of the new energy supply system was 10 years with the positive net present cost when the solar power plant was working 18 h/day.

https://doi.org/10.30501/jree.2022.360155.1440

2423-7469/© 2023 The Author(s). Published by MERC. This is an open access article under the CC BY license (https://creativecommons.org/licenses/by/4.0/).

چکیده

چرخه رانکین آلی خورشیدی (SORC) یک رویکرد موفق برای توسعه پایدار و بهره‌برداری از منابع انرژی پاک است. هدف از این تحقیق، بهبود و ارزیابی کارایی انرژی چرخه رانکین آلی خورشیدی برای ترکیب حرارت و برق یک خانه مسکونی تحت شرایط آب و هوایی بغداد در عراق است. به این منظور از تجزیه و تحلیل ترمواکونومیک برای سیستم تأمین انرژی پیشنهادی استفاده شد. خنک‌کننده مدل HFC-245fa به عنوان سیال کاری در چرخه رانکین آلی خورشیدی استفاده شد و پلی آلکیل بنزن نفتی (TLV-330) به عنوان سیال انتقال حرارت در میدان کلکتور خورشیدی پیشنهاد شد. مطالعات پارامتریک برای برخی از پارامترهای کلیدی برای بررسی تأثیر شرایط عملیاتی مختلف بر بازده انرژی انجام شد. نتایج، حاکی از بهبود قابل توجهی در بهره‌وری انرژی بود. حداکثر بازده چرخه رانکین آلی خورشیدی CHPG زمانی که دمای منبع حرارت خورشیدی در محدوده ۱۰۰ تا ۱۵۰ درجه سانتیگراد بود و تابش خورشیدی در ظهر روز پانزدهم جولای در بغداد حداکثر ۸۷۰ وات بر متر مربع بود، به ۷۹/۱۴ درصد رسید. حداکثر انرژی تولید شده توسط چرخه رانکین آلی خورشیدی CHPG، ۴۷۲/۵ کیلووات بود، درحالی‌که میانگین بهینه تابش خورشیدی جهانی ۷/۵ کیلووات ساعت بر متر مربع در طور روز در ماه ژوئن بود. بررسی‌های اقتصادی نشان داد که اگر نیروگاه خورشیدی ۱۸ ساعت در روز کار کند، دوره بازپرداخت سیستم جدید تأمین انرژی با هزینه مثبت خالص فعلی ۱۰ سال است.

Techno-Economic and Environmental Analyses of Digestate Treatment after Anaerobic Digestion Process

Ali Nazari, Morteza Hosseinpour *, Mahdi Rezaei

Department of Renewable Energy Research, Niroo Research Institute (NRI), Tehran, Iran.

P A P E R I N F O

Paper History:
Received: 22 June 2022
Revised: 11 August 2022
Accepted: 12 September 2022

Keywords:
Anaerobic Digestion,
Biogas,
Sustainability,
Liquid Dairy Manure,
Aspen Plus

A B S T R A C T

In this study, the impact of digestate treatment after Anaerobic Digestion (AD) process in two scenarios is analyzed in the case of an industrial diary unit in the United States. The first scenario involves production of liquid fertilizer and compost, while the second scenario lacks such a treatment process. Aspen Plus is used to simulate the AD process and evaluate the general properties of biogas and digestate. The results of technical analysis show insignificant changes in the net power production from the CHP unit in Scenario 1. The economic analysis, however, indicates the necessity of digestate treatment for AD systems to be profitable. Furthermore, the results of environmental analysis indicate the mitigation of about 93.4 kilotonnes of greenhouse gas (GHG) emissions in Scenario 1, while AD in Scenario 2 saves only 12 kilotonnes of GHG emissions. In other words, digestate treatment has a more significant environmental impact than the power production and its profitability from CHP unit. The reason could be attributed to the enormous consumption of energy during the production of chemical fertilizers where the digestate treatment process (scenario 1) offsets the utilization of chemical fertilizers in the agriculture industry.

https://doi.org/10.30501/jree.2022.347330.1390

2423-7469/© 2023 The Author(s). Published by MERC. This is an open access article under the CC BY license (https://creativecommons.org/licenses/by/4.0/).

چکیده

در این مطالعه، اهمیت فراورش ماده هضم‌شده برای یک واحد دامداری صنعتی در ایالات متحده، که خروجی واحد هضم بی‌هوازی (AD) است، در دو سناریو مورد بررسی قرار گرفته است. در سناریوی اول از ماده هضم‌شده کود مایع و کمپوست تولید می‌گردد، در حالیکه در سناریوی دوم فراورش ماده هضم‌شده در نظر گرفته نشده است. از نرم افزار اسپن پلاس به منظور شبیه‌سازی فرآیند هضم بی‌هوازی (AD) و خصوصیات بیوگاز و ماده هضم‌شده استفاده شده است. نتایج بررسی‌ها نشان می‌دهد که در سناریوی اول، توان نهایی تولیدشده در واحد تولید همزمان حرارت و برق (CHP) قابل توجه نیست، اما ارزیابی اقتصادی نشان می‌دهد که فرآیند فراورش ماده هضم‌شده، برای اقتصادی بودن فرآیند هضم بی‌هوازی (AD) ضروری می‌باشد. در نهایت، تجزیه و تحلیل محیط‌زیستی انجام‌شده نشان می‌دهد که سناریوی اول انتشار حدود ۹۳/۴ کیلوتن گازهای گلخانه‌ای (GHG) را در یک واحد AD کاهش می‌دهد، درحالی‌که در سناریوی دوم (بدون فراورش ماه هضم‌شده) تنها از انتشار ۱۲ کیلوتن گازهای گلخانه‌ای جلوگیری می‌شود. نتیجه این‌که فراورش ماده هضم‌شده دارای اهمیت بیشتری از نظر محیط‌زیست نسبت به واحد تولید همزمان برق و حرارت (CHP) می‌باشد. به این دلیل که فراورش هضم باعث کاهش تولید و استفاده از کودهای شیمیایی در صنعت کشاورزی می‌شود که انرژی قابل توجهی برای تولید آن صرف می‌شود. نتایج این تحقیق، ضرورت فراورش ماده هضم‌شده برای سیستم‌های AD، زمانی که از فضولات دامی استفاده می‌گردد، را خاطرنشان می‌کند.

Numerical Simulation of a Solar Cooling System Based on Variable-Effect NH_3-Water Absorption Chiller using TRNSYS

Abir Hmida [a], Abdelghafour Lamrani [b], Mamdouh El Haj Assad [c*], Yashar Aryanfar [d], Jorge Luis Garcia Alcaraz [e]

[a] *Applied Thermodynamics Research Laboratory, National Engineering School of Gabes, University of Gabes, Zrig Eddakhlania 6029, Gabes, Tunisia.*
[b] *Mohamed Rougui's Lab, Mohammadia School of Engineers, University of King Mohammed V., Rabat, Morocco.*
[c] *Department of Sustainable and Renewable Energy Engineering, University of Sharjah, Sharjah, United Arab Emirates.*
[d] *Department of Electric Engineering and Computers Sciences, Autonomous University of Ciudad Juarez, Ciudad Juárez 32310, Chih, Mexico.*
[e] *Department of Industrial Engineering and Manufacturing, Autonomous University of Ciudad Juarez, Ciudad Juárez 32310, Chih, Mexico.*

PAPER INFO

Paper History:
Received: 09 February 2022
Revised: 18 June 2022
Accepted: 23 June 2022

Keywords:
Absorption Systems,
Solar Collectors,
Simulation,
Energy Efficiency,
TRNSYS

ABSTRACT

Around the globe, a 60 % increase in energy demand is predicted to occur by the end of the year 2030 due to the ever-increasing population and development. With a registered temperature up to 50 °C in August 2020, which is classified as one of the hottest regions in the world, the demand for cool temperatures in Gabes-Tunisia to achieve the thermal comfort of people ensuring the product storage has become more and more intense. Removing heat from buildings represents the most extensive energy consumption process. In this paper, an absorption-refrigeration system driven by solar energy is proposed. A parametric simulation model is developed based on the TRNSYS platform. A comparison between different models for global radiation calculation and experimental meteorological data was carried out. It has been proven that the Brinchambaut model seems to be the most convenient in describing the real global radiation, with an error of up to 3.16 %. An area of 22 m² of evacuated tube solar collector ensures the proper functioning of the generator and achieves a temperature up to 2 °C in the cold room.

https://doi.org/10.30501/jree.2022.326640.1318

2423-7469/© 2023 The Author(s). Published by MERC. This is an open access article under the CC BY license (https://creativecommons.org/licenses/by/4.0/).

چکیده

پیش‌بینی می‌شود با توجه به رشد روزافزون جمعیت و توسعه، تقاضای انرژی در سراسر جهان تا پایان سال ۲۰۳۰، ۶۰ درصد افزایش یابد. با دمای ثبت شده تا ۵۰ درجه سانتی‌گراد در آگوست ۲۰۲۰، که به عنوان یکی از گرم‌ترین مناطق جهان طبقه‌بندی می‌شود، تقاضا برای دمای خنک در گابس-تونس برای دستیابی به آسایش حرارتی مردم با اطمینان از ذخیره سازی محصول، بیشتر شده است. فرآیند حذف گرما از ساختمان‌ها پیچیده‌ترین فرآیند مصرف انرژی محسوب می‌شود. در این مقاله، یک سیستم تبرید جذبی که توسط انرژی خورشیدی هدایت می‌شود، پیشنهاد شده است. یک مدل شبیه‌سازی پارامتریک بر اساس پلت فرم TRNSYS توسعه یافته است. مقایسه بین مدل‌های مختلف برای محاسبه تابش جهانی و داده‌های آزمایشی هواشناسی انجام شد. یافته ها حاکی از آن است که مدل برینچامبو با خطای ۳/۱۶ درصد، ساده ترین روش برای توصیف و تشریح تشعشعات جهانی واقعی می‌باشد. کلکتور خورشیدی لوله خلأ با مساحت ۲۲ متر مربع باعث عملکرد مناسب ژنراتور شده و دما را تا ۲ درجه سانتیگراد در اتاق سرد کاهش می‌دهد.

Analysis and Evaluation of the Formation of a Heat Island in Tehran During Three Decades

Mohammad Javad Amiri *, Ali Sayyadi

Faculty of Environment, College of Engineering, University of Tehran, Tehran, Iran.

PAPER INFO

Paper History:
Received: 13 July 2022
Revised: 04 September 2022
Accepted: 09 September 2022

Keywords:
Land Use Map,
NDVI,
LST,
Remote Sensing

ABSTRACT

The rising temperature of the earth's surface and the formation of heat islands in megacities have become two of the biggest environmental threats. This compound problem affects urban climatology, including urban vegetation and air pollution, human health, and the environment, including the group of vulnerable members of the society and public health, leading to the growing death rate. Hence, the purpose of this study is to investigate the leading causes of temperature changes and the development of a thermal island in the city of Tehran following the expansion of this metropolis in recent decades. This research uses thermal remote sensing and GIS techniques to analyze information from Landsat satellite images in (TM-ETM-TIRS) sensors from 1984 to 2020. The results of the research indicated that the surface temperature of the city of Tehran during the years 1984 to 1996, 1998 to 2008, and 2010 to 2020 experienced a relative increase in the summer and winter seasons. In the first decade, the average temperature of the green layer was -7, while the temperature of the magenta and red layers were 20 and 25 degrees, respectively. In the second decade, the average temperatures of the green and dark green classes were -1 and 3 while they were 23 and 27 degrees for the magenta and red classes, respectively. In the third decade, the average temperatures of the green and dark green classes were -1 and 3, and thost of the magenta and red layers increased to 28 and 31 degrees, respectively. Furthermore, the analysis of vegetation cover based on the NDVI index pointed to the continuing reduction of vegetation in the studied years. Regarding the direct correlation between the heat island and vegetation and the concentration of the heat island in the city center, further measures must be taken and the vegetation cover should be increased to reduce the heat island. The city center needs to be decentralized as part of the remedy via proper urban design and planning.

https://doi.org/10.30501/jree.2022.349418.1396

2423-7469/© 2023 The Author(s). Published by MERC. This is an open access article under the CC BY license (https://creativecommons.org/licenses/by/4.0/).

چکیده

افزایش دمای سطح زمین و شکل‌گیری جزایر حرارتی در کلان‌شهرها به یکی از معضلات و مشکلات زیست‌محیطی تبدیل شده است. جزیره حرارتی عاملی است که بر اقلیم‌شناسی شهری ازجمله پوشش گیاهی شهری و آلودگی هوا، سلامت انسان و محیط‌زیست ازجمله گروه‌های آسیب‌پذیر جامعه و بهداشت عمومی و افزایش نرخ مرگ‌ومیر تأثیر می‌گذارد؛ بنابراین هدف از این مطالعه بررسی دلایل تغییرات دمایی و شکل‌گیری جزیره حرارتی در شهر تهران به دنبال گسترش این کلان‌شهر در دهه‌های اخیر است. در این پژوهش به‌منظور تجزیه و تحلیل اطلاعات از تصاویر ماهواره‌ای لندست در سنجنده‌های (TM-ETM-TIRS) و از فنون سنجش از دور حرارتی و GIS در سال‌های ۱۹۸۴ الی ۲۰۲۰ استفاده شده است. نتایج پژوهش نشان داد دمای سطح زمین شهر تهران در طی سال‌های ۱۹۸۴ الی ۱۹۹۶ و ۱۹۹۸ الی ۲۰۰۸ و ۲۰۱۰ الی ۲۰۲۰ در فصل‌های تابستان و زمستان افزایش نسبی زیادی داشته است، به‌طوری‌که در دهه اول، میانگین طبقه سبز شامل ۷- و طبقه سرخ آبی و قرمز به ترتیب ۲۰ و ۲۵ درجه و در دهه دوم، میانگین طبقه سبز و سبز تیره شامل ۱- و ۳ و طبقه سرخ آبی و قرمز به ترتیب ۲۳ و ۲۷ درجه و در دهه سوم، میانگین طبقه سبز و سبز تیره شامل ۱- و ۳ و طبقه سرخ آبی و قرمز به ترتیب ۲۸ و ۳۱ درجه افزایش پیدا کرده است. همچنین تجزیه و تحلیل پوشش گیاهی با استفاده از شاخص NDVI، روند کاهش پوشش گیاهی در سال‌های مورد مطالعه را نشان. داد. با توجه به رابطه مستقیم جزیره حرارتی و پوشش گیاهی و تمرکز جزیره حرارتی در مرکز شهر، ابتدا برای کاهش جزیره حرارتی باید پوشش گیاهی افزایش پیدا کند و تمرکززدایی در مرکز شهر به‌وسیله‌ی برنامه‌ریزی‌های شهری صورت گیرد.

Investigation of Wind Speed to Generate Energy Using Machine Learning Algorithms Approach Over Selected Nigerian Stations

Francis Olatunbosun Aweda [a*], Segun Adebayo [b], Adetunji Ayokunnu Adeniji [a], Timothy Kayode Samson [c], Jacob Adebayo Akinpelu [a]

[a] *Physics Programme, College of Agriculture Engineering and Science, Bowen University, P.M.B. 284, Iwo, Nigeria.*
[b] *Mechatronics Engineering Programme, College of Agriculture Engineering and Science, Bowen University, P. M. B. 284, Iwo, Nigeria.*
[c] *Statistics Programme, College of Agriculture Engineering and Science, Bowen University, P. M. B. 284, Iwo, Nigeria.*

P A P E R I N F O

Paper History:
Received: 03 August 2022
Revised: 19 October 2022
Accepted: 28 October 2022

Keywords:
Meteorological Data
Machine Learning
Neural Network
Statistical Models

A B S T R A C T

Wind energy has been identified as a critical component in the growth of all countries throughout the world. Nigeria has been identified as having energy issues as a result of poor maintenance of hydro and thermal energy generating stations. As a result, the current study uses some machine learning approaches over wind speed data for energy generation in the country. Machine learning models were employed for wind speed using selected meteorological parameters. Little research was done using some meteorological data and machine learning to investigate wind speed across Nigerian sub-stations, resulting in the need for further research. This research, on the other hand, focuses on a neural network for forecasting, a Long Short-Term Memory (LSTM) network model based on several fire-work algorithms (FWA). The data for this study came from the archive of the Modern-Era Retrospective analysis for Research and Applications, Version 2 (MERRA-2) Web service, which was modeled. The LSTM predicts the wind speed model based on the FWA, which used hyper-parameter optimization and was based on a real-time prediction model that was dependent on the change and dependence of the neural network. The study data was split into two categories: test and training. According to the validation technique, the sample data was reviewed, and the first 80 % of the data was utilized for training, as revealed by the (LSTM) network model. The remaining 20 % of the data was used as forecast data to ensure that the model was accurate. The normalization of the data for the wind speed range of 0 to 1 which illustrates the process data, the high peak in 1985 (a = 0.12 m/s, b = 0.11 m/s, c = 0.13 m/s, d = 0.08 m/s, e = 0.06 m/s, f = 0.10 m/s) was discovered. However, the summary result of the performances of different 11 Machine Learning algorithms of regression type for each of the seven locations in Nigeria has different values. As a result, it is recommended that this study will facilitate the prediction of wind speed for energy generation in Nigeria.

https://doi.org/10.30501/jree.2022.354698.1422

2423-7469/© 2023 The Author(s). Published by MERC. This is an open access article under the CC BY license (https://creativecommons.org/licenses/by/4.0/).

چکیده

انرژی باد به عنوان یک جزء حیاتی در رشد و توسعه همه کشورهای جهان شناخته می‌شود. نیجریه به دلیل نگهداری ناکارآمد از ایستگاه‌های تولید انرژی آبی و حرارتی با مشکلات عدیده ی انرژی دست و پنجه نرم می‌کند. در نتیجه، مطالعه حاضر از برخی از رویکردهای یادگیری ماشین بر روی داده‌های سرعت باد برای تولید انرژی در کشور استفاده می‌کند. مدل‌های یادگیری ماشین برای سرعت باد با استفاده از پارامترهای هواشناسی انتخاب شده استفاده شد. تحقیقات کمی با استفاده از برخی داده‌های هواشناسی و یادگیری ماشینی برای بررسی سرعت باد در ایستگاه‌های فرعی نیجریه انجام شده، که در انتها مبین نیاز به تحقیقات بیشتر می‌باشد. از سوی دیگر، این تحقیق بر روی یک شبکه عصبی برای پیش‌بینی عملکرد یک مدل شبکه حافظه کوتاه‌مدت (LSTM) بر اساس چندین الگوریتم آتش‌کاری (FWA) تمرکز دارد. داده‌های این مطالعه از آرشیو تحلیل گذشته‌نگر عصر مدرن برای تحقیقات و برنامه‌های کاربردی، نسخه ۲ (MERRA-2) سرویس وب، که مدل‌سازی شده بود، به دست آمد. LSTM مدل سرعت باد را بر اساس FWA پیش‌بینی می‌کند که از بهینه‌سازی فراپارامتر استفاده می‌کرد و بر اساس یک مدل پیش‌بینی زمان واقعی بود که به تغییر شبکه عصبی وابسته بود. داده های مطالعه به دو دسته آزمون و آموزش تقسیم شدند. با توجه به تکنیک اعتبار سنجی، داده‌های نمونه بررسی شد و ۸۰ درصد اول داده‌ها برای آموزش استفاده شد، همانطور که توسط مدل شبکه (LSTM) آشکار شد. ۲۰ درصد باقی مانده از داده‌ها به عنوان داده‌های پیش‌بینی برای اطمینان از صحت مدل استفاده شد. نرمال سازی داده‌ها برای محدوده سرعت باد ۰ تا ۱ که داده‌های فرآیند را نشان می‌دهد، اوج بالا در سال ۱۹۸۵ (a = 0.12 m/s ،b = 0.11 m/s ،c = 0.13 m/s ،d = 0.08 m/s ،e = 0.06 m/s ،f = 0.10 m/s) کشف شد. با این حال، نتیجه خلاصه عملکرد ۱۱ الگوریتم مختلف یادگیری ماشین از نوع رگرسیون برای هر یک از هفت مکان در نیجریه دارای مقادیر متفاوتی است. در نتیجه، توصیه می‌شود که این مطالعه پیش‌بینی سرعت باد برای تولید انرژی در نیجریه را تسهیل کند.

Prediction of Anthropogenic Greenhouse Gas Emissions via Manure Management in Indonesia and Alternative Policies for Indonesian Livestock Development

Nur Aini [a*], Widi Hastomo [a], Ratna Yulika Go [b]

[a] *Department of Management, Faculty of Economic and Business, Ahmad Dahlan Institute of Technology and Business, Indonesia.*
[b] *Department of Information Technology, Faculty of Computer Science, Universitas Indonesia, Indonesia.*

P A P E R I N F O

Paper History:
Received: 05 August 2022
Revised: 08 October 2022
Accepted: 17 October 2022

Keywords:
GHG Emission,
Indonesia,
Livestock Policy,
Development,
Emission Prediction

A B S T R A C T

The percentage of production and utilization of hydrocarbon resources from the livestock sector has raised concerns regarding the worldwide issue of global warming. A total of CH_4 emissions from enteric fermentation and waste management has been estimated at 78.3 %. Meanwhile, N_2O emissions are 75-80 % of total agricultural emissions. This raises questions about the extent of global warming due to increased CO_2 resulting in changes in weather and global warming. This research aims to predict Green House Gas (GHG) emissions from manure management and present policy alternatives for Indonesian livestock development. Secondary data was taken from a related website (fao.org) with coverage throughout Indonesia from 1961 to 2021, containing 12,480 rows and 5 column features including item, Element, Year, Unit, and Value emission. LSTM and GRU are used to predict the trend of emission from manure management to provide alternative policies on greenhouse gas mitigation in Indonesia. The results showed that based on 15 types of livestock that emit GHG emissions, 3 types of livestock produce the highest emissions from 1961 to 2021: (a) cattle, (b) cattle and non-dairy, and (c) poultry. Significant reduction in the emission of carbon dioxide (CO_2eq) in 2020 is indicated by reduced public consumption and hampered supply chains with large-scale social restrictions (covid-19 pandemic policy). Based on these results, fertilizer storage duration can be used as a policy to reduce CO_2eq emissions, hence it is desired that fertilizer management techniques can be properly regulated. Mitigation can also be accomplished by utilizing livestock waste as biogas and upgrading animal feed additives with chitosan or potassium nitrate.

https://doi.org/10.30501/jree.2022.354796.1423

2423-7469/© 2023 The Author(s). Published by MERC. This is an open access article under the CC BY license (https://creativecommons.org/licenses/by/4.0/).

چکیده

درصد تولید و استفاده از منابع هیدروکربنی از بخش دام، نگرانی‌هایی را در رابطه با موضوع گرم شدن کره زمین در سراسر جهان ایجاد کرده است. مجموع انتشار گاز متان از تخمیر روده ای و مدیریت ضایعات ۷۸/۳ ٪ برآورد شده است. در همین حال، انتشار گاز N_2O، ۸۰-۷۵ درصد از کل انتشارات حاصل از کشاورزی است. این امر، سؤالاتی را در مورد میزان گرمایش جهانی به دلیل افزایش CO_2 و در نتیجه تغییرات آب و هوا و گرم شدن کره زمین ایجاد می کند. هدف از این تحقیق پیش‌بینی انتشار گازهای گلخانه‌ای (GHG) از مدیریت کود و ارائه سیاست‌های جایگزین برای توسعه دام در اندونزی است. داده‌های ثانویه از یک وب‌سایت مرتبط (fao.org) با پوشش سراسری اندونزی از سال ۱۹۶۱ تا ۲۰۲۱ گرفته شده است که شامل ۱۲۴۸۰ ردیف و ویژگی‌های ۵ ستونی شامل آیتم، عنصر، سال، واحد و مقدار انتشار است. LSTM و GRU برای پیش‌بینی روند انتشار از مدیریت کود برای ارائه سیاست‌های جایگزین در کاهش گازهای گلخانه‌ای در اندونزی استفاده می‌شوند. نتایج نشان داد که بر اساس ۱۵ نوع دام که انتشار گازهای گلخانه ای دارند، ۳ نوع دام بالاترین انتشار را از سال ۱۹۶۱ تا ۲۰۲۱ تولید می کنند: (الف) گاو، (ب) گاو و غیر لبنی و (ج) طیور. کاهش قابل توجه انتشار دی اکسید کربن (CO_2eq) در سال ۲۰۲۰ با کاهش مصرف عمومی و مختل شدن زنجیره تأمین با محدودیت های اجتماعی در مقیاس بزرگ (سیاست همه گیری کووید-۱۹) نشان داده شده است. بر اساس این نتایج، مدت زمان ذخیره سازی کود می تواند به عنوان سیاستی برای کاهش انتشار CO_2eq مورد استفاده قرار گیرد، از این رو مطلوب است که تکنیک های مدیریت کود را بتوان به درستی تنظیم کرد. این نوع کاهش نیز می‌تواند از طریق استفاده از فضولات دام به عنوان بیوگاز و ارتقاء افزودنی های خوراک دام با کیتوزان یا نیترات پتاسیم عملی کرد.

Feasibility Study of Energy Production from Small Archimedes Turbines on the Coast of Bandar Abbas and Calculation of Efficiency Optimization Parameters by Linear Programming

Majid Zarezadeh [a*], Hoda Mansouri [b], Alireza Eikani [c]

[a] *Department of Planning and Support, Administration Standard of Hormozgan, Iranian National Standard Organization, P. O. Box: 7919716839, Bandar Abbas, Hormozgan, Iran.*
[b] *Technical Director of Inspection, Nik Azmai Hormozgan Co., Bandar Abbas, Hormozgan, Iran.*
[c] *Department of Electrical Engineering, Amirkabir University of Technology, Tehran, Iran.*

PAPER INFO

Paper History:
Received: 09 June 2022
Revised: 14 August 2022
Accepted: 21 August 2022

Keywords:
Archimedes Turbine,
Linear Programming,
Feasibility Study,
Numerical Study,
Tidal Waves

ABSTRACT

In this study, in addition to assessing the conditions in the coastal region of Bandar Abbas, the feasibility of utilizing Archimedes torsional turbines for renewable energy production in this area was investigated through a combination of field measurements and numerical simulations. Field studies included the measurement of environmental conditions, depth, and vessel traffic. The determination of a safe depth was based on these measurements. Additionally, the current patterns were assessed in the field, measuring key parameters like salinity, electrical conductivity, and density. To further develop the results, a numerical simulation was conducted using the ROMS numerical model to establish the hydrodynamic current patterns in the target area. Upon reviewing the outcomes with the SOLVER program and employing linear programming methods, effective constraints derived from field monitoring were created. The study explored the optimal energy efficiency of Archimedes torsional turbines under different inclinations relative to the seabed and angular velocities. The research and simulations revealed that varying the tilt of the vertical axis of the turbine within the range of 5 to 15 degrees significantly impacted the turbine's efficiency. The highest efficiency, at 75 %, was achieved at a 15-degree angle with a turbine rotation speed of 150 rpm. This result is particularly notable, considering the low slope of the studied area.

https://doi.org/10.30501/jree.2022.345193.1383

2423-7469/© 2023 The Author(s). Published by MERC. This is an open access article under the CC BY license (https://creativecommons.org/licenses/by/4.0/).

چکیده

در این پژوهش، ضمن بررسی شرایط منطقه ساحلی بندرعباس، امکان استفاده از توربین‌های پیچشی ارشمیدس برای تولید انرژی‌های تجدیدپذیر در این منطقه، با اندازه‌گیری میدانی و شبیه‌سازی عددی مورد بررسی قرار گرفته است. پس از مطالعه میدانی شرایط محیطی، عمق و میزان تردد شناور اندازه‌گیری شد. پس از محاسبه عمق امن منطقه، از طریق اندازه‌گیری میدانی الگوی جریان، پارامترهای مؤثر مانند شوری، هدایت الکتریکی و چگالی اندازه‌گیری شد و به منظور توسعه نتایج با استفاده از شبیه‌سازی عددی با مدل عددی ROMS، الگوی هیدرودینامیکی جریان کشندی برای منطقه مورد مطالعه، شبیه‌سازی شد. پس از بررسی نتایج، با استفاده از برنامه SOLVER و روش برنامه‌ریزی خطی و ایجاد محدودیت‌های مؤثر در پایش میدانی، بازده انرژی بهینه توربین‌های پیچشی ارشمیدس برای سرعت‌های متفاوت و زاویه‌های متفاوت شیب محور افقی توربین نسبت به بستر دریا بررسی شده است. نتایج تحقیق و شبیه‌سازی نشان داد که تغییر شیب محور افقی توربین بین زوایای ۵ تا ۱۵ درجه، منجر به تغییر بازده توربین ارشمیدس می‌شود. بر اساس نتایج، مقدار بازده بهینه، ۷۵ درصد، در زاویه ۱۵ درجه بود و سرعت چرخش توربین ۱۵۰ دور در دقیقه، بالاترین بازده را نشان داد. این نتیجه با توجه به شیب کم بستر منطقه مورد مطالعه نتیجه قابل قبولی است.

CONTENTS

Journal Homepage: www.jree.ir